PhD in Chemical Science and Technology

Cycle XXXVI

Sustainable development of high sensitivity piezoelectric ceramics in the BCZT system for applications in bio-devices

PhD Student: *Marzia Mureddu*

Coordinator of the PhD Program: *Prof. Carla Cannas*

Supervisor: *Prof. Sebastiano Garroni*

Co-Supervisor: *Prof. Lorena Pardo Mata*

Final Exam: Academic Year 2023-2024

25th June 2024

A mio padre,

Devo a te tutto ciò che sono. So che ci saranno sempre delle orme invisibili accanto alle mie.

Summary

1 Introduction

1.1 Problem statement

The mind does its best when the situation requires it. The same is true for scientific progress, in fact any technological advancement stems from a need. The search for new materials has always arisen from the need to replace the materials already used and known with others that could have better properties at lower costs, easiness of availability and versatility. It is precisely the versatility that makes piezoelectric materials so interesting. In fact, during the last century, these have met the needs of the moment and have enabled the technological advancement of already known devices. Piezoelectric materials belong to the macro class of the so called “smart materials” such as electrostrictive materials, magnetostrictive materials, shape memory materials, electrochromic materials, phase change materials [1,2]. Smart materials are a family of materials that are listed in the advanced materials class. These show an environment-dependent self-accommodation and are classified according to their stimulus-dependent responses, which can be physical (pressure, temperature, humidity, light, electric field, magnetic field), chemical (pH, CO_2, etc.) or biological. Thus, they have the intrinsic and extrinsic capacity, firstly, to respond to environmental stimuli and changes and, secondly, to activate their functions according to these changes [3].

Nowadays, in the daily life of an average European citizen, many devices that are routinely used contain, without the user awareness, the so-called smart materials, including piezoelectric ones. As visualized in Figure 1.1.1, that does not pretend to be exhaustive, the use of piezoelectric ranges from well-consolidated technologies (submarines, sonars, actuators, ultrasonic motors, transformers, micro-energy harvesting devices, hydrophones, high-resolution ultrasonic medical imaging, accelerometers in mobile phones, notebooks) to new frontier applications in biomedical field [4–6]; making it possible to search for enemies on the ocean floor, observe the characteristics of unborn children, light fires on the beach, observe the smallest details of living things, and listen to music [7].

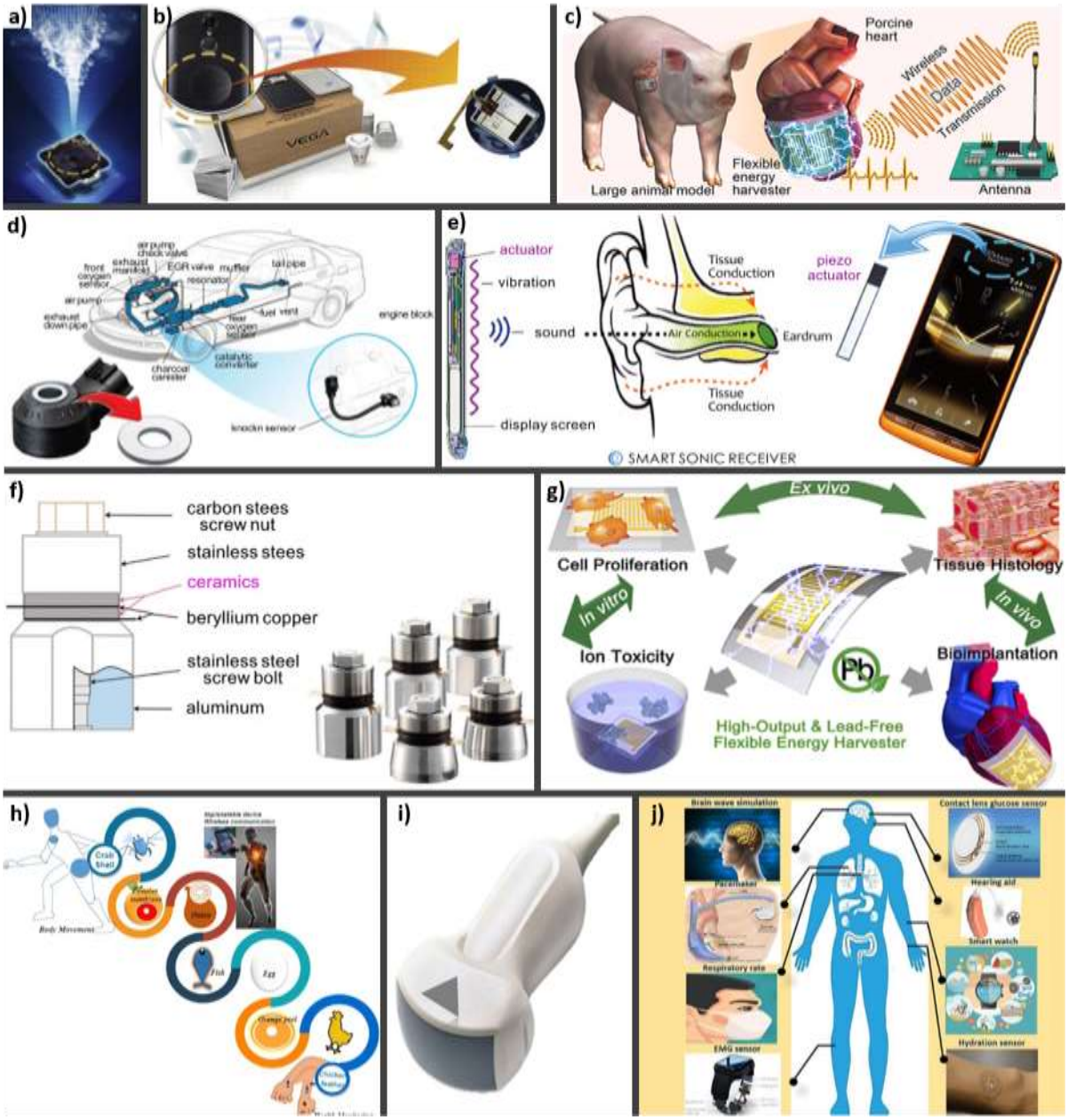

Figure 1.1.1 Some well-consolidated technologies and new applications of lead-free piezoelectric materials: **a)** Piezoelectric-based micro blower [8]; **b)** A smartphone with an embedded piezo-speaker [8]; **c)** Schematics of the bioimplantable self-powered electronic system. The flexible energy harvester mounted on a porcine heart [11]; **d)** A knock sensor for automobile engine monitoring [8]; **e)** A smartphone featured by a 'speaker-less' function based on a bone conduction mechanism [8]; **f)** A piezoelectric transducer [8], **g)** Schematics describing the comprehensive biocompatibility of high-performance lead-free flexible energy harvester [11]; **h)** nanogenerators based on natural materials [10];**i)** A new generation 4D probe for ultrasonic scanner [9]; **j)** other proposed applications. It should be noted that materials used in biomedical flexible sensors, such as natural materials like chitosan (already studied for BT-based biocomposites) [12] together with natural Biodegradable Piezoelectric Polymers [13]are becoming increasingly important for this type of applications.

Piezoelectric materials have the capability of generating an electric charge in response to mechanical deformation and, conversely, to generate a strain (contraction or expansion) under the application of an

electric field. The historical development of discoveries, which consists of several crucial steps, on of piezoelectric ceramic materials and ferroelectric effect, will be described in Chapter 2. These effects, discovered by Curie brothers (Pierre and Jacques Curie) in the late 1880, sparked the interest in piezoelectricity of crystals, starting from Rochelle salt, cane sugar, quartz, tourmaline and topaz. Originally, quartz was used as resonator in SONAR devices for submarines. The ferroelectric effect, strictly related to the piezoelectricity in polycrystals, was discovered by Valasek in 1920 in the Rochelle salt. The real breakthrough in this field was the discovery of the ferroelectricity of Barium Titanate in 1945, a perovskite dielectric oxide material. From this point on, it began the understanding of piezoelectric polycrystals. Then, it came the so-called "proliferation decade" where Lead Titanate, Lead Zirconate Titanate materials were discovered [14–16]. Since 1960, with respect to the well consolidated technologies and commercialized devices, the market-dominant lead-based piezoceramic known as PZT (Lead Zirconate Titanate), a solid-solution system with a general formula $Pb(Zr_xTi_{1-x})O_3$, is still the undisputed leader, thanks to its versatility and good electromechanical properties [17,18]. Besides, piezoceramics are cheaper to fabricate than the piezoelectric crystals used in the first times of the development of the piezoelectric applications and can take desired shapes (cylinders, bowls, and so on) not easily available for crystals.

Currently, needs have changed again, and the ever-increasing interest in environmental defence and protection is driving scientific research toward the design of smart materials that respect human health and do not pollute, while having similar or better properties than the materials to be replaced [19]. The need to find new and eco-friendly materials that accomplish the European Union Directives are pushing the research toward the development of new environmentally benign alternative materials to PZT. Among the recently issued European Directives in this field, we have to take into account: RoHS (Restriction of Hazardous Substances Directive), Ceramic Roadmap to 2050 and CO_2 Carbon Capture and Green Chemistry guidelines [8,20,21,22]. The goal of replacing widespread lead-based materials is becoming increasingly stringent, due to the high toxicity of Lead and Lead oxide for human health, the growing interest in the disposal of processing waste products and the use of toxic raw materials, such as PbO, that is the main precursor of PZT [22,23]. Another key point is developing new processing routes that can guarantee the reduction of CO_2

emissions, by using lower processing temperatures and that can meet the European Directives targets for ceramics market, i.e. finding new routes free of organic solvents [24]. Among the most promising candidates to replace the PZT system, we can find several families of lead-free materials, such as (K, Na) NbO_3 (KNN)-based, ($Bi_{0.5}$, $Na_{0.5}$) TiO_3 (BNT)-based, and BCZT- based piezoceramics, each with its own peculiarities. The main characteristics, reported as strengths and weaknesses of the above-mentioned lead-free materials compared to PZT are graphically summarized in **Figure1.1.2** [25,26]. In this group, the Barium Calcium Zirconate Titanate system, well known as BCZT , with a general formula $(Ba_{1-x}Ca_x)(Ti_{1-y}Zr_y)O_3$, has attracted considerable interest from the scientific community, in particular due to the high quasi static piezoelectric coefficient for an optimal composition, BZT-50 BCT for $Ba(Ti_{0.8}Zr_{0.2})O_3$-$(Ba_{0.7}Ca_{0.3})TiO_3$ solid solution, comparable to those of the commercially available lead-based materials (600pC/N vs up to ≈ 300 pC/N for hard-PZT and up to ≈ 550 pC/N for soft PZT [27–29]) . Compared to the PZT-based systems, it has a lower density (6 g/cm^3 vs 8 g/cm^3) that can be suitable for acoustic applications [30]. Not less important, the absence of volatile alkaline elements (Na,K), which are present in KNN-based system, allows better control of the stoichiometry chosen at the design stage [26].

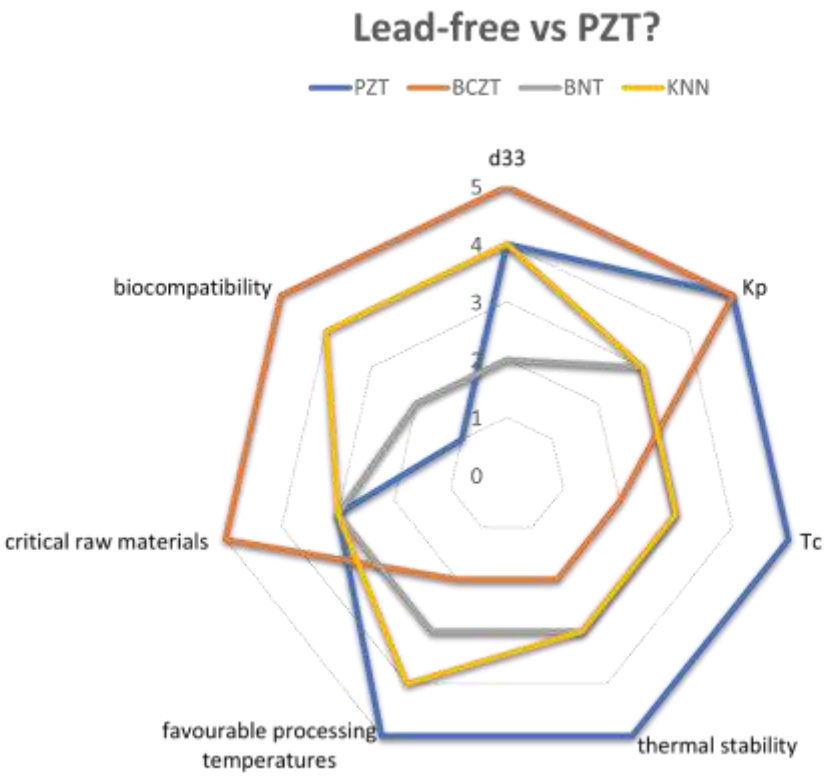

Figure 1.1.2 Some relevant strengths and drawbacks of principal families of lead-free materials. Scores have been attributed on the basis of reported properties. The presence of critical raw materials and biocompatibility have also been considered. Please note that favourable temperatures mean milder conditions [31].

Despite considerable progress in recent years, with good properties being obtained through various processing routes, the commercialization of BCZT is still affected by certain limitations [32]. To date, according to the current state of the art, the main open issues that can be encountered when transferring the ceramic processing to the industrial level, can be summarized as follows: i. Decreasing the high synthesis (up to 1300 °C) and sintering (up to 1550 °C) temperatures required for the solid-state route is absolutely mandatory, ii. Developing water-based and environmentally friendly solid-state routes will be indispensable in the near future for industrial scalability; iii. New insights on the formation mechanism of the BCZT perovskite are desperately needed; iv. Finding non-toxic, alternative and scalable chemical synthesis methods to better control grain growth and achieve a good, homogenous microstructure is crucial for obtaining optimal final properties, v. Given the growing interest in biomedical applications, defining the toxicological profile of this system is now of considerable importance; vi. Propose poling facilities that can be

used for *in situ* XRD experiments with laboratory diffractometer as an easily available alternative to synchrotron beam lines can be helpful to deeply study the transformations that occur in the system [29]. In addition, ensuring reproducibility of properties for precise applications and scalability of the processing route is one of the main goals of research and the main demand of companies [33]. Transferring knowledge on a laboratory scale to an industrial level remains a challenge to be played in the coming years when companies will be forced to accomplish to European Directives and to the lead-free transition. Despite of this, recently, progresses have been achieved by some companies which realize other lead-free ceramics. Some examples have been reported in Figure 1.1.3. On the other hand, nowadays, BCZT ceramics are not produced at industrial scale.

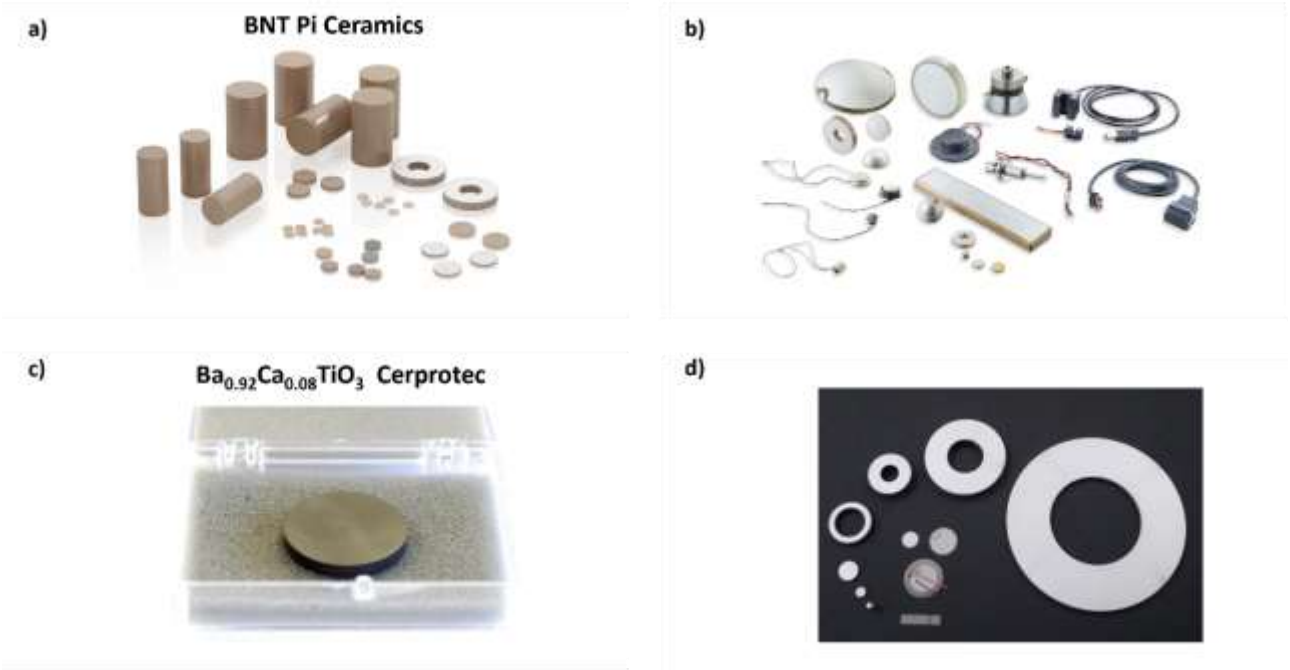

Figure 1.1.3 Some examples of lead-free ceramics realized by piezoceramic leader companies. **a)**bismuth sodium titanate-BNT for ultrasonic transducers in the MHz range as well as for sonar and hydrophone applications by PI Ceramics [34]; **b)**SONOX® P1 LF(composition not declared) by CeramTec [35]; **c)**$Ba_{0.92}Ca_{0.08}TiO_3$ by CerPoTech (that produces other lead-free materials as declared in the web page [36] ; **d)**lead-free ceramics produced by NGK Spark Plug [37].

1.2 Aims of the thesis

All the basic knowledge collected from the literature can help to optimize the entire processing route, the microstructure, the poling conditions and, consequently the electromechanical properties. Given the above-mentioned considerations, the aim of this Doctoral thesis has been here summarized in Figure 1.2.1:

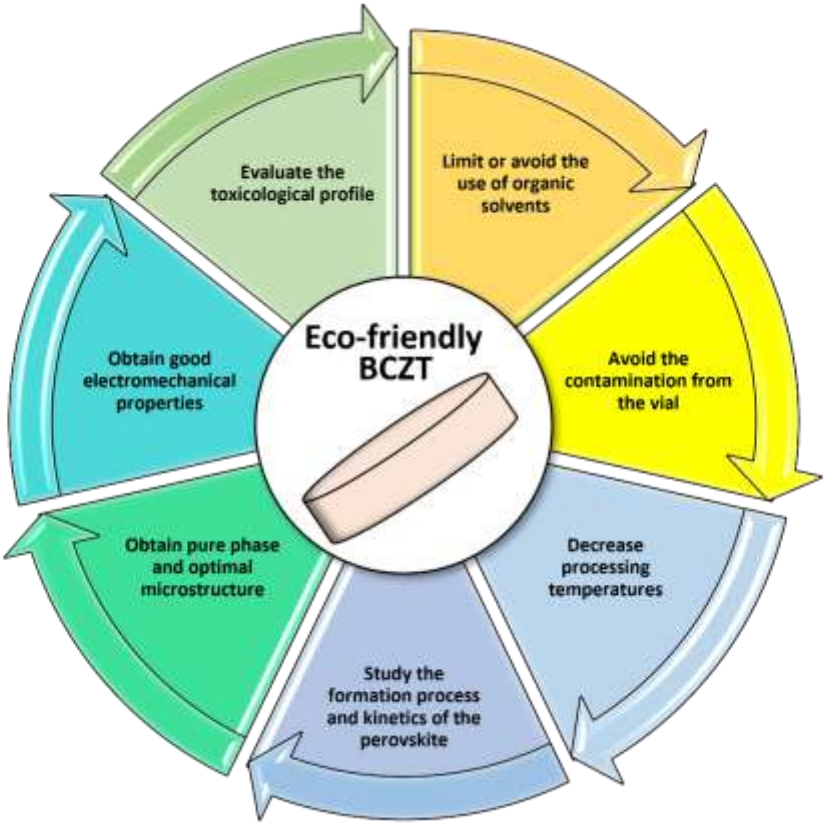

Figure 1.2.1 Graphical representation of the main goals of the present Doctoral Thesis.

- i. Regarding the processing by solid-state route, one of the most useful techniques to decrease the calcination and sintering temperatures is represented by the mechanical or mechanochemical activation of precursors by ball-milling, which can promote the synthesis of the main perovskite and improve the reactivity towards sintering of the system in order to achieve the desired microstructural homogeneity [38–40]. For this technique the main drawback is the contamination of the powder from the milling tools (vial and balls), that can alter the chemical composition and change the stoichiometry chosen, having a negative influence on the ceramic final properties [41,42]. **Starting from the most studied MPB composition, we investigated**

the effect of milling tool contamination on the piezoelectric properties of the final ceramic from the vial, using different milling tools, such as stainless steel and tungsten carbide (Chapter 5).

- ii. Alternative paths, to solid state route, that allow a better stoichiometric control, may be represented by chemical synthesis methods, such as sol-gel techniques and its variations, through which products with a high degree of purity and lower processing temperatures can be obtained, but for which scalability is still difficult [43]. **Hence, we propose an alternative non-toxic sol-gel synthesis -Pechini modified type (Chapter 6).**

- iii. Aiming to overcome the contamination issue and in the search of a scalable processing, we developed a new solid-state route in isopropanol using a non-contaminating ball milling system, exploring a poorly studied composition. **We underlined the effect of mechanical activation of the precursors on the formation temperature of the main BCZT perovskite (Chapter 7).**

- ii. Nowadays, due to economic, environmental and safety reasons, the use of organic solvents at industrial level is very limited. However, in solid-state processing of piezoceramics alcohols and ketones are commonly used. In this respect, generating a novel environmentally friendly water-based solid-state route through which is possible to overcome the main issues that can arise with the use of water (solubility of carbonates, hydrolysis, demixing of the slurry) can promote the production of lead-free piezoceramics. **We managed to tackle these issues by using a combination of non-contaminating attrition ball-milling in water and lyophilization. The synergetic effect of these combined techniques promotes the homogeneity of the obtained powders avoiding the use of polluting organic solvents and allows the decrease of processing temperatures, while maintaining good electromechanical properties (Chapter 8).**

- iii. At the current state of the art, few works on the processes of formation and crystallization kinetics are reported [43]. Further studies can help to have a deep knowledge of this complex pseudo-ternary system. **For these reasons, we present a formation mechanism for BCZT perovskite, the process kinetics and the reactions that occur by using a combination of ball-milling technique and freeze drying. We highlighted the**

influence of mechanical activation of precursors compared to pristine mixed raw materials on the reduction of perovskite formation temperature (Chapter 9).

- v. Due to the growing interest of piezoceramics for biomedical applications, such as implants and bone regeneration and so on, it must be taken into account the toxicological profile of BCZT-based materials. To date, this aspect has been analysed considering only specific routes and compositions [45]. A careful analysis of the toxicological behaviour of this system, regardless of the route of process and its composition, seems to be essential today. **We analyse the toxicological profile of BCZT-based systems employing two widely used human and environmental cellular models (A549 cell line and *Saccharomyces cerevisiae*), taking into consideration the different vials used for activating the powders and exploring different compositions (Chapter 10).**

- vi. Recently, *in situ* XRD experiments have been performed to monitor the change of the crystal structure of the piezoceramic as a function of the applied poling electric field [46].The same apparatus can be used to confirm the temperature at which the ferro-para polymorphic phase transition can be observed (Curie Point), and ferro-ferro polymorphic transitions previously measured by using dielectric measurements. **We propose an alternative poling apparatus, suitable for common laboratory diffractometer, to perform *in situ* poling/temperature diffraction experiments for BCZT piezoceramics., already tested for BT-based ceramics (Chapter 11).**

1.3 Structure of the thesis

The layout of thesis is described as follows:

Chapter 1 introduces the general aims and structure of the thesis.

Chapter 2 provides an overview of piezoelectricity, starting with a historical introduction, and then continues with a classification of piezoelectric materials as polar dielectrics, with a special focus on perovskite-type structure ferroelectric ceramics. A brief overview of piezoelectric coefficients and commonly used measurement techniques, specifically the resonance methods to perform electromechanical characterization

is supplied, with a description of the alternative automatic iterative method of analysis of complex impedance curves. An understanding of the piezoelectric effect, its coefficients and perovskite structures as is essential for the final application.

Chapter 3 represents a current state of art in the field of BCZT piezoceramics. It begins by illustrating the fundamentals of the system, starting from the historical evolution of the BCZT phase diagram. Furthermore, the effect of the Morphotropic Phase Boundary (MPB) in enhancing the piezoelectric properties will be also presented. Subsequently followed by a brief overview on the solid-state route and the influence of the processing on the properties of BCZT ceramics. Specific focus is given to the effect of mechanical activation and the processing temperatures reported. In addition, the state of the art concerning chemical methods used for the synthesis of BCZT system will be present. In conclusion, the state of the art of biomedical applications will be discussed.

Chapter 4 reports the description of the methodology used to characterise each and every step of the processing route.

The following chapters focuses with results of different research activities obtained during this PhD program.

Chapter 5 will provide preliminary results obtained using stainless steel and tungsten carbide vials for mechanically activate both precursors and calcined powders with particular emphasis on the effect of contamination coming from the jar material on the ceramics final electromechanical properties.

Chapter 6 will present the results obtained by using a nontoxic Pechini modified sol-gel route as an alternative chemical method to the solid-state route.

Chapter 7 will provide analysis and comments of the experimental results obtained on the BCZT-based systems prepared through the widespread solid-state route, using the mechanical activation method. Particular emphasis is given to the optimization of the milling process by using non-contaminant attrition ball milling apparatus and isopropanol as liquid medium that leads to a strong reduction of processing temperatures. In this section, the structure / electrical properties relationship will be deeply analysed.

Chapter 8 will be devoted to the comments on the experimental results obtained on the BCZT-system prepared by using an innovative environmentally friendly water-based solid-state route, using a combination of efficient attrition ball-milling and lyophilization method. The effect on final ceramics electromechanical properties has been also evaluated.

Chapter 9 describes the results obtained at synchrotron beam line that allowed to shed light on the formation mechanism of BCZT perovskite. The process kinetics, the activation energy, and the reactions that occur in the ball-milled and lyophilized precursors in comparison to unmilled raw materials were also evaluated.

Chapter 10 will focus on the evaluation of the toxicological profile, assessed on human and environmental cellular models (A549 cell line and *Saccharomyces cerevisiae*), of BCZT ceramics obtained via solid-state by using different milling tools.

Chapter 11 provides a description of *in situ* poling/temperature diffraction experiments setup and the results achieved, using a common laboratory diffractometer as an alternative of synchrotron facilities, thanks to an innovative multifunctional device.

Chapter 12 provides a general overview of the main results achieved and the future perspectives opened by the research activities conducted during this Phd thesis.

1.4 Bibliography

1. J. Holterman, P.G. An Introduction to Piezoelectric Materials and Applications; Stichting Applied Piezo, 2013;

2. Qader, I.N.; Kök, M.; Dagdelen, F.; Aydogdu, Y. A Review of Smart Materials: Researches and Applications. El-Cezeri J. Sci. Eng. **2019**, 6, 755–788, doi:10.31202/ecjse.562177.

3. Bahl, S.; Nagar, H.; Singh, I.; Sehgal, S. Smart Materials Types, Properties and Applications: A Review. Mater. Today Proc. **2020**, 28, 1302–1306, doi:10.1016/j.matpr.2020.04.505.

4. Lionetto, F.; Licciulli, A.; Montagna, F.; Maffezzoli, A. Piezoceramici : **2004**, 107–127.

5. Rödel, J.; Webber, K.G.; Dittmer, R.; Jo, W.; Kimura, M.; Damjanovic, D. Transferring Lead-Free Piezoelectric Ceramics into Application. J. Eur. Ceram. Soc. **2015**, 35, 1659–1681, doi:10.1016/j.jeurceramsoc.2014.12.013.

6. Yang, C.; Ji, J.; Lv, Y.; Li, Z.; Luo, D. Application of Piezoelectric Material and Devices in Bone Regeneration. Nanomaterials **2022**, 12, doi:10.3390/nano12244386.

7. Szabo, T.L.; Lewin, P.A. Ultrasound Transducer Selection in Clinical Imaging Practice. J. Ultrasound Med. **2013**, 32, 573–582, doi:10.7863/jum.2013.32.4.573.

8. Hong, C.H.; Kim, H.P.; Choi, B.Y.; Han, H.S.; Son, J.S.; Ahn, C.W.; Jo, W. Lead-Free Piezoceramics – Where to Move On? J. Mater. 2016, 2, 1–24.

9. Garroni, S.; Senes, N.; Iacomini, A.; Enzo, S.; Mulas, G.; Pardo, L.; Cuesta-Lopez, S. Advanced Synthesis on Lead-Free KxNa(1−x)NbO3 Piezoceramics for Medical Imaging Applications. Phys. Status Solidi Appl. Mater. Sci. **2018**, 215, 1–15, doi:10.1002/pssa.201700896.

10. Divya, S.; Oh, T.H.; Bodaghi, M. 1D Nanomaterial Based Piezoelectric Nanogenerators for Self-Powered Biocompatible Energy Harvesters. Eur. Polym. J. **2023**, 197, 112363, doi:10.1016/j.eurpolymj.2023.112363.

11. Jeong, C.K. Toward Bioimplantable and Biocompatible Flexible Energy Harvesters Using Piezoelectric Ceramic Materials. MRS Commun. **2020**, 10, 365–378, doi:10.1557/mrc.2020.48.

12. Guzmán Sierra, D.L.; Bdikin, I.; Tkach, A.; Vilarinho, P.M.; Nunes, C.; Ferreira, P. Flexible Piezoelectric Chitosan and Barium Titanate Biocomposite Films for Sensor Applications. Eur. J. Inorg. Chem. **2021**, 2021, 792–803, doi:10.1002/ejic.202000938.

13. Ali, M.; Bathaei, M.J.; Istif, E.; Karimi, S.N.H.; Beker, L. Biodegradable Piezoelectric Polymers: Recent Advancements in Materials and Applications. Adv. Healthc. Mater. **2023**, 12, 1–32, doi:10.1002/adhm.202300318.

14. Uchino, K. Advanced Piezoelectric Materials: Science and Technology.; Woodhead Publishing, 2017;

15. Li, J.F. Lead-Free Piezoelectric Materials; John Wiley & Sons, 2020;

16. Behera, A., & Behera Piezoelectric Materials. Advanced Materials: An Introduction to Modern Materials Science. In Advanced Materials: An Introduction to Modern Materials Science; 2022; pp. 43–76.

17. Zhang, S.; Xia, R.; Shrout, T.R. Lead-Free Piezoelectric Ceramics vs. PZT? J. Electroceramics **2007**, 19, 251–257, doi:10.1007/s10832-007-9056-z.

18. Sekhar, M.C.; Veena, E.; Kumar, N.S.; Naidu, K.C.B.; Mallikarjuna, A.; Basha, D.B. A Review on Piezoelectric Materials and Their Applications. Cryst. Res. Technol. **2023**, 58, 1–22,

doi:10.1002/crat.202200130.

19. Panda, P.K.; Thejas, B.S.T.S.; Krishna, M. High d 33 Lead ‐ Free Piezoceramics : A Review. J. Electron. Mater. **2022**, 51, 938–952, doi:10.1007/s11664-021-09346-0.

20. Pardo, L.; Villafuerte-Castrejón, M.E.; Morán, E.; Reyes-Montero, A.; Vivar-Ocampo, R.; Gonzalez, A.M. Ecological, Lead-Free Ferroelectrics. Magn. Ferroelectr. Multiferroic Met. Oxides **2018**, 201–219, doi:10.1016/B978-0-12-811180-2.00009-8.

21. Rödel, J.; Li, J.F. Lead-Free Piezoceramics: Status and Perspectives. MRS Bull. 2018, 43, 576–580. 10.1557/mrs.2018.181

22. Restriction of the Use of Certain Hazardous Substances in Electrical and Electronic Equipment (RoHS) Statement on the " RoHS " Directive. **2019**, 44, 1999463.

23. Ibn-Mohammed, T.; Reaney, I.M.; Koh, S.C.L.; Acquaye, A.; Sinclair, D.C.; Randall, C.A.; Abubakar, F.H.; Smith, L.; Schileo, G.; Ozawa-Meida, L. Life Cycle Assessment and Environmental Profile Evaluation of Lead-Free Piezoelectrics in Comparison with Lead Zirconate Titanate. J. Eur. Ceram. Soc. **2018**, 38, 4922–4938, doi:10.1016/j.jeurceramsoc.2018.06.044.

24. Bell, A.J.; Deubzer, O. Lead-Free Piezoelectrics - The Environmental and Regulatory Issues. MRS Bull. **2018**, 43, 581–587, doi:10.1557/mrs.2018.154.

25. Lead-Free Piezoceramics. *Mrs Bulletin*. Cambridge University press. August **2018**, 43-8. www.mrs.org/bulletin

26. Villafuerte-Castrejón, M.E.; Morán, E.; Reyes-Montero, A.; Vivar-Ocampo, R.; Peña-Jiménez, J.A.; Rea-López, S.O.; Pardo, L. Towards Lead-Free Piezoceramics: Facing a Synthesis Challenge. Materials (Basel). **2016**, 9, 1–27, doi:10.3390/ma9010021.

27. Marsilius, M.; Granzow, T.; Jones, J.L. Effect of Electrical and Mechanical Poling History on Domain Orientation and Piezoelectric Properties of Soft and Hard PZT Ceramics. Sci. Technol. Adv. Mater. **2011**, 12, doi:10.1088/1468-6996/12/1/015002.

28. Liu, W.; Ren, X. Large Piezoelectric Effect in Pb-Free Ceramics. Phys. Rev. Lett. **2009**, 103, 1–4, doi:10.1103/PhysRevLett.103.257602.

29. Zhang, Y.; Sun, H.; Chen, W. A Brief Review of Ba(Ti0.8Zr0.2)O3-(Ba0.7Ca0.3)TiO3 Based Lead-Free Piezoelectric Ceramics: Past, Present and Future Perspectives. J. Phys. Chem. Solids 2018, 114, 207–219.

30. Yap, E.W.; Glaum, J.; Oddershede, J.; Daniels, J.E. Effect of Porosity on the Ferroelectric and Piezoelectric Properties of (Ba0.85Ca0.15)(Zr0.1Ti0.9)O3 Piezoelectric Ceramics. Scr. Mater. **2018**, 145, 122–125, doi:10.1016/j.scriptamat.2017.10.022.

31. Zheng, T.; Wu, J.; Xiao, D.; Zhu, J. Recent Development in Lead-Free Perovskite Piezoelectric Bulk Materials. Prog. Mater. Sci. **2018**, 98, 552–624, doi:10.1016/j.pmatsci.2018.06.002.

32. Liu, W.; Cheng, L.; Li, S. Prospective of (BaCa)(ZrTi)O 3 Lead-Free Piezoelectric Ceramics. Crystals **2019**, 9, doi:10.3390/cryst9030179.

33. Zhang, S.; Malič, B.; Li, J.F.; Rödel, J. Lead-Free Ferroelectric Materials: Prospective Applications. J. Mater. Res. **2021**, 36, 985–995, doi:10.1557/s43578-021-00180-y.

34. www.piceramic.com/en/expertise/piezo-technology/piezoelectric-materials#c15144.

35. www.ceramtec-industrial.com/en/products-applications/piezo-technology/piezoceramics-material.

36. www.cerpotech.com/products/barium-calcium-titanate.

37. www.ngkntk.co.jp/english/product/piezoelectric-ceramics/piezoelectric_ceramics.html.

38. Gaffet, E.; Michel, D.; Mazerolles, L.; Berthet, P. Effects of High Energy Ball Milling on Ceramic Oxides. Mater. Sci. Forum **1997**, 235–238, 103–108, doi:10.4028/www.scientific.net/msf.235-238.103.

39. Cousin, P.; Ross, R.A. Preparation of Mixed Oxides: A Review. Mater. Sci. Eng. A **1990**, 130, 119–125, doi:10.1016/0921-5093(90)90087-J.

40. Liu, X.; Li, Y.; Zeng, L.; Li, X.; Chen, N.; Bai, S.; He, H.; Wang, Q.; Zhang, C. A Review on Mechanochemistry: Approaching Advanced Energy Materials with Greener Force. Adv. Mater. **2022**, 34, 1–30, doi:10.1002/adma.202108327.

41. Suryanarayana, C. Mechanical Alloying and Milling. Prog. Mater. Sci. **2001**, 46, 1–184, doi:10.1016/S0079-6425(99)00010-9.

42. Zhang, Y.; Xu, J.; Zhang, Z.; Zhao, L.; Li, M.; Li, M.; Zhao, D.; Zhong, G.; Hu, X.; Zhang, X.; et al. Mechanochemical Synthesis of Nanostructured and Composite Oxide Ceramics: From Mechanisms to Tailored Properties. Int. J. Appl. Ceram. Technol. **2023**, 1–39, doi:10.1111/ijac.14598.

43. Louaer, A.; Chaguetmi, S.; Taibi, A.; Layachi, A.; Satha, H. Crystallization Kinetics and Growth Mechanism of 0.5 (Ba 0.85 Ca 0.15) TiO 3 −0.5 Ba (Zr 0.1 Ti 0.9) O 3 Powders Prepared via Solid-State Reaction. Phase Transitions **2020**, 93, 116–133, doi:10.1080/01411594.2019.1692014.

44. Jaimeewong, P.; Promsawat, M.; Watcharapasorn, A.; Jiansirisomboon, S. Comparative Study of Properties of BCZT Ceramics Prepared from Conventional and Sol-Gel Auto Combustion Powders. Integr. Ferroelectr. **2016**, 175, 25–32, doi:10.1080/10584587.2016.1199913.

45. Poon, K.K.; Wurm, M.C.; Evans, D.M.; Einarsrud, M.A.; Lutz, R.; Glaum, J. Biocompatibility of (Ba,Ca)(Zr,Ti)O3 Piezoelectric Ceramics for Bone Replacement Materials. J. Biomed. Mater. Res. - Part B Appl. Biomater. **2020**, 108, 1295–1303, doi:10.1002/jbm.b.34477.

46. Li, B.; Ehmke, M.C.; Blendell, J.E.; Bowman, K.J. Optimizing Electrical Poling for Tetragonal, Lead-Free BZT-BCT Piezoceramic Alloys. J. Eur. Ceram. Soc. **2013**, 33, 3037–3044, doi:10.1016/j.jeurceramsoc.2013.05.032.

2 Fundamentals of the piezoelectricity in ferroelectric ceramics

2.1 Historical introduction: The discovery of piezoelectricity and the development of the ferro-piezoelectric ceramic materials.

The history of the development of piezoelectric materials and technologies is a revolutionary journey with several important milestones, that changed the world forever. The discovery of the direct piezoelectric effect that still exerts its fascination today, can be officially dated in 1880 when the Curie brothers, Pierre and Jacques, published the results of the first experiment performed on quartz single crystal [1]. They stated that "some crystals when compressed in particular directions show positive and negative charges on their surfaces that are proportional to pressure and disappear when removed". The history of piezoelectric materials includes the work of many distinguished scientists who have made contributions that help us to understand this complex phenomenon today. Among them, we can mention : Hankel for the term piezoelectric, Lippman for the converse piezoelectric effect (the expansion or contraction generated by the electric field), Voigt who formulated a comprehensive and rigorous mathematical approach to the piezoelectric effect, formulating the theory of thermodynamic potentials associated with it, Schrödinger who, based on Debye's theory of electrical polarisation, determined the order of magnitude of the piezoelectric constants of tourmaline and quartz, Born who published the first theoretical calculation of a piezoelectric coefficient, that of ß-ZnS, Bragg and Gibbs who qualitatively described piezoelectric polarisation in quartz through X-ray analysis [2,3]. Each of them and many other researchers who have come later, up to the present day, gave a contribution, as a piece of a complex puzzle.

It is important to underline that the study and history of piezoelectricity in materials, as structured scientific discipline, began with the Curie brothers (1880), whereas the study of the ferro-piezoelectric ceramics began, as a structured scientific discipline, with Von Hippel's work on the ferroelectricity of the Barium Titanate and the understanding on why polycrystals, after application an strong external electrical field

(poling), can show piezoelectricity (1950) [4]. Before this work, the piezoelectric ceramics were a useful but puzzling material, whose performance contradicted what was known about piezoelectric materials at that time. In this way, the history of the piezoelectric ceramics, a very important class of the piezoelectric materials, is related with the phenomena of the ferroelectricity, that was discovered in 1920 by Valasek [5] while studying the application of the piezoelectricity of La Rochelle salt to build up a high sensitivity device to detect vibrations. This history can be summarized on a time scale by the following periods (**Figure 2.1.1**): the discovery of the ferroelectricity in Barium Titanate (Second World War) [6]; the discovery of Lead-Titanate and the explosion of ferroelectricity of complex perovskites, particularly lead titanate zirconate (PZT) for its wide range of applications, but, also, the main lead-free materials under consideration nowadays (1950-1965); the ceramic actuators (1965-1980) and the era of the miniaturization (1980-).

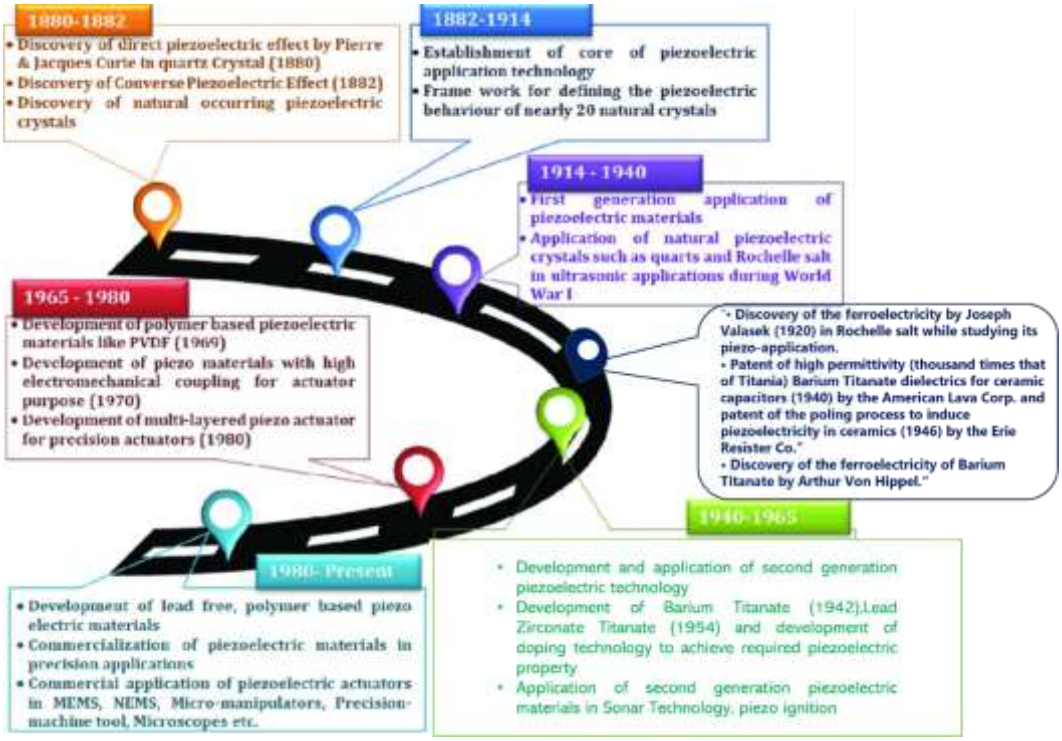

Figure 2.1.1 Chronogram of the development of piezoelectric technology and its application [7]. Another frame was added to the original Figure, here reported in dark blue.

2.2 The piezoelectricity and its relationship with the crystal structure.

The etymology of the term piezoelectricity is to be researched in the ancient Greek "πιέζειν (piézein)" that joins the concepts of "to press" and "electron". Electron was in ancient times the name of the amber, a

material known for being capable to develop electrostatic charges by friction. In this point it is of utmost importance to refresh Neumann's symmetry principle that states that: “the symmetry elements of any physical property of a crystal must include all the symmetry elements of the point group of the crystal” [8]. The piezoelectricity is a property that requires a unique direction and, therefore, it is non-centrosymmetric. For this reason, piezoelectricity is shown only by non-centrosymmetric crystals (**Figure 2.2.1**).

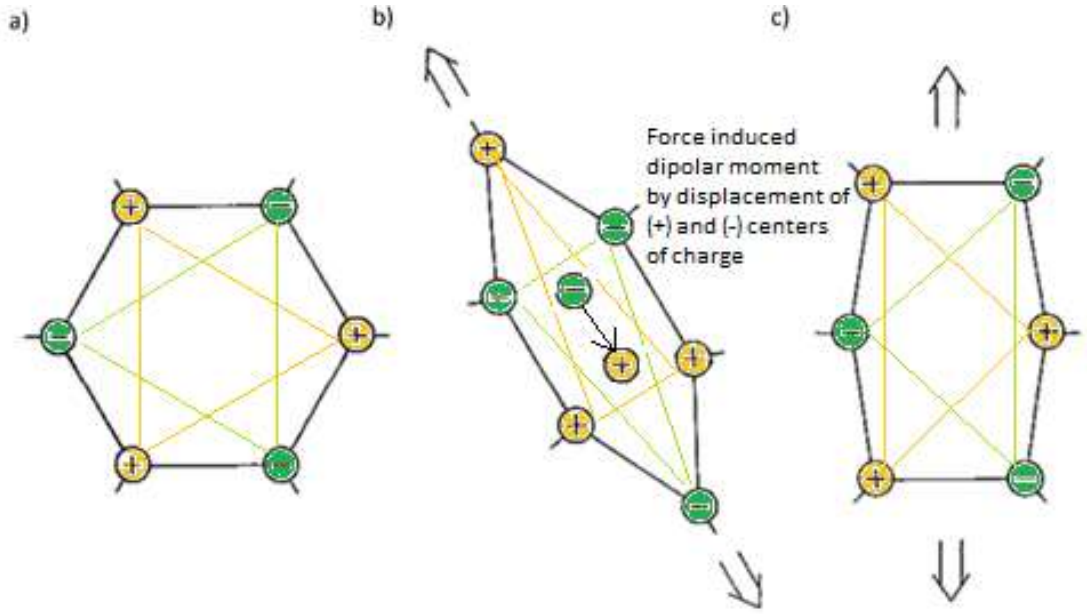

Figure 2.2.1 Schematic of the piezoelectric effect in an ionic crystal. Some piezoelectrics crystals do not have spontaneous polarisation, but this is induced by an external electric field or mechanical force, however, this can only be induced in one direction. a) absence of net dipoles in the absence of a mechanical force, b) the material is polarizable only in a specific direction in which the applied mechanical force creates dipoles by separation of the center of positive and negative charges, c) direction in which is not possible to create dipoles as the center of positive and negative charges remains in the same position after the application of the force [9].

As stated above, an essential requirement for a material to be piezoelectric is the absence of a centre of symmetry and according to the Neuman’s principle, the properties are critically related to the crystallographic structure. It follows that when the material becomes centro-symmetrical, e.g. due to a temperature induced phase transition with a change in crystal symmetry, the piezoelectric properties disappear. As well-known from crystallography, crystals are classified into 32-point groups based on their symmetry [10]. Therefore, only 20 non-centro-symmetric classes can show piezoelectric effects, as shown in **Table 2.2.1.** (point group 432 is an exception).

Table 2.2.1 Summary of Centro-symmetric and non-centro-symmetric point groups in crystals with different symmetries [11].

Crystal system	Symmetry element	Centro symmetric	Non-centro symmetric
Triclinic	Center		1
Monoclinic	Center,axis, plane	2/m	2, m
Orthorhombic	Center,axis, plane	mmm	222, mm2
Tetragonal	Center,axis, plane	4/m;4/mmm	4,$\overline{4}$,442,4mm, $\overline{4}$,2m
Trigonal	Center,axis, plane	$\overline{3}$, $\overline{3}$,m	3,32,3m
Hexagonal	Center,axis, plane	6/m,6/mmm	6, $\overline{6}$,622,6mm, $\overline{6}$m2
Cubic	Center,axis, plane	m3, m3m	23, $\overline{4}$3m,432

Of the 20-point groups, 10 of the crystal classes contain a unique axis where the dipole moment is oriented in the unstrained condition, and they exhibit spontaneous polarisation, these are the pyroelectrics.

When a piezoelectric material is subjected to a mechanical stress in a specific direction of the crystal, a separation of charges is observed, and an electrical charge is generated (polarisation) (**Figure 2.2.1(b)**). This effect is known as *direct piezoelectric effect*. The polarisation is proportional to the stress and changes with it. On the contrary, when an electric field is applied, a contraction or expansion is generated in the material. This is called *converse piezoelectric effect* [12]. These effects, here graphically represented in **Figure 2.2.2**, are respectively exploited in generators and motors [13].

The piezoelectric response to fields and forces is directly proportional to them and reversible in the linear range up to certain values. In this regard, it has to be remarked that above this limit the relationship between the expansion-strain and field is not linear, hysteretic and irreversible.

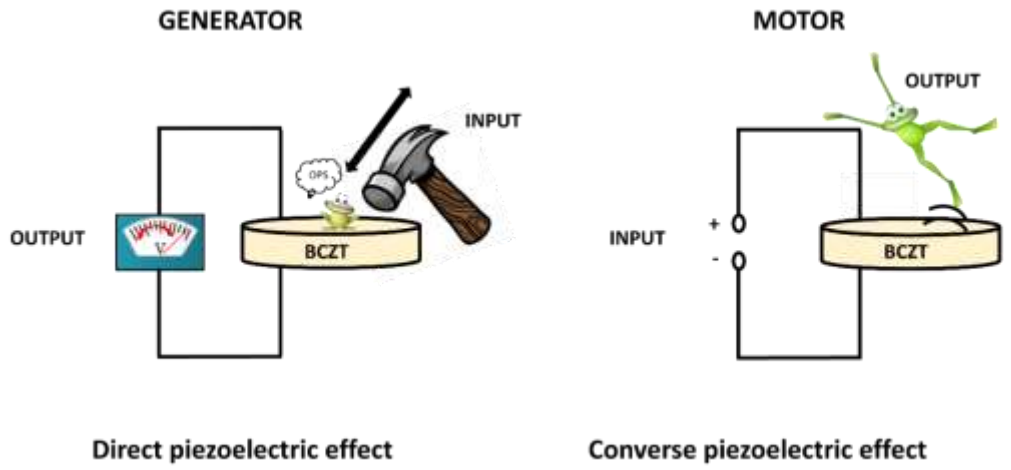

Figure 2.2.2 Piezoelectric effect :(left) direct and (right) converse piezoelectric effect.

2.3 Types of piezoelectrics

As depicted in **Figure 2.3.1**, piezoelectric materials can be classified into several categories, based on their origin: natural (Quartz, Rochelle salt, Tourmaline) or synthetic ones such as ceramics, polymers and composites.

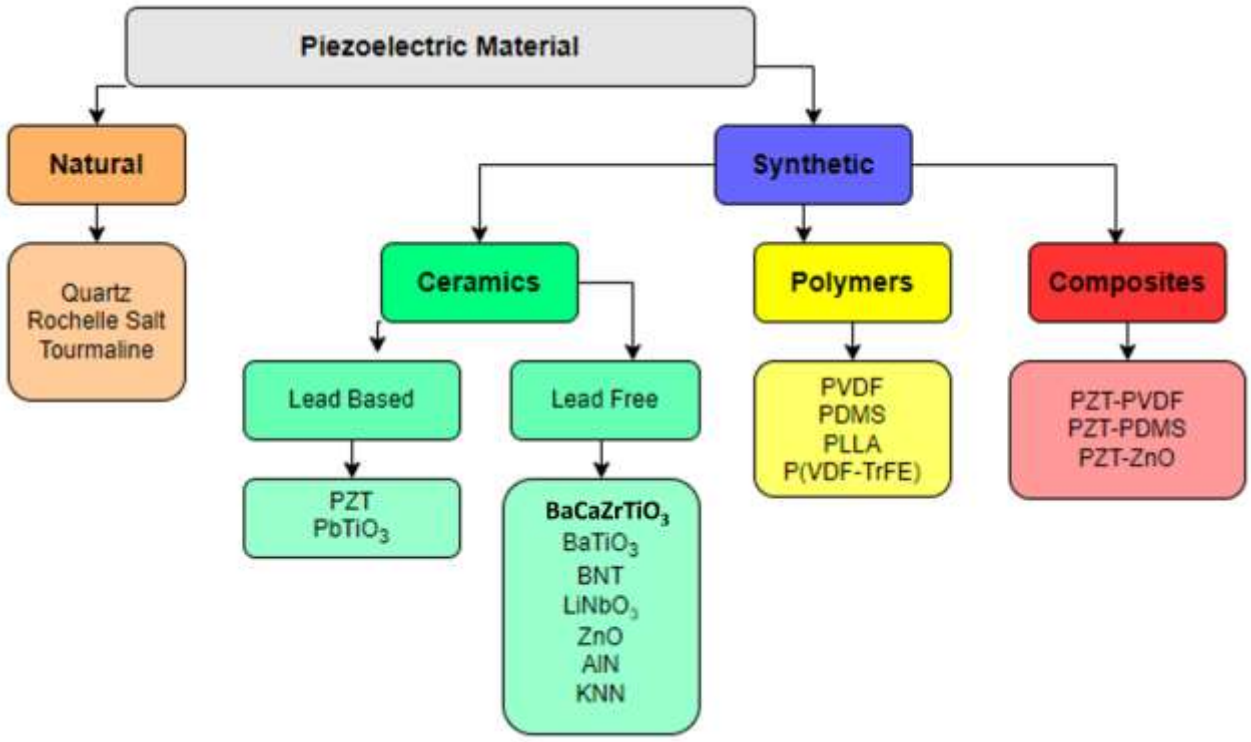

Figure 2.3.1 A classification of piezoelectric materials[14].

Lead-based and lead-free ceramic materials, like Barium Titanate ($BaTiO_3$, BT) and its derivatives like Barium Calcium Zirconate Titanate ((Ba Ca) (Zr Ti)O_3, BCZT); like Sodium Potassium Niobate ((K Na)NbO_3, KNN); like Lead Zirconate Titanate (Pb(Zr Ti)O_3, PZT), are **ionic crystals with a Perovskite-type structure ABO_3,** in which A and B are metallic cations and oxygen as anion like in BT (**Figure 2.3.2**). In addition to these there is a variety of perovskite materials, generally indicated with the formula ABX_3, suitable for many applications, where the A cation can be mono, di or trivalent, whereas B can be a di, tri, tetra, penta or hexavalent cation and the anion can be also a halogen, giving the possibility of a huge amount of combinations[15]. Based on the chemical composition, to predict the stability of perovskite structures and develop new materials, introducing other ions, it can be used the well-known Goldschmidt tolerance factor t (equation 2.1) [16] and its implementation, as reported in the recent literature [17,18].

$$t = \frac{r_A + r_O}{\sqrt{2} r_B + r_O} \qquad (2.1)$$

Where r_A is the radius of the A cation, r_B is the radius of the B cation and r_O is the radius of the anion (usually oxygen).

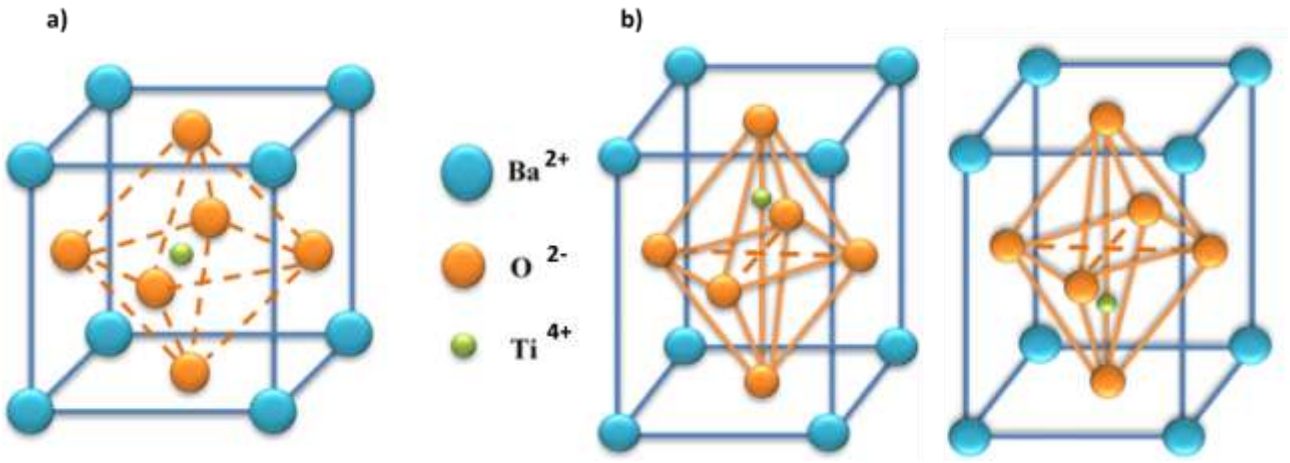

Figure 2.3.2 Crystal structure of $BaTiO_3$. (a) High temperature centrosymmetric cubic prototype lattice and (b) Room temperature non-centrosymmetric tetragonally distorted lattice with two equivalent states. The crystal distorsion defines the dipolar moment of the cell arising from the distance between the positive and negative centers of charge. At high temperature (above 120°C for the BT) the lattice gains symmetry, consequently, losing the piezoelectric activity.

2.4 Fundamentals of polar materials and connexions between piezoelectricity and ferroelectricity. Dielectric permittivity

To better understand the piezoelectric behaviour of ferro-piezoelectric ceramics, one must refer to the relationship between dielectrics, piezoelectrics, pyroelectrics and ferroelectrics, graphically reported in **Figure 2.4.1**. A dielectric material is an insulator which can store electric charges as it is polarisable as shown in **Figure 2.3.2**, by the action of the electric field. Piezoelectric is a type of dielectric that it is also polarisable by the action of a mechanical stress in a given (unique) crystal direction. For this the crystal must be non-centrosymmetric. Pyroelectric is a polar material (built-in polarisation) whose polarisation changes with the electric field (die-) or the mechanical stress (piezo-) or the temperature (pyro-). Ferroelectric is a polar material (built-in polarisation) whose polarisation can be reversed (bi-stability) by the application of a sufficiently high external electric field (ferro-) and changes with the temperature and disappears at the Curie point (pyro-) or the mechanical stress (piezo-). The ferroelectric ceramics are ionic polycrystal. Based on this relationship, it can be inferred that any ferroelectric material is a piezoelectric one, but not every piezoelectric is a ferroelectric.

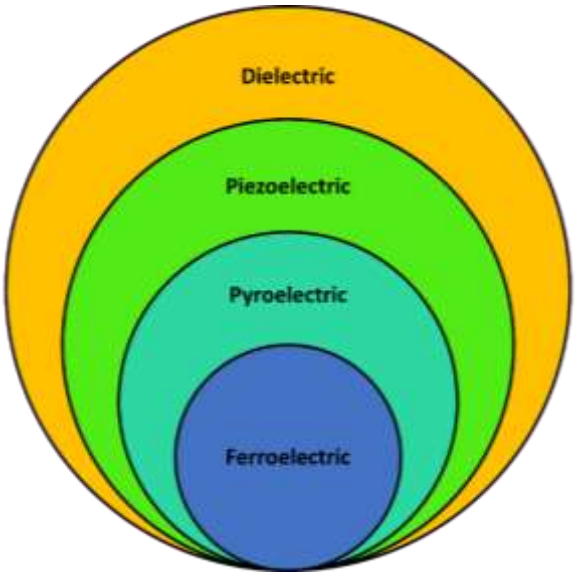

Figure 2.4.1 Schematic of the relations between the various types of dielectrics.

When a dielectric is inserted between the plates of a plane-parallel capacitor, the capacitance or ratio between the charge stored to the voltage applied, increases compared to that of vacuum, because with the application of the electric field, additional charges are generated due to the fact that the displacement of charge carriers in the dielectric material charges the surfaces of the dielectric, neutralising part of the charges stored in the capacitor, which, consequently, can store more charges, as summarised graphically in **Figure 2.4.2**.

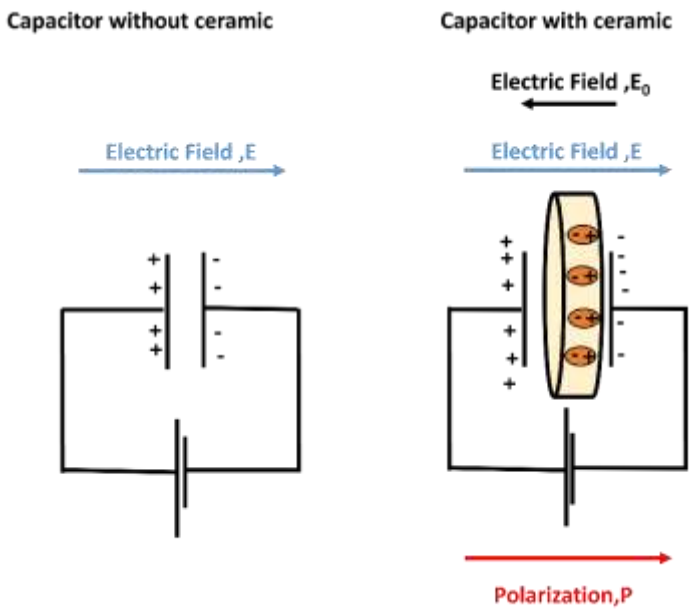

Figure 2.4.2 Showing the polarisation of a **dielectric material, e.g. a BCZT ceramic**. E_0 is the internal Electric Field originated by the field-induced Polarization.

As shown in **Figure 2.4.3(a),** a dependence of dielectric permittivity on frequency is observed, as only the lighter polar species can follow the higher frequencies of the field. The polarisation in the dielectric can be explained through several mechanism following reported and graphically summarized in **Figure 2.4.3(b):** space charges, orientation of dipoles, ionic and electronic displacements. As shown in **Figure 2.4.2**., when a dielectric, e.g. a ferro-piezoelectric ceramic, is inserted into a plane parallel capacitor with an area of the plates A and distance between them d, the capacitance (C) increases compared to that of vacuum (C_0) that is defined as:

$$C_{0=}\ Q/V = A/d \cdot \varepsilon_0 \qquad (2.2)$$

Where Q is the charge stored in the capacitor when a voltage V is applied and ε_0 is the permittivity of the vacuum. The capacitance when there is a dielectric inserted gets the value of:

$$C_{=} Q/V = A/d \cdot \varepsilon_a = (C_0/\varepsilon_0) \cdot \varepsilon_a = C_0 \cdot (\varepsilon_a/\varepsilon_0) \qquad (2.3)$$

where ε_a is the absolute permittivity of the material and $\varepsilon = (\varepsilon_a/\varepsilon_0)$ is the relative dielectric permittivity. Therefore, the relative dielectric permittivity has no dimensions, and it depends on the frequency of the AC voltage applied to the capacitor (**Figure 2.4.2**). It can be measured in two conditions: under a constant (zero) stress (ε^T), low frequency or free permittivity, or under a constant (zero) strain (ε^S), high frequency or clamped permittivity.

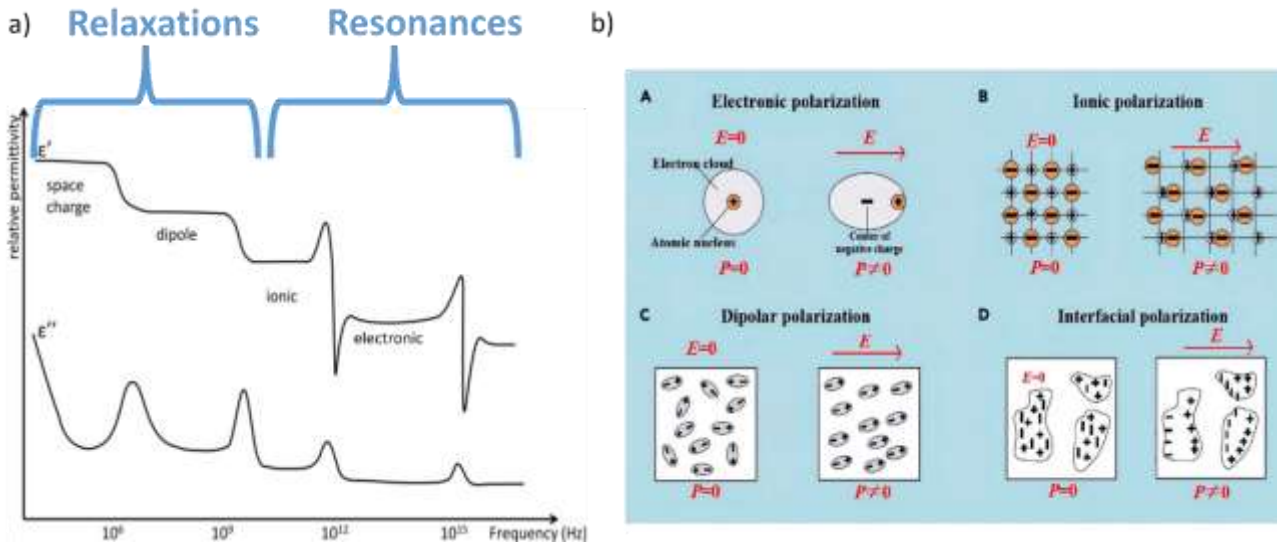

Figure 2.4.3 Dependence of the dielectric permittivity on frequency :a)relaxations and **dielectric resonances** b)different mechanisms of dielectric **polarisation** occurring at different frequencies[19].

Ferroelectricity: Crystallographic basis, structural phase transitions, domains

Summarizing the previous section, piezoelectrics are non-centrosymmetric dielectrics and ferroelectrics are a class of piezoelectrics. Ferroelectrics are characterized by phase transition to the paraelectric (non-polar) high temperature phase (centrosymmetric crystal polymorph (**Figure 2.3.2(a)**) taking place near the so called Curie temperature[20] by similarity with the well know transition temperature in ferromagnetism. These materials are also characterized by their bi-stability in the low temperature non-centrosymmetrical long-range ordered polar state (two polar states of the crystal with identical stability **(Figure2.3.2(b)),** occurring

when the crystal has a deformation that reduces its symmetry and makes it piezoelectric. Consequently, the ferroelectricity has also a close relationship with the crystal structure and only some crystal within the 10 pyroelectric classes (**Table 2.2.1**) shows ferroelectricity. At the ferro-paraelectric the polarization is completely lost (**Figure 2.4.4(a)**). The transition is measurable, by a thermal anomaly of the dielectric permittivity (a *maximum*, called lambda curve for its shape in single crystal ferroelectrics (**Figure2.4.4(b)),** as well as for the thermal variation of the cell parameters, among other techniques [4,21]. Furthermore, some ferroelectrics show other anomalies (=relative maxima of the permittivity) at different temperatures where ferroelectric-to-ferroelectric phase (FE/FE) transitions occur (**Figure 2.4.4**). The dielectric permittivity changes with the frequency of the applied electric field in all dielectrics (**Figure 2.4.3(a)**) and in ferroelectrics also changes as a function of the temperature at the polar transitions linked with their structural transitions (**Figure2.4.4**).

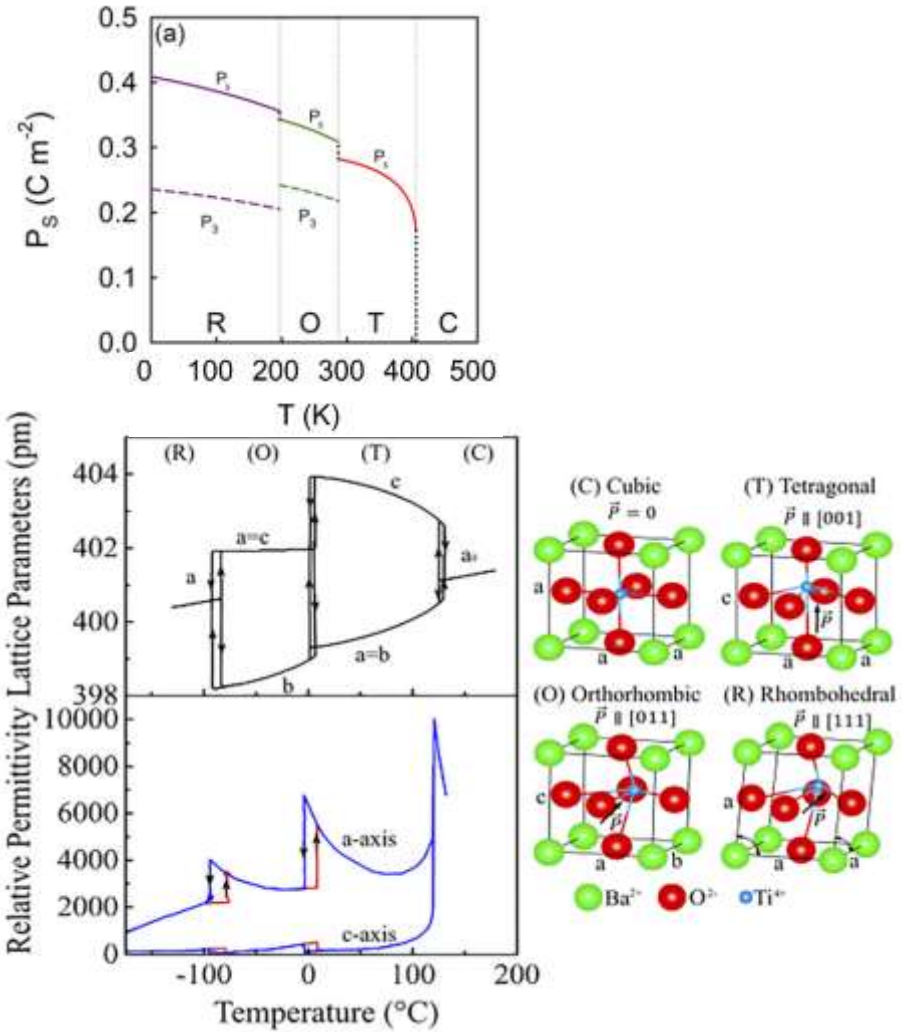

Figure 2.4.4 Changes in the predicted spontaneous polarization, crystal lattice parameters and anomalies in the relative permittivity during the sequence of phase transitions in $BaTiO_3$. The right side of the figure illustrates the crystal structure of the cubic prototype phase and the unit cell distortions in each of the ferroelectric phases of $BaTiO_3$. Note that the cell-doubled orthorhombic structure is represented as a primitive pseudo-monoclinic cell for ease of comparison with the tetragonal and rhombohedral phases[21].

Because of the characteristic bi-stability of ferroelectrics, there is the non-linearity between the spontaneous polarisation (P_s) and the applied electric field (E), as explained in **Figure 2.4.5(a)** for a unit cell of the crystal **(Figure 2.3.2 and Figure 2.4.4**) or a single domain single crystal.

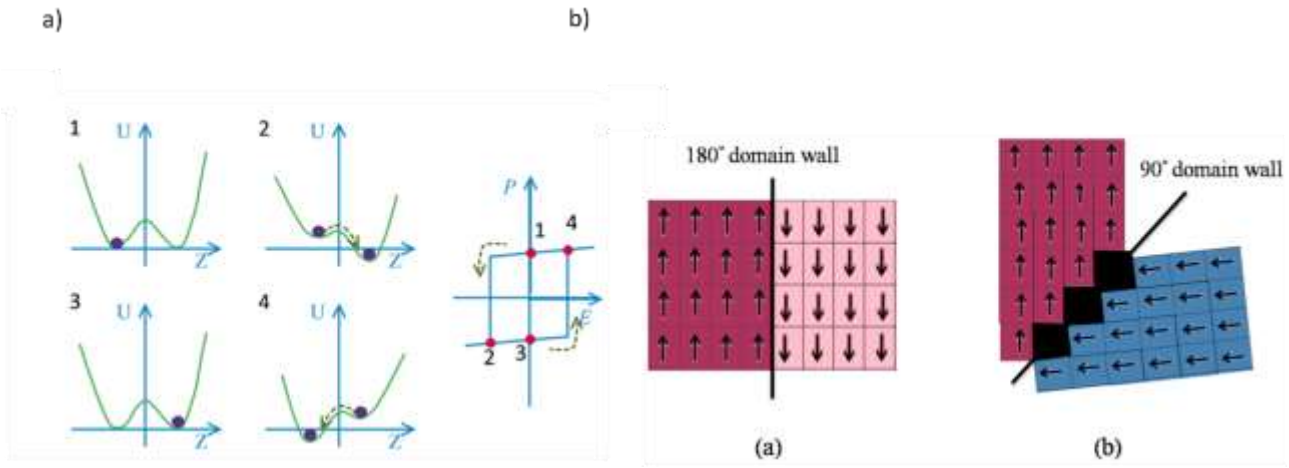

Figure 2.4.5 a) Schematic energy model to explain the existence of a hysteresis cycle in a model single-domain single-crystal ferroelectric material: (1) and (3) are the two equilibrium states with the same value of polarisation ($P=P_s$) in the absence of electric field. The effect of electric fields of inverse polarity on the potential energy curve is shown in (2) and (4) and causes polarization reversal. The hysteresis cycle of spontaneous polarisation in which 1, 2, 3, 4 states are indicated with red dots,b) Types of ferroelectric domains and walls in between them (a) 180° domain wall, (b) 90° domain wall in a tetragonal crystal [22].

The ferroelectric crystal is in fact characterized in real life by the occurrence of ferroelectric domains (**Figure 2.4.5(b)**). A ferroelectric domain is a region of the crystal in which the neighbouring dipoles are aligned along the same direction with a uniform spontaneous polarisation direction (long-range ordered polar state). The domain configuration is built in the crystal as the electric charges at the faces of the material must be compensated and the elastic energies must be minimized for an equilibrium state of the ferroelectric. In ferroelectric materials, 180° path for ferroelectric domain reorientation essentially exists. Besides, allowed by certain lattice symmetry, non-180° ferroelastic domains may also exist [22]. The motion of 180° domains provides a reorientation of the polarization that is not accompanied by the change of dimensions in the crystal cell, these are purely ferroelectric domains. However, the motion of non-180° domain walls (e.g. 90° domain walls in a tetragonally distorted perovskite) as shown in (**Figure2.4.5(b))** means a simultaneous domain reorientation and change of the crystal cell dimensions, reflected in a macroscopic change of dimensions. Such domains are ferroelectric-ferroelastic ones.

The actual ferroelectric material (multidomain single crystal or polycrystal) can be identified by its characteristic Polarisation-Electric field (P,E) hysteresis cycle and butterfly-shaped Strain-Field (S,E) loop, that work as the fingerprints of the material [23]. As depicted in (**Figure2.4.6**) for a multidomian single crystal, the

(P,E) curve of increasing polarization from an electrostatically and elastically stable configuration (E=0, P=0) as the field increases shows a **hysteretic** (the path with increasing field is not the same path as with decreasing field) and **irreversible nature** (there is a remanent, permanent, polarization when the field is removed). Similarly, there is an associated permanent strain in the (S, E) loop (**Figure 2.4.6 (b)**). When the electric field changes polarity the polarization first goes to zero and subsequently to a maximum value in the opposite sense to the previous one.

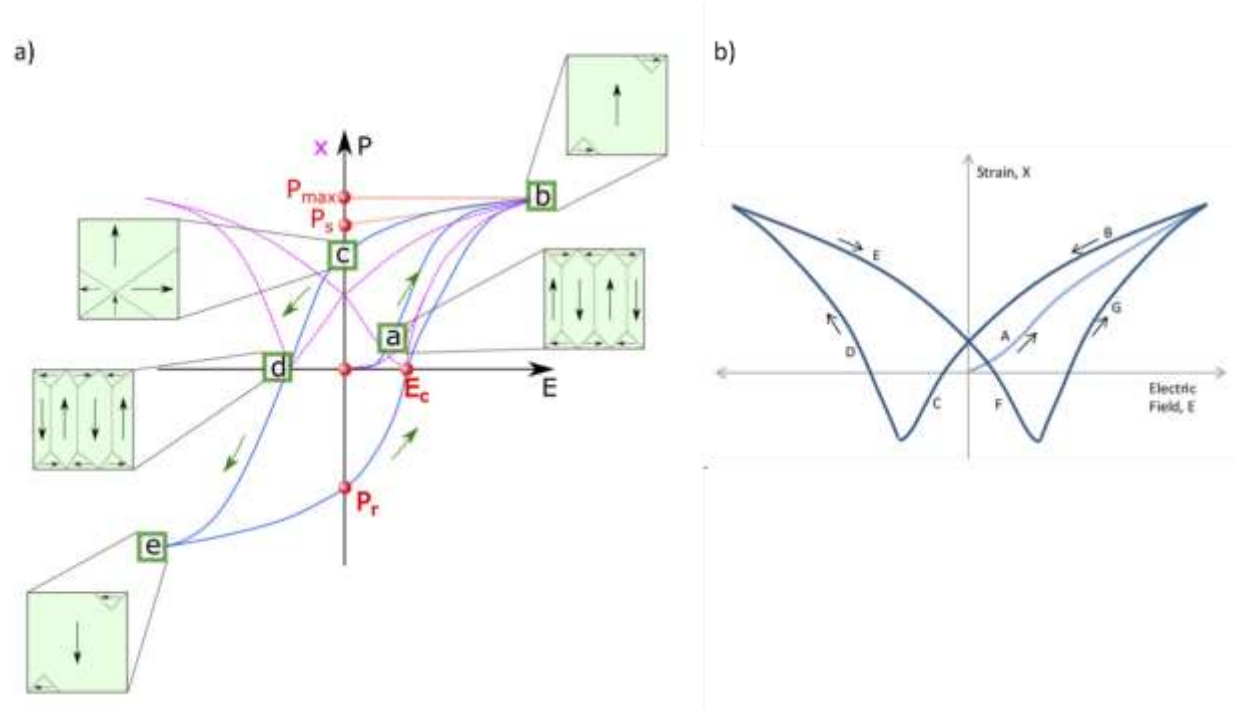

Figure 2.4.6 (a) (P-E) hysteresis cycle of a multi-domain single-crystal or polycrystalline ferroelectric material and plausible domain configurations corresponding to the different points marked in the cycle. The maximum polarization is the result of the complete orientation of the polarization and its deformation by the electric field and it is higher than the spontaneous polarization (P_s). The remanent polarization (P_r) is lower than the spontaneous polarization (P_s) as some of the domains lose their orientation when the field is removed to be back to a minimum of elastic energy. The coercive field (E_c) is the minimum field needed to activate the polarization reversal. The strain-electric field butterfly loop is also shown. (b) the characteristic butterfly-shaped Strain-Field loop [21].

Further information can be extracted from the hysteresis cycle by more elaborated analyses like the First Order Reversal Curves (FORC)method[24], that gives information on the tunability and hysteresis of the ferro-piezoelectric ceramic and that can be interpreted in terms of the microstructural defects taking into account the Preisach model[25]. The tunability of a ferroelectric describes the ability to change its permittivity by the electric field. This property is directly related to the non-linear variation of polarization (and implicitly of the

permittivity) with the applied Field. The FORC method has successfully been applied to BT derivatives ceramics, such as $Ba(Zr,Ti)O_3$[26].

2.5 Inside a ferroelectric ceramic

Ceramics are a class of synthetic polycrystals that are solidified or densified by a high temperature thermal treatment, called sintering. The structure of a ferroelectric polycrystalline material, as reported in **Figure 2.5.1**, is organized on various levels at different length scales (from mm to Å): macroscopic ceramic bodies, grains, ferroelectric domains, and crystal lattice. It should be stressed that in this complex organisation, each level has a close relationship with the higher levels, and each type of organisation is characteristic of a certain material feature (the domain size is dependent on the grain size of ferroelectric ceramic [27]. Owing to the requirement of the energy *minima*, the grains in polycrystalline materials are always splitting into many domains and both antiparallel 180° domains and non-180° domains (e.g. 90° domains in tetragonally distorted, or 71° and 109°, representing the two cell diagonals, in rhombohedral distorted, perovskite structure) are permissible. A clear example of a highly hierarchically organised domain structure is the BCZT microstructure: system **stripe-like/lamellar and herringbone patterns** are considered the typical feature of the domain configuration in the ferroelectric **tetragonal phase**, whereas **wedge-shaped** domains are typical of **rhombohedral phase**, suggesting a huge variability depending on the composition [27,28]. Then, the nanodomains are assembled in micrometre wedge-shaped and lamellar-shaped domains and their dimensions strongly related to the grain size.

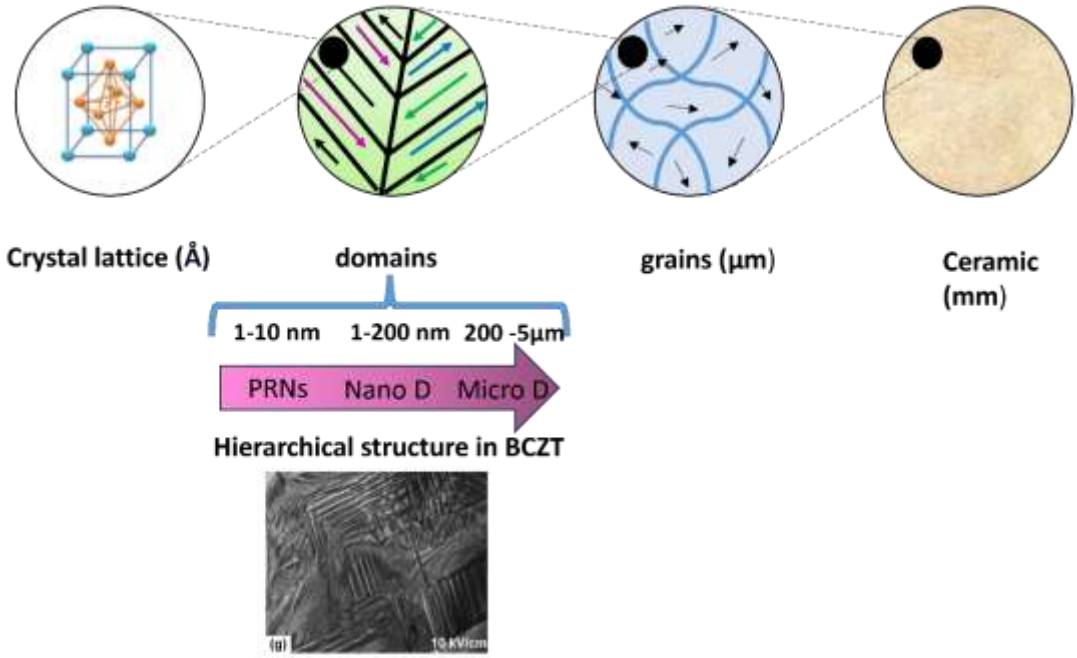

Figure 2.5.1 Schematic representation of a ceramic at different length scales, showing the four levels of dimensions determining the properties: macroscopic, ceramic microstructure, domains size and crystallographic phase (the herringbone patterns are the consequence of the combination of two sets of alternating 90° domains for a tetragonally distorted perovskite. In the bottom part of this image, an example of hierarchically organised structure in BCZT ceramics is displayed[29].

These levels of dimensions in the ceramic structure visualizes the great complexity of the system, that derives in the great challenge of the control of the properties of the ferro-piezoelectric ceramics. There are factors at each level that affect the overall properties of the ceramic and that can be manipulated, or must be avoided, to tailor the ceramic properties. At the crystal structure level, the composition defines possible stable polymorphs and the possible stable coexistence of these and, ultimately, the value of the spontaneous polarization[30]. We can also speak about volatility of components to determine point defects (vacancies and interstitials) or extended defects (dislocations) [31]. Defects that enhances the cell polarization mobility or fix it, giving place to so called “hard” and “soft” ferroelectrics, can also be created by small amounts (≤ 3at.%) of donor and acceptors dopants, among others, that also controls the polarization value [2]. As for the domain structure, which is defined by the crystal structure and is related with the grain size, it can achieve great complexity and there are several factors that defines their mobility[25]. Among them the point defects of the crystal that may pin the domain walls and stop of reduce the velocity of their displacement [32]. The intergranular stress in the ceramic is another factor affecting this mobility as it transfers to the domain walls,

which is of primary importance for thin film polycrystals. At the level of the grain size we must consider all factors defining the ceramic microstructure [33] as second phases, grain boundary characteristics, core-shell structures of the grains, grain growth habit and orientation, porosity and pore size distributions, etc. Finally, the ceramic may have undesired inhomogeneous structure including delamination or cracks with origin in the moulding or thermal treatments, abnormal grain growth, macropores or other defects due to volatility (intended or accidental), compositional or grain size or porosity gradients, among others.

This picture also helps to understand the intrinsic and extrinsic contributions to the piezoelectric effect. Extrinsic contributions to the piezoelectric effect can be defined as those contributions that to do not originate from the field induced polarization or deformation of a single domain. Typical examples are displacement of domain walls and interphase boundaries. From the application point of view, these contributions are important, as they are responsible for nonlinearity (field dependence of the piezoelectricity), weak-field hysteresis, frequency dispersion of the properties, creep, and aging [34].

Under AC electric field, there are small reversible movements of domain walls that give place to the extrinsic contribution of the piezoelectric response of the ceramic. So, it has to be pointed out that domains are not static components, but during the application of the Electric Field they can be also subjected to reversible transformation (from multi domain to single domain) and to the switching between two multi-domain states, as observed for lead-free materials, like in the BCT-BZT system [35].

2.6 The poling processes of ferro-piezoelectric ceramics

The ferroelectric polycrystals, the ceramics, are isotropic materials, as the polarization in each grain, as its crystal structure, is randomly oriented. Consequently, they are centrosymmetric, and, in principle, they cannot be piezoelectrics. Piezoelectricity of ceramics remained as a scientific puzzle until the discovery of ferroelectricity in the $BaTiO_3$ perovskite took place (Von Hippel) [6] and the role of the so-called *poling process* was revealed.

To confer piezoelectric properties to the ferroelectric material it is necessary to align these randomly oriented domains, through the *poling process* (**Figure 2.6.1)** in which an external electric field is applied. This process is only feasible when the composition of each crystal in the ceramic is ferroelectric, because only in this case a domain reorientation takes place under the action of the electric field. This is why piezoelectric ceramics are properly called ferro-piezoelectric ceramics. To enhance the domains alignment a relatively high electric field can be applied, at a temperature below the Curie temperature of the material (to avoid the loss of the polarisation). This can be followed, to further promote the stability of the alignment by a so-called Field Cooling (FC), which consists of maintaining the field while lowering the temperature to room temperature. When the applied field is removed, most of crystallites remain in their aligned direction (**Figure 2.4.6**)[36,37]. After the poling process, the polycrystalline ceramic material is piezoelectric as a consequence of the induced macroscopic non-centrosymmetry defined by the direction of the poling electric field. In fact, after poling, the ceramic has a non-zero net polarisation in the absence of electric field that responds linearly to an applied electric field or mechanical stress. The net dipole moment comes from irreversible domain wall motions, as shown in **Figure 2.4.5(b).** To conclude, the result of the poling process is that any ferroelectric ceramic, as a consequence of its bi-stability, have the net polarization of each constituent crystallite in a cone of directions, the closest to the one of the electric field that is permitted by each crystallite structure. The sum of these creates a non-zero net polarization (remanent polarization) in the absence of the applied electric field. This cone of directions around the direction and orientation of the applied electric field results in a macroscopic cylindrical symmetry for the ceramic. For this, any direction in a plane perpendicular to the field is equivalent and this is independent of the actual crystal symmetry of the specific ferro-piezoelectric composition of the ceramic. This is ascribed to the non-centrosymmetric 6mm point group (see Table of point groups), containing 6 mirrow planes parallel to the direction of the applied field. This is also referred sometimes as ∞mm, as it can be understood as ∞ number of mirror planes parallel to the direction of the applied electric field. Consequently, the poled polycrystalline ferroelectric, also properly known as ferro-piezoelectric ceramic, is not centrosymmetric any longer, but fulfils the needed condition for the appearance of the piezoelectric response.

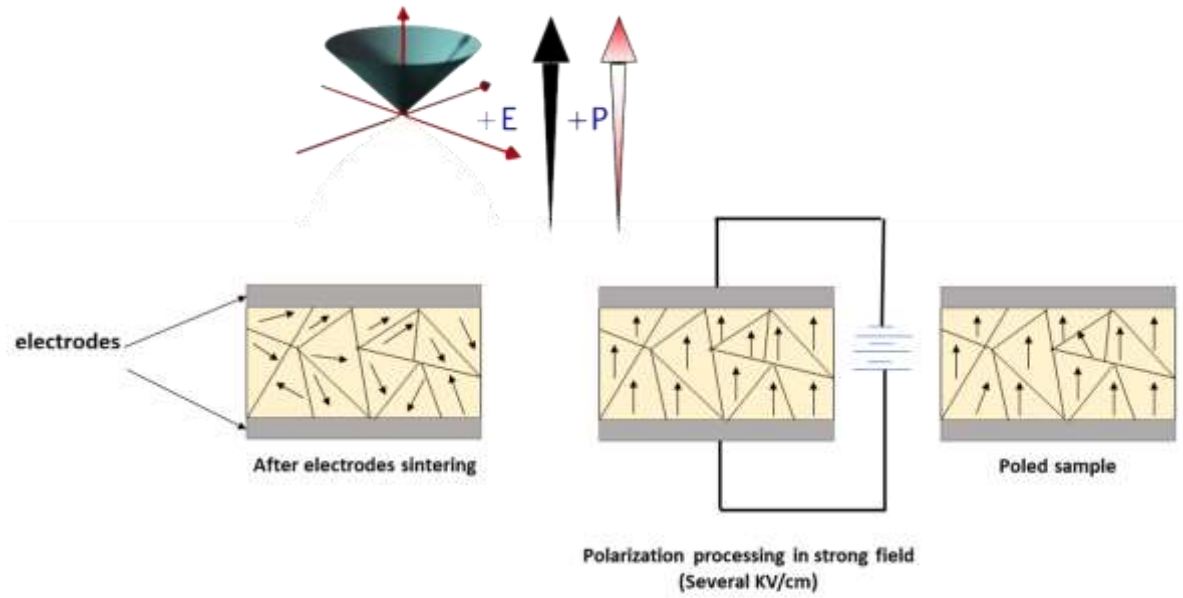

Figure 2.6.1 Schematic illustration of the poling process of a ferro-piezoelectric ceramic.

The remanent polarization, P_r, of the poled-ferro-piezoelectric ceramic and, consequently, the piezoelectric performance, is always lower than that corresponding to the single-domain single crystal (P_s). P_r is limited by the symmetry of the crystal structure of the ferroelectric (tetragonal: $P_r^{máx}$= 0.83 P_s , with six <001> equivalent directions of P_s; rhombohedal: $P_r^{máx}$=0.87 P_s, with eight allowed <111> equivalent directions; orthorhombic: $P_r^{máx}$=0.91 P_s, with twelve allowed <110> equivalent directions) that defines the aperture of the cone of allowed polarization directions [38,39]. Those solid solution systems with the so called Morphotropic Phase Boundary (MPB), with coexistence of two symmetries in a narrow compositional range, are seeked when optimization of the properties of the ferro-piezoelectric ceramic is desired. This increases the number of equivalent directions of P_s and, consequently, increases the P_r value. It is also possible to increase P_r over the values of the classical randomly oriented ferro-piezoelectric ceramics by the processing of textured ceramic, although it highly increases the complexity of their manufacture [40]. The energy considerations leading to the existence of MPBs in a solid solution system like the BCZT one will be studied in Chapter 3.

2.7 Piezoelectric coefficients and other physical properties of ferro-piezoelectric ceramics

- **Dielectric permittivity and losses**

The definition of the dielectric permittivity (**equations 2.2 and 2.3**) must be extended with the concept of dielectric losses when the electric field applied to the materials is an AC field. Dielectric losses express the phase difference between the AC applied electric voltage and the resulting polarization or charge between the capacitor plates. To consider the phase lag, the dielectric permittivity is conveniently expressed in complex form as follow:

$$\varepsilon = \varepsilon' - i\varepsilon'' \qquad (2.4)$$

The dielectric loss is often expressed as dielectric loss tangent ($tan\delta_e$) which is the ratio between the imaginary and the real part of the dielectric permittivity.

$$tan\delta_e = \frac{\varepsilon''}{\varepsilon'} \qquad (2.5)$$

Alternatively, can be expressed as dielectric quality factor (Q_e), which is essentially the reciprocal of the dielectric loss tangent:

$$Q_e = \frac{1}{tan\delta_e} \qquad (2.6)$$

- **Piezoelectric Charge (or Strain) Constant:**

Quasi-static piezoelectric coefficient d is the piezoelectric constant that relates the mechanical strain generated by an applied electric field or the charge produced by the application of a mechanical stress, described by the following equation:

$$d = \frac{strain\ development}{applied\ electric\ field}\left[\frac{m}{V}\right] \qquad (2.7)$$

$$d = \frac{short\ circuit\ charge\ density}{applied\ mechanical\ stress\left[\frac{C}{N}\right]} \qquad (2.8)$$

- **Piezoelectric Voltage Constant:**

g voltage constant can be defined as the electric field (open circuit) generated by a piezoelectric material per unit of mechanical stress applied. This constant can be also defined like the ratio of strain developed over the applied charge density.

$$g = \frac{strain\ developed}{applied\ charge\ density}\left[\frac{m^2}{C}\right] \qquad (2.9)$$

or

$$g = \frac{open\ circuit\ electric\ field}{applied\ mechanical\ stress}\left[\frac{V/m}{N/m^2}\right] \qquad (2.10)$$

The piezoelectric voltage constant (g) is related to the piezoelectric constant (d) by the relative permittivity of the medium:

$$g = \frac{d}{\varepsilon_r} \qquad (2.11)$$

- **Electromechanical coupling coefficient:**

It can be defined as the efficiency of the material in converting the mechanical energy to electrical one and *vice versa.* It results from the ratio between the converted energy of one type (mechanical or electrical) and the input energy of the second type (electrical or mechanical).

$$k^2 = \frac{mechanical\ energy\ converted\ into\ electric\ energy}{supplied\ mechanical\ energy} \qquad (2.12)$$

$$k^2 = \frac{electric\ energy\ converted\ into\ mechnical\ energy}{input\ electric\ energy} \qquad (2.13)$$

Since complete energy conversion is not possible, the electromechanical coupling factor is always less than unity: k < 1. This factor can be useful for directly comparing, from a piezoelectric point of view, materials with very different efficiency values.

- **Mechanical losses:**

Mechanical losses are often expressed by the mechanical quality factor Q_m. Mechanical quality factor gives information on the energy that is lost, producing heat or hysteretic behaviour, when the ferro-piezoelectric

ceramic is subjected to and AC electrical field. In analogy with the dielectric permittivity, the elastic coefficients can be expressed in complex form as follow:

$$s = s' - is'' \qquad (2.14)$$

Therefore, the corresponding quality factor is:

$$Q_m = \frac{1}{tan\delta_m} = \frac{s'}{s''} \qquad (2.15)$$

2.8 The anisotropy of piezoelectric ceramics

One of the four types of the constitutive equations describing the direct and inverse piezoelectric effect in the linear range with respect to, i.e. the charge created or the displacement under mechanical force or electrical field, respectively, coupled with the elastic and electrostatic effects, are:

$$D = dT + \varepsilon^T E \qquad (2.16)$$

$$S = s^E T + dE \qquad (2.17)$$

Where D is the dielectric displacement (assumed to be equal to the polarisation), T is the stress, E is the electric field, S is the deformation, d is a piezoelectric coefficient, s is the material compliance and ε is the dielectric permittivity.

The quantity kept constant (zero), is indicated as uppercase apex. Superscripts like “S, T, E, D” describe an electrical or mechanical boundary condition:

S = strain = constant (clamped)

T = stress = constant (free)

E = field = constant (short circuit)

D = electrical displacement = constant (open circuit)

Of considerable importance is the fact that piezoelectric coefficients described here vary with temperature, pressure and frequency electric field, mechanical and electrical boundary conditions, etc., and they describe material properties under small-signal conditions, i.e. in the linear range.

The direct and inverse piezoelectric effect and the material properties that describe this effect are closely dependent on the anisotropy symmetry of the material and depend on the directions in which the electric field or mechanical force are applied (**Figure 2.2.2**) and the directions in which the corresponding displacement, voltage or charge are measured. Piezoelectrics are anisotropic materials. Therefore, the above-mentioned constitutive equations must take tensor notation to properly have a tridimensional description of the piezolectricity.

Taking into account the vector nature of the electric field (E_k), that the permittivity and the elastic magnitudes are tensors of second order (ε^T_{ik}, S_{ij} and T_{ij}), that the piezoelectric coefficients are tensors of third order (d_{ijk}) and that the elastic coefficients are tensors of fourth order (s^E_{ijkl}), those equations became unmanageable. Due to symmetry reasons and using the Einstein summation convention of repeated subscripts (i,k=1,2,3; ij=α; kl=β; α,β=1,2,...6), the piezoelectric coefficients in the three-dimensional description of the material refer to the direction of the applied electrical or mechanical force and are defined in a given crystalline using the coordinate system. By convention, as illustrated in **Figure 2.8.1.** The direction of polarisation (in ferro-piezoelectric ceramics the same as the direction of the electric poling field (**Figure 2.4.6**)) is the same as the Z axis. The Cartesian directions X, Y, Z are represented by subscripts 1, 2 and 3. The shear forces or displacements are denoted by subscripts 4, 5 and 6 when they take place, respectively, with respect to the 1, 2 and 3 axes[41].

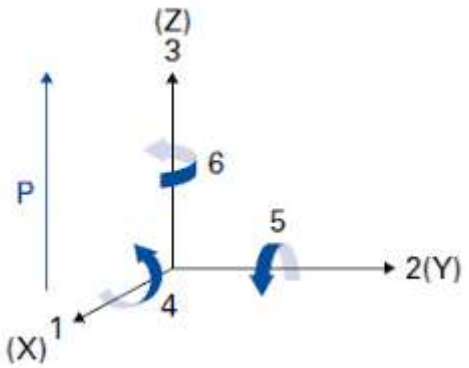

Figure 2.8.1 Conventional notation of reference axes for piezoelectric properties, in case of ceramics the 3 axes is the direction of the applied field in the poling process.

Customarily, the first subscript indicates the direction of the electrical property (the voltage applied, or the charge produced), whereas the second subscript gives information about the direction of the mechanical property (stress or strain).

As piezoelectrics are anisotropic, and the mechanical forces and electrical field are tensors () the constitutive; therefore, all physical constants are tensor quantities, necessitating the use of tensors [8]. In this way, the complete (linearised) description of electrical, elastic and piezoelectric behaviour in matrix notation (**Figure 2.8.2**) for the specific symmetry of a poled ferro-piezoelectric ceramic (6*mm*) is then reduced. For poled ferro-piezoelectric ceramics with 6mm symmetry, the reduced matrix has 2 independent dielectric permittivity values ($\varepsilon_{33}^{T}, \varepsilon_{11}^{T}$) , 3 independent piezoelectric coefficients (d_{33}, d_{31}, d_{15}) and 5 independent elastic coefficients, which are: $s_{11}^{E}, s_{33}^{E}, s_{44}^{E}, s_{12}^{E}, s_{13}^{E} and\ s_{66}^{E} = 2\ (s_{11}^{E} - s_{12}^{E})$.

$$\begin{pmatrix} S_1 \\ S_2 \\ S_3 \\ S_4 \\ S_5 \\ S_6 \\ D_1 \\ D_2 \\ D_3 \end{pmatrix} = \begin{pmatrix} s_{11}^{E} & s_{12}^{E} & s_{13}^{E} & 0 & 0 & 0 & 0 & 0 & d_{31} \\ s_{12}^{E} & s_{11}^{E} & s_{13}^{E} & 0 & 0 & 0 & 0 & 0 & d_{31} \\ s_{13}^{E} & s_{13}^{E} & s_{33}^{E} & 0 & 0 & 0 & 0 & 0 & d_{33} \\ 0 & 0 & 0 & s_{44}^{E} & 0 & 0 & 0 & d_{15} & 0 \\ 0 & 0 & 0 & 0 & s_{44}^{E} & 0 & d_{15} & 0 & 0 \\ 0 & 0 & 0 & 0 & 0 & s_{66}^{E} & 0 & 0 & 0 \\ 0 & 0 & 0 & 0 & d_{15} & 0 & \varepsilon_{11}^{T} & 0 & 0 \\ 0 & 0 & 0 & d_{15} & 0 & 0 & 0 & \varepsilon_{11}^{T} & 0 \\ d_{31} & d_{31} & d_{33} & 0 & 0 & 0 & 0 & 0 & \varepsilon_{33}^{T} \end{pmatrix} x \begin{pmatrix} \sigma_1 \\ \sigma_2 \\ \sigma_3 \\ \sigma_4 \\ \sigma_5 \\ \sigma_6 \\ E_1 \\ E_2 \\ E_3 \end{pmatrix}$$

Figure 2.8.2 Reduced matrix for poled ferro-piezoelectric ceramics with 6*mm* symmetry. The colours represent in each of the elastic.

According to the various directions of application of the stress (T) or the electric field (E) with respect to the electric poling direction, it is possible to have three different operation modes in ferro-piezoelectric ceramics. **Table 2.8.1** summarizes them.

Table 2.8.1 three different operation modes in ferro-piezoelectric ceramics: longitudinal operation mode, transverse operation mode and shear operation mode.

Longitudinal operation mode (L) 	$\begin{pmatrix} \boldsymbol{S_3} \\ \boldsymbol{D_3} \end{pmatrix} = \begin{bmatrix} \boldsymbol{s_{33}^E} & \boldsymbol{d_{33}} \\ \boldsymbol{d_{33}} & \boldsymbol{\varepsilon_{33}^T} \end{bmatrix} \begin{pmatrix} \boldsymbol{T_3} \\ \boldsymbol{E_3} \end{pmatrix}$	d_{33} the deformation and electric field are in (3) direction, thus parallel to the polarization.
Transverse operation mode (T) 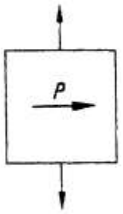	$\begin{pmatrix} \boldsymbol{S_1} \\ \boldsymbol{D_3} \end{pmatrix} = \begin{bmatrix} \boldsymbol{s_{11}^E} & \boldsymbol{d_{31}} \\ \boldsymbol{d_{31}} & \boldsymbol{\varepsilon_{33}^T} \end{bmatrix} \begin{pmatrix} \boldsymbol{T_1} \\ \boldsymbol{E_3} \end{pmatrix}$	d_{31} the electric field is parallel to the polarization (3) and the deformation is perpendicular to the polarization direction (1)
Shear operation modes 	$\begin{pmatrix} \boldsymbol{S_5} \\ \boldsymbol{D_1} \end{pmatrix} = \begin{bmatrix} \boldsymbol{s_{55}^E} & \boldsymbol{d_{15}} \\ \boldsymbol{d_{15}} & \boldsymbol{\varepsilon_{11}^T} \end{bmatrix} \begin{pmatrix} \boldsymbol{T_5} \\ \boldsymbol{E_1} \end{pmatrix}$	d_{15} the electric field is perpendicular to the polarization direction (1), and the relevant deformation is shear deformation around one of the two other perpendicular axis.

2.9 The Heckman diagram. Losses and multifunctionality in ferro-piezoelectric ceramics

The phenomena linking the different external forces, among them the electric fields and mechanical forces (stress), with the responses of the material, like the electric displacement (polarization) or the displacement (strain), were summarized in the well-known Heckman diagram (**Figure 2.9.1**) [20].The mechanical losses, which correspond to the elasticity phenomena, and the dielectric losses, which correspond to the dielectric permittivity are universally accepted, it must be pointed out that all the phenomena represented in the diagram must have the same consideration, as they refer to energy conversion processes and no conversion has a 100% of efficiency. Therefore, both the direct and converse piezoelectric phenomena are affected by the corresponding piezoelectric losses [42]. This must be considered for a complete description of a piezoelectric material and are of key importance for piezoelectric ceramics, complex systems whose properties are governed by features at four different length scales (**Figure 2.4.6**).

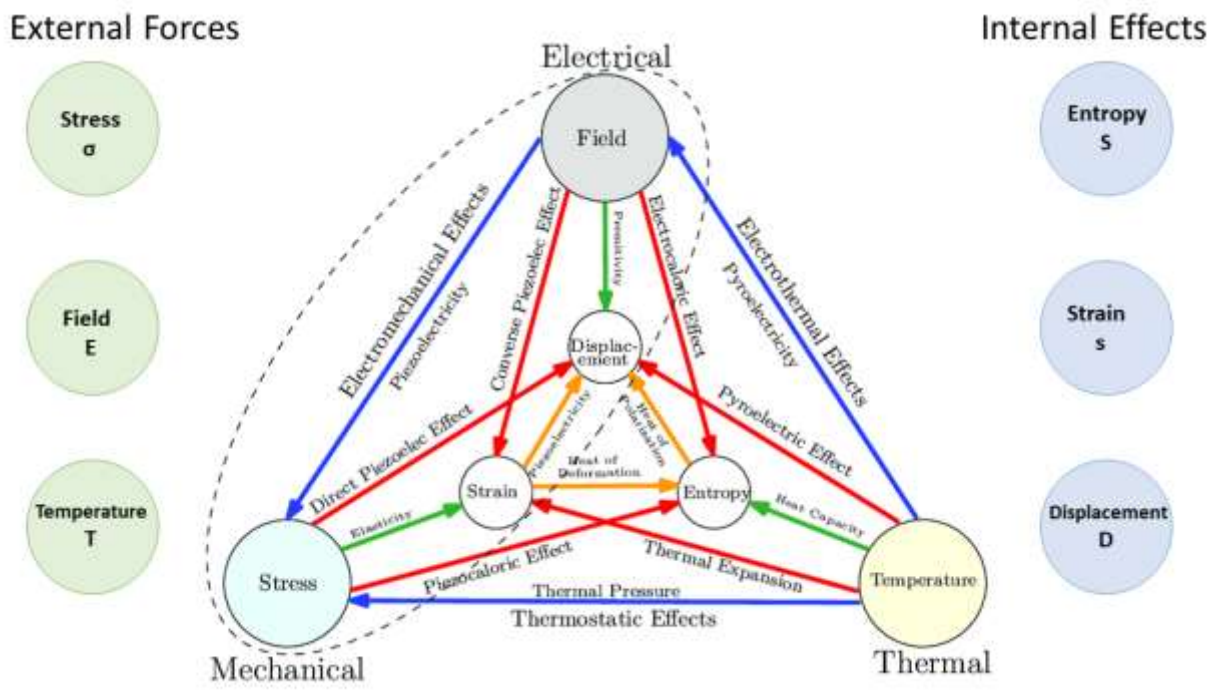

Figure 2.9.1 A Heckman diagram[20] representing the interrelationships between mechanical, thermal and electrical external forces of materials and the material response to them as changes in the entropy, strain or displacement in terms of its properties.

The piezoelectric ceramics, as they are ferroelectrics and these an exemplary group of multifunctional materials, have numerous applications other than piezoelectricity [2,43]. Among the most important ones, derived from their bi-stability (**Figure 2.4.6**), as non-volatile ferroelectric memories; due to their high dielectric permittivity, in capacitors; due to the changes of their spontaneous polarization with temperature (**Figure 2.4.4**) as pyroelectric sensors. The Electrocaloric effect and the ferroelectric electron emission are also sources of applications in these materials. Moreover, as ferroelectrics can be processed as transparent ceramics, they can be used by their electrooptic properties [2].

2.10 Characterization methods of the properties of ferro-piezoelectric ceramics

As already explained above, one of the constants describing the behaviour of a piezoelectric material is the piezoelectric charge constant. Multiple measuring methods are used to provide the value of this coefficient.

At present, the most common measurement approaches consist of the three following methods: the resonance method, the laser interferometry method and the quasi-static method [44]. The laser interferometry method is based on the converse piezoelectric effect and measures the displacement of the sample surface after the application of a voltage (AC electric field in the 10- 350 KHz range) to the electrodes of the measured ferro-piezoelectric ceramic. This method requires the use of expensive high sensitivity laser interferometers in an experimental set-up that must be well isolated from vibrations, as the displacements to be measured may be in the range of nanometers [45].The quasi-static approach to measurement the direct piezoelectric effect determines the charge released by the tested sample is comparison to that of a reference sample, of a known piezoelectric coefficient, under the application of a relatively low frequency (100 Hz) sinusoidal mechanical force. This is the method most commonly used as there are several commercial devices that provides a direct reading of the charge coefficient. This reading can be mainly used for comparison purposes with the literature when developing a processing route for a ferro-piezoceramics or a new composition. However, there are serious limitations to use the obtained value in the design of piezoelectric actuators or sensors [46]. Both methods are mainly used to measure d_{33} and can be adapted to measure d_{31} piezoelectric coefficients.

2.11 The resonance method.

The resonance method is based primarily on the converse piezoelectric effect, by which the application of a low signal AC voltage creates a mechanical vibration in the ferro-piezoelectric ceramic sample. When, as a function of the AC frequency, the vibration reaches one of the natural mechanical resonance modes (maximum amplitude of the vibration) of a given ceramic geometry, e.g. a thin disk poled in thickness (**Figure 2.11.1(a)**), it undergoes a change in its electrical impedance at very precise and stable frequencies. This was observed in in piezoelectric single crystal first (1918–1919) and in ceramics later by Walter G. Cady, American physicist, electrical engineer and father of the modern piezoelectricity in crystals and ceramics[47,48]The electrical impedance of the ceramic resonator (modulus and phase) changes as depicted in **Figure 2.11.1(b)**

for the two main resonances, the planar extensional resonance and the thickness extensional resonance for the thin disk in **Figure 2.11.1(a).**

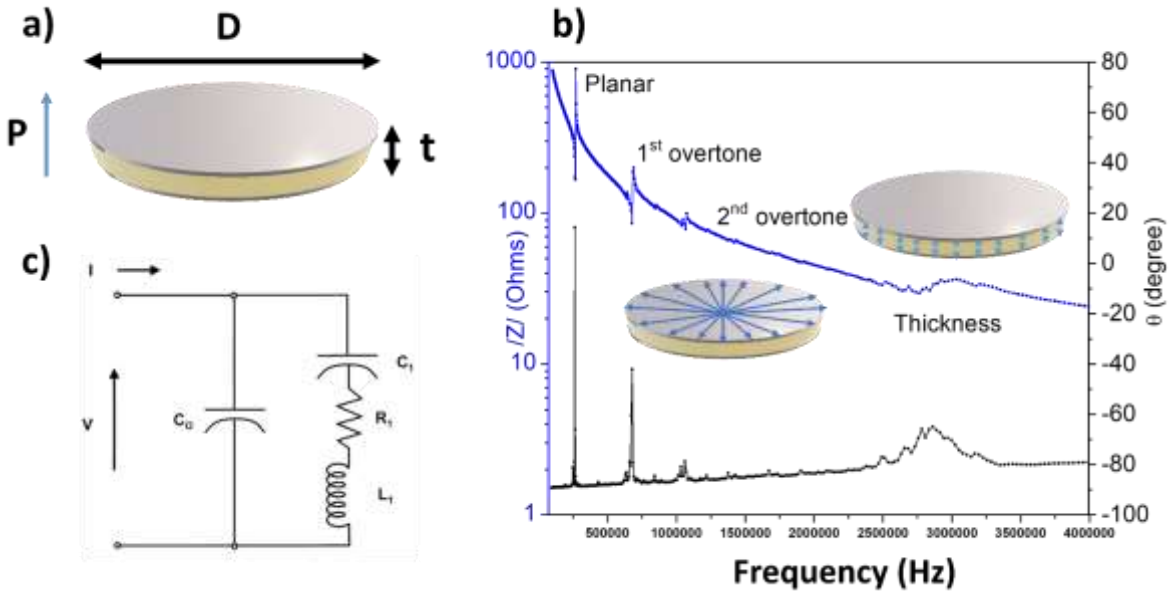

Figure 2.11.1 a) Thin disk-shaped ceramic resonator, b) impedance spectrum modulus and phase of the disk resonator and c) Butterworth-Van Dyke's equivalent circuit of the piezoelectric ceramic resonator, valid in the vicinity of a single resonance.

Each electromechanical resonance mode defines two characteristic frequencies, resonance (f_r minimum Z) and antiresonance (f_a maximum Z) frequencies, this are accompanied by a peak in the phase of the impedance. Phenomenologically, this material response to the applied AC voltage is identical to the one of an electric resonant circuit. This analogy allowed the analysis of the resonance curves to determine the electromechanical coupling factor of the material:

$$k_{eff}^2 = \frac{f_p^2 - f_s^2}{f_p^2} = \frac{C_1}{C_0 + C_1} \qquad (2.18)$$

The resulting values of the material coefficients strongly depend on the accuracy achieved within the reading of the frequencies and on other materials values required for the calculation of all the material coefficients. Thus, for this type of measurement, an impedance analyser providing a very high measuring accuracy for the resonance and antiresonance frequencies is used.

The first standard method of characterization of ferro-piezoelectric ceramics from resonances of quartz crystals was issued in 1961 [49]. These were updated several times and finally substituted by those of the Institute of Electrical and Electronic Engineers (IEEE) in 1987 [50].Later, other standards procedures for calculation of the ferro-piezoceramics, based on the 1987 ones, were issued in Japan and Europe.

The resonance, also called frequency method, is used to obtain the piezoelectric coefficient in cases where the complete matrix of the material coefficients, including dielectric and elastic parameters, must be known. Typically, this is the case of the modelling using numerical methods as the Finite Element Analysis[51]. The greatest disadvantage of the resonance method is the required construction of a complete set of samples made up of a disc, a plate, and a cylinder from the ferro-piezoelectric ceramic to be fully characterized. In each geometry, there are specific natural mechanical resonances that can be excited. A set of coefficients and the associated electromechanical coupling factors can be determined from the analysis of the corresponding impedance curves at the resonance. The needed parameters of the piezoelectric ceramics to calculate their coefficients from the knowledge of the impedance curve are, in addition to the characteristic frequencies obtained from this, the value of the impedance at the resonance frequency, and the free capacitance at 1 kHz, the dimensions of the piezoelectric ceramic sample (resonator) and its density. However, standards commonly used have some well-known critical limitations and they are strictly valid only for low-loss and high electromechanical coupling factor materials [37]. Standards provide material losses only in terms of the mechanical quality factor ($Q_m = s'/s''$) and the dielectric loss tangent ($\tan\delta = \varepsilon'/\varepsilon$). When the need to characterize high loss materials (as polymers and porous ceramics) was approached, alternatives to the standard methods of analysis of impedance curves at resonance were developed to quantify the losses in piezoceramics. This was possible by considering all material parameters, including the piezoelectric coefficients as complex quantities ($P^* = P' - iP''$) [52] .One of these alternative methods have been used in this work [53].

From the point of view of materials characterization aiming to study the potential application of a given ferro-piezoelectric ceramic composition, the resonance method provides key information as it allows the

calculation of the figure of merit (FOM), that is the combination of materials properties of interest, for a variety of applications (**Table 2.11.1**).

Table 2.11.1 Current and future applications of piezoelectric materials, their critical figures of merit for each type of application[54]k: electromechanical coupling coefficient, Q_m: mechanical quality factor, d: piezoelectric strain coefficient, g: piezoelectric voltage coefficient, Fr-TC: temperature coefficient of resonance frequency, xmax/Emax: normalized strain, vmax: vibration velocity.

Temperature range	Resonant or non-resonant	Applications well-established impending		Figures of merit
		well-established	impending	
Special use $T_C > 500\,°C$	Resonant		Aerospace, aircraft, nuclear power plant or geothermal power plant sensors	$k^2 \cdot Q_m, d \cdot g$
SMD piezoelectric Sounders $T_C > 250\,°C$	Resonant	Filter		$k, F_r - TC$
		Oscillator		$Q_m, F_r - TC$
		Gyro sensor		$k^2 \cdot Q_m$
	Non-resonant	Acceleration sensor and HDD shock sensor		$d \cdot g$
Automotive $T_C = -40–125\,°C$	Resonant	Knocking sensor and back sonar	Energy harvesting (TPMS)	$k^2 \cdot Q_m$
	Non-resonant	Knocking sensor	Energy harvesting (TPMS)	$d \cdot g$
		Fuel injection		x_{max}/E_{max}
Consumer $T_C = -20–80\,°C$	Resonant	Fish sonar, flow meter, and medical probe	Energy harvesting (Burglar alarm), ultrasonic transducer (data entry device), and non-destructive testing	$k^2 \cdot Q_m$
		Ultrasonic cleaner, ultrasonic machining tool, camera lens autofocus (motor), power window (motor), backlight inverter, and high-voltage supply transformer	Wind blower and air ionizer	$k^2 \cdot Q_m, v_{max}$
			Micro-mass sensor	Q_m
	Non-resonant	Microphone	Energy harvesting (Burglar alarm)	$d \cdot g$
		Stove burner, lighter, buzzer, and vibration damping (sports gear)		d
		Ink jet, loud speaker, and camera lens module	HDD tracking and pump	x_{max}/E_{max}

2.12 Bibliography

1. Curie, J.; Curie, P. Développement Par Compression de l'électricité Polaire Dans Les Cristaux Hémièdres à Faces Inclinées. *Bull. la Société minéralogique Fr.* **1880**, *3*, 90–93, doi:10.3406/bulmi.1880.1564.

2. Haertling, G.H. Ferroelectric Ceramics: History and Technology. In *Ferroelectricity*; Wiley, 2005; Vol. 818, pp. 157–178 ISBN 9783527404865.

3. Katzir, S. The Emergence of the Principle of Symmetry in Physics. *Hist. Stud. Phys. Biol. Sci.* **2004**, *35*, 35–65, doi:10.1525/hsps.2004.35.1.35.

4. Von Hippel, A. Ferroelectricity, Domain Structure, and Phase Transitions of Barium Titanate. *Rev. Mod. Phys.* **1950**, *22*, 221–237, doi:10.1103/RevModPhys.22.221.

5. Brennecka, G.; Sherbondy, R.; Schwartz, R.; Ihlefeld, J. Ferroelectricity - A Revolutionary Century of Discovery. *Am. Ceram. Soc. Bull.* **2020**, *99*, 24–30.

6. Randall, C.A.; Newnham, R.E.; Cross, L.E. Hystory of the First Ferroelectric Oxide, BaTiO3, In Materials Research Institute, The Pennsylvania State University, University Park, Pa, USA, 1., 2004; pp. 1–11. https://ceramics.org›wp-content›uploads›2009›05› first_ferroelectric_oxide_ba_tio3.pdf"

7. Mohith, S.; Upadhya, A.R.; Navin, K.P.; Kulkarni, S.M.; Rao, M. Recent Trends in Piezoelectric Actuators for Precision Motion and Their Applications: A Review. *Smart Mater. Struct.* **2021**, *30*, doi:10.1088/1361-665X/abc6b9.

8. Nye, J.F. *Physical Properties of Crystals: Their Representation by Tensors and Matrices*; Oxford university press, 1985;

9. R.E. Newnham *Structure-Property Relations.*; Springer -Verlag: New York, 1975; ISBN 0-387-07124-5.

10. Klapper, H.; Hahn, T. Point-Group Symmetry and Physical Properties of Crystals. *Int. Tables Crystallogr.* **2006**, 804–808, doi:10.1107/97809553602060000521.

11. J Tichý, J Erhart, E Kittinger, J Přívratská, J Tichý, J Erhart, E Kittinger, J.P. Principles of Piezoelectricity. In *Fundamentals of Piezoelectric Sensorics: Mechanical, Dielectric, and Thermodynamical Properties of Piezoelectric Materials*; 2010; pp. 1-14.

12. Curie J, C.P. Contractions et Dilatations Produites Par Des Tensions Électriques Dans Les Cristaux Hémièdres à Faces Inclinées. *Comptes rendus l'Académie des Sci.* **1881**, *93*, 1137–1140.

13. Van Randeraat, J., & Setterington, R.E. Electronic Components and Materials. In *Piezoelectric Ceramics*; Eindhoven, The Netherland, 1974.

14. Brusa, E.; Carrera, A.; Delprete, C. A Review of Piezoelectric Energy Harvesting: Materials, Design, and Readout Circuits. *Actuators* **2023**, *12*, doi:10.3390/act12120457.

15. Moure, C.; Peña, O. Recent Advances in Perovskites: Processing and Properties. *Prog. Solid State Chem.* **2015**, *43*, 123–148, doi:10.1016/j.progsolidstchem.2015.09.001.

16. Goldschmidt, V.M. Die Gesetze Der Krystallochemie. *Naturwissenschaften* **1926**, *14*, 477–485, doi:10.1007/BF01507527.

17. Kieslich, G.; Sun, S.; Cheetham, A.K. Solid-State Principles Applied to Organic–Inorganic Perovskites: New Tricks for an Old Dog. *Chem. Sci.* **2014**, *5*, 4712–4715, doi:10.1039/c4sc02211d.

18. Bartel, C.J.; Sutton, C.; Goldsmith, B.R.; Ouyang, R.; Musgrave, C.B.; Ghiringhelli, L.M.; Scheffler, M. New Tolerance Factor to Predict the Stability of Perovskite Oxides and Halides. *Sci. Adv.* **2019**, *5*, 1–9,

doi:10.1126/sciadv.aav0693.

19. Cheng, R.; Wang, Y.; Men, R.; Lei, Z.; Song, J.; Li, Y.; Guo, M. High-Energy-Density Polymer Dielectrics via Compositional and Structural Tailoring for Electrical Energy Storage. *iScience* **2022**, *25*, 104837, doi:10.1016/j.isci.2022.104837.

20. Heckmann, G. Die Gittertheorie Der Festen Körper. In *Ergebnisse der Exakten Naturwissenschaften*; Springer Berlin Heidelberg: Berlin, Heidelberg, 1925; pp. 100–153.

21. Acosta, M.; Novak, N.; Rojas, V.; Patel, S.; Vaish, R.; Koruza, J.; Rossetti, G.A.; Rödel, J. BaTiO3-Based Piezoelectrics: Fundamentals, Current Status, and Perspectives. *Appl. Phys. Rev.* **2017**, *4*, doi:10.1063/1.4990046.

22. Potnis, P.R.; Tsou, N.T.; Huber, J.E. A Review of Domain Modelling and Domain Imaging Techniques in Ferroelectric Crystals. *Materials (Basel).* **2010**, *4*, 417–447, doi:10.3390/ma4020417.

23. Jin, L.; Li, F.; Zhang, S. Decoding the Fingerprint of Ferroelectric Loops: Comprehension of the Material Properties and Structures. *J. Am. Ceram. Soc.* **2014**, *97*, 1–27, doi:10.1111/jace.12773.

24. Stancu, A.; Ricinschi, D.; Mitoseriu, L.; Postolache, P.; Okuyama, M. First-Order Reversal Curves Diagrams for the Characterization of Ferroelectric Switching. *Appl. Phys. Lett.* **2003**, *83*, 3767–3769, doi:10.1063/1.1623937.

25. Robert, G.; Damjanovic, D.; Setter, N. Preisach Distribution Function Approach to Piezoelectric Nonlinearity and Hysteresis. *J. Appl. Phys.* **2001**, *90*, 2459–2464, doi:10.1063/1.1388855.

26. Ciomaga, E.; Buscaglia, M.; Viviani, M.; Buscaglia, V.; Mitoseriu, L.; Nanni, P.; Galassi, C. Composition and Grain Size-Driven Ferroelectric-Relaxor Crossover in Ba(Zr,Ti)O3 Ceramics. *Process. Appl. Ceram.* **2009**, *3*, 51–57, doi:10.2298/pac0902051c.

27. Cao, W.; Randall, C.A. Grain Size and Domain Size Relations in Bulk Ceramic Ferroelectric Materials. *J. Phys. Chem. Solids* **1996**, *57*, 1499–1505, doi:10.1016/0022-3697(96)00019-4.

28. Randall, C.A.; Kim, N.; Kucera, J.; Cao, W.; Shrout, T.R. Intrinsic and Extrinsic Size Effects in Fine-Grained Morphotropic-Phase-Boundary Lead Zirconate Titanate Ceramics. *J. Am. Ceram. Soc.* **1998**, *81*, 677–688, doi:10.1111/j.1151-2916.1998.tb02389.x.

29. Guo, H.; Voas, B.K.; Zhang, S.; Zhou, C.; Ren, X.; Beckman, S.P.; Tan, X. Polarization Alignment, Phase Transition, and Piezoelectricity Development in Polycrystalline 0.5Ba(Zr0.2 Ti0.8)O3-0.5(Ba0.7 Ca0.3)TiO3. *Phys. Rev. B - Condens. Matter Mater. Phys.* **2014**, *90*, 1–10, doi:10.1103/PhysRevB.90.014103.

30. Setter, N. What Is a Ferroelectric–a Materials Designer Perspective. *Ferroelectrics* **2016**, *500*, 164–182, doi:10.1080/00150193.2016.1232104.

31. Tsuji, K.; Fan, Z.; Bang, S.H.; Dursun, S.; Trolier-McKinstry, S.; Randall, C.A. Cold Sintering of the Ceramic Potassium Sodium Niobate, $(K_{0.5}Na_{0.5})NbO_3$, and Influences on Piezoelectric Properties. *J. Eur. Ceram. Soc.* **2022**, *42*, 105–111, doi:10.1016/j.jeurceramsoc.2021.10.002.

32. Rojac, T.; Kosec, M.; Budic, B.; Setter, N.; Damjanovic, D. Strong Ferroelectric Domain-Wall Pinning in $BiFeO_3$ Ceramics. *J. Appl. Phys.* **2010**, *108*, doi:10.1063/1.3490249.

33. Arlt, G. The Influence of Microstructure on the Properties of Ferroelectric Ceramics. *Ferroelectrics* **1990**, *104*, 217–227, doi:10.1080/00150199008223825.

34. Damjanovic, D. Contributions to the Piezoelectric Effect in Ferroelectric Single Crystals and Ceramics. *J. Am. Ceram. Soc.* **2005**, *88*, 2663–2676, doi:10.1111/j.1551-2916.2005.00671.x.

35. Lv, X.; Zhang, X.X.; Wu, J. Nano-Domains in Lead-Free Piezoceramics: A Review. *J. Mater. Chem. A* **2020**, *8*, 10026–10073, doi:10.1039/d0ta03201h.

36. Mendiola, J.; Alemany, C.; Jidienez, B.; Maurer, E. Poling Strategy of PLZT Ceramics. *Ferroelectrics* **1984**, *54*, 195–198, doi:10.1080/00150198408215849.

37. Genenko, Y.A.; Glaum, J.; Hoffmann, M.J.; Albe, K. Mechanisms of Aging and Fatigue in Ferroelectrics. *Mater. Sci. Eng. B* **2015**, *192*, 52–82, doi:10.1016/j.mseb.2014.10.003.

38. Subbarao, E.C.; McQuarrie, M.C.; Buessem, W.R. Domain Effects in Polycrystalline Barium Titanate. *J. Appl. Phys.* **1957**, *28*, 1194–1200, doi:10.1063/1.1722606.

39. Baerwald, H.G. Thermodynamic Theory of Ferroelectric Ceramics. *Phys. Rev.* **1957**, *105*, 480–486, doi:10.1103/PhysRev.105.480.

40. Messing, G.L.; Trolier-McKinstry, S.; Sabolsky, E.M.; Duran, C.; Kwon, S.; Brahmaroutu, B.; Park, P.; Yilmaz, H.; Rehrig, P.W.; Eitel, K.B.; et al. Templated Grain Growth of Textured Piezoelectric Ceramics. *Crit. Rev. Solid State Mater. Sci.* **2004**, *29*, 45–96, doi:10.1080/10408430490490905.

41. Safari, A.; Akdoğan, E.K. Piezoelectric and Acoustic Materials for Transducer Applications. *Piezoelectric Acoust. Mater. Transducer Appl.* **2008**, 1–481, doi:10.1007/978-0-387-76540-2.

42. González, A.; García, Á.; Benavente-Peces, C.; Pardo, L. Revisiting the Characterization of the Losses in Piezoelectric Materials from Impedance Spectroscopy at Resonance. *Materials (Basel).* **2016**, *9*, 72, doi:10.3390/ma9020072.

43. Scott, J.F. Applications of Modern Ferroelectrics. *Science (80-.).* **2007**, *315*, 954–959, doi:10.1126/science.1129564.

44. Fialka, J.; Benes, P. Comparison of Methods for the Measurement of Piezoelectric Coefficients. *IEEE Trans. Instrum. Meas.* **2013**, *62*, 1047–1057, doi:10.1109/TIM.2012.2234576.

45. Li, J.-F.; Moses, P.; Viehland, D. Simple, High-Resolution Interferometer for the Measurement of Frequency-Dependent Complex Piezoelectric Responses in Ferroelectric Ceramics. *Rev. Sci. Instrum.* **1995**, *66*, 215–221, doi:10.1063/1.1145261.

46. Mendiola, J.; Alemany, C.; Pardo, L.; Gonzalez, A. Poling Reversal Effects on Piezoelectricity of Calcium Modified Lead Titanate Ceramic. *Ferroelectrics* **1989**, *94*, 209–214, doi:10.1080/00150198908014255.

47. Katzir, S. From Ultrasonic to Frequency Standards: Walter Cady's Discovery of the Sharp Resonance of Crystals. *Arch. Hist. Exact Sci.* **2008**, *62*, 469–487, doi:10.1007/s00407-008-0020-3.

48. Cady, W.G. Introduction to the Theory and Applications of Electromechanical Phenomena in Crystals. In *Piezoelectricity*; Mc Graw Hill Book Co.: New York, NY, USA, 1946.

49. USA Institute of Radio Engineers (IRE) Standard on Piezoelectric Crystals: Measurements of Piezoelectric Ceramics, 1961". *Proc. IRE* **1961**, *49(7)*, 1161–1169.

50. Publication and Proposed Revision of ANSI/IEEE Standard 176-1987 "ANSI/IEEE Standard on Piezoelectricity." *IEEE Trans. Ultrason. Ferroelectr. Freq. Control* **1996**, *43*, 717, doi:10.1109/TUFFC.1996.535477.

51. L. Pardo, K.B. Properties of Ferro-Piezoelectric Ceramic Materials in the Linear Range: Determination from Impedance Measurements at Resonance. In *Multifunctional Ferroelectric Materials.Processing and Properties*; L.Pardo and J. Ricote, Ed.; 2010; p. Volume 140.

52. Holland, R. Representation of Dielectric, Elastic, and Piezoelectric Losses by Complex Coefficients. *IEEE Trans. Sonics Ultrason.* **1967**, *14*, 18–20, doi:10.1109/T-SU.1967.29405.

53. Alemany, C.; Pardo, L.; Jimenez, B.; Carmona, F.; Mendiola, J.; Gonzalez, A.M. Automatic Iterative Evaluation of Complex Material Constants in Piezoelectric Ceramics. *J. Phys. D. Appl. Phys.* **1994**, *27*, 148–155, doi:10.1088/0022-3727/27/1/023.

54. Rödel, J.; Webber, K.G.; Dittmer, R.; Jo, W.; Kimura, M.; Damjanovic, D. Transferring Lead-Free Piezoelectric Ceramics into Application. *J. Eur. Ceram. Soc.* **2015**, *35*, 1659–1681, doi:10.1016/j.jeurceramsoc.2014.12.013.

3 State of the Art: Hallmarks of BCZT-based piezoceramics: from chemical fundamental to processing route

3.1 Introduction

Nowadays, global growing concern about environment protection, scarcity of raw materials, human health, climate change and CO_2 levels seem to have a sense of urgency. The scientific community, research, and innovation are constantly moving towards the development of more sustainable processes with efficient materials. In this regard, national and supranational institutions are trying to meet these requirements by issuing various directives, e. g. the EU's Restriction of Hazardous Substances (RoHS) in 2002, its revision (RoHS 2) in 2011 [1] and the Roadmap for moving to a competitive low-carbon economy in 2050 [2]. Therefore, research and innovation are rapidly moving towards optimum processing routes for obtaining non-toxic materials with enhanced properties. In this scenario the market for functional ceramics, such as piezoelectric materials is affected by this environmental revolution [3]. During the last few decades, many researchers have addressed their attention to replacing the toxic market-dominant Lead Zirconate Titanate, well known as PZT, by developing lead-free materials with an environmentally friendly nature and benign processing route. One of the most promising candidates is $(Ba,Ca)(Zr,Ti)O_3$ (BCZT), a modified $BaTiO_3$-based system, which has been widely reported due to its notable electrical properties. Unfortunately, like other lead-free alternatives ($(K\ Na)\ NbO_3$, KNN; $(BiNaBaTi)O_3$, BNBT), the Achilles' heel is the non-guaranteed reproducibility of this complex system. Besides, the high processing costs prevent the industrial scaling up. In this perspective, assuming that the processing route constitutes a key point for obtaining high-sensitivity piezoelectric ceramics with a pure single phase, the present review of the state of the art proposes an overview of different solid-state routes used for processing BCZT ceramics. The fundamentals of BCZT system and the main drawbacks for fabricating the material at industrial level will be analysed. The core of this Chapter focuses on the main ball-milling setup used for mechanically activating BCZT precursors as oxides and carbonates and calcined powders. Moreover, the milestones achieved during the last few years and the

newly reported applications have been also discussed. However, as stated in **Chapter 2**, as a complex system, it possesses four levels of dimensions of microstructural characteristics (ceramic, ferroelectric domain configuration, solid solution, crystal lattice) to consider tailoring their performance. Therefore, there are several aspects that must be considered during the ceramic development.

3.1.1 BCTZ: a Lead-free alternative to PZT system.

Many researchers have been summarizing the pros (environmentally friendly nature, availability of precursors, non-toxic nature) and cons (difficult reproducibility, high processing temperatures, difficulties in transferring to technology) of lead-free systems in order to be able to carry out a systematic study of these systems and to understand which are the key points to be thoroughly investigated [4–11]. Indeed, especially in the case of piezoelectric ceramics, there are many parameters that must be considered, such as: i) the fundamentals of the solid solution, ii) the occurrence of secondary phases that can limit the formation of the pure perovskite, iii) the system-specific phase transition at precise different temperatures, iv) the physical and chemical mechanisms for obtaining good electromechanical properties [12].

The processing route plays a crucial role for obtaining pure phase powders and an optimal microstructure leading to an enhancement of the electromechanical characteristics [13]. In fact, despite seemingly minor aspects, all stages of processing must be carefully controlled, especially in the case of the solid-state route, such as: i. the contamination from the vial and grinding media when the powders are activated via ball-milling, ii. the contamination/activation from organic solvents that can influence the final product, as well as iii. the reactions that can occur with the crucible used during the calcination and sintering steps, particularly in high melting temperature compositions, as barium titanate (>1600° C), requiring high sintering temperatures and long times. All these aspects modify the chemical composition of the system. In addition, the chosen synthesis method (solid-state or sol-gel route) has an influence on the final microstructure of the densified polycrystal in terms of the evolution of particle size throughout the material processing, which is closely related to the final properties [14].

Over the last decade, several reviews on BCZT-based ceramics have been reported [6,12,15–19], however a focused review on the influence of ball milling parameters (vessel materials, ball-to-powder ratio, ball-milling apparatus used and rotation/vibration frequencies) and processing parameters that could lead to a variation of the synthesis/sintering temperatures is lacking.

There are challenges in the synthesis and processing of BCTZ piezoelectric ceramics that must be solved. Stoichiometric control, especially when volatile and heavy elements are involved, the search for a morphotropic phase boundary (MPB) composition, softer synthesis conditions, proper sintering conditions, adequate grain size and consequently ferroelectric domain size and distribution, together with scalability and cost are among the main challenges for their industrial transfer. Nevertheless, it is essential to know the mechanisms which are the basis of the piezoelectricity of the system to promote actions through which processing costs can be reduced. In this review, at first instance, the intrinsic and extrinsic contributions to piezoelectricity in the BCZT system will be presented. Then an analysis on the influence of the processing route, with a particular focus on the ball-milling techniques exploited for solid-state route will be provided. Finally, the toxicity evaluation of the BCTZ system and its applications in the biomedical field, will be discussed. The various aspects concerning BCZT will be examined using an analytical approach.

For the sake of clarity, it will be divided into several sections**: (I) Critical and historical overview of the phase diagram and pseudo MPB. (II) The role of processing on properties, with focus on mechanical activation in the solid-state route. (III) Piezoelectric materials and human health: new emerging applications in the biomedical field.**

3.2 Fundamentals

3.2.1 Historical and critical overview of the phase diagram.

Although the most influential manuscript on their piezoelectricity by Liu and Ren [20], was published in the early 2000s, BCZT ceramics were discovered in 1954, when McQuarrie and Behnke reported for the first time the baria-calcia-titania-zirconia tetrahedron phase diagram [21]. It was during the age of the explosive

development of ferroelectric oxide ceramics that followed the discovery of the ferroelectricity of barium titanate [22] and that led as well to the discovery of lead titanate zirconate (PZT). BCZT was first studied as a relevant system for capacitor applications at the time and have been studied as such ever since [21]. A planar square section was extracted from this solid-solution system, showing at the corners the composition of barium titanate (BT), barium zirconate (BZ), calcium titanate (CT) and calcium zirconate (CZ), respectively. It should be noted that the materials, weighed in the desired proportions, were pre-processed by wet grinding. This pioneering study shows that authors inspected the variation of lattice constants for the pseudo-binary composition along the four edges. The near-edge of $BaTiO_3$-$BaZrO_3$ and $CaTiO_3$-$CaZrO_3$ compositions shows evidence of a complete formation of a solid solution, whereas all intermediate compositions contained two separate phases. In particular, the crystalline phases of the $(Ba_{1-x}Ca_x)$ $(Ti_{1-y}Zr_y)$ O_3 system, and their lattice parameters determined from the X-ray powder patterns of the fired ceramic discs were identified. The values of the lattice constants along the different sides of the square composition showed marked deviations from Vegard's law indicating site occupancy changes, at some points [23], especially in the corner of the barium zirconate. However, variations of Curie point temperature and ageing rate correlated reasonably well with changes in the character of the crystal structure [23]. One year later, in 1955, this fervent activity of the two coexisting ternary systems, viz. the systems $CaTiO_3$-$BaTiO_3$-$BaZrO_3$ and $CaTiO_3$-$CaZrO_3$-$BaZrO_3$, was augmented by a study of the stability of materials with perovskite-like structure [24]. The value of the Gibbs free energy, which determines the phase stability, was related to the degree to which the ions may or not fit into the perovskite lattice. After definition of a tolerance factor *t* for perovskite structure and taking the value $|t-1|$ as a measure of the Gibbs free energy, then the most stable combination in the (Ba, Ca) (Ti, Zr) O_3 system was found to be $BaZrO_3$ + $CaTiO_3$. Twenty and more years later (1977), the BCZT system subject was reconsidered by Hennings and Schreinemacher with a focus on the separated paraelectric phase of $CaTiO_3$ that may influence the ferroelectric and dielectric properties of BCZT [25]. It was observed that the amount of secondary phase depends on the temperature of heat treatment and subsequent cooling rate. The authors suggested that the microstructure may affect the observed permittivity and reported also on the presence of contamination from milling tools although they could not establish any correlation between energy

impacts and critical temperatures. It was also recommended to consider the effect of microstructure parameters, typically crystallite size and strain.

Interesting for the further development of ferro-piezoelectric compositions in the BCZT system are the initiation in the late fifties and early sixties of two separated lines of research of the dielectric properties in the $BaTiO_3$-$CaTiO_3$ [26,27]and $BaTiO_3$-$BaZrO_3$ [28–31] systems, respectively. These merged in the work by Ravez in 1999, in which to summarize their findings the authors drew the well-known quasi-ternary diagram $BaZrO_3$-$BaTiO_3$-$CaTiO_3$ [32]. This diagram would inspire later work on the piezoelectricity of the BCZT system, specifically within the line of the solid solution system with end members $(Ba_{0.70}Ca_{0.30})TiO_3$ and $Ba(Ti_{0.8}Zr_{0.2})O_3$ [24]. The optimum piezoelectric in this system is found for the composition 0.50 $(Ba_{0.7}Ca_{0.3})TiO_3$-0.50 $Ba(Ti_{0.8}Zr_{0.2})O_3$, which can also be rewritten as $(Ba_{0.85}Ca_{0.15})(Ti_{0.90}Zr_{0.10})O_3$ and is commonly referred to as BCT-50BZT or, simply BCZT. However, many other interesting compositions have also been studied outside this specific line of the ternary diagram [33].

Simultaneously, following the parallel research line of thin films, in 1999 Toyoda and Lubis reported the synthesis of thin films of nominal composition $(Ba_{0.92}Ca_{0.08})$ $(Ti_{0.92}$ $Zr_{0.08})$ O_3 (BC_8TZ_8) with single-phase perovskite structure with very good dielectric performances [34]. For thin films heat-treated at 800°C, the value of the relative dielectric permittivity and dielectric loss, were ε= 1200 and tan δ=0.005 respectively, with nonlinear coefficient α = 0.92, and break-down voltage of 980 V. A few years later, Sen and Choudhary performed the synthesis of polycrystalline powders of $(Ba_{1-x}Ca_x)$ $(Zr_{0.05}Ti_{0.95})$ O_3 (BC_xTZ_5) with compositions for x=0, 0.03, 0.06 and 0.09 [35]. Detailed studies of dielectric parameters as a function of temperature at 10 kHz suggested that the substitution of Ca^{2+} ion at the Ba-site and Zr^{4+} at Ti-site has a strong effect on the dielectric properties of $BaTiO_3$. It was reported that the R-T tetragonal structure of $BaTiO_3$ can be changed to orthorhombic structure by doping. Preliminary X-ray diffraction results suggested that R-T tetragonal structure of $BaTiO_3$ can be changed to orthorhombic by doping, but the evidence provided remains questionable [35]. As mentioned above, the breakthrough article for the $zBC_{30}T$- (1-z) BTZ_{20} system, hereinafter called BCZT system, was the 2009 article by Liu and Ren, which boosted considerably the interest in this system thanks to the surprisingly quasi-static piezoelectric coefficient d_{33} ≈ 620 pC/N reported at the

optimal composition (for $50BC_{30}T$-$50BTZ_{20}$ or $BC_{15}TZ_{10,}$ hereinafter called BCZT composition) [20]. The phase diagram of the pseudo-binary ferro-piezoelectric system was constructed and the evaluation of the dielectric permittivity (ε) versus temperature curves (T) was reported. The structures of different phases were assessed by X-ray diffraction. The phase diagram turned out to be characterized by a so called Morphotropic Phase Boundary (MPB) separating a ferroelectric rhombohedral *R-3m* R (BZT side) and tetragonal *P4mm* T (BCT side) phases. The most important feature of this BCZT system, is the existence of a Cubic-Rhombohedral-Tetragonal triple point in the phase diagram located at x ≈ 32% and at T = 57 °C. According to the authors, the high piezoelectricity of the MPB compositions stems from the proximity to the critical triple point. Therefore, when a suitable Tri-critical point type MPB is designed, lead-free systems may exhibit equally excellent or even better piezoelectricity than those Pb-based at RT [20]. Following this important report, other authors attempted to reproduce and detail the phase diagram with high resolution. Keeble et al. reinvestigated this BCZT system using high-resolution synchrotron X-ray powder diffraction [36]. Contrary to previous reports of unusual rhombohedral-tetragonal phase transition, they observed an intermediate orthorhombic *Amm2* phase, isostructural to that present in the parent phase, $BaTiO_3$, and the previously assigned T-R transition as a T-O transition can be identified. They also reported the O-R transition coalescing with the previously observed triple point, forming a phase convergence region. However, the SXRD evidence to favour the orthorhombic existence at 42 °C remains difficult to attribute entirely to the *Amm2*. In fact, the a/b'/c' pseudo cubic ratio for the three lattice parameters extracted from the Supporting Information of their paper are 1/1.0021/1.0012 respectively [36]. According to RT coexistence evaluation of tetragonal and orthorhombic phases the same ratio holds 1:0.9914:0.9944 for the "pure" $BaTiO_3$ compound, where in this case the a-axis was determined to be 4.0093 Å [37]. Strictly speaking on a powder crystallography basis the reported differences, though coming from highly resolved patterns, are not making a clear conclusive difference from a tetragonal habit. It was also demonstrated that Ca off-centring plays a critical role in stabilizing the ferroelectric phase and tuning the polarization state in the $(Ba_{1-x}Ca_x)(Zr_{0.1}Ti_{0.9})O_3$ with x ≈ 0.1–0.18 compositions [38]. The Ca off-centring effect also allowed us to shift the R–O and O–T phase boundaries to room temperature, leading to the occurrence of electromechanical coupling factors at RT, comparable to those of PZT, in the system over a large composition range. Nevertheless, Acosta et al. (2014) reported a

detailed compositional study of the (1 - z) Ba ($Zr_{0.2}Ti_{0.8}$) O_3–z($Ba_{0.7}Ca_{0.3}$) TiO_3 with x = 0.3, 0.32, 0.35, 0.37, 0.4, 0.45, 0.5 and 0.6 compositions analysing dielectric, small signal d_{33} and large signal d_{33}^* properties as functions of temperature [39]. The methodology employed allowed a complete assessment of the role of the convergence region on the electromechanical properties. The authors posed the question whether the convergence region is responsible for the outstanding electromechanical properties rather this is related to the ferroelectric/ferroelectric phase transitions in the system previously denominated as MPB. They concluded that the highest piezoelectric coefficients occur at ferroelectric–ferroelectric phase transitions and are rather small at the phase convergence region. This behaviour is attributed to the low spontaneous polarization related to the small distortion of the cubic perovskite at the phase convergence region [39]. Soon after, other authors analysed the RT coexistence of phases as well as electric field driven transformation from tetragonal to orthorhombic +rhombohedral transformation both by XRD [40] and *in situ* TEM [41]. Later, Yang et al. (2016) reconstructed theoretically this BCZT system diagram by formulating a generic sixth-order Landau free energy polynomial showing a good agreement with the experimentally measured one, confirming the presence of the orthorhombic region [42]. After all these interesting studies, another key unresolved point is the presence of a monoclinic phase, already observed for the PZT system, as remarked by Cordero in his review on the factors that promote the piezoelectric effect [43]. Indeed, analysing the relationship between the crystalline systems from a crystallographic point of view, it should be noticed the presence of a monoclinic phase transition between the rhombohedral and orthorhombic phases, as suggested for pure $BaTiO_3$. This phase appears to be an adaptive nano-winned tetragonal/pseudo-orthorhombic phase. Furthermore, this M-bridge phase would allow for a better accommodation between the O and T domains [43]. Theoretical work soon confirmed the existence of this phases in the BCZT composition using a large-scale atomistic scheme [44]. Besides, Liu et al. [45] constructed the three-dimensional compositional phase diagrams this BCZT system for the relative energies per unit cell, the lattice constants, the cell volumes and the band gaps, as functions of the Ca (up to x=0.20) and Zr (up to y=1.00) amounts by first-principles calculations and Landau-Devonshire theory. The authors claimed that the energy and structural parameters of the C, T, O, and R phases of BCZT become smaller on increasing the Zr content, and the four phases eventually merge into a multiphase condition with coexisting cubic structures under Zr-

rich conditions, indicating a phase transition from normal to relaxor ferroelectrics, characterized by ferroelectric microdomains and nanodomains, respectively, in agreement with experimental observations [28–31]. Similarly to what other authors did before with the BCZT composition using dielectric or Raman spectroscopy vs. temperature measurements or combination with other techniques [40,46–48] Aredes [49] used a multi-technique approach to investigate the temperature-induced phase transitions and phase coexistence in ceramics of $0.44(Ba_{0.70}Ca_{0.30})TiO_3$-$0.66Ba(Zr_{0.20}Ti_{0.80})O_3$ ($44BC_{30}T$-$66BTZ_{20}$) composition. Results showed that this composition presents also three-phase transitions at temperatures of 11, 41 and 84 °C, respectively. The evidence from this study suggested that such composition presents the coexistence of the tetragonal and orthorhombic phases in the temperature range from 41 to 71 °C. Because of all these studies, the orthorhombic phase nowadays is considered well documented. To conclude, a summarized historical evolution of the BCZT phase diagram is presented in **Figure 3.2.1**.

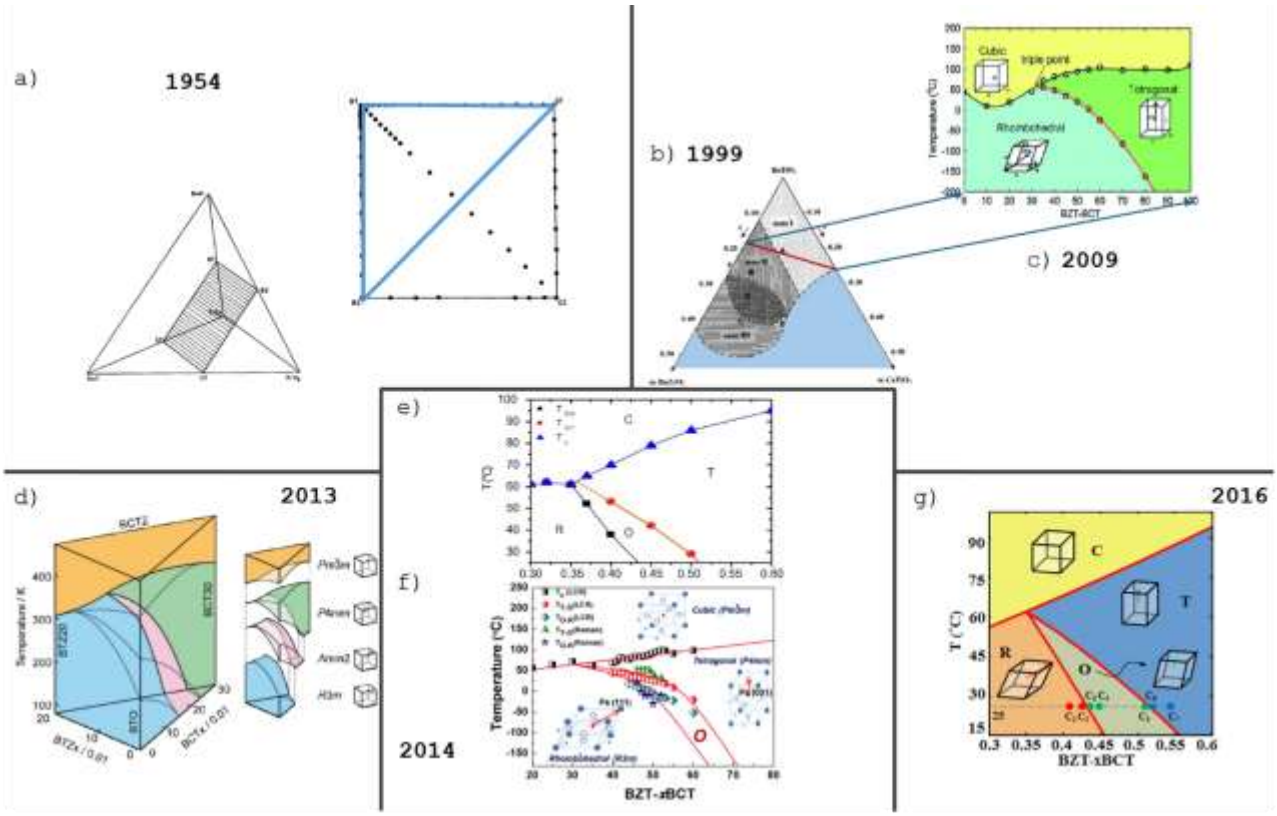

Figure 3.2.1 ***a)****Historical evolution of BCZT phase diagram: From 1954 McQuarrie and Behnke reported for the very first time the Baria-calcia-titania-zirconia composition tetrahedron showing the plane composition square of barium titanate (BT), barium zirconate (BZ), calcium titanate (CT), and calcium zirconate (CZ)* [21]*;* ***b)*** *Ravez 1999 pseudo-ternary phase diagram* [32]*;* ***c)*** *Liu and Ren -2009- Phase diagram of pseudobinary ferroelectric system BZT- BCT. At the triple point where there is the R-T-C phase coexistence the piezoelectric properties are excellent* [20]*;* ***d)*** *Kebble-2013 Revised Phase diagrams of BCZT solid-solutions. In this new phase diagram an orthorhombic phase has been added* [36] *;****e)*** *Acosta et al. phase diagram obtained from the peaks of the imaginary part of the relative permittivity that confirmed the O/FE phase* [39]*;* ***f)*** *The updated temperature-composition phase diagram using Raman and permittivity results (The solid lines are guide to the eyes)* [47] ***g)*** *Calculated pseudo-binary phase diagram of BZT-xBCT, which confirmed the experimentally obtained one. Dots corresponds to the investigated following compositions: x = 0.41, 0.43360, 0.43450, 0.44750, 0.51905, 0.51913 and 0.55000* [42].

3.2.2 Overview of the pseudo MPB

The enhancement of the complex piezoelectric phenomenon in piezoceramics is essentially related to two main contributions [50]. The intrinsic one is represented by the effect of the electric field on the crystalline lattice, which requires the presence of crystal structure lattice non-centrosymmetric distortion (spontaneous polarization) and it is affected by dopants, crystalline defects, phase coexistence at the MPB, FE-FE phase transitions and the working temperature with respect to the FE-PE transition at the Curie Point. It is also affected by the field-induced transitions between polymorphs with distinct lattice distortion (such as polarization clock-like rotations between allowed crystal directions and polarization extension). The extrinsic

contribution is mainly represented by the domains movement that depends also on the ceramic microstructure (grain size determining the domain size, density and porosity determining intergranular stresses) [51].

Considering the intrinsic factors, one of the key points is represented by the effective coexistence of one or more phases in a, compositionally dependent, given region of the phase diagram, usually called Morphotropic Phase Boundary (MPB). In fact, the classical approach to achieve high piezoelectricity is to place the composition of such solid solutions in the proximity of a multi- phase range or MPB, where the polarization direction can be easily rotated by an external stress or an electric field, resulting in a high piezoelectric and dielectric response [52]. So, if there are two or more polymorphs there is the possibility to have more polarization directions permitted. In this way, under and external field the polarization direction can easily assume more allowed directions close to that of the field [43].

Before discussing the characteristics of MPB in the BCZT system, it is essential to clarify the nomenclature used in the literature as it is substantive and not just formal. With specific reference to the BCZT phase diagram, unlike PZT, the MPB is not normal to the x-axis (**Figure 3.2.1**), being strongly dependent on the temperature. For this the region of the phase diagram of the system is more appropriated called Polymorphic Phase Boundary [53–56], though it is reported also as conventional MPB [39,52,57–61] and Thermotropic phase boundary (TPB) [43]. Furthermore, another term has been found for this system, the multiphase coexistence point (MPC), which is not only a point where the FE (R, O, T) phase and the PE (C) phase coexist but, is a point where no energy barrier exists between the three polymorphs. In this sense, some interesting studies report a correlation between free energy ΔG and spontaneous polarization of a given polymorph, P, showing the reduction in the height of the energy barrier at this tricritical point (TCP), described as *isotropic free energy surface* for TCP [20]. Cordero underlined that at the TCP the thermal hysteresis of all these transitions vanishes, indicating that the free energy is particularly flat for both changes of the magnitude and orientation of the polarization [43]. Considering the polarization anisotropy(P), the correct reproduction of ferroelectric phases with different symmetries implies the introduction of free energy expansion terms anisotropic. In **Figure 3.2.2(c)** is shown that the minima of G (P) depend on βan for P|| {100}, {110} and {111}

and the angular plots of min G. When βan > 0 the absolute minima are along {100}, reproducing the T phase, whereas for βan < 0 the absolute minima are along {111} characteristic of the R phase. When more phases coexist , in the intermediate situation, at MPB, βan = 0 is isotropic [43]. This means that at the MPC there is no energy barrier between the four phases. This situation corresponds to a flat or pan-shaped free energy landscape, as shown in the MPB composition(**Figure 3.2.2(a)**) [62].This aspect differentiates the generic BZT-BCT systems from other BT-based systems and thus provides an explanation for the high piezoelectricity for a particular composition [63]. Although Acosta et al. provided a key study on the anisotropy energy of a sixth-order Landau potential for the BZT-xBCT system, underlining that the anisotropy energy approaches zero near the O-R rather than near the T-O phase boundary, the quantification of the degree of flatness of a free energy landscape in terms of its relation to the polarization anisotropy was still unclear [39]. Later, Yang et al. [42] tried to shed light on this open topic formulating a theoretical study in which a generic sixth-order Landau free energy polynomial was used (**Figure 3.2.2(b)**). They concluded by affirming that the energy differences (energy barrier EBs) between the stable phase and the *saddle* point on the minimum energy pathway (MEP), reported as EBs and MEP, are the lowest for domain switching and polarization rotation at the T-O phase boundary. This theory is in agreement with the experimental observations of the highest piezoelectricity and highest elastic compliance (reported by Cordero [43] and shown in **Figure 3.2.2(d)**.) for this region . This study suggests that the EB can be an effective technique for measuring the degree of polarization anisotropy and the piezoelectric property of a ferroelectric system [42]. To summarize, as reported by Damjanovic and Rossetti, the rotation mechanism is associated with a reduction in the crystallographic anisotropy of polarization taking place at the MPB or TCP and the weakening of first-order phase transitions from paraelectric to ferroelectric [64]. The piezoelectricity is promoted by the presence of a commonly called MPB in synergic action with the elastic compliance that allow for the optimal domain orientation during the poling process thanks to the presence of a larger number of thermodynamically equivalent states, represented by the oriented dipolar sites inside the unit cells, as well accepted for PZT system [64].

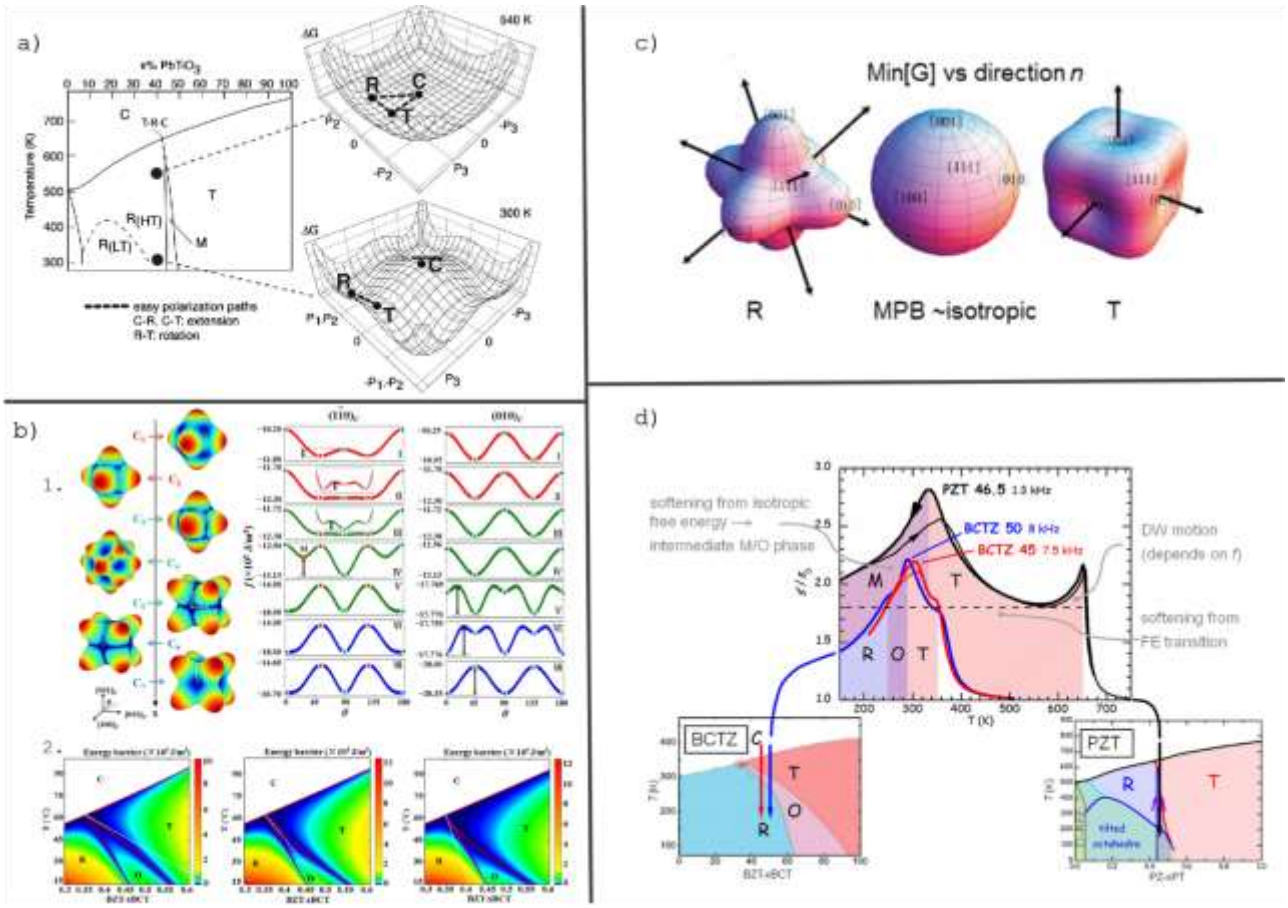

Figure 3.2.2 a)composition-temperature phase diagram for PZT and Gibbs free energy profiles[62]; **b)**1.Energy surfaces of selected compositions . On the right: the corresponding energy profiles intersected by the (110)C plane [42].2. Distribution of energy barrier superimposed on the computed pseudo-binary phase diagram of BZT-xBCT [42] ; **c)**A representation of loss of anisotropy of the spontaneous polarization in the PZT system as a function of the increase of Ti content at the MPB. The R phase obtained with βan < 0 changes into T obtained with βan > 0 [43]; **d)**Comparison between the elastic compliances of BCTZ and PZT and paths followed in the respective phase diagrams [43].

3.3 The role of processing on properties

3.3.1 Accurate choice of reagents

With regard to the raw materials that can be used for the synthesis of ceramic materials, a reference must be made to the European list of the so-called critical raw materials and the criteria for determining whether an element or rare earth can be considered as such [65, 66]. In order to define a profile for each raw material, the Directorate-General (DG) Joint Research Centre (JRC) in cooperation with the DG for Internal Market, Industry, Entrepreneurship and SMEs (GROWTH) have elaborated The European Commission's (EC) Raw Materials Information System (RMIS) to monitor trends in real time [67].

An important but underestimated aspect that can have an influence on the overall processing route is the choice of precursors. In their seminal work Liu and Ren used $BaZrO_3$ instead of ZrO_2 [20].This aspect has been recently taken into account by Amorin et al. [68] who underlined that the amorphization of monoclinic ZrO_2 has been found to be the limiting step for the formation of pure BCZT perovskite by Mechanosynthesis. Substituting monoclinic polymorph with $BaZrO_3$ as raw material can enhance the reaction kinetic, that can be further promoted by the use of tetragonal ZrO_2 [68]. Analysing the influence of TiO_2 polymorph Chao et al. demonstrated that using anatase (D_{50} = 532 nm, 99.99%) and or rutile (D_{50} = 614 nm, 99.99%) TiO_2 type modifies the microstructure and electromechanical properties of BZT-50BCT. The introduction of the rutile allotrope seems to increase the grains size from about 5-10 µm to 10-20 µm and, consequently, several properties such as d_{33} = 590 pC/N, k_p = 0.46, ε_r= 2810, tanδ= 0.014, resulted significantly improved. On the other hand, it has not influence on Tc and Coercitive Field [69]. Another study finds the relationship between the purity of $BaCO_3$ used and the resulting grains size obtained of show an average grains size of 10 ± 2 for ≥99% and 35 ± 8(µm) for ≥99.98% powder. The authors concluded that by increasing the $BaCO_3$ chemical purity, the grains growth is promoted leading to enhanced properties [70]. Another preliminary study reports the synthesis of BCZT powder starting from $CaZrO_3$ (CZ) previously prepared using ultra-fine $CaCO_3$. According to the authors' findings, fine CZ powder enhanced the reaction of $BaTiO_3$(BT) and CZ [71].

3.3.2 Industrial scalability

Another aspect to consider is the processing of the material in terms of industrial scalability (costs, CO_2 emissions, availability and transport of raw materials, processing temperatures) and the possibility of transferring basic research into real applications, depending on the material properties [72]. What is more, the reproducibility of properties still represents a significant issue in lead-free systems, as they are complex ferroelectrics polycrystals.

3.4 Solid-state route as a straightforward method to produce BCZT-based ceramics. Focus on mechanical activation of powders via ball-milling.

Solid-state chemistry in perovskite systems has been increasingly concerned with complex (e.g., deviation from stoichiometry) and disordered systems. Specifically, non-stoichiometry in perovskite oxides and related structures (including transition metal oxides) are of special interest not only for the diversity of the crystallographic features, but, also, to their relevant impact on different physical properties. In the search for an optimum stoichiometry control in developing polar electroceramics, softer conditions based on wet chemistry methods have been employed [73]. These include several methods for the synthesis of different type of "lead-free ceramics". In particular, for the synthesis of BCZT ceramics are employed rather than traditional oxide reactions: sol-gel [58,74–79], Glycine co-precipitation [61], Pechini modified reaction [80], auto-combustion [81], hydrothermal [59,82,83], modified by introducing the use of different chelants, such as citric acid [84]. Moreover, the use of a combined synthesis route such as the microwave-assisted hydrothermal method offers many advantages: short reaction times, low synthesis temperature, and small and homogeneous grain size [85–87]. On the other hand, the grain sizes of ceramics obtained from powders processed by using these approaches, resulted excessively small, making them not suitable for polarization when DC electric filed is applied. A significant reduction for both ferroelectric and piezoelectric properties has been observed for systems obtained by sol-gel methods and characterized by grain size of 1.5 μm [13]. Recently, it has been demonstrated that grain size in the range of 1-5 μm, obtained through a combination of mechanosynthesis and Spark-Plasma-Sintering (SPS), allow to maintain high electromechanical properties [88]. Furthermore, if on the one hand, the BCZT systems prepared by wet chemistry approaches are characterized by a homogenous distribution of particles sizes and lower processing temperatures; on the other hand, the reaction efficiency (very low synthesis yields), remains its major drawback for industrial scalability. For this reason, the solid-state route (SSR), schematically represented in **Figure 3.4.1**, is still the most used and useful method to produce ceramics oxides. Firstly, the precursors are weighted in stoichiometry proportions according to the composition chosen, then annealed to form a different new solid

compound, step commonly called “calcination”. To obtain dense materials, the powder particles are pressed and shaped through a process called “forming “. The as-obtained green body is heated at higher temperatures to obtain dense ceramics. Two intermediate ball-milling steps are introduced for homogenizing/activating the mixture and for decreasing the particle size of the calcined powder. However, the critical dependence of the synthetic powder and ceramics on the synthesis and sintering conditions is identified as a drawback for their processing.

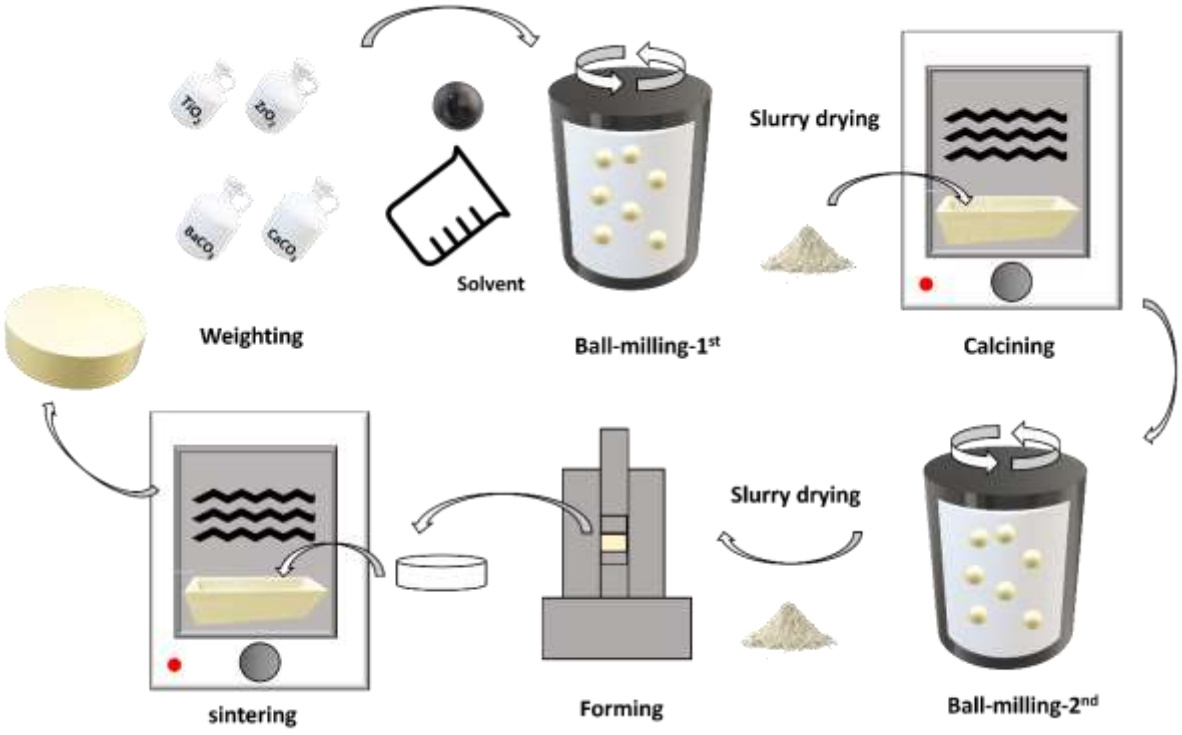

Figure 3.4.1 Graphical representation of different steps of the solid-state route.

Since the pioneering work of Benjamin and co-workers in the late 1976, the mechanical treatment of powders by ball milling (BM) has rapidly become one of the most extensively powder processing methods used to activate and produce solid materials [89]. In BM technique, typically, a reactor is filled with powders and milling tools in an appropriate mass ratio, and then periodically moved by an electric motor with a fixed or variable velocity, allowing milling tools to collide with each other and powders. The intensity of each collision, which depends on the ball size and material (density), milling speed and ball to powder volume/weight ratio, can be sufficient to induce particles mixing and particles size reduction accompanied by several structural

and microstructural modifications [90]. Furthermore, grinding leads to the generation of fresh surfaces and defects which significantly increases the overall reactivity of the system [91–93].

Hence, the ball milling technique, is expected to have an influence on the intrinsic piezoelectric contribution via its effect on the lattice distortion and solubility limits of the precursors [44]. This could lead to a variation in the number and amount (weight/volume percentage) of secondary phases formed after heat treatment and, subsequently, on the temperatures at which they form, and finally on the ceramic microstructure, so having an influence also on the extrinsic contribution of piezoelectricity [44].

In the current literature, several types of high-energy ball milling equipment have been exploited to produce BCZT ceramic. They differ in their efficiency, milling intensity (speed) and milling materials. Principally, SPEX shaker mills, attritor mills and planetary ball mills, reported in **Figure 3.4.2**, represent the most popular and conventional ball-milling apparatus for BCZT processing by solid state route. A detailed description of these deferent mills is available in an interesting key work [94]. Another main aspect is the material used for the milling vial and balls, because during the collisions of the grinding medium on the inner walls of the vial, some material could be incorporated into the powders, modifying their initial stoichiometry. Hardened stainless steel, yttrium stabilized zirconia, zirconia, and tungsten carbide are the most common types of materials used for the vials and grinding medium. Vial and balls made of polymers-based materials (Teflon, polycarbonates, etc.) are, only recently, exploited for producing ceramics. In this perspective, the next paragraphs aim at elucidating how the several grinding parameters, among them, variety of vials and balls materials, milling speed and time , impact energy (if estimable), kind of milling apparatus, ball to powder ratio (BPR), milling atmosphere and liquids medium, can play a crucial role into the processing of BCZT ceramics [95–97]. Furthermore, the purpose is also to highlight which issues can be encountered when using this well-established method, drawbacks that can strongly affect the electromechanical properties of the final as processed piezo ceramic.

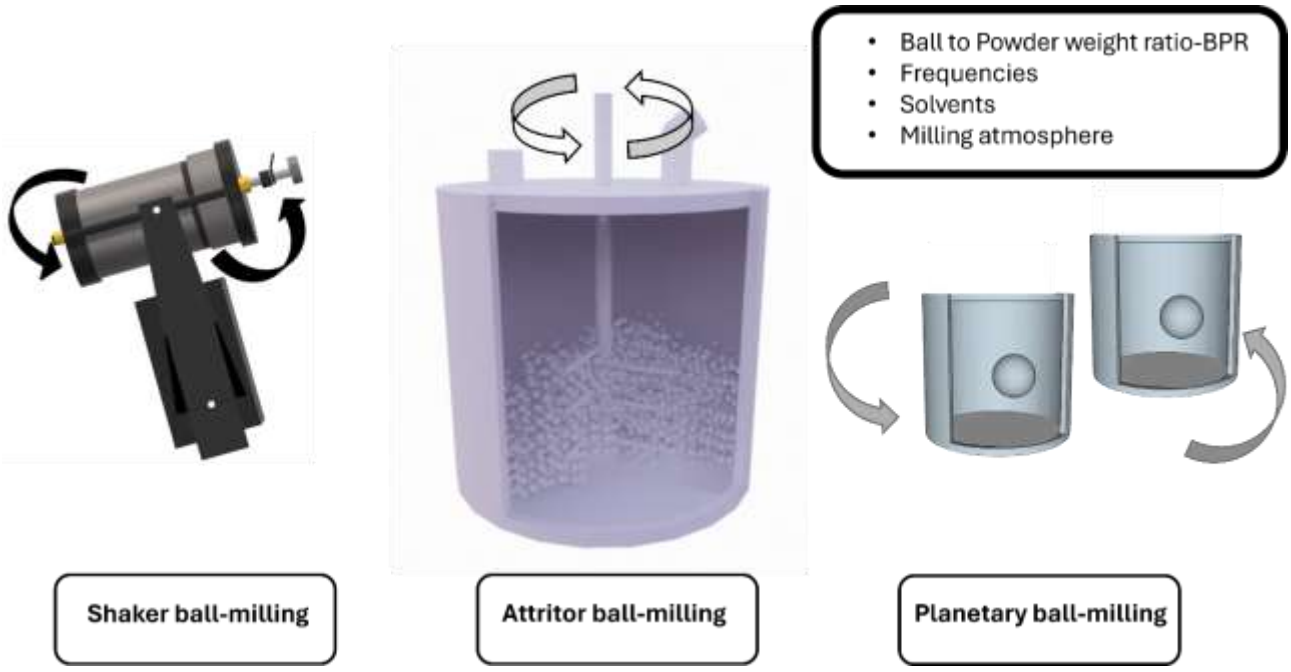

Figure 3.4.2 Different ball-milling setup reported in the literature for processing BCZT ceramics [98].

3.4.1 Impact of the vial and grinding media materials on purity of BCZT powders

In a typical synthetic protocol of BCZT, once the nominal composition is defined, an appropriate milling setup has to be selected in order to efficiently activate the starting reagents [91]. In this step, it is strictly important to limit, as much as possible, any contamination coming from the vial and balls materials. In fact, the unvoluntary introduction of foreign ions could have an effect similar to that of doping (lowering or raising the Curie Point, alteration of the chosen stoichiometry, formation of unwanted secondary phases). Even though the BCZT system does not contain volatile elements, the desired stoichiometry can be altered if other elements are introduced during the processing steps of the SSR [12]**.** This aspect was already explored in the late 1990 by Cousin and Ross for the preparation of titanates and aluminates through mixed powders, co-precipitation and sol-gel techniques. In this work, they concluded that the most direct method for preparing these compounds is the reaction of a mixture of metal oxides, paying attention to particle size growth while avoiding contamination of the grinding media and ensuring the homogeneity and purity of the powder [99]**.** Thakur and collaborators studied the influence of attrition ball-milling and the contamination of the powder due to the milling media (yttria-stabilized zirconia) on the electrical properties of undoped $BaTiO_3$. They reported that the variation in lattice parameter, polymorphic phase transitions and changes in dielectric

properties. For ≤2 h of attrition ball-milling the reduction in Curie Temperature can be explained by the unintentional Zr-doping in Ti-site (5 %at.). After 3 h of attrition Ball-milling the Curie Point decreases from 135°C for undoped BT to 100°C, showing a relaxor behaviour; whereas the increasing in bulk conductivity can be explained by unintentional donor-doping from the milling media (in this case Y^{3+} on the Ba-site) [100].

Since the BCZT is based on zirconium, it is not surprising that in the current literature the milling process is usually performed using zirconia and Yttria stabilized zirconia balls [101] and vials [49,70,102,103]. Recently, mechanochemical reactors internally covered with Teflon [97,104] and Nylon [39] have been successfully used avoiding most of the contaminants above reported. Of course, the level of contamination depends on the ball-milling parameters, precursors and time since absence of contamination has been reported for the mechanosynthesis of BCZT in Tungsten Carbide grinding media for 15h of ball-milling [68,105].

Since ball milling technique allows to modulate final ceramic grains and particles size, its utilization has a profound effect on the electromechanical properties of BCZT. First of all, a distinction must be made between the activation of precursors prior to calcination and the destruction of agglomerates formed prior to the sintering step (see **Figure 3.4.1**). Depending on the milling conditions, the mechanical treatment can induce different modifications on the precursor by creating an intimate mixture [106], enhancing their reactivity [97,107], and also leading to the final product (mechanosynthesis) avoiding the calcination step [68]. To this regard, different ball-milling apparatuses are used such as [108]: attrition ball-milling [97,109,110] planetary mills [68,111–114] horizontal ball-milling [106] and shaker ball milling [115]. Concerning the grinding media materials, the reactants for the preparation of BCZT are often mechanically processed with WC [68,105,116,117] and agate [57].

3.4.2 First ball-milling and calcination temperature

Although it is known that particle size reduction and precursor homogenization lead to a decrease in the synthesis temperature, at the current state of the art, the correlation between the mechanical activation of powders and the reduction in calcination temperature is poorly studied. In this regard, Frattini and coauthors evidenced the influence of calcination temperature (800 - 1200 °C), on precursors previously milled using a

planetary ball milling for 4 h zirconia into a zirconia jar. They underlined that BCZT pure phase was obtained only above 1100°C. In this work the authors also reported in detail the secondary phases that can occur as a function of the calcination temperature ($BaZrO_3$, $CaZrO_3$) [111]. In a recent interesting work of Ciomaga and colleagues [52] it is pointed out how ball-milling conditions and synthesis temperatures can affect the final properties of ceramics keeping all other processing steps fixed. The best properties (compromise between good piezoelectric properties and low losses) were obtained by using a vibratory ball-milling apparatus for 60 min (d_{33}=280 pC/N). The processing method used leads to the achievement of phase coexistence (MPB) in the final ceramic with majoritarian orthorhombic phase (O>T) [52]. Although this is not explored in depth, fairly low synthesis temperatures are reported in the literature, such as 1150°C/2h for powders milled for 2h with SPEX 8000 [115]. Bai et al reported the calcination temperature of 1000 °C /4 h for the $BC_{15}TZ_{10}$ doped - system by $Bi(Mg_{0.5}T_{i0.5})O_3$, milled for 24 h in a planetary mill [118]. In another work Bai and colleagues report a low synthesis temperature of 1100 °C for 4h after horizontal ball milling in distilled water with zirconia balls, not analysing neither particles size nor the effect of water on precursors, but performing a study on the effect of second ball-milling on the final microstructure [106]. Nan et al. used a low temperature specifying the milling conditions. They employed an attritor ball milling apparatus using ethanol as medium (zirconia balls with 3 mm diameter and the ball-to-powder ratio 1.5:1) for 2.5 hours at the rate of 700 rpm. The powder mixture was calcined at 1100°C for 4 hours obtaining pure BCZT system [109].

Table 3.4.1 Ball milling apparatuses, working conditions of milling, calcination and sintering steps of the BCZT processing and the corresponding physical and electrical parameters of the BCZT ceramics obtained. These works have been selected among the most interesting studies on mechanical activation of precursors by ball-milling.

Compo-sition	BM-a	t (min) f (Hz)	$T_{Calc.}$(°C) D_{time} (h)	CL_{BCZT}	SP	M	T_{sint} (°C) D_{time} (h)	T_m T_0-T_{cw} °C	ρ %	G.S. µm	CL_{BCZT}	d_{33} pC/N	K_p-Q_m	Ref.
$BC_{15}TZ_{10}$	P	30 5.8	1000 4	T>O	BZ	HYP	1450 2	93 92	76	20	T>O	180	-	[52]
$BC_{15}TZ_{10}$	V	30 30	1000 4	T-O	BZ	HYP	1450 2	93 87	96	-	O>T	230	-	[52]
$BC_{15}TZ_{10}$	V	60 30	1000 4	T>O	BZ	HYP	1450 2	87- 88	95	-	O>T	280	-	[52]
$BC_{15}TZ_{10}$	P	30 5.8	1200/1350 24/6	T>O	-	SPS SPS	1300 10	103 97	97	-	O>T	283	-	[52]
$BC_{15}TZ_{10}$	S	120 14.6	1150 4	-	-	UX HP	1500 6	71 85	94 98	10 20	-	350 510	33 - 80 44 - 66	[115]
$BC_{11}TZ_{10}$	P	240 5.8	900/1200	-	BZ	UX	1400 2	-		5-15	-	-	-	[111]

Legend. BM-a: ball milling apparatus. P: Planetary mill. V: Vibratory mill. S: Shaker mill (Spex). t: ball milling time. f: ball milling frequency. T_{calc}: Temperature of calcination. D_{time}: Dwell time refereed to the calcination step. CL_{BCZT}: crystal phase of BCZT obtained after calcination. SP: Secondary phases after calcination. BZ: $BaZrO_3$. M: Moulding method. UX: Uniaxial, HP: Hot-Pressing. HYP: hydrostatic Pressing. T_{sint}: Temperature of sintering. D_{time}: Dwell time referred to the sintering step. T_m: Transition temperature corresponding to Maximum of permittivity. T_0 and T_{cw}: the result of the fitting with Curie–Weiss and Curie–Weiss-modified laws. ρ (%) = relative density of the sintered pellet. G.S.: Grains size. d_{33}: quasi-static piezoelectric coefficient. CL_{BCZT}: crystal phase of the sintered BCZT. K_p/Q_m: electromechanical coupling coefficient and mechanical losses. T: Tetragonal. O: Orthorhombic.

As emerged from **Table 3.4.1** , despite the high energy mechanical processing to activate the precursors, the calcination temperature resulted too high (≥1000 °C) if compared with wet-chemical approaches already mentioned. According to the specific literature, to trigger any physical and chemical modifications, a threshold dose of kinetic energy has to be transferred, which mainly depends on the mass of each ball and milling velocity. The apparatus type and the frequency of milling indicated in **Table 3.4.1** for each composition, reveal that the powders have been subjected to impact of energy in the range of $8x10^{-3}$ – 0.1 J, $2x10^{-3}$ – $1x10^{-2}$ J, $1x10^{-3}$ J - 0.2 J, for shaker, planetary and vibratory mills, respectively. These values have been estimated also taking into in account different mass of balls and the equations applied in these manuscripts [119–122].

3.4.3 Second ball-milling and sintering temperature

Another important point is represented by the need of a second ball-milling before sintering so that the agglomerates formed during calcination are broken up, step well described and studied for other systems like KNN [97,114,123,124]. Regarding the BCZT system, Yan et al. [112], investigated the effect of post-calcined dry ball milling treatment on BCZ-60 BCT ($Ba_{0.82}Ca_{0.18}$) ($Ti_{0.92}Zr_{0.08}$) O_3 powder using a Fritsch Pulverisette 7 planetary ball-milling and 45-mL Zirconia vial and Zirconia balls as grinding media for increasing milling time (0-40 min, at 600 rpm, BPR 25:1). They obtained a significant reduction of the particle sizes starting from an irregular morphology of 1 µm to achieve regular shaped particles of 3.8 $x10^{-3}$ µm just after 10 minutes of milling processing. For further increasing milling time, particles become more uniform, but agglomeration can be noticed. They conclude that the best dielectric and piezoelectric properties were reach for a grain size of 12.9 µm obtained with the best combination of 30 min of the second BM (2.4 $x10^{-3}$ µm particle size) and an optimal inverse two step sintering method (1475°C/1300°C) [112]. The same was confirmed by Mittal et al. [114] that used high-energy ball mill on calcined powders for obtaining good piezoceramics without creating any undesired secondary phase in its perovskite structure. The authors declared that the key point is selecting adequate milling parameters. In this work, contrary to the previous one, they changed the ball-milling frequencies (100 rpm, 150 rpm, 200 rpm, 250 rpm, 300 rpm and 350 rpm) keeping the milling time fixed for 20 h. The best d_{33} and K_p have been reached by using a speed of 250 rpm for an average particle size of $4.5*10^{-3}$ µm as reported in **Table 3.4.2**. An increase of the milling velocity induces a further decrease of particle sizes. In addition, by reducing the particle size to such a small scale, the surface area of the particles begins to dominate over the volume (increasing the specific surface energy), and, as a result, modifying its thermodynamic properties. To reach the equilibrium position, the particles begin to agglomerate, reducing the surface energy, which shows the agglomeration of particles in the powder milled at 300 rpm [114]. In the investigation of Di Loreto et al. [125] on post-calcination grinding, the authors highlighted the influence of grinding intensity on BCZT powder, using zirconium balls (ball/powder weight ratio = 10) for 6 h. The comparison between Liquid Milling (LM) and Dry milling (DM) showed that more energetic Dry milling (DM) deteriorates the piezoelectric response: the d_{33} coefficient measured for the LM

ceramic was 380 pC/N, higher compared to that obtained for the DM sample (90 pC/N). They also highlighted that Tc depends on the grinding process of the calcined powders, 40°C-50°C for the DM sample and 96°C for LM sample. They concluded that an intense degree of milling affects drastically the structural homogeneity. This occurs due to a mechanically activated phase decomposition process. They detected inhomogeneity in grains, resulting in BCZT grains, $CaTiO_3$ nanocubes and an amorphous phase rich in Ba and Ti. The grinding intensity of calcined BCZT powders is a key parameter for obtaining proper sintered ceramics [125]. Nan et al. [109] consider the need of a second ball-milling to deagglomerate the powder. They treated the calcined powder with attritor ball milling (700 rpm, 5 hours). They underlined that before being milled, the particle-size distribution exhibits three populations, including two main peaks, one centred at around 0.20 µm, another small peak around 2.2 µm, and a shoulder at ~8 µm corresponding to the coarser agglomerates, with D_{50} = 1.0 µm and D_{90} = 4.6 µm. After milling, the particle-size distribution exhibits a bimodal distribution with a main large peak centred at around 0.2 µm and another small peak around 1.8 µm, and with overall D_{50} = 0.17 µm and D_{90} = 0.38 µm. These results show that attrition milling is essential for achieving a homogeneous particle-size distribution by destroying the agglomerates. Bai et al. [106] used and horizontal ball milling with ZrO_2 balls to yield a calcined powder with an average particle size (D_{50}) of about 5 µm. In order to obtain powders with different particle sizes so that their effects on material microstructures and piezoelectric properties could be investigated, vibratory milling and planetary milling were applied on portions of the calcined 5/5 BCZT powder, resulting in reductions in D_{50} to about 3 µm and 1 µm, respectively, leading to different grain size and relative density of the sintered ceramics.

Table 3.4.2 Ball milling apparatuses, working conditions of milling, calcination and sintering steps of the BCZT processing and the corresponding physical and electrical parameters of the BCZT ceramics obtained. These works have been selected among the most interesting studies on mechanical activation of calcined powders by ball-milling.

Composition	BM-a 1°	BM-t (min) BM-f (Hz)	TCalc.(°C) Dtime (h)	BM-a 2°	BM-t (min) BM-f (Hz)	M-binder	Tsint (°C) Dtime (h)	Tm T0-Tcw °C	ρ %	G.S. µm	CLBCZT	d33 pC/N	Kp-Qm	Ref.
(BZT-60BCT) $BC_{01}TZ_{08}$	P	600 6.7	1350 3	P	0-40 10	- -	1475 - 1300 0.02-6	105	94	13	T-O	330	40	[112]
$BC_{15}TZ_{10}$	P	1200 1.7	1200 4	P	1200 4.16	HYP PVA	1450 4	79	94	3	T	210	22.4	[114]
5/5BCZT $BC_{15}TZ_{10}$	H	1440 -	1100 4	V-P	- -	UX PVA	1475 4	95	96	32	T-O	466	-	[106]
$BC_{15}TZ_{10}$	P LM DM	-	1300 4	P LM DM	360 -	- PVB	1400 6	96 40	-	-	T	380 90		[125]

Legend. BM-a: ball milling apparatus (1° first ball milling. 2° second ball milling). P: Planetary mill. A: Attritor mill. H: Horizontal mill. V: Vibratory mill. LM: Liquid Milling, DM:Dry Milling. BM-t = ball milling time BM-f: ball milling frequency. $T_{calc:}$ Temperature of calcination. D_{time}: Dwell time refereed to the calcination step. CL_{BCZT}: crystal phase of BCZT obtained after calcination. M: Moulding method. UX: Uniaxial, HP: Hot-Pressing. HYP: hydrostatic Pressing. T_{sint}: Temperature of sintering. D_{time} : Dwell time refereed to the sintering step. T_m: Transition temperature corresponding to maximum of permittivity. T_0 and T_{cw}: the result of the fitting with Curie–Weiss and Curie–Weiss-modified laws. ρ % = relative density of the sintered pellet. G.S.: Grains size. d_{33}: quasi-static piezoelectric coefficient. CL_{BCZT}: crystal phase of the sintered BCZT. K_p/Q_m: electromechanical coupling coefficient and mechanical losses. T: Tetragonal. O: Orthorhombic.

The literature also contains works in which the authors employed high-energy ball milling techniques but treated the powders at high temperatures. Syal et al. used planetary ball milling (FRITSCH, P5) for 12 h before synthesis (1350°C for 4 h)and for 6 h prior to the sintering (1565°C for 6 h), obtaining good properties for $BC_{15}TZ_{10}$ composition (d_{33} =512 pC/N, K_p=51%,T_c=104°C) [113]. In two investigations on the effect of sintering dwell time the authors reported the use of unspecified ball-milling in combination with high processing temperatures, 1350 °C/2h for the synthesis and 1450°C and 1500°C for the sintering, respectively [126,127]. Other authors declare the use of ball-milling always using very high temperatures, 1200°C and 1350°C [128], long roll jar milling [70], attrition milling in combination with 1300°C and 1400°C as processing temperatures [110].

Up to this point, scarce literature is reported on the use of attrition ball-milling for activating the precursors and calcined powders in order to decrease the processing temperatures (calcination step and sintering step), allowing the industrial scalability.

3.5 Water-based solid-state routes: an urgent target for industrial scaling up

Analysing the literature, at research level the processing of BCZT precursors involves the use of organic solvents , such as isopropanol, ethanol [126,129,130] unspecified alcohol [107,110] and acetone[113]. At industrial scale, the introduction of organic solvents represents a limiting factor, due to economic, environmental, and safety reasons. In this context, the growing demand from industries for more ecological water-based routes is triggering the interest of researchers in the development of synthetic protocols based on solvent-free routes. Unfortunately, as properly reported in the literature, there are some issues that can be encountered when using water for processing ceramics: possible leaching of metal ions, deviations from the chosen composition due to the solubility of carbonates in water, formation of unwanted secondary phases, hydrolysis, demixing of the slurry due to the segregation of heavy elements as a function of the density during the slurry drying, interactions due to the high polarity of water. As remarked in an interesting review some approaches to overcome these drawbacks can be: adjustment of the pH value, or addition of surfactants, and the use of spray- or freeze- drying (lyophilization) [131].So far, few articles on the use of distilled water for processing BCZT employing a horizontal ball-milling setup have been reported [106,132]. In this respect, Kaushal and colleagues, investigated the behaviour of 50BCT untreated and di-hydrogen phosphate surface-treated powders in aqueous suspensions monitoring their pH value for 7 days. The authors concluded that in treated powders was detected a "negligible leaching of $Ba^{2+,}$ Ca^{2+},and Zr^{4+}"[133]. In a subsequent work, the same authors explored the possibility to produce micron-sized spherical granulates via freeze granulation in surface-treated BZT- 50BCT, concluding that the green bodies obtained after this procedure demonstrated good sinterability and homogeneity [134]. In this respect, Acosta et al pointed out that in both works of Kaushal et al. the BZT-50BCT was actually obtained by a two-step calcination route with conventional ethanol processing [18].

Up to this point, the challenge of a totally aqueous-based processing of BCZT ceramics remains open. Furthermore, these authors did not report the piezoelectric properties of the final ceramics. However, they highlighted that processing strongly influenced the dielectric properties of the materials. It must be

underlined that these results refer to ceramics obtained starting from calcined powders aged in water for 24 h, step not usually performed for obtaining functional ceramics.

3.6 Toxicity: biocompatibility and new applications

Over the last decades, there has been a trend to expand the use of piezoelectric ceramics in new areas of biotechnology. The electricity has a vital role in living systems, as biological piezoelectricity, endogenous electric fields, transmembrane potentials that enhance cellular growth and differentiation. The biological piezoelectricity was firstly reported in 1941 in the wool by Martin [135]. In 1957, Fukada and Yasuda [136] reported the same behaviour in bone tissue. Then, endogenous electric fields have been discovered in cardiac and nerve tissue, demonstrating that electrophysiological microenvironment is essential for maintaining the normal physiological activities of the human body [137]. From this moment on, researchers have tried to reproduce these endogenous effects to repair tissues injuries as peripherical nerve and bones damages. In this context, piezoceramics can be promising for tissues engineering [138]. Thanks to the piezoelectric effect shown, they can promote cells adhesion and migration.

The two main features that a material must have to be employed in this field are biocompatibility and piezoelectricity. Due to the well-known toxicity of lead-based materials that provoke neurotoxicity pregnancy complications, attention deficit, hyperactivity and so on, new lead-free piezoceramics can be a promising alternative in this case [139, 140]. In view of this, the BCZT system has what it takes, a high d_{33} values and a theoretical good biocompatibility. Its main drawback, the relatively low Curie Point (~100 °C) - which is still a tangible problem for technology transfer, as it reduces the operating temperature of out-of-body devices in general (sonar, sensors and so on.) – it is not a limitation for biomedical applications, and other new emerging innovative technologies, since under physiological conditions, the body temperature is about 35.5–37.5 °C. With regard to the biocompatibility, a good compatibility of BCZT material with human osteoblast and endothelial cells has been demonstrated for the most studied BCZT1510 composition [70]. The material seems promising for bone regeneration in combination with hydroxyapatite, as reported by Manohar et al. [141]. Among other applications, outstanding importance can be attributed to BCZT thin films

for biocompatible and flexible devices, such as BCZT-based coatings on Kapton substrate as a support for osteogenic differentiation, obtained by PLD (pulsed laser depositing) and MAPLE (matrix-assisted pulsed-laser evaporation) techniques [130]. In this sense, further progress has been made in developing more sustainable, biodegradable, flexible and biocompatible substrates, such as chitosan bio composites for sensors application[142], self-poled and bio-flexible films BCZT-based as piezoelectric nanogenerator (BF-PNG) functionalized with polydopamine and embedded in the polylactic acid [143]. In the recent literature, the BCZT system has been used in bio-glass-(BG)based ceramics systems to improve both the electrical properties and bioactivity as potential electroactive materials for orthopaedic applications [144]. Other interesting applications include bio-piezoelectric coatings for dental implants. The chewing as mechanical input is used to produce a piezoelectric response that promotes the alveolar bone growth. Moreover, it has been demonstrated that the BCZT/TiO_2 coating was non-toxic, and the proliferation of osteoblast was higher compared to the simple TiO_2 coatings. What is more, a higher Ca deposition as apatite was observed.

Thanks to the sensibility of the ceramic system to low-intensity pulsed ultrasound, another interesting application could be physical therapy, amplifying the piezoelectric effect within the system [145]. Recently, the production of BCZT coatings on titanium surface was implemented by adding silver as antimicrobial agent for inhibiting bacteria adhesion and proliferation that at the same time promotes the activity of osteoblasts, being suitable for orthopaedic implants [146]. Other studies present the possibility to produce functional BCZT-based bilayer coatings on Ti alloy for biomedical implants too [147]. In addition to *in vitro* studies, the most recent literature includes the report of some relevant *in vivo* applications such as bio implantable energy harvesters[148], implantable and wearable electronic devices on human and animal bodies [149] and intravascular ultrasound transducers[150]. Another step forward is the fusion between the piezoelectric effect and catalysis. By using piezoelectric materials, we can initiate or accelerate reactions. This feature is triggering the interest of the scientific community towards the so called “Piezocatalytic Medicine“ for tumour therapy [151], antisepsis, biosensing, organics degradation and tissues repair and regeneration [152]. In order to push these frontier studies towards alternative applications, some crucial key points must be deeply investigated, such as material design, safety evaluation, scalability and standardization of processing routes,

studies on mechanisms. In fact, although the biocompatibility of this system seems to be straightforward, at least for the absence of toxic elements, barium-based compounds can be potentially toxic depending on their solubility due to the release of Ba^{2+} in water environment. Therefore, on one hand compounds like chlorides, nitrates, hydroxides and carbonates can interfere with potassium provoking gastrointestinal problems, muscles weakness, paralysis in chronic assumption. On the other hand, insoluble barium-based compounds, such as sulphates are safe and absolutely non-toxic [153]. In this sense, an aspect that must be considered is the presence of foreign elements that can be introduced into the lattice during the processing route. These ions can form other secondary compounds or diffuse into the main perovskite affecting or changing the biocompatibility of the system [154]. For these reasons, the study of toxicity in relation to the processing route of ceramics is a key issue and it needs to be further investigated. The behaviour of these materials changes drastically depending on the site of application/action and the micro-environment in which they are found, the interaction with the immune system, the possibility of interaction with assumed drugs and different diseases.

3.7 Conclusions and insights for the future

Since BCZT ceramic can be a material that meets all new requirements and can be a valuable ally in the discovery and development of new technologies and applications, in the near future to refine some of the main crucial points in its production is of outstanding importance.

The complexity of the BCZT system requires further study to understand the mechanisms that lead to good piezoelectric response and lower processing temperatures that enable industrial scaling up. Developing a trustworthy, scalable, environmentally friendly route to obtain good properties is still a big challenge. The complexity of BCZT system requires further studies to understand the internal mechanisms that lead to a good piezoelectric response, such as investigations on individual synthesis step (synthesis mechanisms, formation Kinetics), detailed information on solubility limits, stability diagrams, and surface hydrolysis.

Furthermore, there is the need to monitor the toxicity of the system under acute and chronic conditions for biomedical applications. Taking into account a number of key factors that have been identified as crucial to the processing route, in addition to the choice of composition at MPB, we can mention: particle size selection to maximise c/a ratios in the sintered ceramic, the design of sintering procedures to allow grain growth control for optimising electromechanical properties and new scalable routes.

The purpose of this SOTA analysis is to present an overview of the BCZT system as a potential candidate to replace the widely used toxic PZT in both established commercial technologies and as a material suitable for new biomedical applications due to its non-toxicity and environmentally friendly nature. The review aims at understanding if there is the possibility to overcome the disadvantages with respect to PZT system by analysing the fundamentals of the pseudo-ternary system, the milling techniques that are available to decrease the processing temperatures and to make the material fabrication route suitable for industrial scaling up. In particular, it highlights how mechanical or mechano-chemical activation of precursors and synthesised powders is a key point for developing a scalable solid-state route and reducing energy consumption according to new EU directives. Moreover, as here reported, the BCZT material is a promising smart material that can be used also in many emerging applications in the field of biotechnology. Further studies on the correlation between mechanical activation and synthesis temperature are needed in the near future. In particular, in this respect, in-depth investigations of synthesis steps are lacking. As already pointed out, further studies on the toxicity of the system are needed to implement possible biomedical applications. Of considerable interest is the new frontier use of this material for reducing environmental pollution.

3.8 Bibliography

1. Restriction of the Use of Certain Hazardous Substances in Electrical and Electronic Equipment (RoHS) Statement on the " RoHS " Directive. **2019**, *44*, 1999463.

2. Carvalho, G. EU Energy and Climate Change Strategy Q. *Energy* **2020**, *40*, 19–22, doi:10.1016/j.energy.2012.01.012.

3. Ros-Dosdá, T.; Fullana-i-Palmer, P.; Mezquita, A.; Masoni, P.; Monfort, E. How Can the European Ceramic Tile Industry Meet the EU's Low-Carbon Targets? A Life Cycle Perspective. *J. Clean. Prod.* **2018**, *199*, 554–564, doi:10.1016/j.jclepro.2018.07.176.

4. Pardo, L.; Villafuerte-Castrejón, M.E.; Morán, E.; Reyes-Montero, A.; Vivar-Ocampo, R.; Gonzalez, A.M. Ecological, Lead-Free Ferroelectrics. *Magn. Ferroelectr. Multiferroic Met. Oxides* **2018**, 201–219, doi:10.1016/B978-0-12-811180-2.00009-8.

5. Zheng, T.; Wu, J.; Xiao, D.; Zhu, J. Recent Development in Lead-Free Perovskite Piezoelectric Bulk Materials. *Prog. Mater. Sci.* **2018**, *98*, 552–624, doi:10.1016/j.pmatsci.2018.06.002.

6. Villafuerte-Castrejón, M.E.; Morán, E.; Reyes-Montero, A.; Vivar-Ocampo, R.; Peña-Jiménez, J.A.; Rea-López, S.O.; Pardo, L. Towards Lead-Free Piezoceramics: Facing a Synthesis Challenge. *Materials (Basel).* **2016**, *9*, 1–27, doi:10.3390/ma9010021.

7. Ibn-Mohammed, T.; Koh, S.C.L.; Reaney, I.M.; Sinclair, D.C.; Mustapha, K.B.; Acquaye, A.; Wang, D. Are Lead-Free Piezoelectrics More Environmentally Friendly? *MRS Commun.* **2017**, *7*, 1–7, doi:10.1557/mrc.2017.10.

8. Ibn-Mohammed, T.; Reaney, I.M.; Koh, S.C.L.; Acquaye, A.; Sinclair, D.C.; Randall, C.A.; Abubakar, F.H.; Smith, L.; Schileo, G.; Ozawa-Meida, L. Life Cycle Assessment and Environmental Profile Evaluation of Lead-Free Piezoelectrics in Comparison with Lead Zirconate Titanate. *J. Eur. Ceram. Soc.* **2018**, *38*, 4922–4938, doi:10.1016/j.jeurceramsoc.2018.06.044.

9. Zhang, S.; Xia, R.; Shrout, T.R. Lead-Free Piezoelectric Ceramics vs. PZT? *J. Electroceramics* **2007**, *19*, 251–257, doi:10.1007/s10832-007-9056-z.

10. Rödel, J.; Li, J.F. Lead-Free Piezoceramics: Status and Perspectives. *MRS Bull.* 2018, *43*, 576–580. 10.1557/mrs.2018.181

11. Hong, C.H.; Kim, H.P.; Choi, B.Y.; Han, H.S.; Son, J.S.; Ahn, C.W.; Jo, W. Lead-Free Piezoceramics – Where to Move On? *J. Mater.* 2016, *2*, 1–24.

12. Zhang, Y.; Sun, H.; Chen, W. A Brief Review of Ba(Ti0.8Zr0.2)O3-(Ba0.7Ca0.3)TiO3 Based Lead-Free Piezoelectric Ceramics: Past, Present and Future Perspectives. *J. Phys. Chem. Solids* 2018, *114*, 207–219.

13. Coondoo, I.; Panwar, N.; Alikin, D.; Bdikin, I.; Islam, S.S.; Turygin, A.; Shur, V.Y.; Kholkin, A.L. A Comparative Study of Structural and Electrical Properties in Lead-Free BCZT Ceramics: Influence of the Synthesis Method. *Acta Mater.* **2018**, *155*, 331–342, doi:10.1016/j.actamat.2018.05.029.

14. Chen, B.; Liang, P.; Wu, D.; Zhao, X.; Qiao, X.; Peng, Z.; Wei, L.; Chao, X.; Yang, Z. High-Efficiency Synthesis of High-Performance K 0.5 Na 0.5 NbO 3 Ceramics. *Powder Technol.* **2019**, *346*, 248–255, doi:10.1016/j.powtec.2019.01.039.

15. Zhang, Y.; Sun, H.; Chen, W. A Brief Review of Ba(Ti0.8Zr0.2)O3-(Ba0.7Ca0.3)TiO3 Based Lead-Free Piezoelectric Ceramics: Past, Present and Future Perspectives. *J. Phys. Chem. Solids* **2018**, *114*, 207–219, doi:10.1016/j.jpcs.2017.10.041.

16. Panda, P.K.; Sahoo, B.; Thejas, T.S.; Krishna, M. High d 33 Lead-Free Piezoceramics: A Review. *J. Electron. Mater.* **2022**, *51*, 938–952, doi:10.1007/s11664-021-09346-0.

17. Liu, W.; Cheng, L.; Li, S. Prospective of (BaCa)(ZrTi)O 3 Lead-Free Piezoelectric Ceramics. *Crystals* **2019**, *9*, doi:10.3390/cryst9030179.

18. Acosta, M.; Novak, N.; Rojas, V.; Patel, S.; Vaish, R.; Koruza, J.; Rossetti, G.A.; Rödel, J. BaTiO3-Based Piezoelectrics: Fundamentals, Current Status, and Perspectives. *Appl. Phys. Rev.* **2017**, *4*, doi:10.1063/1.4990046.

19. Gao, J.; Xue, D.; Liu, W.; Zhou, C.; Ren, X. Recent Progress on BaTiO3-Based Piezoelectric Ceramics for Actuator Applications. *Actuators* **2017**, *6*, doi:10.3390/act6030024.

20. Liu, W.; Ren, X. Large Piezoelectric Effect in Pb-Free Ceramics. *Phys. Rev. Lett.* **2009**, *103*, 1–4, doi:10.1103/PhysRevLett.103.257602.

21. McQuarrie, M.; Behnke, F.W. Structural and Dielectric Studies in the System (Ba, Ca) (Ti, Zr)O3. *J. Am. Ceram. Soc.* **1954**, *37*, 539–543.

22. Von Hippel, A. Ferroelectricity, Domain Structure, and Phase Transitions of Barium Titanate. *Rev. Mod. Phys.* **1950**, *22*, 221–237, doi:10.1103/RevModPhys.22.221.

23. Lee, S.; Randall, C.A. A Modified Vegard's Law for Multisite Occupancy of Ca in BaTiO3–CaTiO3 Solid Solutions. *Appl. Phys. Lett.* **2008**, *92*, doi:10.1063/1.2857475.

24. G.H.Jonker Capacitor Materials with High Dielectric Constant. **1955**, *17*, 129–160, doi:537.226 :621.315.612 :62~.319.4 In.

25. Hennings, D.; Schreinemacher, H. Temperature Dependence of the Segregation of Calcium Titanate from Solid Solutions of (Ba, Ca) (Ti, Zr)O3 and Its Effect on the Dielectric Properties. *Mater. Res. Bull.* **1977**, *12*, 1221–1226, doi:10.1016/0025-5408(77)90177-5.

26. Mitsui, T.; Westphal, W.B. Dielectric and X-Ray Studies of CaxBa1−xTiO3 and CaxSr1−xTiO3. *Phys. Rev.* **1961**, *124*, 1354–1359, doi:10.1103/PhysRev.124.1354.

27. Pardo, L.; Carmona, F.; Gonzalez, A.M.; Alemany, C.; Mendiola, J. 90° Domain Reorientation as a Function of the Field on Ca-Modified Lead Titanate Ceramics by XRD. *Ferroelectrics* **1992**, *126*, 329–333, doi:10.1080/00150199208227081.

28. T. N. Verbitskaja, G.S. Zhdanow, Yu. N. Venevtsev, and S.P. Soloviev Electrical and X-Ray Diffraction Studies of the BaTiO3-BaZrO3 System. *Sov. Phys.-Cryst.* **1958**, *3*, 182–92.

29. HENNINGS, D.; SCHNELL, A.; SIMON, G. Diffuse Ferroelectric Phase Transitions in Ba(Ti 1 - y Zr y)O 3 Ceramics. *J. Am. Ceram. Soc.* **1982**, *65*, 539–544, doi:10.1111/j.1151-2916.1982.tb10778.x.

30. Maiti, T.; Guo, R.; Bhalla, A.S. Structure-Property Phase Diagram of BaZr x Ti 1− x O 3 System. *J. Am. Ceram. Soc.* **2008**, *91*, 1769–1780, doi:10.1111/j.1551-2916.2008.02442.x.

31. Ricinschi, D.; Ciomaga, C.E.; Mitoseriu, L.; Buscaglia, V.; Okuyama, M. Ferroelectric–Relaxor Crossover Characteristics in Ba(ZrxTi1−x)O3 Ceramics Investigated by AFM-Piezoresponse Study. *J. Eur. Ceram. Soc.* **2010**, *30*, 237–241, doi:10.1016/j.jeurceramsoc.2009.05.022.

32. Ravez, J.; Broustera, C.; Simon, A. Lead-Free Ferroelectric Relaxor Ceramics in the BaTiO3-BaZrO3-CaTiO3 System. *J. Mater. Chem.* **1999**, *9*, 1609–1613, doi:10.1039/a902335f.

33. Zhang, Y.; Glaum, J.; Groh, C.; Ehmke, M.C.; Blendell, J.E.; Bowman, K.J.; Hoffman, M.J. Correlation Between Piezoelectric Properties and Phase Coexistence in (Ba,Ca)(Ti,Zr)O3. *J. Am. Ceram. Soc.* **2014**, *97*, 2885–2891, doi:10.1111/jace.13047.

34. Toyoda, M.; Sahriza Lubis, M.Y. Preparation and Characterization of (Ba,Ca)(Ti,Zr)O3 Thin Films

through Sol-Gel Processing. *J. Sol-Gel Sci. Technol.* **1999**, *16*, 7–12, doi:10.1023/a:1008700802301.

35. Sen, S.; Choudhary, R.N.P. Effect of Doping Ca Ions on Structural and Electrical of Ba(Zr0.05Ti0.95)O3 electroceramics. **2004**, *5*, 671–675. DOI:10.1023/B:JMSE.0000038922.74021.d6

36. Keeble, D.S.; Benabdallah, F.; Thomas, P.A.; Maglione, M.; Kreisel, J. Revised Structural Phase Diagram of (Ba0.7Ca 0.3TiO3)-(BaZr0.2Ti0.8O3). *Appl. Phys. Lett.* **2013**, *102*, 0–12, doi:10.1063/1.4793400.

37. Xiao, C.J.; Jin, C.Q.; Wang, X.H. Crystal Structure of Dense Nanocrystalline BaTiO3 Ceramics. *Mater. Chem. Phys.* **2008**, *111*, 209–212, doi:10.1016/j.matchemphys.2008.01.020.

38. Fu, D.; Kamai, Y.; Sakamoto, N.; Wakiya, N.; Suzuki, H.; Itoh, M. Phase Diagram and Piezoelectric Response of (Ba1-XCa x)(Zr0.1Ti0.9)O3 Solid Solution. *J. Phys. Condens. Matter* **2013**, *25*, doi:10.1088/0953-8984/25/42/425901.

39. Acosta, M.; Novak, N.; Jo, W.; Rödel, J. Relationship between Electromechanical Properties and Phase Diagram in the Ba(Zr0.2Ti0.8)O3-x (Ba0.7Ca 0.3)TiO3 Lead-Free Piezoceramic. *Acta Mater.* **2014**, *80*, 48–55, doi:10.1016/j.actamat.2014.07.058.

40. Brajesh, K.; Tanwar, K.; Abebe, M.; Ranjan, R. Relaxor Ferroelectricity and Electric-Field-Driven Structural Transformation in the Giant Lead-Free Piezoelectric (Ba,Ca)(Ti, Zr)O3. *Phys. Rev. B* **2015**, *92*, 224112, doi:10.1103/PhysRevB.92.224112.

41. Guo, H.; Voas, B.K.; Zhang, S.; Zhou, C.; Ren, X.; Beckman, S.P.; Tan, X. Polarization Alignment, Phase Transition, and Piezoelectricity Development in Polycrystalline 0.5Ba(Zr0.2Ti0.8)O3-0.5(Ba0.7Ca0.3)TiO3. *Phys. Rev. B* **2014**, *90*, 014103, doi:10.1103/PhysRevB.90.014103.

42. Yang, T.; Ke, X.; Wang, Y. Mechanisms Responsible for the Large Piezoelectricity at the Tetragonal-Orthorhombic Phase Boundary of (1-x)BaZr0.2Ti0.8O3-x Ba0.7Ca0.3TiO3 System. *Sci. Rep.* **2016**, *6*, 1–8, doi:10.1038/srep33392.

43. Cordero, F. Elastic Properties and Enhanced Piezoelectric Response at Morphotropic Phase Boundaries. *Materials (Basel).* **2015**, *8*, 8195–8245, doi:10.3390/ma8125452.

44. Nahas, Y.; Akbarzadeh, A.; Prokhorenko, S.; Prosandeev, S.; Walter, R.; Kornev, I.; Íñiguez, J.; Bellaiche, L. Microscopic Origins of the Large Piezoelectricity of Leadfree (Ba,Ca)(Zr,Ti)O3. *Nat. Commun.* **2017**, *8*, 15944, doi:10.1038/ncomms15944.

45. Liu, S.-Y.; Meng, Y.; Liu, S.; Li, D.-J.; Li, Y.; Liu, Y.; Shen, Y.; Wang, S. Compositional Phase Diagram and Microscopic Mechanism of Ba 1−x Ca x Zr y Ti 1−y O 3 Relaxor Ferroelectrics. *Phys. Chem. Chem. Phys.* **2017**, *19*, 22190–22196, doi:10.1039/C7CP04530A.

46. Damjanovic, D.; Biancoli, A.; Batooli, L.; Vahabzadeh, A.; Trodahl, J. Elastic, Dielectric, and Piezoelectric Anomalies and Raman Spectroscopy of 0.5Ba(Ti0.8Zr0.2)O3-0.5(Ba0.7Ca0.3)TiO3. *Appl. Phys. Lett.* **2012**, *100*, doi:10.1063/1.4714703.

47. Zhang, L.; Zhang, M.; Wang, L.; Zhou, C.; Zhang, Z.; Yao, Y.; Zhang, L.; Xue, D.; Lou, X.; Ren, X. Phase Transitions and the Piezoelectricity around Morphotropic Phase Boundary in Ba(Zr0.2Ti0.8)O3-x(Ba0.7Ca0.3)TiO3 Lead-Free Solid Solution. *Appl. Phys. Lett.* **2014**, *105*, doi:10.1063/1.4899125.

48. Reyes-Montero, A.; Rubio-Marcos, F.; Fuentes-Cobas, L.E.; Del Campo, A.; Castañeda-Guzmán, R.; Villafuerte-Castrejón, M.E.; Pardo, L. Confocal Raman Microscopy, Synchrotron X-Ray Diffraction, and Photoacoustic Study of Ba 0.85 Ca 0.15 Ti 0.90 Zr 0.10 O 3 : Understanding Structural and Microstructural Response to the Electric Field. *ACS Appl. Electron. Mater.* **2021**, *3*, 2966–2976, doi:10.1021/acsaelm.1c00103.

49. Aredes, R.G.; Bonaventura, A.L.; Boschilia Junior, R.; Silva, R.S.; Antonelli, E. Investigation of Temperature-Induced Phase Transitions in (Ba,Ca)(Zr,Ti)O3 Ceramics. *J. Therm. Anal. Calorim.* **2021**, *146*, 2411–2415, doi:10.1007/s10973-020-10543-y.

50. Damjanovic, D. Contributions to the Piezoelectric Effect in Ferroelectric Single Crystals and Ceramics. *J. Am. Ceram. Soc.* **2005**, *88*, 2663–2676, doi:10.1111/j.1551-2916.2005.00671.x.

51. Lv, X.; Zhang, X.X.; Wu, J. Nano-Domains in Lead-Free Piezoceramics: A Review. *J. Mater. Chem. A* **2020**, *8*, 10026–10073, doi:10.1039/d0ta03201h.

52. Ciomaga, C.E.; Curecheriu, L.P.; Lukacs, V.A.; Horchidan, N.; Doroftei, F.; Valois, R.; Lheureux, M.; Chambrier, M.H.; Mitoseriu, L. Optimization of Processing Steps for Superior Functional Properties of (Ba, Ca)(Zr, Ti)O3 Ceramics. *Materials (Basel).* **2022**, *15*, doi:10.3390/ma15248809.

53. Li, W.; Xu, Z.; Chu, R.; Fu, P.; Zang, G. Polymorphic Phase Transition and Piezoelectric Properties of (Ba 1-XCax)(Ti0.9Zr0.1)O3 Lead-Free Ceramics. *Phys. B Condens. Matter* **2010**, *405*, 4513–4516, doi:10.1016/j.physb.2010.08.028.

54. Zhang, S.W.; Zhang, H.; Zhang, B.P.; Yang, S. Phase-Transition Behavior and Piezoelectric Properties of Lead-Free (Ba0.95Ca0.05)(Ti1-XZrx)O 3 Ceramics. *J. Alloys Compd.* **2010**, *506*, 131–135, doi:10.1016/j.jallcom.2010.06.157.

55. Li, W.; Xu, Z.; Chu, R.; Fu, P.; Zang, G. High Piezoelectric D33 Coefficient in (Ba1 - XCa x)(Ti0.98Zr0.02)O3 Lead-Free Ceramics with Relative High Curie Temperature. *Mater. Lett.* **2010**, *64*, 2325–2327, doi:10.1016/j.matlet.2010.07.042.

56. Li, W.; Xu, Z.; Chu, R.; Fu, P.; Zang, G. High Piezoelectric D33 Coefficient of Lead-Free (Ba 0.93Ca0.07)(Ti0.95Zr0.05)O 3 Ceramics Sintered at Optimal Temperature. *Mater. Sci. Eng. B Solid-State Mater. Adv. Technol.* **2011**, *176*, 65–67, doi:10.1016/j.mseb.2010.09.003.

57. Wu, J.; Xiao, D.; Wu, W.; Chen, Q.; Zhu, J.; Yang, Z.; Wang, J. Composition and Poling Condition-Induced Electrical Behavior of (Ba 0.85Ca 0.15)(Ti 1-XZr x)O 3 Lead-Free Piezoelectric Ceramics. *J. Eur. Ceram. Soc.* **2012**, *32*, 891–898, doi:10.1016/j.jeurceramsoc.2011.11.003.

58. Wang, X.W.; Zhang, B.H.; Li, Y.Y.; Shi, Y.C.; Sun, L.Y.; Feng, G.; Li, C.L.; Liang, Y.F.; Zheng, Y.P.; Shang, S.Y.; et al. Structure, Dielectric, and Ferroelectric Properties of Ba0.85Ca0.15Zr0.1Ti0.9O3 Ceramics Sintered at Various Temperatures. *J. Mater. Sci. Mater. Electron.* **2020**, *31*, 4732–4742, doi:10.1007/s10854-020-03030-5.

59. Ji, X.; Wang, C.; Zhang, S.; Tu, R.; Shen, Q.; Shi, J.; Zhang, L. Structural and Electrical Properties of BCZT Ceramics Synthesized by Sol–Gel-Hydrothermal Process at Low Temperature. *J. Mater. Sci. Mater. Electron.* **2019**, *30*, 12197–12203, doi:10.1007/s10854-019-01578-5.

60. Uchino, K. Ferroelectric Ceramics. In *Materials Science and Technology*; Wiley, 2006; Vol. 16, pp. 279–286.

61. Castkova, K.; Maca, K.; Cihlar, J.; Hughes, H.; Matousek, A.; Tofel, P.; Bai, Y.; Button, T.W. Chemical Synthesis, Sintering and Piezoelectric Properties of Ba0.85Ca0.15 Zr0.1Ti0.9O3 Lead-Free Ceramics. *J. Am. Ceram. Soc.* **2015**, *98*, 2373–2380, doi:10.1111/jace.13642.

62. Damjanovic, D. A Morphotropic Phase Boundary System Based on Polarization Rotation and Polarization Extension. *Appl. Phys. Lett.* **2010**, *97*, doi:10.1063/1.3479479.

63. Gao, J.; Ke, X.; Acosta, M.; Glaum, J.; Ren, X. High Piezoelectricity by Multiphase Coexisting Point: Barium Titanate Derivatives. *MRS Bull.* **2018**, *43*, 595–599, doi:10.1557/mrs.2018.155.

64. Damjanovic, D.; Rossetti, G.A. Strain Generation and Energy-Conversion Mechanisms in Lead-Based and Lead-Free Piezoceramics. *MRS Bull.* **2018**, *43*, 588–594, doi:10.1557/mrs.2018.157.

65. European Commission Report on Critical Raw Materials for the EU, Report of the Ad Hoc Working Group on Defining Critical Raw Materials. **2014**, 41, doi:Ref. Ares(2015)1819595 - 29/04/2015.

66. Leal Filho, W.L.; Kotter, R.; Özuyar, P.G.; Abubakar, I.R.; Eustachio, J.H.P.P.; Matandirotya, N.R.

Understanding Rare Earth Elements as Critical Raw Materials. *Sustainability* **2023**, *15*, 1919, doi:10.3390/su15031919.

67. RMIS – Raw Materials Information System Available online: https://rmis.jrc.ec.europa.eu/.

68. Amorín, H.; Venet, M.; Chinarro, E.; Ramos, P.; Algueró, M.; Castro, A. Lead-Free Ba0.85Ca0.15Zr0.1Ti0.9O3 Ferroelectric Ceramics with Refined Microstructure and High Strain under Electric Field by Mechanosynthesis. *J. Eur. Ceram. Soc.* **2022**, *42*, 4907–4916, doi:10.1016/j.jeurceramsoc.2022.04.061.

69. Chao, X.; Wang, J.; Wang, Z.; Zhang, T.; Yang, Z.; Li, G. The Enhancing Performance of (Ba0.85Ca0.15Ti0.90Zr0.10)O3 Ceramics by Tuning Anatase-Rutile Phase Structure. *Mater. Res. Bull.* **2016**, *76*, 450–453, doi:10.1016/j.materresbull.2015.12.022.

70. Poon, K.K.; Wurm, M.C.; Evans, D.M.; Einarsrud, M.A.; Lutz, R.; Glaum, J. Biocompatibility of (Ba,Ca)(Zr,Ti)O3 Piezoelectric Ceramics for Bone Replacement Materials. *J. Biomed. Mater. Res. - Part B Appl. Biomater.* **2020**, *108*, 1295–1303, doi:10.1002/jbm.b.34477.

71. Amagai, J.; Kato, Y.; Ueki, A.; Saito, N.; Ohashi, N.; Haneda, H. Synthesis of (Ba,Ca)(Zr,Ti)O3 Ceramics from Ultra-Fine Precursors. *Key Eng. Mater.* **2006**, *301*, 235–238, doi:10.4028/www.scientific.net/kem.301.235.

72. Rödel, J.; Webber, K.G.; Dittmer, R.; Jo, W.; Kimura, M.; Damjanovic, D. Transferring Lead-Free Piezoelectric Ceramics into Application. *J. Eur. Ceram. Soc.* **2015**, *35*, 1659–1681, doi:10.1016/j.jeurceramsoc.2014.12.013.

73. Danks, A.E.; Hall, S.R.; Schnepp, Z. The Evolution of “sol-Gel” Chemistry as a Technique for Materials Synthesis. *Mater. Horizons* **2016**, *3*, 91–112, doi:10.1039/c5mh00260e.

74. Praveen, J.P.; Kumar, K.; James, A.R.; Karthik, T.; Asthana, S.; Das, D. Large Piezoelectric Strain Observed in Sol-Gel Derived BZT-BCT Ceramics. *Curr. Appl. Phys.* **2014**, *14*, 396–402, doi:10.1016/j.cap.2013.12.026.

75. Khomyakova, E.; Wenner, S.; Bakken, K.; Schultheiß, J.; Grande, T.; Glaum, J.; Einarsrud, M.A. On the Formation Mechanism of Ba0.85Ca0.15Zr0.1Ti0.9O3 Thin Films by Aqueous Chemical Solution Deposition. *J. Eur. Ceram. Soc.* **2020**, *40*, 5376–5383, doi:10.1016/j.jeurceramsoc.2020.07.042.

76. Wang, Z.; Wang, J.; Chao, X.; Wei, L.; Yang, B.; Wang, D.; Yang, Z. Synthesis, Structure, Dielectric, Piezoelectric, and Energy Storage Performance of (Ba0.85Ca0.15)(Ti0.9Zr0.1)O3 Ceramics Prepared by Different Methods. *J. Mater. Sci. Mater. Electron.* **2016**, *27*, 5047–5058, doi:10.1007/s10854-016-4392-x.

77. Zhang, Q.; Cai, W.; Li, Q.; Gao, R.; Chen, G.; Deng, X.; Wang, Z.; Cao, X.; Fu, C. Enhanced Piezoelectric Response of (Ba,Ca)(Ti, Zr)O3 Ceramics by Super Large Grain Size and Construction of Phase Boundary. *J. Alloys Compd.* **2019**, *794*, 542–552, doi:10.1016/j.jallcom.2019.04.247.

78. Praveen, J.P.; Kumar, K.; James Raju, C.K.; Das, D. A Study of Piezoelectric Properties of (Ba0.85Ca 0.15)(Zr0.9Ti0.1)O3 Ceramics Synthesized by Sol-Gel Process. *AIP Conf. Proc.* **2013**, *1536*, 891–892, doi:10.1063/1.4810515.

79. Ji, X.; Wang, C.; Li, S.; Zhang, S.; Tu, R.; Shen, Q.; Shi, J.; Zhang, L. Structural and Electrical Properties of BCZT Ceramics Synthesized by Sol–Gel Process. *J. Mater. Sci. Mater. Electron.* **2018**, *29*, 7592–7599, doi:10.1007/s10854-018-8751-7.

80. Reyes-Montero, A.; Pardo, L.; López-Juárez, R.; González, A.M.; Cruz, M.P.; Villafuerte-Castrejón, M.E. Lead-Free Ba0.9Ca0.1Ti0.9Zr 0.1O3 Piezoelectric Ceramics Processed below 1300°C. *J. Alloys Compd.* **2014**, *584*, 28–33, doi:10.1016/j.jallcom.2013.08.165.

81. Jaimeewong, P.; Promsawat, M.; Watcharapasorn, A.; Jiansirisomboon, S. Comparative Study of

Properties of BCZT Ceramics Prepared from Conventional and Sol-Gel Auto Combustion Powders. *Integr. Ferroelectr.* **2016**, *175*, 25–32, doi:10.1080/10584587.2016.1199913.

82. Hanani, Z.; Mezzane, D.; Amjoud, M.; Gagou, Y.; Hoummada, K.; Perrin, C.; Razumnaya, A.G.; Kutnjak, Z.; Bouzina, A.; Marssi, M. El; et al. Structural, Dielectric, and Ferroelectric Properties of Lead-Free BCZT Ceramics Elaborated by Low-Temperature Hydrothermal Processing. *J. Mater. Sci. Mater. Electron.* **2020**, *31*, 10096–10104, doi:10.1007/s10854-020-03555-9.

83. Ji, X.; Wang, C.; Luo, W.; Chen, G.; Zhang, S.; Tu, R.; Shen, Q.; Shi, J.; Zhang, L. Effect of Solution Concentration on Low-Temperature Synthesis of BCZT Powders by Sol–Gel-Hydrothermal Method. *J. Sol-Gel Sci. Technol.* **2020**, *94*, 205–212, doi:10.1007/s10971-019-05177-y.

84. Wang, X.W.; Zhang, B.H.; Feng, G.; Sun, L.Y.; Shi, Y.C.; Hu, Y.C.; Shang, J.; Shang, S.Y.; Yin, S.Q.; Wang, X.E. Effects of Calcining Temperature on Structure and Dielectric and Ferroelectric Properties of Sol-Gel Synthesized Ba0.85Ca0.15Zr0.1Ti0.9O3 Ceramics. *J. Electron. Mater.* **2020**, *49*, 880–887, doi:10.1007/s11664-019-07769-4.

85. Ji, X.; Peng, Q.; Wang, C.; Shi, J. Structure and Sintering Characteristics of Rapid Synthesizing BCZT Powders by Microwave Assisted Sol–Gel-Hydrothermal Method at Low Temperature. *J. Mater. Sci. Mater. Electron.* **2023**, *34*, 1–10, doi:10.1007/s10854-023-11346-1.

86. Ji, X.; Wang, C.; Harumoto, T.; Zhang, S.; Tu, R.; Shen, Q.; Shi, J. Structure and Electrical Properties of BCZT Ceramics Derived from Microwave-Assisted Sol–Gel-Hydrothermal Synthesized Powders. *Sci. Rep.* **2020**, *10*, 1–8, doi:10.1038/s41598-020-73784-9.

87. Prado-Gonjal, J.; Schmidt, R.; Morán, E. Microwave-Assisted Routes for the Synthesis of Complex Functional Oxides. *Inorganics* **2015**, *3*, 101–117, doi:10.3390/inorganics3020101.

88. Amorín, H.; Venet, M.; García, J.E.; Ochoa, D.A.; Ramos, P.; López-Sánchez, J.; Rubio-Zuazo, J.; Castro, A.; Algueró, M. Insights into the Early Size Effects of Lead-Free Piezoelectric Ba0.85Ca0.15Zr0.1Ti0.9O3. *Adv. Electron. Mater.* **2023**, *2300556*, 1–12, doi:10.1002/aelm.202300556.

89. Benjamin, J.S. Mechanical Alloying. Scientific American. In; 1976; pp. 234(5), 40–49.

90. Zhang, Y.; Xu, J.; Zhang, Z.; Zhao, L.; Li, M.; Li, M.; Zhao, D.; Zhong, G.; Hu, X.; Zhang, X.; et al. Mechanochemical Synthesis of Nanostructured and Composite Oxide Ceramics: From Mechanisms to Tailored Properties. *Int. J. Appl. Ceram. Technol.* **2023**, 1–39, doi:10.1111/ijac.14598.

91. Gaffet, E.; Michel, D.; Mazerolles, L.; Berthet, P. Effects of High Energy Ball Milling on Ceramic Oxides. *Mater. Sci. Forum* **1997**, *235–238*, 103–108, doi:10.4028/www.scientific.net/msf.235-238.103.

92. Shuai, C.; He, C.; Peng, S.; Qi, F.; Wang, G.; Min, A.; Yang, W.; Wang, W. Mechanical Alloying of Immiscible Metallic Systems: Process, Microstructure, and Mechanism. *Adv. Eng. Mater.* **2021**, *23*, 1–15, doi:10.1002/adem.202001098.

93. Delogu, F.; Cocco, G. Kinetics of Structural Evolution in Immiscible Ag-Cu and Co-Cu Systems under Mechanical Processing Conditions. *Mater. Sci. Eng. A* **2005**, *402*, 208–214, doi:10.1016/j.msea.2005.04.007.

94. Suryanarayana, C. Mechanical Alloying and Milling. *Prog. Mater. Sci.* **2001**, *46*, 1–184, doi:10.1016/S0079-6425(99)00010-9.

95. Tan, D.; García, F. Main Group Mechanochemistry: From Curiosity to Established Protocols. *Chem. Soc. Rev.* **2019**, *48*, 2274–2292, doi:10.1039/c7cs00813a.

96. Tsuzuki, T. Mechanochemical Synthesis of Metal Oxide Nanoparticles. *Commun. Chem.* **2021**, *4*, doi:10.1038/s42004-021-00582-3.

97. Mureddu, M.; Bartolomé, J.F.; Lopez-Esteban, S.; Dore, M.; Enzo, S.; García, Á.; Garroni, S.; Pardo, L. Solid State Processing of BCZT Piezoceramics Using Ultra Low Synthesis and Sintering Temperatures. *Materials (Basel).* **2023**, *16*, 945, doi:10.3390/ma16030945.

98. Zolriasatein, A.; Shokuhfar, A.; Safari, F.; Abdi, N. Comparative Study of SPEX and Planetary Milling Methods for the Fabrication of Complex Metallic Alloy Nanoparticles. *Micro Nano Lett.* **2018**, *13*, 448–451, doi:10.1049/mnl.2017.0608.

99. Cousin, P.; Ross, R.A. Preparation of Mixed Oxides: A Review. *Mater. Sci. Eng. A* **1990**, *130*, 119–125, doi:10.1016/0921-5093(90)90087-J.

100. Thakur, O.P.; Feteira, A.; Kundys, B.; Sinclair, D.C. Influence of Attrition Milling on the Electrical Properties of Undoped-BaTiO3. *J. Eur. Ceram. Soc.* **2007**, *27*, 2577–2589, doi:10.1016/j.jeurceramsoc.2006.10.013.

101. Tangsritrakul, J.; Sonkami, T.; Wichittanakom, C.; Dokkhan, C.; Wiroonpochit, P. Investigations on Phase Coexistence and Functional Properties of BCZT Lead-Free Piezoceramic. *J. Met. Mater. Miner.* **2021**, *31*, 20–26, doi:10.14456/jmmm.2021.35.

102. Cai, W.; Zhang, Q.; Zhou, C.; Gao, R.; Zhang, S.; Li, Z.; Xu, R.; Chen, G.; Deng, X.; Wang, Z.; et al. Synergistic Effect of Grain Size and Phase Boundary on Energy Storage Performance and Electric Properties of BCZT Ceramics. *J. Mater. Sci. Mater. Electron.* **2020**, *31*, 9167–9175, doi:10.1007/s10854-020-03446-z.

103. Hayati, R.; Fayazi, M.; Diargar, H.; Kaveh, M.; Tayebi, L. Electrical and Mechanical Properties of BZT – XBCT Lead-Free Piezoceramics. *Int. J. Appl. Ceram. Technol.* **2020**, *17*, 1891–1898, doi:10.1111/ijac.13494.

104. Mureddu, M.; Bartolomé, J.F.; Lopez-Esteban, S.; Dore, M.; Enzo, S.; García, Á.; Garroni, S.; Pardo, L. BaZrO3-BaTiO3-CaTiO3 Piezoceramics by a Water-Based Mixed-Oxide Route: Synergetic Action of Attrition Milling and Lyophilization. *J. Eur. Ceram. Soc.* **2023**, doi:10.1016/j.jeurceramsoc.2023.12.037.

105. López-Blanco, S.; Ochoa, D.A.; Amorín, H.; Castro, A.; Algueró, M.; García, J.E. Fine-Grained High-Performance Ba0.85Ca0.15 Zr0.1Ti0.9O3 Piezoceramics Obtained by Current-Controlled Flash Sintering of Nanopowders. *J. Eur. Ceram. Soc.* **2023**, 0–5, doi:10.1016/j.jeurceramsoc.2023.08.012.

106. Bai, Y.; Matousek, A.; Tofel, P.; Bijalwan, V.; Nan, B.; Hughes, H.; Button, T.W. (Ba,Ca)(Zr,Ti)O3 Lead-Free Piezoelectric Ceramics-The Critical Role of Processing on Properties. *J. Eur. Ceram. Soc.* **2015**, *35*, 3445–3456, doi:10.1016/j.jeurceramsoc.2015.05.010.

107. Hanani, Z.; Merselmiz, S.; Danine, A.; Stein, N.; Mezzane, D.; Amjoud, M.; Lahcini, M.; Gagou, Y.; Spreitzer, M.; Vengust, D.; et al. Enhanced Dielectric and Electrocaloric Properties in Lead-Free Rod-like BCZT Ceramics. *J. Adv. Ceram.* **2020**, *9*, 210–219, doi:10.1007/s40145-020-0361-1.

108. Baláž, P.; Achimovicová, M.; Baláž, M.; Billik, P.; Zara, C.Z.; Criado, J.M.; Delogu, F.; Dutková, E.; Gaffet, E.; Gotor, F.J.; et al. Hallmarks of Mechanochemistry: From Nanoparticles to Technology. *Chem. Soc. Rev.* **2013**, *42*, 7571–7637, doi:10.1039/c3cs35468g.

109. Nan, B.; Olhero, S.; Pinho, R.; Vilarinho, P.M.; Button, T.W.; Ferreira, J.M.F. Direct Ink Writing of Macroporous Lead-Free Piezoelectric Ba 0.85 Ca 0.15 Zr 0.1 Ti 0.9 O 3. *J. Am. Ceram. Soc.* **2019**, *102*, 3191–3203, doi:10.1111/jace.16220.

110. Orlik, K.; Lorgouilloux, Y.; Marchet, P.; Thuault, A.; Jean, F.; Rguiti, M.; Courtois, C. Influence of Microwave Sintering on Electrical Properties of BCTZ Lead Free Piezoelectric Ceramics. *J. Eur. Ceram. Soc.* **2020**, *40*, 1212–1216, doi:10.1016/j.jeurceramsoc.2019.12.010.

111. Frattini, A.; Di Loreto, A.; de Sanctis, O.; Benavidez, E. BCZT Ceramics Prepared from Activated

Powders. *Procedia Mater. Sci.* **2012**, *1*, 359–365, doi:10.1016/j.mspro.2012.06.048.

112. Yan, X.; Zheng, M.; He, Y.; Zhu, M.; Hou, Y. Origin of Superior Dielectric and Piezoelectric Properties in 0.4Ba(Zr0.2Ti0.8)O3–0.6(Ba0.7Ca0.3)TiO3 at Intermediate Grain Sizes. *J. Eur. Ceram. Soc.* **2020**, *40*, 3936–3945, doi:10.1016/j.jeurceramsoc.2020.03.071.

113. Syal, R.; Kumar, M.; Singh, A.K.; De, A.; Thakur, O.P.; Kumar, S. Enhancement in the Piezoelectric Properties in Lead-Free BZT-XBCT Dense Ceramics. *J. Mater. Sci. Mater. Electron.* **2020**, *31*, 21651–21660, doi:10.1007/s10854-020-04678-9.

114. Mittal, S.; Pahi, S.; Singh, K.C. Size Effect of Nano-Scale Powders on the Microstructure and Electrical Properties of Ba0.85Ca0.15Zr0.1Ti0.9O3 Ceramics. *J. Mater. Sci. Mater. Electron.* **2019**, *30*, 15493–15503, doi:10.1007/s10854-019-01926-5.

115. Ye, S.; Fuh, J.; Lu, L.; Chang, Y.L.; Yang, J.R. Structure and Properties of Hot-Pressed Lead-Free (Ba0.85Ca 0.15)(Zr0.1Ti0.9)O3 Piezoelectric Ceramics. *RSC Adv.* **2013**, *3*, 20693–20698, doi:10.1039/c3ra43429j.

116. Shang, M.; Ren, P.; Wan, Y.; Lu, X. Tailoring Curie Temperature and Dielectric Properties by Changing the Doping Sites of Y Ions in (Ba, Ca)(Zr, Ti)O3 Ceramics. *J. Eur. Ceram. Soc.* **2023**, *43*, 2488–2497, doi:10.1016/j.jeurceramsoc.2023.01.033.

117. Panda, P.K.; Sahoo, B.; Sureshkumar, V.; Politova, E.D. Effect of Zr 4 + on Piezoelectric, Dielectric and Ferroelectric Properties of Barium Calcium Titanate Lead-Free Ceramics. *J. Adv. Dielectr.* **2021**, *11*, 1–9, doi:10.1142/S2010135X21500247.

118. Bai, W.; Hao, J.; Shen, B.; Zhai, J. Dielectric Properties and Relaxor Behavior of High Curie Temperature (Ba0.85Ca0.15)(Zr0.1Ti0.9)O 3-Bi(Mg0.5Ti0.5)O3 Lead-Free Ceramics. *Ceram. Int.* **2013**, *39*, S19–S23, doi:10.1016/j.ceramint.2012.10.028.

119. Hirosawa, F.; Iwasaki, T.; Iwata, M. Particle Impact Energy Variation with the Size and Number of Particles in a Planetary Ball Mill. *MATEC Web Conf.* **2021**, *333*, 02016, doi:10.1051/matecconf/202133302016.

120. Garroni, S.; Minella, C.B.; Pottmaier, D.; Pistidda, C.; Milanese, C.; Marini, A.; Enzo, S.; Mulas, G.; Dornheim, M.; Baricco, M.; et al. Mechanochemical Synthesis of NaBH4 Starting from NaH-MgB 2 Reactive Hydride Composite System. *Int. J. Hydrogen Energy* **2013**, *38*, 2363–2369, doi:10.1016/j.ijhydene.2012.11.136.

121. Abdellaoui, M.; Gaffet, E. The Physics of Mechanical Alloying in a Planetary Ball Mill: Mathematical Treatment. *Acta Metall. Mater.* **1995**, *43*, 1087–1098, doi:10.1016/0956-7151(95)92625-7.

122. Delogu, F.; Mulas, G.; Schiffini, L.; Cocco, G. Mechanical Work and Conversion Degree in Mechanically Induced Processes. *Mater. Sci. Eng. A* **2004**, *382*, 280–287, doi:10.1016/j.msea.2004.05.047.

123. Singh, R.; Patro, P.K.; Kulkarni, A.R.; Harendranath, C.S. Synthesis of Nano-Crystalline Potassium Sodium Niobate Ceramic Using Mechanochemical Activation. *Ceram. Int.* **2014**, *40*, 10641–10647, doi:10.1016/j.ceramint.2014.03.047.

124. Hao, J.; Bai, W.; Li, W.; Zhai, J. Correlation between the Microstructure and Electrical Properties in High-Performance (Ba 0.85 Ca 0.15)(Zr 0.1 Ti 0.9) O 3 Lead-Free Piezoelectric Ceramics. *J. Am. Ceram. Soc.* **2012**, *95*, 1998–2006, doi:10.1111/j.1551-2916.2012.05146.x.

125. Di Loreto, A.; Frattini, A.; Stachiotti, M.G. Influence of Post-Calcination Grinding on the Properties of Ba0.85Ca0.15Zr0.1Ti0.9O3 Lead-Free Piezoceramics. *Mater. Lett.* **2017**, *191*, 69–72, doi:10.1016/j.matlet.2017.01.034.

126. Pisitpipathsin, N.; Kantha, P. Ferroelectric and Piezoelectric Properties of Ba0.85Ca0.15Zr0.1Ti0.9O3 Ceramic with Various Sintering Times. *Integr. Ferroelectr.* **2018**, *187*, 138–146,

doi:10.1080/10584587.2018.1444886.

127. Kantha, P.; Bunthod, T.; Jansrabua, S.; Barnthip, N.; Tigunta, S.; Pengpat, K.; Pisitpipathsin, N. Effect of Sintering Method on the Microstructure and Dielectric Properties of Lead-Free BCZT Ceramics. *Appl. Mech. Mater.* **2017**, *866*, 263–266, doi:10.4028/www.scientific.net/amm.866.263.

128. Xu, K.; Yang, P.; Peng, W.; Li, L. Temperature-Stable MgO-Doped BCZT Lead-Free Ceramics with Ultra-High Energy Storage Efficiency. *J. Alloys Compd.* **2020**, *829*, 154516, doi:10.1016/j.jallcom.2020.154516.

129. Reyes-Montero, A.; Rubio-Marcos, F.; Fuentes-Cobas, L.E.; Campo, A. Del; Castañ Eda-Guzmán, R.; Villafuerte-Castrejón, E.; Pardo, L. Confocal Raman Microscopy, Synchrotron X-Ray Diffraction, and Photoacoustic Study of Ba 0.85 Ca 0.15 Ti 0.90 Zr 0.10 O 3 : Understanding Structural and Microstructural Response to the Electric Field. **2021**, doi:10.1021/acsaelm.1c00103.

130. Scarisoreanu, N.D.; Craciun, F.; Ion, V.; Birjega, R.; Bercea, A.; Dinca, V.; Dinescu, M.; Sima, L.E.; Icriverzi, M.; Roseanu, A.; et al. Lead-Free Piezoelectric (Ba,Ca)(Zr,Ti)O3 Thin Films for Biocompatible and Flexible Devices. *ACS Appl. Mater. Interfaces* **2017**, *9*, 266–278, doi:10.1021/acsami.6b14774.

131. Koruza, J.; Bell, A.J.; Frömling, T.; Webber, K.G.; Wang, K.; Rödel, J. Requirements for the Transfer of Lead-Free Piezoceramics into Application. *J. Mater.* **2018**, *4*, 13–26, doi:10.1016/j.jmat.2018.02.001.

132. Bijalwan, V.; Tofel, P.; Erhart, J.; Maca, K. The Complex Evaluation of Functional Properties of Nearly Dense BCZT Ceramics and Their Dependence on the Grain Size. *Ceram. Int.* **2019**, *45*, 317–326, doi:10.1016/j.ceramint.2018.09.169.

133. Kaushal, A.; Olhero, S.M.; Ferreira, J.M.F. Lead-Free 0.5Ba(Zr0.2Ti0.8)O3–0.5(Ba0.7Ca0.3)TiO3 Powder Surface Treated against Hydrolysis – a Key for a Successful Aqueous Processing. *J. Mater. Chem. C* **2013**, *1*, 4846, doi:10.1039/c3tc30741g.

134. Kaushal, A.; Olhero, S.M.; Singh, B.; Zamiri, R.; Saravanan, V.; Ferreira, J.M.F. Successful Aqueous Processing of a Lead Free 0.5Ba(Zr 0.2 Ti 0.8)O 3 –0.5(Ba 0.7 Ca 0.3)TiO 3 Piezoelectric Material Composition. *RSC Adv.* **2014**, *4*, 26993–27002, doi:10.1039/C4RA03172E.

135. Martin, A.J.P. Tribo-Electricity in Wool and Hair. *Proc. Phys. Soc.* **1941**, *53*, 186–189, doi:10.1088/0959-5309/53/2/310.

136. Fukada, E.; Yasuda, I. On the Piezoelectric Effect of Bone. *J. Phys. Soc. Japan* **1957**, *12*, 1158–1162, doi:10.1143/JPSJ.12.1158.

137. Zheng, T.; Huang, Y.; Zhang, X.; Cai, Q.; Deng, X.; Yang, X. Mimicking the Electrophysiological Microenvironment of Bone Tissue Using Electroactive Materials to Promote Its Regeneration. *J. Mater. Chem. B* **2020**, *8*, 10221–10256, doi:10.1039/d0tb01601b.

138. Yang, C.; Ji, J.; Lv, Y.; Li, Z.; Luo, D. Application of Piezoelectric Material and Devices in Bone Regeneration. *Nanomaterials* **2022**, *12*, 4386, doi:10.3390/nano12244386.

139. Rajabi, A.H.; Jaffe, M.; Arinzeh, T.L. Piezoelectric Materials for Tissue Regeneration: A Review. *Acta Biomater.* **2015**, *24*, 12–23, doi: 10.1016/j.actbio.2015.07.010.

140. Jin, Z.; Lu, B.; Xu, Y.; Zhang, X. Lead-Free Piezoelectric Ceramics – An Electroactive Material That Provides Electrical Stimulation Cues for Bone Regeneration. *Process. Appl. Ceram.* **2023**, *17*, 214–235, doi:10.2298/PAC2303214J.

141. Manohar, C.S.; Kumar, B.S.; Sadhu, S.P.P.; Srimadh, S.K.; Muthukumar, V.S.; Venketesh, S.; Varma, K.B.R. Novel Lead-Free Biocompatible Piezoelectric Hydroxyapatite (HA)-BCZT (Ba0.85Ca0.15Zr0.1Ti0.9O3) Nanocrystal Composites for Bone Regeneration. *Nanotechnol. Rev.* **2019**, *8*, 61–78, doi:10.1515/ntrev-2019-0006.

142. Guzmán Sierra, D.L.; Bdikin, I.; Tkach, A.; Vilarinho, P.M.; Nunes, C.; Ferreira, P. Flexible Piezoelectric Chitosan and Barium Titanate Biocomposite Films for Sensor Applications. *Eur. J. Inorg. Chem.* **2021**, *2021*, 792–803, doi:10.1002/ejic.202000938.

143. Hanani, Z.; Izanzar, I.; Amjoud, M.; Mezzane, D.; Lahcini, M.; Uršič, H.; Prah, U.; Saadoune, I.; Marssi, M. El; Luk'yanchuk, I.A.; et al. Lead-Free Nanocomposite Piezoelectric Nanogenerator Film for Biomechanical Energy Harvesting. *Nano Energy* **2021**, *81*, doi:10.1016/j.nanoen.2020.105661.

144. Tigunta, S.; Pisitpipathsin, N.; Kantha, P.; Eitssayeam, S.; Rujijanagul, G.; Tunkasiri, T.; Pengpat, K. Electrical Properties of Calcium Phosphate/BZT Bioglass-Ceramics Prepared by Incorporation Method. *Ferroelectrics* **2014**, *459*, 188–194, doi:10.1080/00150193.2013.849527.

145. Wu, C.; Zhang, C.; Yan, X.; Cheng, J.; Chen, L.; Tang, Y.; Zhao, K. Preparation and Biological Properties of BCZT/TiO2 Electrokinetic Conversion Coating on Titanium Surface in Vitro for Dental Implants. *Surf. Coatings Technol.* **2023**, *468*, 129746, doi:10.1016/j.surfcoat.2023.129746.

146. Wu, C.; Zhang, C.; Yan, X.; Liang, Q.; Zhao, K.; Tang, Y. Preparation and Antibacterial Properties of BCZT-Ag Piezoelectric Coating on Titanium Surface for Orthopedic Implants. *Ceram. Int.* **2024**, *50*, 4296–4306, doi:10.1016/j.ceramint.2023.10.261.

147. Poon, K.K.; Schafföner, S.; Einarsrud, M.A.; Glaum, J. Barium Titanate-Based Bilayer Functional Coatings on Ti Alloy Biomedical Implants. *J. Eur. Ceram. Soc.* **2021**, *41*, 2918–2922, doi:10.1016/j.jeurceramsoc.2020.12.023.

148. Jeong, C.K. Toward Bioimplantable and Biocompatible Flexible Energy Harvesters Using Piezoelectric Ceramic Materials. *MRS Commun.* **2020**, *10*, 365–378, doi:10.1557/mrc.2020.48.

149. Divya, S.; Oh, T.H.; Bodaghi, M. 1D Nanomaterial Based Piezoelectric Nanogenerators for Self-Powered Biocompatible Energy Harvesters. *Eur. Polym. J.* **2023**, *197*, 112363, doi:10.1016/j.eurpolymj.2023.112363.

150. Yan, X.; Lam, K.H.; Li, X.; Chen, R.; Ren, W.; Ren, X.; Zhou, Q.; Shung, K.K. Correspondence: Lead-Free Intravascular Ultrasound Transducer Using BZT-50BCT Ceramics. *IEEE Trans. Ultrason. Ferroelectr. Freq. Control* **2013**, *60*, 1272–1276, doi:10.1109/TUFFC.2013.2692.

151. Wang, Y.; Zang, P.; Yang, D.; Zhang, R.; Gai, S.; Yang, P. The Fundamentals and Applications of Piezoelectric Materials for Tumor Therapy: Recent Advances and Outlook. *Mater. Horizons* **2023**, *10*, 1140–1184, doi:10.1039/d2mh01221a.

152. Chen, S.; Zhu, P.; Mao, L.; Wu, W.; Lin, H.; Xu, D.; Lu, X.; Shi, J. Piezocatalytic Medicine: An Emerging Frontier Using Piezoelectric Materials for Biomedical Applications. *Adv. Mater.* **2023**, *35*, doi:10.1002/adma.202208256.

153. ATSDR *Toxicological Profile for Barium and Barium Compounds*; 2007; p. 184.

154. Fernandes, C.; Taurino, I. Biodegradable Molybdenum (Mo) and Tungsten (W) Devices: One Step Closer towards Fully-Transient Biomedical Implants. *Sensors* **2022**, *22*, 1–22, doi:10.3390/s22083062.

4 Experimental procedure applied to methodology.

A thorough understanding of the structure-property relationship is the key to fabricate environmentally friendly piezoceramics showcasing optimal electromechanical properties. In a rigorous methodology which allows to obtain well-densified ceramics, a deep characterization, combining different physicochemical techniques, is mandatory. Since the ceramic processing requires many steps, previously evidenced in the SOTA (State of the Art analysis) of this dissertation (**Chapter 3.3**), all of them have an influence on the resulting properties. The characterisation, which is equally complex, must be thoroughly performed at each stage of the manufacturing process. Laying on these bases, this Chapter describes the general methodology adopted for the research activities of this PhD thesis and the techniques employed to characterize the pristine materials, the intermediate products, and the final ceramics (as graphically summarized in **Figure 4.1**. Details on the specific methodology implemented for a particular processing route will be provided in Chapters (5-11) on results.

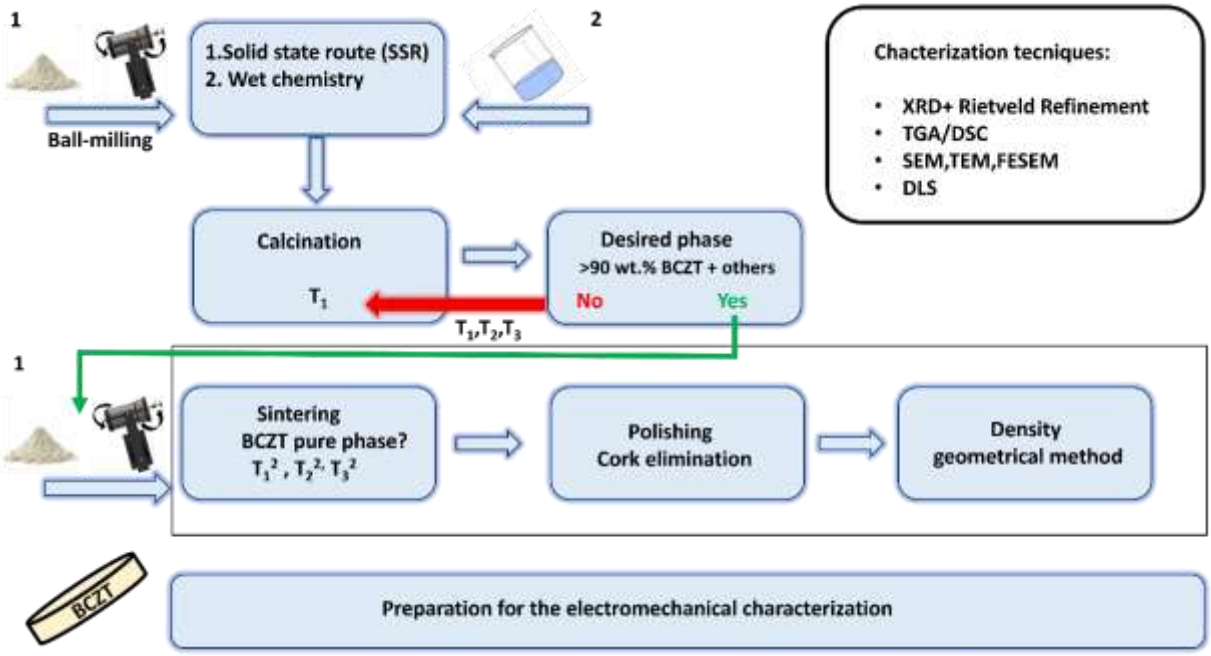

Figure 4.1 Methodology adopted to characterise each step of the processing route.1.Indicates that the same ball-milling setup is used for the ball-milling after calcination.

Preliminarily, based on the phase diagram, the most promising candidate solid solutions were identified, to achieve the desired properties. In particular, two compositions $(Ba_{0.85}Ca_{0.15})$ $(Ti_{0.90}Zr_{0.10})0_3$ and $(Ba_{0.92}Ca_{0.08})$

$(Ti_{0.95}Zr_{0.05})O_3$, shortened as **$BC_{15}TZ_{10}$** and **$BC_{08}TZ_{05}$**, respectively, were studied in this work. Materials of selected compositions have been synthesized endeavouring different and innovative routes, such as the modified solid-state route and the wet chemistry route, with the final goal of proposing economical, tuneable, and scalable preparation methods for the further development of this technology. The powders have been extensively characterized to gain information on the optimal synthesis conditions. Hence, using this rigorous methodology the information collected is continuously feedbacked to optimize each step of the processing route. The as-obtained powders have been then shaped into pellets, characterised, and subsequently prepared for the electromechanical characterization with the final purpose of obtaining microstructural and compositional features as well as on the entire set of electrical and mechanical properties obtained by using the iterative automatic method. In this way, it was possible to correlate the optimal processing conditions with the best microstructure and properties obtained.

4.1 Mechanical milling

As already introduced in the previous Chapter, the solid-state route is the most widely used technique for processing ceramics. However, it requires very high processing temperatures for BCZT systems (up to 1300°C for the synthesis and up to 1550 °C for the sintering). In this respect, to reduce the processing temperatures, it was decided to treat both raw materials and calcined powders *via* ball-milling technique [1–7]. As previously emphasized, the mechanical action of a grinding medium in high-energy ball-milling can promote physical and chemical transformations within a solid, depending on several milling parameters (*i.e.* ball-to-powders weight ratio (BPR), milling time, grinding media, solvents, atmosphere within the vial) in order to tune the amount of mechanical energy transferred to the system, which affects the final properties of the products. It is important to underline that in the present work this technique was limited to the mere activation of the powders prior to calcination in the furnace and prior to sintering and should not be considered as a mechanosynthesis [1]. This technique is widespread owing to the necessary tools are readily available and easy to use, consisting essentially of a ball-mill apparatus (attritor, shaker, planetary and horizontal roll), a jar, which is basically a vial that can have different inner volumes and be made of various

materials (stainless-steel, zirconia, polymers, tungsten carbide, agate, etc.) and, as essential elements, one or more spheres (of different weights and sizes) that can be of the same or different materials, depending on the characteristics of the powder (grinding media should be harder than the particles to be milled).It should not be underestimated that, for these materials, it is important to choose the right setup to avoid the problem of contamination that may arise from the vial/spheres, leading to an alteration of the stoichiometry, eventually altering the electromechanical properties.

In the present work, the impact of the contamination from the material of both jar and spheres was evaluated. Firstly, was used a shaker mill type (3D Mix/Miller 8000 – SPEX) (**Figure 4.1.1(a)**), then a laboratory-made attrition ball-milling apparatus (ABM) (**Figure 4.1.1(b)**).

Figure 4.1.1 Two different mills employed: a) Shaker miller type (3D Mix/Miller 8000 – SPEX) working at 875 rounds per minute (rpm), b) homemade attritor mill, working at 700 rpm.

Two different jars were used with the Miller SPEX 8000 (stainless-steel and tungsten carbide, shown in **Figure 4.1.2(a** and **b**, respectively) and for the laboratory-made attrition ball milling apparatus (**Figure 4.1.2(b)**) a vial internally coated with Teflon (**Figure 4.1.2(c)**).

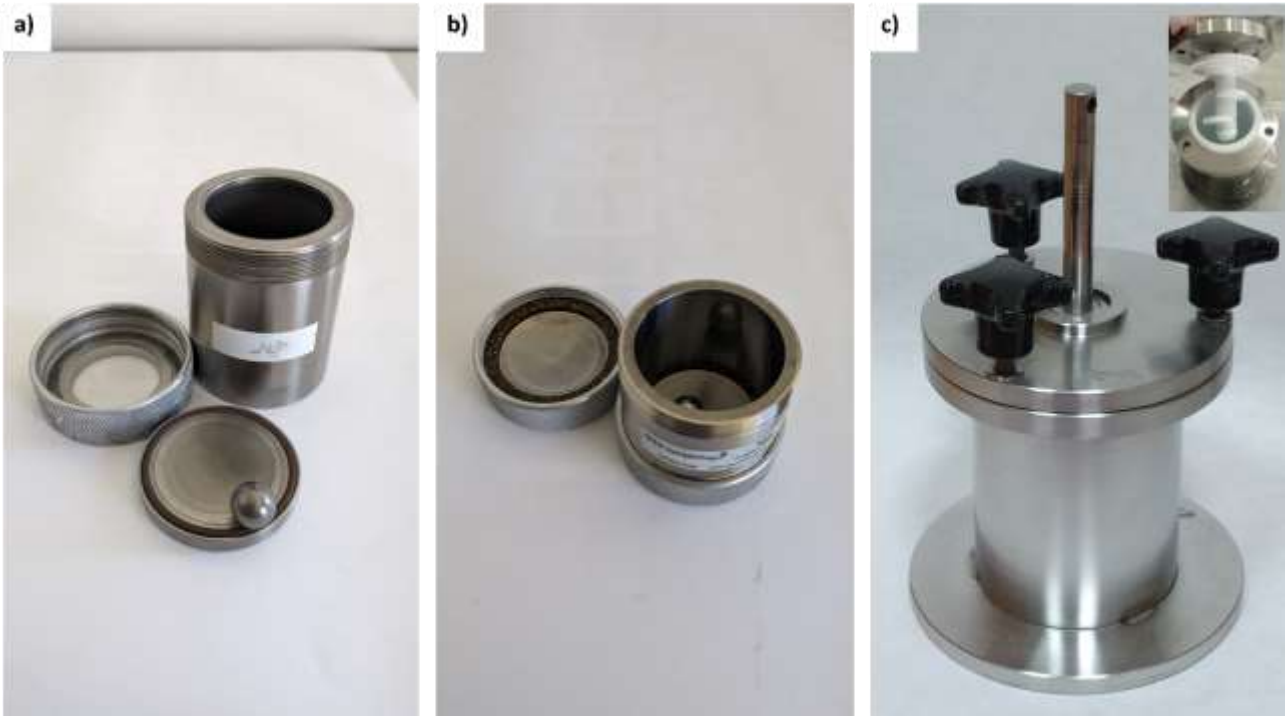

Figure 4.1.2 a) stainless-steel jar with one sphere made of the same material, b) tungsten carbide jar with one sphere made of the same material, c) stainless-steel jar internally covered by Teflon, as shown in the upper Figure, used with 3Y-TZP spheres.

The precursors were, in general, used as received (after characterising them by XRD, to ensure their purity and check their composition) and their characteristics are listed in **Table 4.1.1.** It should be emphasised that all experiments were conducted in air (the precursors used are not oxygen-sensitive), weighing the powders after a pre-degassing (24 hours at 100°C) to remove any contamination from moisture.

Table 4.1.1. Reagents used for the solid-state route.

Reagent	Supplier	Purity declared	Composition checked by XRD analysis
$BaCO_3$	Merck, Darmstadt, Germany	>99%	orthorhombic (Witherite)
$BaCO_3$	Sigma Aldrich, St. Louis, MO, USA,	>99%	orthorhombic (Witherite)
$CaCO_3$	Sigma Aldrich, St. Louis, MO, USA,	>99%	trigonal (Calcite)
$CaCO_3$	Fluka	>99%	trigonal (Calcite)
TiO_2	Merck, Darmstadt, Germany	>99%	85 wt.% anatase,15 wt.% rutile
TiO_2	Sigma Aldrich, St. Louis, MO, USA,	>99.9%	99 wt.% anatase,1 wt.% rutile
ZrO_2	Tosoh, Tokyo, Japan,	>99%	monoclinic
ZrO_2	Alfa Aesar	>99%	monoclinic

Before choosing the best ball-milling setup, a preliminary study was performed, varying the BPR and the milling time. For the sake of brevity, in **Table 4.1.2** are reported only the selected ball-milling conditions useful to discuss the obtained results.

Table 4.1.2 Summary of the chosen setup for each BM treatment.

Stoichiometry/ abbreviation	Type of mill	Milling Jar	Grinding medium	Milling speed (rpm)- Frequency (Hz)	Atm	BPR	1°BM	2°BM	Solvent
$(Ba_{0.85}Ca_{0.15})(Ti_{0.9}Zr_{0.10})O_3$/ $BC_{15}TZ_{10}$	Shaker SPEX	SS	SS	875 14.58	Air	1	6 h	2-8-16 h	Absolute Ethanol
$(Ba_{0.85}Ca_{0.15})(Ti_{0.9}Zr_{0.10})O_3$/ $BC_{15}TZ_{10}$	Shaker SPEX	WC	WC	875 14.58	Air	1	5h	2-8 h	Absolute Ethanol
$(Ba_{0.92}Ca_{0.08})(Ti_{0.95}Zr_{0.05})O_3$/ $BC_{08}TZ_{05}$	ABM	Teflon	3Y-TZP	700 11.7	Air	30	6h	3h	Isopropanol
$(Ba_{0.92}Ca_{0.08})(Ti_{0.95}Zr_{0.05})O_3$/ $BC_{08}TZ_{05}$	ABM	Teflon	3Y-TZP	700 11.7	Air	30	6h	3h	Distilled Water

Legend. 1°BM: First ball-milling before calcination step. 2°BM: Second ball-milling before the sintering step. Stainless-steel (SS), tungsten carbide (WC), Attrition ball-mill (ABM).Atm: Atmosphere.

4.2 Characterisation

4.2.1 X-ray diffraction (XRD)

X-Ray powder diffraction (as well as the companion techniques of neutron and electron scattering, micro diffraction, time- and temperature-resolved scattering techniques) is one of the most useful approaches to characterize piezo ceramics. Generally speaking, powder crystallography techniques are employed for several purposes, such as: lattice type identification, chemical composition, phase evolution, crystallographic texture, domain size switching, lattice strains, etc. [8][9][10].

In the present Thesis, the X-rays diffraction has been extensively used to characterize powders and ceramics obtained after each step of the processing route for the following aims:

- assessing the geometry and symmetry of lattices;
- defining chemical nature and composition of as received precursors and checking the presence of impurities;
- verifying the effectiveness of mechanical activation for optimizing ball-milling parameters;
- proving the formation of the desired phase and the side formation of secondary phases;
- performing *in situ* poling and temperature experiments for monitoring the effects of temperature and electric field on the crystalline lattice.

The powders of tiny crystal size if distributed randomly in the sample holders, once irradiated, may conduct to a 1-D pattern representing the 3-D projection of the reciprocal space. The location of the peaks may be precise to a sufficient level for identifying the chemical composition of the substances responsible for the scattering conditions recorded in the total experimental pattern **I** vs **2θ** [11]. After data recording of an X-ray powder pattern, the Rietveld method appears as very useful for extraction of the maximum structure and microstructure information. This approach carries out a comparison between experiment and numerical modelling based on the knowledge of the crystal structure of each scattering phase. On the basis of

Crystallography Information Files (CIF), archived in specific databases (some free-of-charges and other commercial), the hypothised structure information can be expressed numerically in the reciprocal space. In addition to phase fractions, after taking into account the convolution of the geometry and optics of the instrument and systematic errors in the scale 2theta due to zero-offset in the model, lattice parameters, crystallographic structure, average crystallite size and microstrain can be adjusted. The computed model matches the experimental data according to an iterative search procedure and ends once reached the minimization in the least-squares sense. The parameters optimized in the model accounting closely for the experimental data allow estimating quantitative data of phase contributions and microstructure features. While lattice parameters can be determined with a highly reliable precision, this is not so for the microstructure parameters, since they are derived *in primis* from the line broadening peaks across a sufficiently wide angular range [12].

For this work, two diffractometers have been used: Rigaku SMARTLAB with a Cu rotating anode, (**Figure 4.2.1(a)**) and Bruker D8 Advance diffractometer **(Figure 4.2.1(b)**).

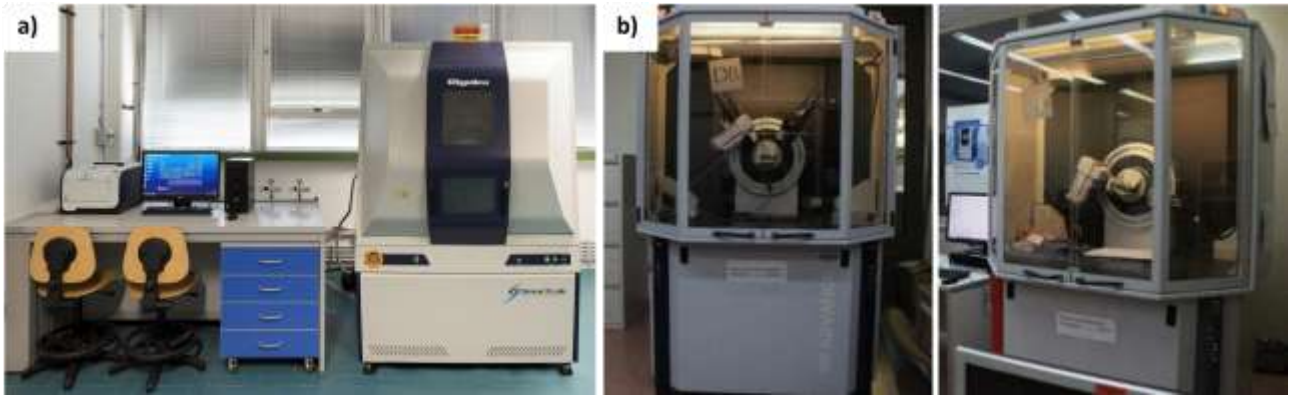

Figure 4.2.1 a) Rigaku SMARTLAB with a Cu rotating anode, b) Bruker D8 Advance

The two laboratory machines have substantially similar setup, and both can be sketched according to the figure reported below. The diffraction data obtained in the chosen conditions (step size, integration time, angular range of 2 theta) were compared with the calculated after using the search-and-match analysis software High Score Plus for phase identification. Other software free-of-charge for such important step can be recommended such as QualX (qualitative analysis using powder diffraction data) [13] or FPSM(Full Profile

Search and Match) [14]. As it was previously anticipated, all the information concerning the unit cell of a crystal is stored in crystallography (single crystals and/or powder) according to the CIF files. Such files are considering the space group (collection of symmetry ad geometry properties), lattice parameters of the unit cell, occupancy of each atomic species located in their specific Wyckoff sites, in turn expressed as spatial fractional coordinates. The latter triplet of coordinates (x, y and z) may be identified as special positions (0, ½, 1/3, ¼ and 1/6) or simply general (that is the fractional coordinates assume real values between 0 and 1). The quantitative phase composition and structure and microstructure parameters were determined by the application of Rietveld refinement on the experimental pattern using the freely available MAUD (Material Analysis Using Diffraction) software developed by L. Lutterotti and based on the Rietveld method [15]. As stated before, this is a refinement method for structure solution available for multiphase samples firstly reported in 1969 [16]. It uses the least squares approach to bend a theoretical line profile until it matches the experimental data profile. In this method the weight fraction (w_i) of each crystalline phase in a mixture can be calculated from the following equation:

$$\frac{w_i}{\sum_j w_j} = \frac{S_i(Z_i M_i V_i)}{\sum_j S_j(Z_j M_j V_j)} \qquad (4.1)$$

where S_i is the refined scale factor, Z_i is the number of formula units in the unit cell, M_i is the mass of the unit formula and V_i is the elementary cell volume. Quantitative phase analysis by the Rietveld method is based on the normalisation condition $\sum_i w_i = 1$. This is valid when the mixture contains no amorphous phases [17]. The CIF file is "refined" in order to construct a new simulated profile that coincides as closely as possible with the one obtained experimentally. The software, after completing the iterative calculation procedure, returns as feedback the index of correspondence of the calculated pattern with the experimentally obtained one (R_{wp}) together with the required crystallographic data. The selected CIFs are shown below in **Table 4.2*.1.***

Table 4.2.1 Selected CIF files.

Name	Symmetry	Chemical formula	Space group		Database
			Symbol	No.	
Anatase	Tetragonal	TiO_2	*I*41/*amd*:1	141	COD
Rutile	Tetragonal	TiO_2	*P42/mnm*	134	COD
Witherite	Orthorhombic	$BaCO_3$	*Pmcn*:*bca*	62	COD
HT	Trigonal	$BaCO_3$	*R*-3*c*	167	COD
Calcite	Trigonal	$CaCO_3$	*R*-3*c*:*H*	167	COD
Baddeleyte	monoclinic	ZrO_2	*P*21/*c: b*1	14	COD
BCZT (BT)	Tetragonal	$(Ba_{(1-x)}Ca_x)(Ti_{1-y})Zr_y)O_3$	*P*4*mm*	99	COD
BZ	cubic	$BaZrO_3$	*Pm*-3*m*	6	COD
CT	Orthorhombic	$CaTiO_3$	*Pbnm*	62	COD

Legend. BCZT: Barium-Calcium Zirconate Titanate.BZ: Barium Zirconate. CT:Calcium Titanate.

The quality of the agreement between the experimental and calculated data was evaluated using as numerical criterion, the R_{wp} parameter (weighted-pattern factor), that is the difference between the observation pattern and the XRD calculation [18]. We remind that the CIF file for $(Ba_{(1-x)}Ca_x)(Ti_{1-y})Zr_y)O_3$ was elaborated using MAUD program starting from the $BaTiO_3$ parental structure and according to A/B perovskite site doping amount.

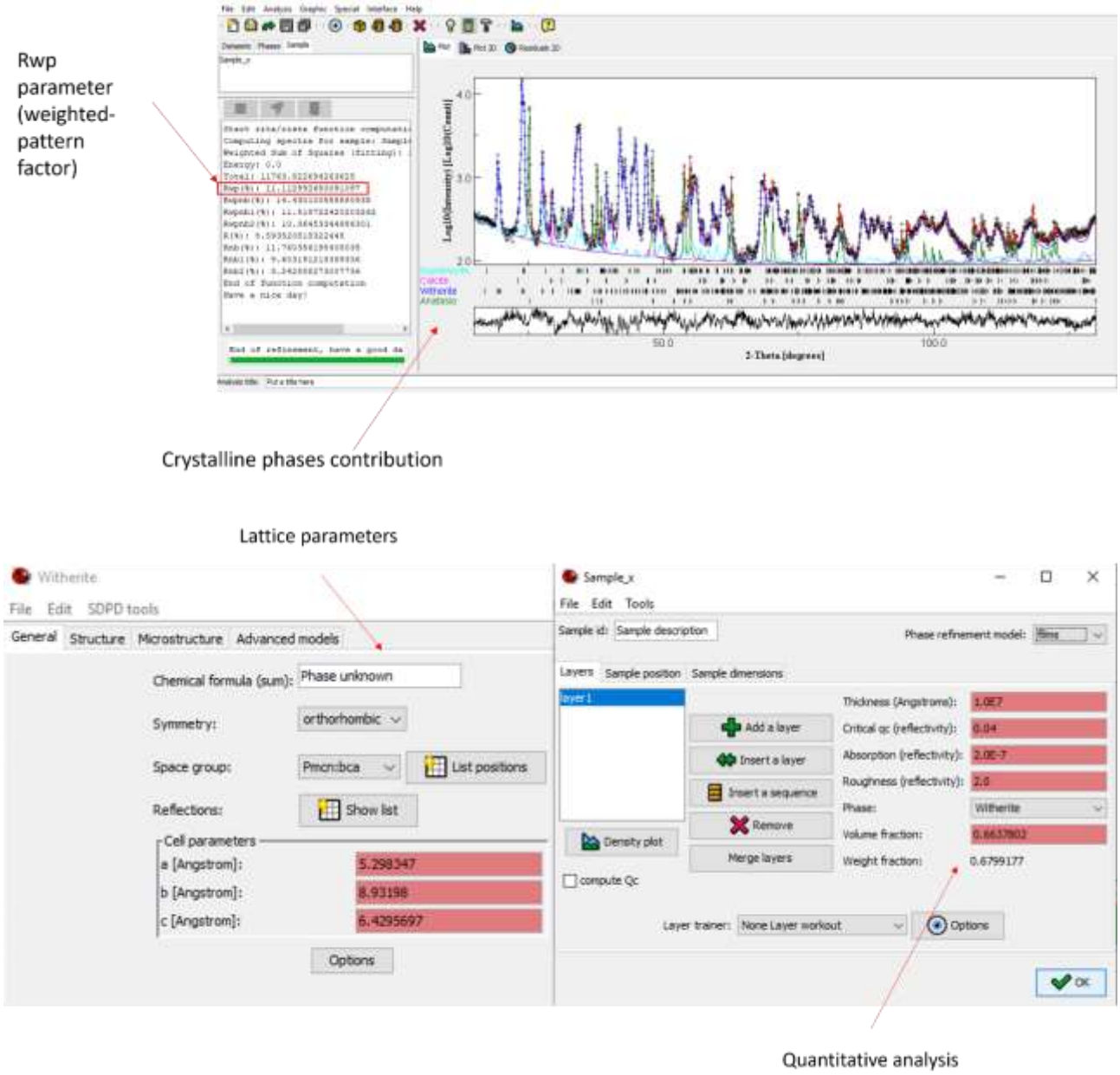

Figure 4.2.2 Interface of the MAUD software showing the lattice parameters of the cell of $BaCO_3$ (Witherite), the spatial group and lattice symmetry and the calculated weight contribution of the $BaCO_3$ (witherite) phase within the analysed powder.

4.2.2 Synchrotron measurements

For the present Thesis, powder x-ray diffraction using synchrotron radiation has been employed mainly for two purposes:

-To assess the tetragonality of BCZT perovskite at RT (25°C) as previously inferred from our laboratory instrument (experiment performed at NOTOS beamline);

- To conduct *in situ* XRD experiments following the crystalline phase evolution of precursors as a function of the temperature. (Experiments carried out at the Swiss-Norwegian beamline BM01 at the European Synchrotron Radiation Facility, ESRF – Grenoble, France);

In particular, the latter appears particularly useful in order *i)* to ascertain the formation mechanism of the main perovskite together with side secondary phases that can form during the heating or crystallize after cooling; and *ii)* to assess the effects of combining mechanical activation of precursors and lyophilization on the perovskite formation process.

- **BL16 NOTOS beamline**

The high-resolution XRD beamline operates between 4.5 and 30 KeV (Bending Magnet source) and it is equipped with a position sensitive detector for PD Mythen (6 modules). The main elements available are: two circles diffractometer and 10-channels Ge (111) analyser detector combined with a single point detector without analyser (**Figure 4.2.3.)**

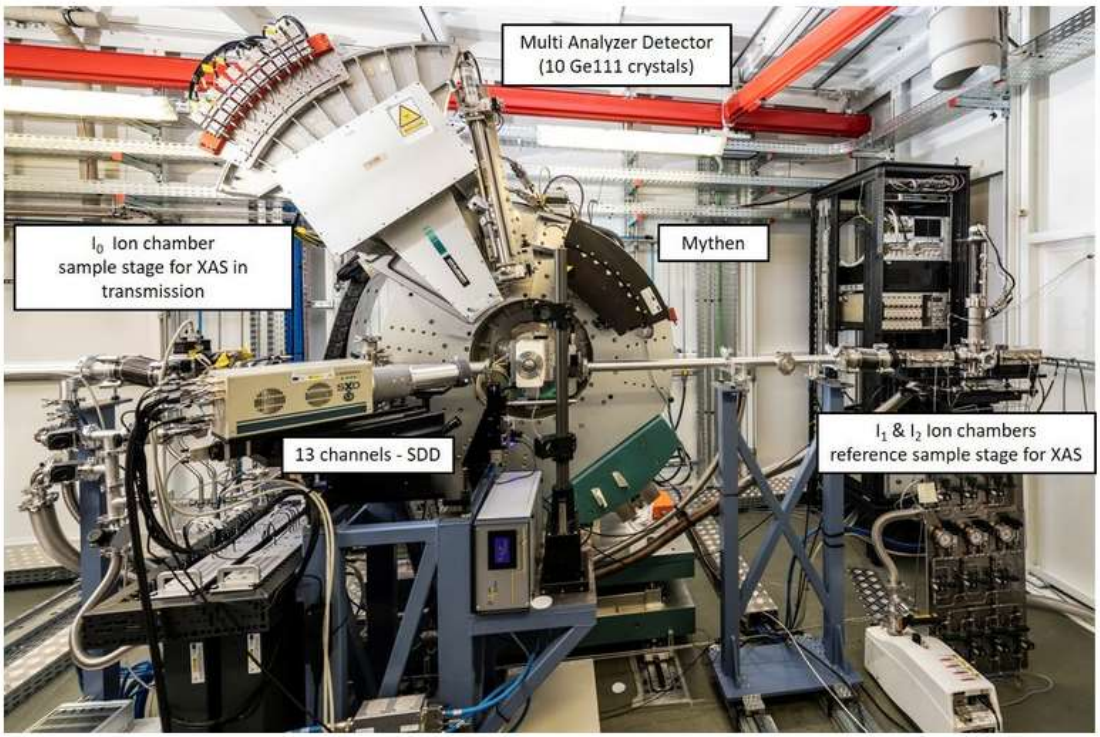

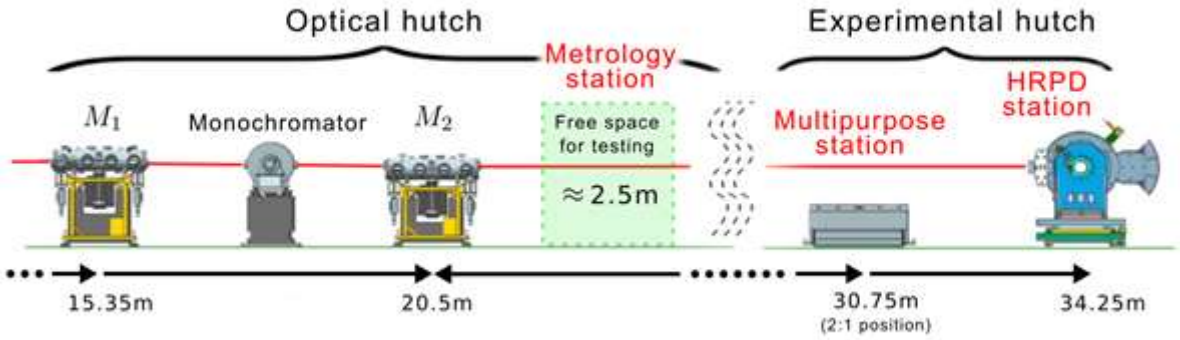

Figure 4.2.3. Layout of BL16 Notos beamline.

It is important to underline that the huge decrease in intensity is due to the geometry of the measurement, at lower angles the beam path is smaller compared to higher angles and the absorption is higher. For this measurement Si was taken as standard.

- **Swiss-Norwegian beamline BM01**

The high-resolution XRD Swiss-Norwegian beamline BM01 can be employed for single-crystal diffraction, small molecules, and for macromolecular crystallography. The geometry can be summarized as follows: mirror 1 (distance from source of 25.9 m, focusing type Rh coated Vertical collimator), Double crystal monochromator (distance from source of 25.9 m, focusing type Si (111) Sagittally focusing) mirror 2 (distance from source of 30.8 m, focusing type Rh coated Vertical focusing). It is installed on a bending magnet source (dipole BM 1), it works in the range 10 - 22 keV, and is equipped with PILATUS 2M detector (**Figure 4.2.4.)**

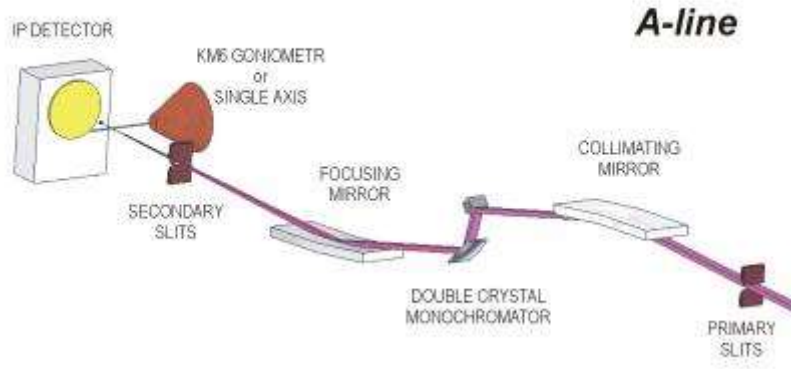

Figure 4.2.4 Schematic layout of the Swiss-Norwegian beamline BM01

4.2.3 Simultaneous thermal analysis (TG/DTA/DSC).

Simultaneous thermal analysis (STA) is a combined technique in which thermogravimetric (TG), Differential Thermal Analysis (DTA) and Differential Scanning Calorimetry (DSC) of solid materials are performed simultaneously in a single instrument (**Figure 4.2.5**). The main advantage is that the test conditions are exactly the same for TG and DSC (atmosphere, gas flow rate, water vapour pressure on the sample, heating rate, thermal contact between the sample crucible and sensor, radiation effect and so on). In general, the information obtained with TG analysis can be here summarized: mass changes, temperature stability, oxidation/reduction behaviour, decomposition, composition analysis, thermokinetics; whereas by DSC: melting and crystallization behaviour and enthalpy, solid-solid transitions, polymorphism, degree of crystallinity, glass transitions, cross-linking reactions, oxidative stability, purity determination, specific heat capacity and thermokinetics. In this Thesis this technique has been used to:

- Evaluate the influence of the mechanical processing on the activation of the starting raw materials;
- Determine the activation energy for the formation of the main perovskite phase;
- Establish the kinetics of BCZT formation.

The experimental temperature ranges from 25 °C to 1200 °C, while heating rates between 1 °C min^{-1} and 30 C min^{-1}. The studies can be carried out either in an inert atmosphere or in a tuneable flow of chemically active gases. In particular, for this work the experiments have been conducted in air (100ml min^{-1}) into alumina

crucibles, with different heating rates, depending on the final purpose of the analysis (2-5-10 °C min^{-1}), ranging from 25°C to 1100°C.

Figure 4.2.5 TA Instruments Q600 thermobalances (TG/ATD/DSC). High sensitivity microbalance for studies of thermogravimetric (TG), Differential Thermal Analysis (DTA) and Differential Scanning Calorimetry (DSC) of solid materials in general.

4.2.4 Microscopy (TEM, SEM, FESEM)

Scanning Electron Microscopy (SEM) Transmission Electron Microscopy (TEM) and Field Emission Scanning Electron Microscopy (FESEM) [19–21]**,**coupled with EDS (Energy Dispersive X-Ray Spectroscopy), have been used essentially for the main purposes listed as follows:

- Analysing the evolution of particle morphology and size throughout the whole processing (precursors, and powders processed after each step);
- For investigating freshly fractured surfaces of densified ceramics: microstructure grain size, porosity, nature of grain boundaries (transgranular or intergranular fracture);

- To assess the degree of homogeneity and the presence of secondary phases within grains and at triple junctions using backscattering mode and EDS analysis, confirming the maintenance of selected stoichiometry.

Powders and pellets were deposited on a C-based conductive tape. The powders were analysed in general without any other treatment, whereas for the analysis of the pellets, a freshly fractured surface was required to avoid surface alteration after exposure to air. EDS analysis was also performed to verify the homogeneity and the composition of the powder, to assess the presence or absence of contamination and the maintenance of the chosen stoichiometry in powders and densified ceramics until the end of the processing route. In the literature the most widely used method to correctly relate average grain size and ceramic properties is based on the analysis of flat, optically polished and subsequently thermally or chemically etched surfaces. As quantitative relations between the grain size and the properties are not in the focus of our study the grain size determination, that properly done involves the collection of a statistical sample of measurements of typically 1000 measurements in properly polished samples was not carried out in this work. The aspect of the fractured surface, with transgranular or intergranular character, grain morphology and other characteristics of the ceramic microstructure provide alternative information, which is of primary interest in the sintering study we conducted.

In particular, TEM analysis helped to clarify the particle shape of BCZT after the synthesis in the furnace and to evaluate the distance between the rows of grains. As shown in **Figure 4.2.6**, different equipment was used throughout this thesis to thoroughly investigate the system at different length scales.

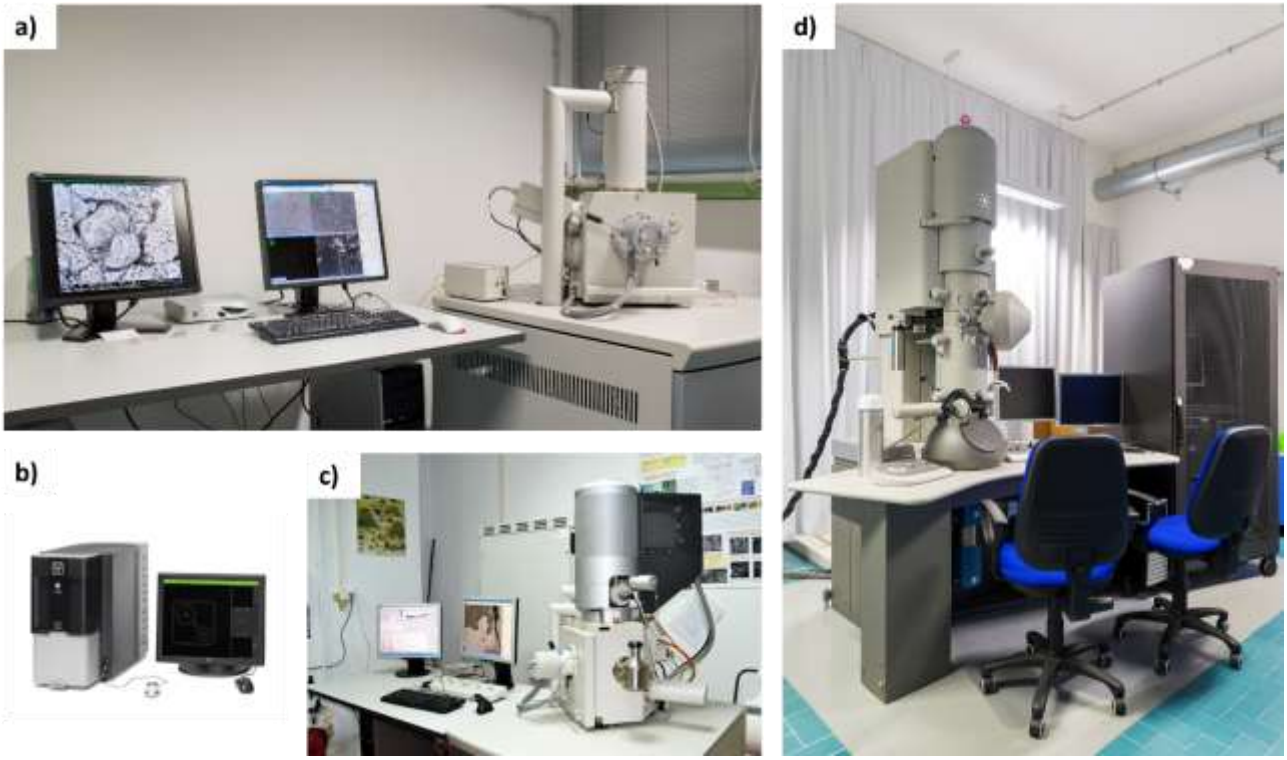

Figure 4.2.6 a) Scanning Electron Microscope (FEI Quanta 200) with variable pressure and high vacuum (High-vacuum, Low-Vacuum and ESEM mode), equipped with EDS Microanalysis - Genesis XM2i - Apollo 10SSD LNfree Detector; **b)** Phenom G2 pro desktop SEM with high brightness CeB6 electron source equipped with optimized the backscatter electron detector (BSED) and detection chain; **c)** Field Emission Scanning Electron Microscopy at ultra-high resolution with Energy Dispersive X-ray spectroscopy (FESEM-EDS), with a FEI NOVA NanoSEM 230 FE-SEM with Apollo 10 EDAX detector; **d)** TEM FEI Tecnai 20 field emission 200kV S/TEM with an X-TWIN objective lens and high brightness field emission electron gun (FEG) optimized for analytical work and equipped with a EDS.

Details on the preparation of the samples measured have been introduced into the experimental part of each corresponding chapter.

4.2.5 Dynamic Light Scattering (DLS)

Dynamic Light Scattering[22–26] is a helpful technique, that in combination with microscopy can help in analyzing the distribution of particles size during the ceramic processing. The particle size distribution of a powder can be obtained from the DLS experimental curve and represented in different ways based on the well-known relationships between intensity, number and volume. The preparation of the sample is a crucial point to have data of good quality. In this work the powder has been pour in water and subjected to ultrasonic bath for 3 minutes to have a well-dispersed suspension, then the measurement has been repeated for five

times. The measurement was conducted at 25°C and started immediately after inserting the cuvette into the instrument (**Figure 4.2.7.)**

Figure 4.2.7 Zetasizer Nano S (Malvern Instruments, United Kingdom).

4.2.6 Crucibles and Furnaces

As already mentioned in Chapter 2, one aspect that should not be underestimated is the material of the crucibles. Given the observed interaction between the alumina crucibles and the platinum sheet, crucibles made of yttria-stabilised zirconia were manufactured in the laboratory specifically for this thesis work and a horizontal furnace was used for high-temperature sintering (**Figure 4.2.8**).

Figure 4.2.8 a) Laboratory made yttria-stabilised zirconia crucibles used for calcination and sintering; **b)**Nabertherm Horizontal Furnace 30-1700°C used for high temperature sintering.

Poling and electromechanical characterization

After the manufacturing process, the ceramic must be poled to become piezoelectric and then prepared for the electromechanical characterization, as shown in **Figure 4.2.9**.

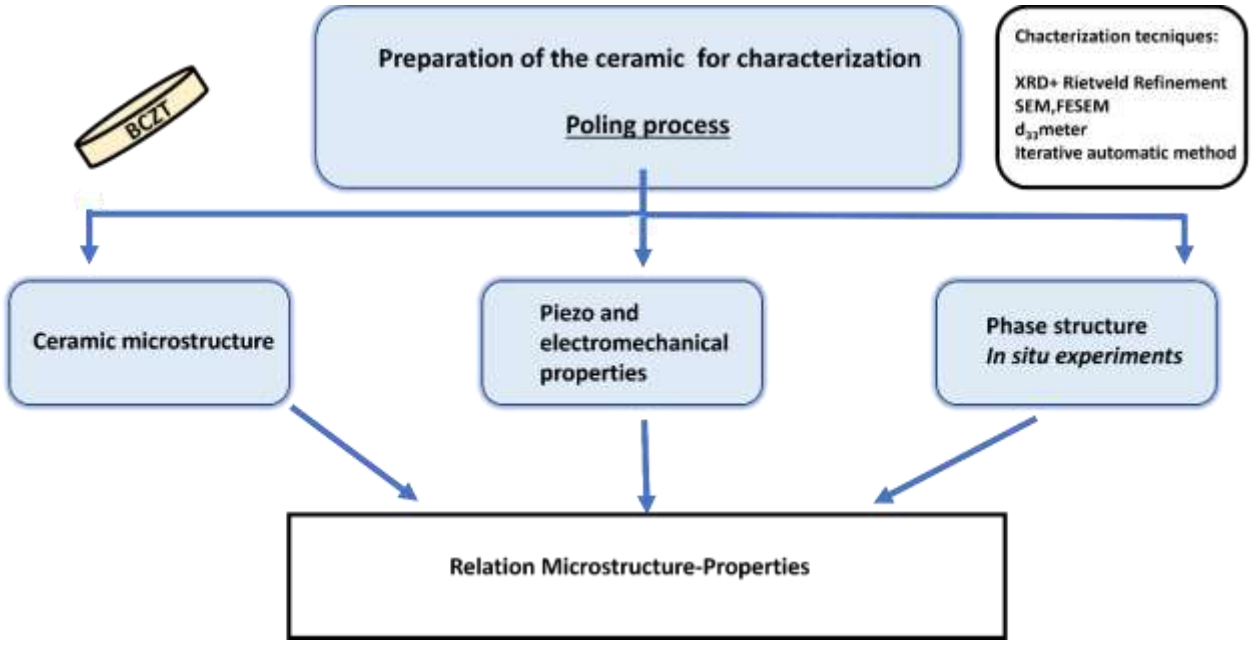

Figure 4.2.9 Post-processing treatments.

Then, the ceramic has been attentively polished to eliminate the cork and then the electrodes have been applied. In this work two methods have been employed:

- Conductive Ag-based paste has been manually applied and then the electrodes have been sintered into an oven at 400°C for 1 hours (**Figure 4.2.10**);
- Sputtering deposition of Au electrodes have been used for *in situ* XRD experiments (temperature/poling), reported in **Figure 4.2.11**).

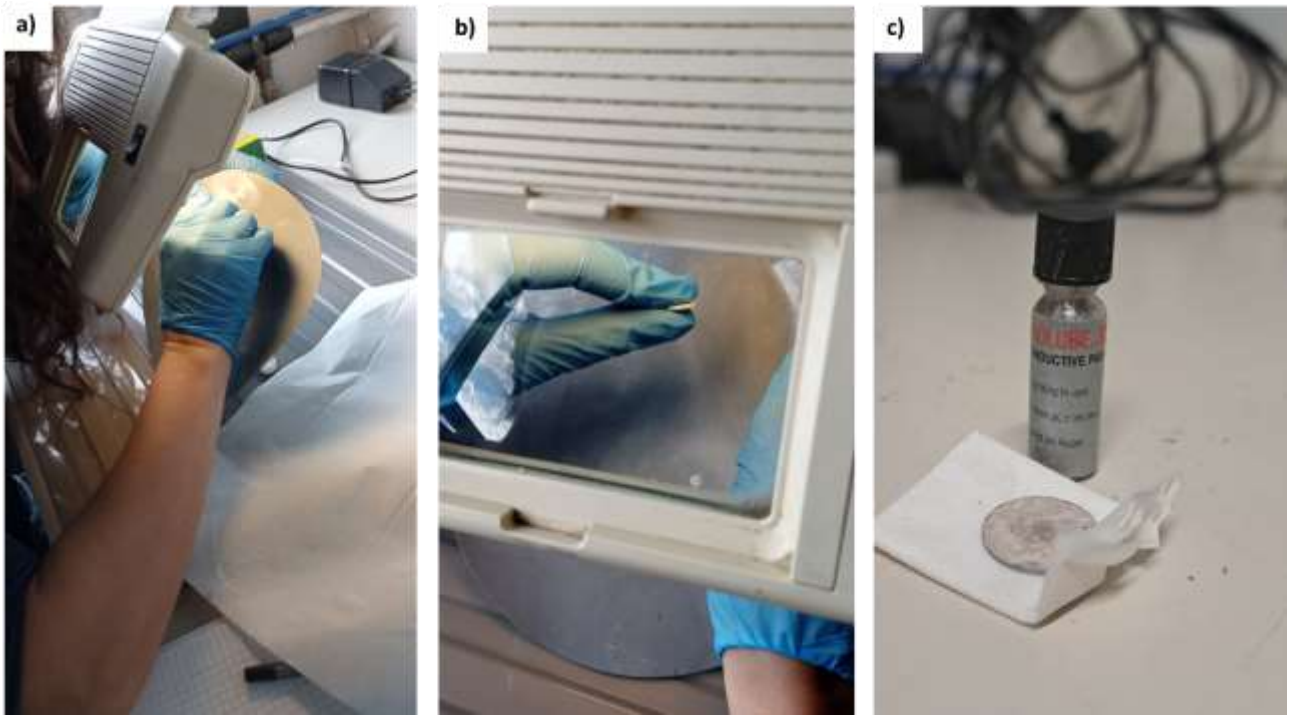

Figure 4.2.10 . a) Checking the correct deposition and the uniformity of the Ag electrodes to ensure that **b)**there is no Ag residue on the edges before the further check of resistance with the multimeter; **c)**pellet after electrodes sintering.

At the end of the process, the electrodes are examined to test the resistance with a multimeter. Finally, the surface area of the electrode can be measured.

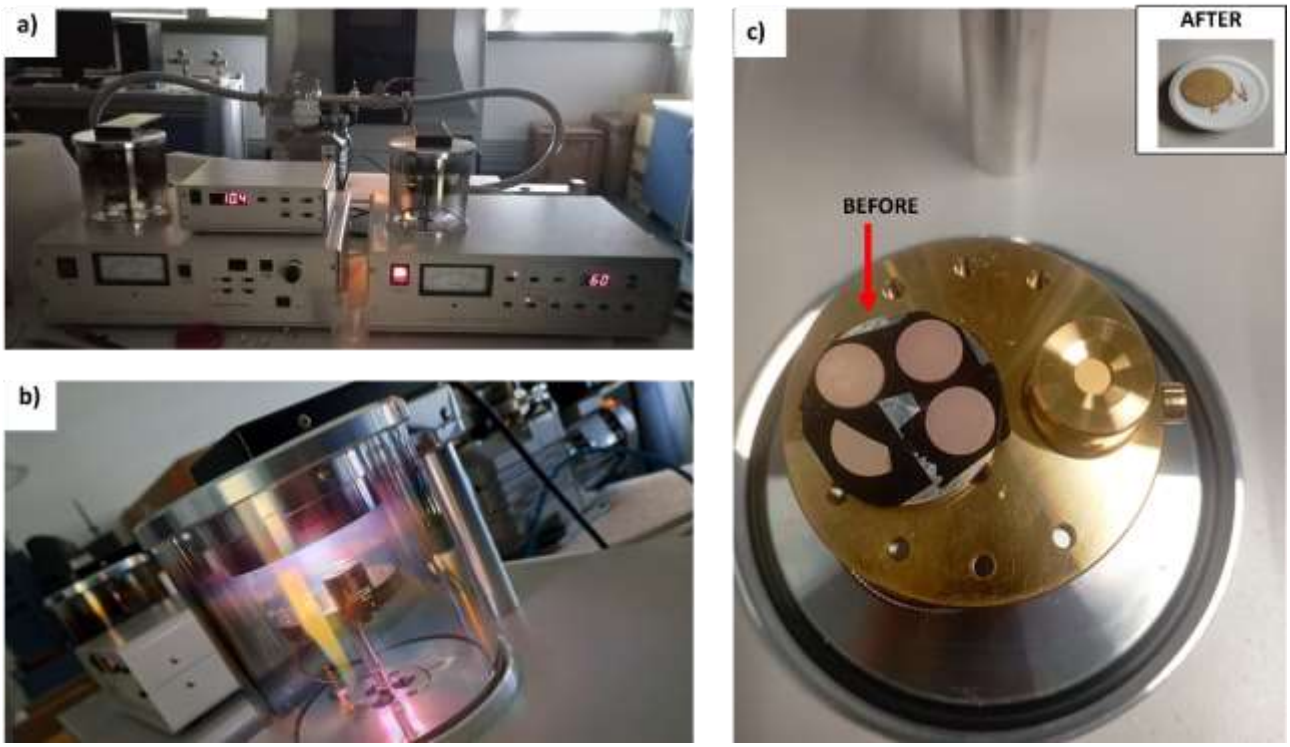

Figure 4.2.11 a) Auto sputter coater (Agar Scientific) equipped with graphite and Au deposition system. Automatic deposition of Au electrodes. The thickness of the layer can be modulated. **b)**detail of the Chamber depositing the Au film, **c)**BCZT ceramics placed in the specimen stub lodged inside the chamber before and after the deposition.

Each deposition method presents its own advantages and issues. On one hand, Ag electrodes deposited by the manual method, after the sintering treatment, are more resistant than the others. On the other hand, the thin layer of Au electrodes allowed one to perform *in situ* poling XRD experiments.

4.2.7 Poling apparatus

For the poling process, two different devices have been used:

- A traditional poling apparatus (**Figure 4.2.12**);
- An innovative device, entirely designed and developed at University of Sassari (PCT/IT2023/050121. WO2023/214441) X-poll cell[27], shown in **Figure 4.2.13**.

The poling set-up, described in **Figure 4.2.12**, was used to perform the ceramic poling at a relatively high temperature in a silicone oil bath. A step-by-step increase of the electric field procedure is required to find

the best setup conditions, whereas the exact voltage to be applied can be known by measuring the thickness of the sample, since electric field and voltage are linked by the following equation:

$$E = \frac{V}{t} \qquad (4.2)$$

Being *E* the electric field, *V* the applied voltage and *t* the thickness of the pellet. In this work the poling has been performed by the Field cooling method: once the sample is placed inside the oil bath, the voltage is applied until it reaches the desired temperature. Finally, the thermostat is turned off and the system cooled to room temperature keeping the same electric field. The poling set-up is described in **Figure 4.2.12**.

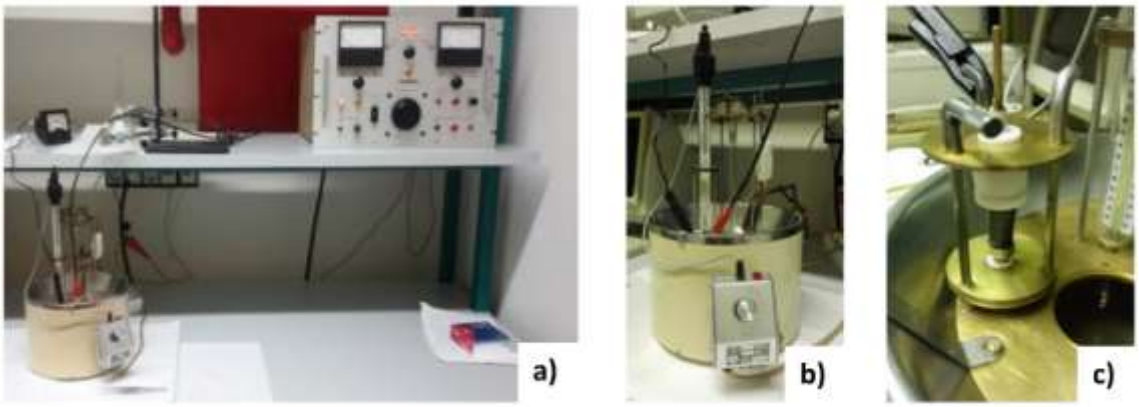

Figure 4.2.12 a) Poling set-up: HV supply; **b)**Thermostatic silicone oil bath; **c)**Sample holder.

The poling patented cell, named X-poll system (**Figure 4.2.13**) was developed at the University of Sassari with the scope of performing *in situ* diffraction experiments of piezoceramics during poling or during the heat treatment using the laboratory available diffractometer. Briefly, this apparatus is composed by: *i)* a cell made of acrylonitrile styrene acrylate (ASA) having a U-shape Cu electrode as upper electrode and a Cu screw as the bottom one. This particular U shape allows the cell to ensure electrical contact and, at the same time, keeps the sample to be targeted by the X-ray beam; *ii)* current generator or power supply; *iii)* ARDUINO temperature control circuit with the heating system power supply.

The current generator, or power supply, is provided by Consort BVBA, EV3330 model with a voltage range from 300 V up to 3000 V. The EV3330 allows one to set the electric field as a function of the time controlling the electric field speed application, choosing the current (from 0 to 300 mA) and power (from 0 to 300 W)

values. EV3330 permits programming different methods, each with 9 steps. Each step can recall the next, providing a flexible multiple-step function for special techniques. The method mode also allows a linear voltage gradient to be programmed for any step as long as the current and/or power limit is not reached.

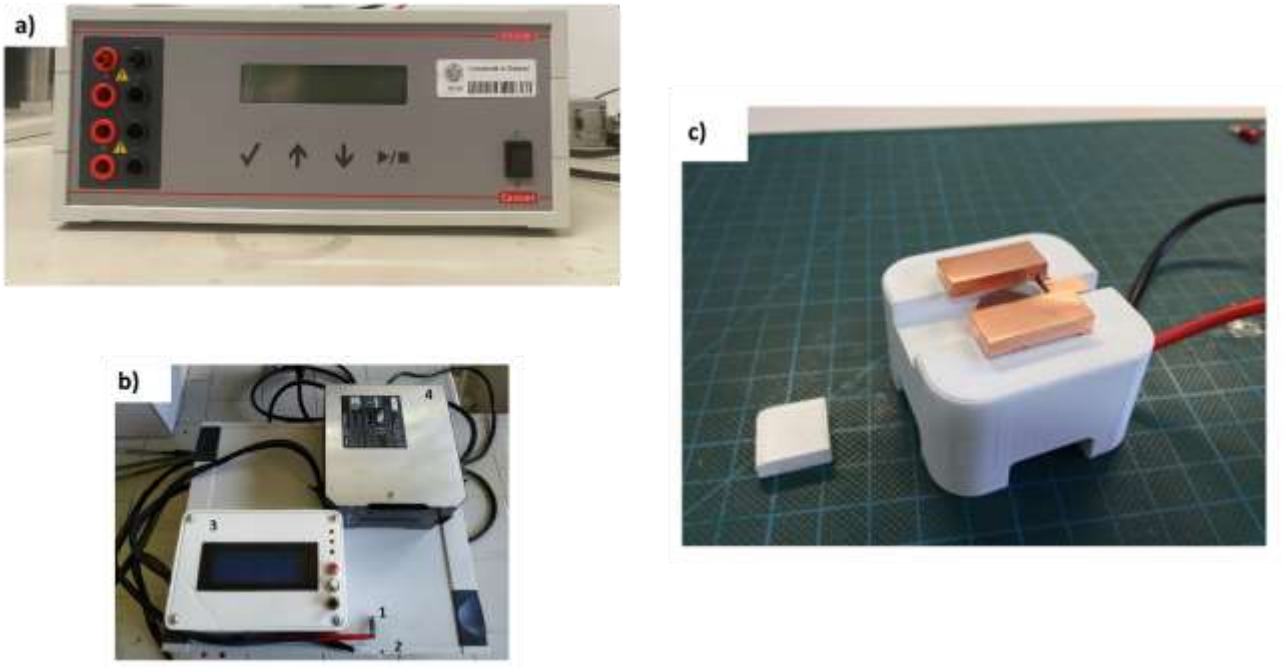

Figure 4.2.13 Images of multifunctional apparatus X-Poll cell.**a)**Current generator or power supply **b)**3 ARDUINO temperature control circuit,4- Heating system power supply. **c)**X-poll cell [27].

4.2.8 Berlincourt d_{33} meter

As stated in Chapter 2, the most reported parameter associated to piezoelectricity is the quasi-static piezoelectric coefficient d_{33}. This coefficient is the most reported in a direct or inverse piezoelectric measurement. The tests were done simply with equipment Berlincourt d_{33} meter (**Figure 4.2.14**) working at low frequency (100 Hz). It can be used for different materials like ceramics, single crystals and polymers of various shapes. The apparatus is composed by two probes, one in top and other in bottom, in which the sample is placed to be measured.

Figure 4.2.14 Berlincourt d_{33} meter working at 100 Hz **a)**Sinocera **b)**CP.

In this work, an automatic iterative method proposed at CSIC [28]graphically summarized in **Figure 4.2.15** has been used for the ceramic characterization. This method overcomes the issues of the high inconsistency of the parameters obtained depending on the number of the samples to be used for the characterization and considering the need of quantifying all material losses. This is done by considering the impedance values of the resonance curve (apparatus shown in **Figure 4.2.16**) instead of just the characteristic frequencies obtained from the resonance curves.

This new methodology: (i) allows to accurately determine all the complex coefficients of poled piezoceramics (advantage 1), (ii) is the only that have been systematically applied to the full set of resonator geometries (only 3) and resonance modes (only 4) needed for the full matrix characterization (advantage 2) and (iii) contains a built-in reliability criterium for each one (advantage 3).

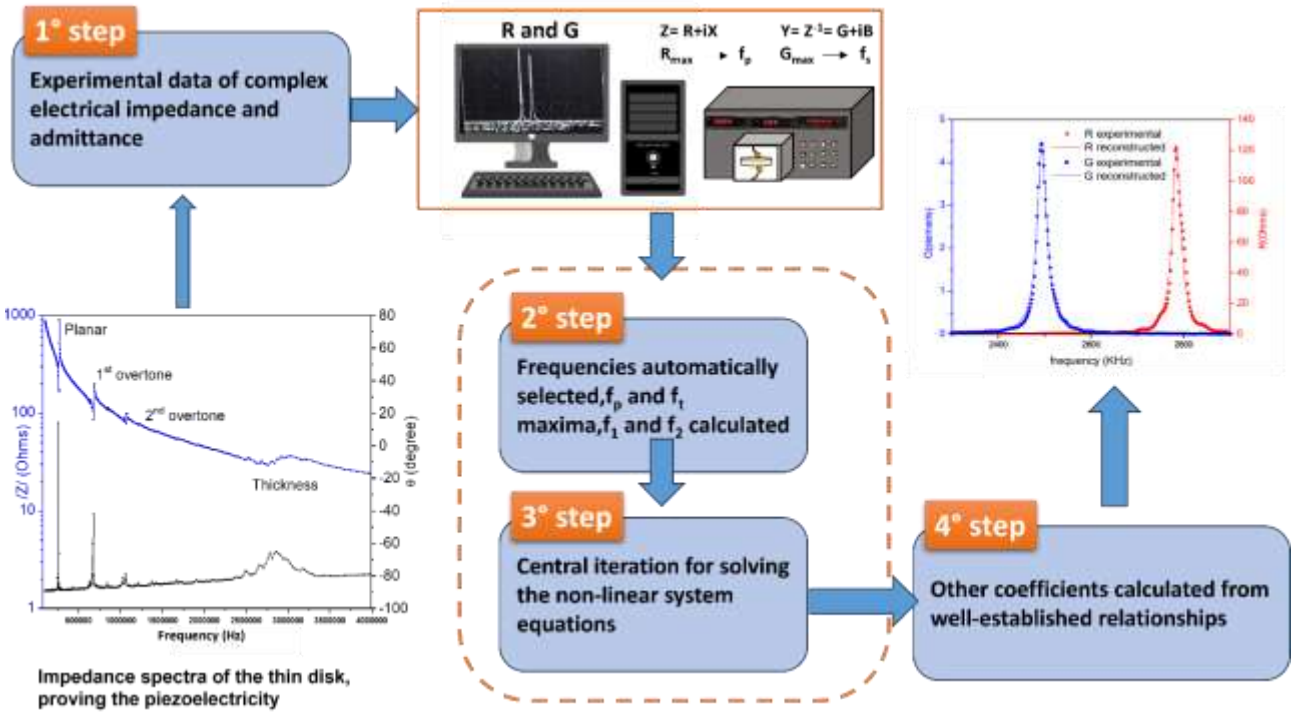

Figure 4.2.15 Flow chart describing the steps of the iterative automatic method for piezoelectric characterization at resonance: i) impedance spectrum collection, ii) calculation of R and G peaks, iii) determination of characteristic frequencies, electromechanical coupling factor and initial material coefficients, iv) set-up of the non-linear system of equations with impedance data and iterative resolution of these to determine the directly obtained material coefficients for the given resonance mode, v)calculation of derived coefficients and, finally, vi) reconstruction of the spectrum with the calculated coefficients to determine the regression factor with the experimental spectrum as a reliability factor of these coefficients.

For the sake of clarity, it should be noted that this program uses an alternative representation of Z* or Y* as a function of the frequency (the traditional one :(/Z/,θ) plots). In this method, instead, peaks of resistance (R) and conductance (G) values are plotted vs. frequency, being Z*=R+iX (Z= impedance, R= Resistance, X= Susceptance) and Y*=G+iB (where Y= Admittance, G= Conductance and B= Reactance).

Basically, this method consist of 3 main steps: (i) The experimental data of complex impedance (Z*) or admittance (Y*=1/Z*) are introduced in the program to calculate the R and G plot vs. frequency, (ii) from this plot, the frequencies are selected automatically (maximum G value gives the resonance frequency= fs and maximum R value gives the antiresonance frequency= fp), a peripherical interaction is performed to determine f_1 and f_2; (iii) in this step the experimental impedance data at these automatically selected four frequencies are introduced into the analytical solution of the wave equation corresponding to the resonance to set a system of four non-linear equations . At each point of the central iteration, the system of non-linear

of equations is solved (Smit's method with automatically selected f_1 and f_2) and the solution compared with the one of the previous steps, until a convergence criterion is fulfilled, and the complex coefficients obtained.

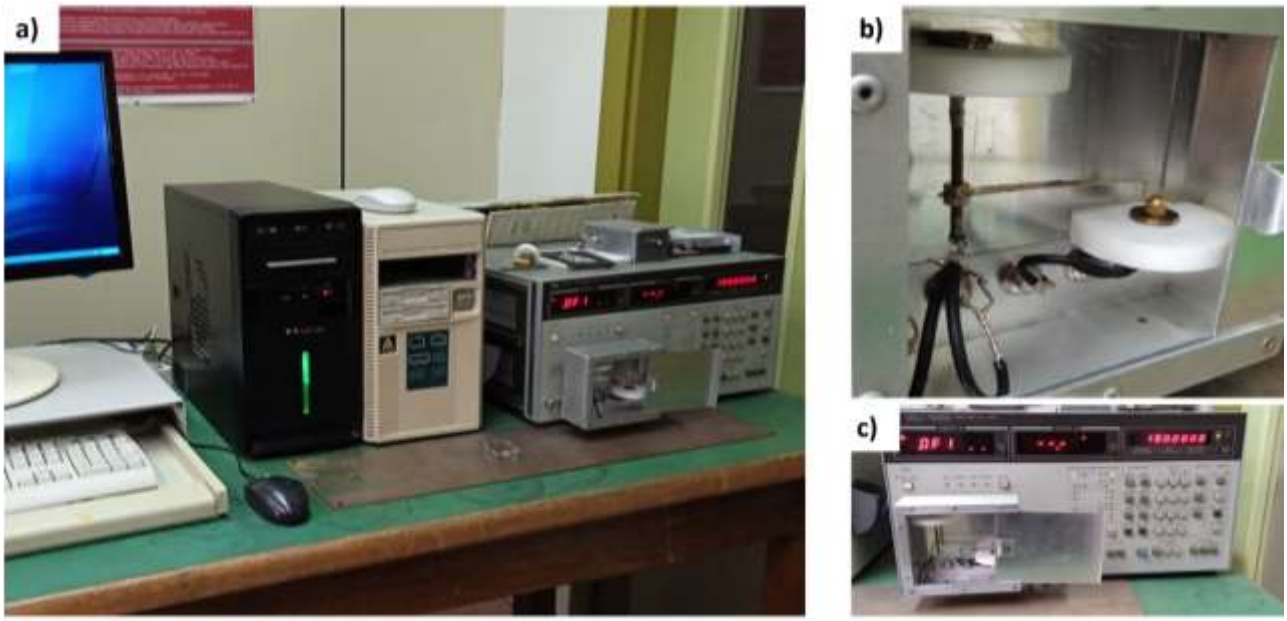

Figure 4.2.16 a) Impedance analyser (Model HP4192A LF, 5Hz-13MHz) for measurements and calculations in thickness and planar modes, both analysers connected to PCs with Windows XP OS; **b)** and **c)** details of sample holder.

4.3 Bibliography

1. Suryanarayana, C. Mechanical Alloying and Milling. *Prog. Mater. Sci.* **2001**, *46*, 1–184, doi:10.1016/S0079-6425(99)00010-9.

2. Delogu, F.; Mulas, G.; Schiffini, L.; Cocco, G. Mechanical Work and Conversion Degree in Mechanically Induced Processes. *Mater. Sci. Eng. A* **2004**, *382*, 280–287, doi:10.1016/j.msea.2004.05.047.

3. Baláž, P.; Achimovicová, M.; Baláž, M.; Billik, P.; Zara, C.Z.; Criado, J.M.; Delogu, F.; Dutková, E.; Gaffet, E.; Gotor, F.J.; et al. Hallmarks of Mechanochemistry: From Nanoparticles to Technology. *Chem. Soc. Rev.* **2013**, *42*, 7571–7637, doi:10.1039/c3cs35468g.

4. Tan, D.; García, F. Main Group Mechanochemistry: From Curiosity to Established Protocols. *Chem. Soc. Rev.* **2019**, *48*, 2274–2292, doi:10.1039/c7cs00813a.

5. Tsuzuki, T. Mechanochemical Synthesis of Metal Oxide Nanoparticles. *Commun. Chem.* **2021**, *4*, doi:10.1038/s42004-021-00582-3.

6. Liu, X.; Li, Y.; Zeng, L.; Li, X.; Chen, N.; Bai, S.; He, H.; Wang, Q.; Zhang, C. A Review on Mechanochemistry: Approaching Advanced Energy Materials with Greener Force. *Adv. Mater.* **2022**, *34*, 1–30, doi:10.1002/adma.202108327.

7. Zhang, Y.; Xu, J.; Zhang, Z.; Zhao, L.; Li, M.; Li, M.; Zhao, D.; Zhong, G.; Hu, X.; Zhang, X.; et al. Mechanochemical Synthesis of Nanostructured and Composite Oxide Ceramics: From Mechanisms to Tailored Properties. *Int. J. Appl. Ceram. Technol.* **2023**, 1–39, doi:10.1111/ijac.14598.

8. Hammond, C. The Basics of Crystallography and Diffraction. In *The basics of crystallography and diffraction*; 2015.

9. Jones, J.L. The Use of Diffraction in the Characterization of Piezoelectric Materials. *J. Electroceramics* **2007**, *19*, 67–79, doi:10.1007/s10832-007-9048-z.

10. Harold P. Klug, L.E.A. *X-Ray Diffraction Procedures: For Polycrystalline and Amorphous Materials, 2nd Edition*; 1974;

11. Hammond, C. The Basics of Crystallography and Diffraction (Vol. 21). In *International Union of Crystallography texts on crystallography.*; 2015.

12. Http://Pd.Chem.Ucl.Ac.Uk/Pdnn/Pdindex.Htm.

13. Altomare, A.; Cuocci, C.; Giacovazzo, C.; Moliterni, A.; Rizzi, R. QUALX: A Computer Program for Qualitative Analysis Using Powder Diffraction Data. *J. Appl. Crystallogr.* **2008**, *41*, 815–817, doi:10.1107/S0021889808016956.

14. Lutterotti, L.; Pillière, H.; Fontugne, C.; Boullay, P.; Chateigner, D. Full-Profile Search–Match by the Rietveld Method. *J. Appl. Crystallogr.* **2019**, *52*, 587–598, doi:10.1107/S160057671900342X.

15. Lutterotti, L.; Scardi, P. Simultaneous Structure and Size-Strain Refinement by the Rietveld Method. *J. Appl. Crystallogr.* **1990**, *23*, 246–252, doi:10.1107/S0021889890002382.

16. Rietveld, H.M. A Profile Refinement Method for Nuclear and Magnetic Structures. *J. Applyied Crystallogr.* **1969**, *2*, 65–71, doi:10.1107/S0021889869006558.

17. Gualtieri, A.F.; Riva, V.; Bresciani, A.; Maretti, S.; Tamburini, M.; Viani, A. Accuracy in Quantitative Phase Analysis of Mixtures with Large Amorphous Contents. the Case of Stoneware Ceramics and Bricks. *J. Appl. Crystallogr.* **2014**, *47*, 835–846, doi:10.1107/S160057671400627X.

18. Lafuente, B.; Downs, R.T.; Yang, H.; Stone, N. The Powder of Databases: The RRUFF Project. In

Highlights in Mineralogical Crystallography; 2016; p. 201 ISBN 9783110417043.

19. Kannan, D.M. Scanning Electron Microscopy: Principle, Components and Applications. *Textb. Fundam. Appl. Nanotechnol.* **2018**, 82–92.

20. Zhou, W.; Apkarian, R.; Wang, Z.L.; Joy, D. Fundamentals of Scanning Electron Microscopy (SEM). *Scanning Microsc. Nanotechnol. Tech. Appl.* **2007**, 1–40, doi:10.1007/978-0-387-39620-0_1.

21. Cosslett, V.E. Introducing the Electron Microscope. *Nature* **1963**, *198*, 820–821, doi:10.1038/198820a0.

22. J.W.B.R. Strutt On the Scattering of Light by Small Particles. *London, Edinburgh, Dublin Philos. Mag. J. Sci.* **1871**, *41*, 447–454., doi:doi.org/10.1080/1478644710864050.

23. Sandhu, R.; Singh, N.; Dhankhar, J.; Kama, G.; Sharma, R. Dynamic Light Scattering (DLS) Technique, Principle, Theoretical Considerations and Applications. *Nanotechnological Biochem. Tech. Assess. Qual. Saf. Milk Milk Prod.* **2018**, 135–137.

24. Yin, L. *Dynamic Light Scattering*; 2012; ISBN 9780813817316.

25. Yin, L. Dynamic Light Scattering. In *Nanotechnology Research Methods for Foods and Bioproducts*; Wiley, 2012; pp. 145–161.

26. Chu, B. Soft Matter Characterization. In *Dynamic light scattering.*; 2008.

27. Antonio Iacomini, Davide Sanna, Sebastiano Garroni, Andrea Melis, Pier Nicola Labate, Alberto Mariani, Stefano Enzo, G.M. Polarisation and Measurement Cell for Piezoelectric Ceramic Materials 2023.

28. L. Pardo, K.B. Properties of Ferro-Piezoelectric Ceramic Materials in the Linear Range: Determination from Impedance Measurements at Resonance. In *Multifunctional Ferroelectric Materials.Processing and Properties*; L.Pardo and J. Ricote, Ed.; 2010; p. Volume 140.

5 The effect of the milling tool contamination on the piezoelectric properties of the final BCZT ceramic

5.1 Introduction

As stated in the SOTA of this thesis, the ball milling conditions chosen to process both precursors and calcined powders have a great influence on the final microstructure of the ceramic leading to optimal or degraded electromechanical properties. As already pointed out, Thakur and colleagues investigated the influence of the grinding medium (yttrium-stabilised zirconia) on the electrical properties of undoped $BaTiO_3$, demonstrating that the contamination due to these milling materials altered both the dielectric behaviour and the bulk conductivity [1]. As deducible from the work of Ciomaga et al, the optimal set-up for mechanically activating precursors is a key factor to obtain a good microstructure and properties[2]. Furthermore, as demonstrated by Di Loreto and colleagues, a too energetic ball-milling after calcination can lead to a decrease in piezoelectric properties [3]. Based on these premises, the influence of the jar material and the energy transferred to the powder on the final properties was evaluated in this thesis. Firstly, a stainless-steel jar with a Shaker ball mill (Spex8000 Mixer-Mill) was used. Subsequently, it was decided to use a tungsten carbide vessel using the same Spex equipment. Although these preliminary results were neither optimal nor conclusive, this step was fundamental for this thesis work because it allowed us to overcome the problems that arose and to develop a contamination-free powder processing. For the sake of brevity, only the most relevant results on powders and final ceramics will be presented in this section.

Since no cases have been found in the literature reporting the effects of contamination from the jar used on BCZT ceramics, the effect of Fe contamination was assimilated to an intentional Fe-doping. In this sense, Fe^{3+} incorporates into the main lattice [4] leading to a cubic structure of BCZT at room temperature [5] and shifting the tetragonal-cubic phase boundary toward lower temperature [6]. Fe^{3+} doping in BCZT also results in a gradual transition from typical ferroelectrics to even quantum paraelectrics [7]. All the reported works evidenced the reduction in grains size from a maximum of 20 μm until a minimum of 2 μm [4]. The presence of ferromagnetism, due to the interaction between the Fe^{3+} ions and oxygen vacancies, represents a further

sign of that contamination [8]. To the best of our knowledge, no works on the effect of tungsten-doping have been reported in the recent literature.

5.2 Materials and methods

5.2.1 Materials

Ceramic powders of nominal composition $(Ba_{0.85}Ca_{0.15})(Ti_{0.90}Zr_{0.10})O_3$ (abbreviated as $BC_{15}TZ_{10}$) were prepared by a solid-state route starting from a stoichiometric mixture of $BaCO_3$ (Sigma Aldrich, St. Louis, MO, USA,>99%), $CaCO_3$ (Fluka, >99%), TiO_2 (Sigma Aldrich, St. Louis, MO, USA>99.9%) and ZrO_2 (Alfa Aesar, >99%).

5.2.2 Powders and Ceramics processing

The raw materials were dried at 100°C overnight, weighted according to the nominal composition indicated above and mixed. Once mixed, these raw materials were mechanically treated by ball-milling (BM) using a Shaker apparatus (SPEX8000) at 875 rpm in isopropanol as liquid medium, using a stainless-steel jar and a tungsten carbide jar for 6 h and 5 h respectively with a BPR of 1. The slurry obtained has been dried at 80°C for 24 h. The as-obtained powder has been then calcined into a closed alumina crucible at 1200°C for 4 h with a heating rate of 3°C/min. After the calcination step, the powder has been ball-milled with the same apparatus and the same vial used for the first ball milling, for increasing times (0,2, 8h,16 h).

The as-obtained powders were finely ground in a mortar and mixed with few drops of polyvinyl alcohol (PVA) solution (3 wt.%) before compacting into a disk by using a hydraulic press (220 kg/cm^2 for 30 min). The pellets have been then sintered with an intermediate debinding step at 600°C for 2 h and a final plateau of 1450°C for 2h with a heating rate of 3°C/min. The density was measured by using geometrical method. The sintered disks were then reduced in thickness by polishing down to ~ 1mm and prepared for the electromechanical characterization. Silver paste was attached on both surfaces of the thin disks and sintered at 400°C for 1 hour to get the electrodes. After that, samples were poled in thickness under a field of 25 kV/cm at 40°C for 30 min in a silicone oil bath, followed by field cooling (FC) to room temperature.

5.2.3 Structural and Microstructural Characterization

Structural investigations were conducted using a SMARTLAB diffractometer with a rotating anode source of copper (λCu Kα = 1.54178 Å) working at 40 kV and 100 mA. The spectrometer is equipped with a graphite monochromator and a scintillation tube in the diffracted beam. Quantitative analysis of the crystalline phases and structure determinations were performed with the MAUD software (Materials Analysis Using Diffraction), a Rietveld extended program [10]. The fresh fracture surface morphology of the samples was studied by using Quanta FEI 200 scanning electron microscope (SEM). Morphology on the calcined particles was analysed using a TEM FEI Tecnai 20 field emission 200kV S/TEM with an X-TWIN objective lens and high brightness field emission electron gun (FEG).

5.2.4 Electromechanical characterization

The quasi-static d_{33} piezoelectric charge coefficient was measured with a Berlincourt d_{33}-meter at 100Hz. Complex impedance, modulus and phase, as a function of the frequency, the so-called resonance curve, was measured with an impedance analyser (HP 4192A-LF) at the, electrically induced, radial extensional resonance of the thickness poled thin disks. An automatic iterative method was used in the analysis of the resonance curves to determine the complex electromechanical, elastic and dielectric properties of the ceramics, together with the electromechanical coupling factor [9].

5.3 Results and Discussion: Stainless-steel jar

5.3.1 Processing and Characterization of the Powders

Microstructure and morphology of the particles upon calcination have been characterized by TEM. The analysis confirmed the characteristic BCZT particle shape, as shown in Figure 1a. After calcination the presence of agglomerates can be observed at low magnification (**Figure 5.3.1(a)**), while the boundaries of the particulates are clear (**Figure 5.3.1(b)**) and the powder size from TEM image is around 500-700 nm. Crystalline nature of the material is better evidenced at higher magnification (**Figure 5.3.1(c)**) where the presence of crystalline planes can be confirmed.

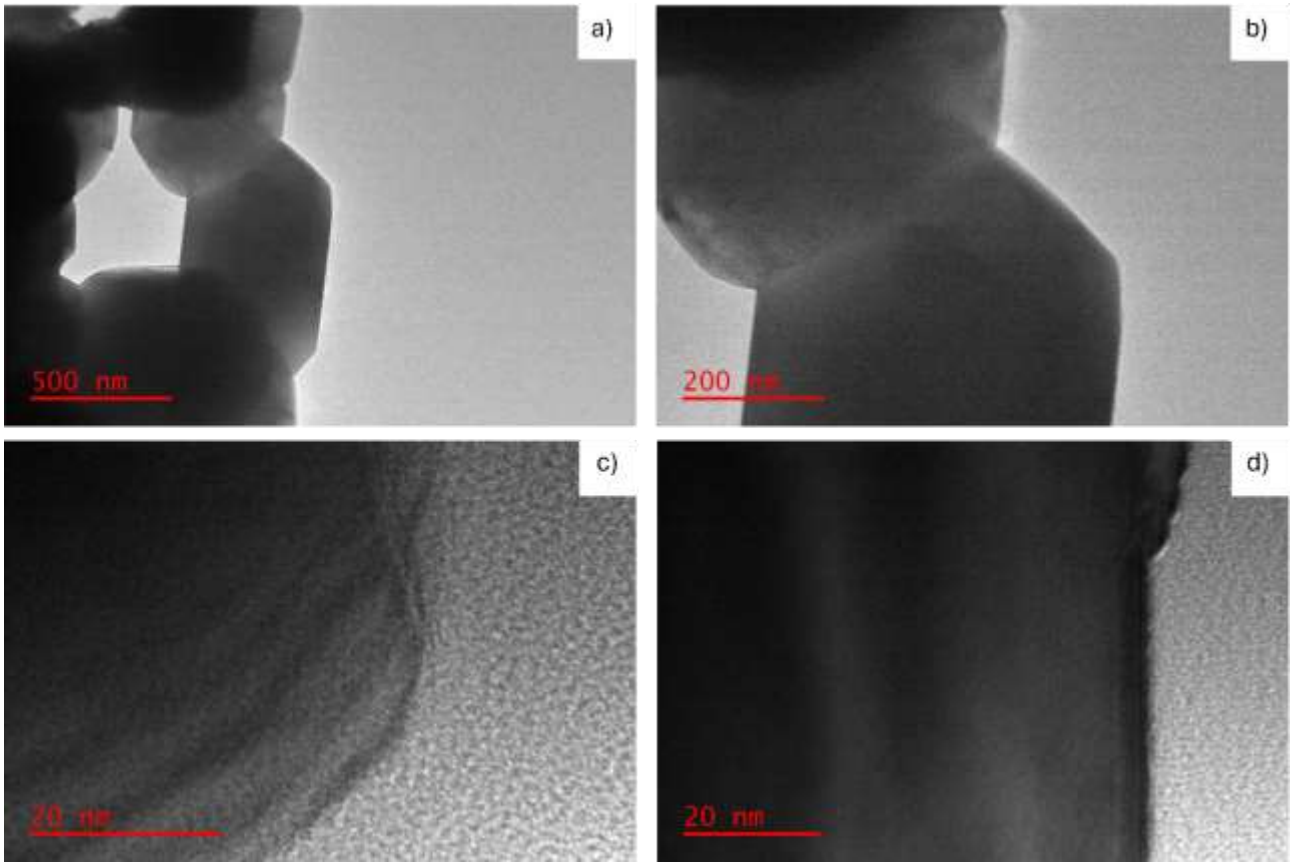

Figure 5.3.1 TEM image of calcined BCZT powders: **a)** BCZT particles morphology, **b)** necks between particles **c)**, **d)**crystalline planes.

The high crystallinity and the presence of agglomerates (up to 1.5 µm), as shown in Figure 5.3.1(a) and Figure 5.3.2(a) , support the necessity to use a second ball milling step to better refine the particles sizes of the calcined system. As shown in Figure 5.3.2(b) after only 2 h of ball-milling after calcination the necks between the particles are broken and single particles are distinguishable (0.4 µm-0.5 µm).

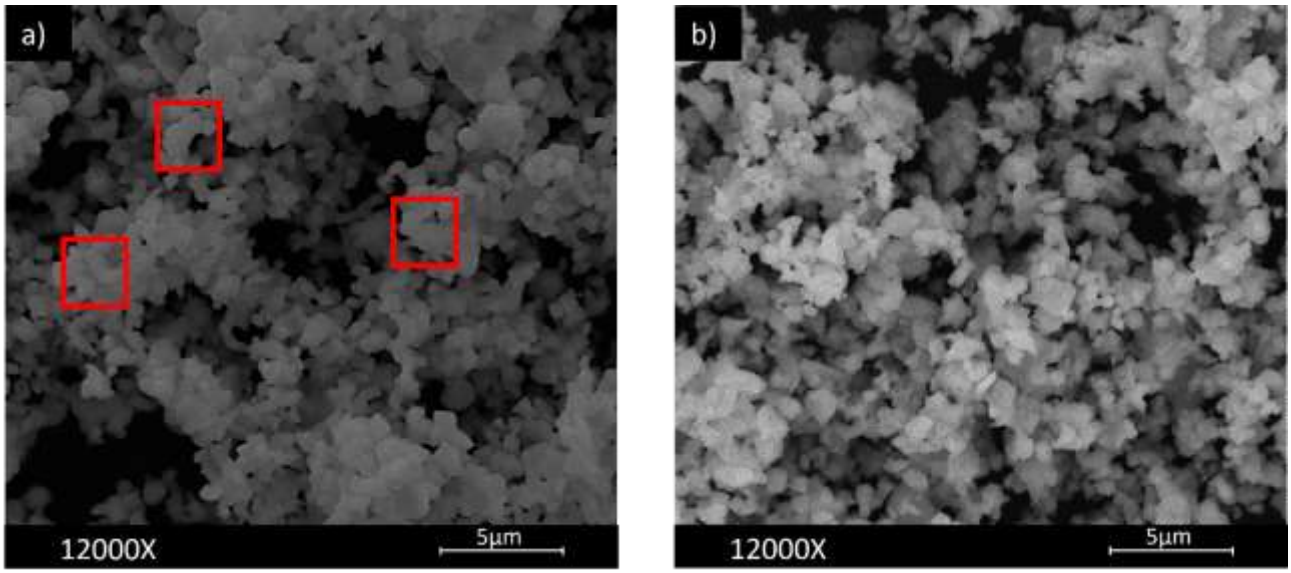

Figure 5.3.2 a) In the areas indicated with red squared inserts the necks between the particles and agglomerates formed after calcination are clearly visible, **b)**distinguishable particles obtained after the second ball-milling(0.5-0.7µm).

The EDX spectroscopy performed on as calcined (0h BM) and ball-milled for 2,8 and 16-hours powders, revealed slightly deviations of Ba and Ti from calculated atomic percentages for the specifical composition chosen. Indeed, it can be observed an increase of Ba at. % (except for 8h of BM) and a decrease of Ti at. % content increasing the ball milling time from 2h to 16 h (**Figure 5.3.3a**). It emerged that Fe contamination (**Figure 5.3.3b**), coming from the stainless-steel after 16 h of ball-milling, reached almost the theoretical Ca content (estimated to be around the 2 at. %). For the sake of clarity, residual Fe content (0.3 at. %) was already present in the powders after the first ball milling step.

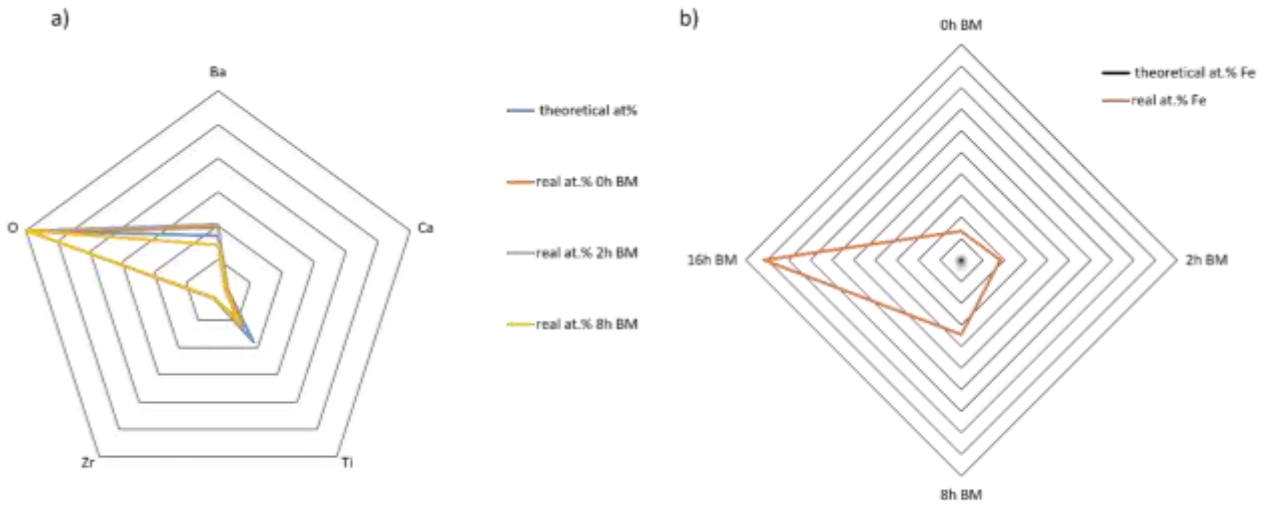

Figure 5.3.3 EDS quantitative results. **a)** Theoretical and real elements atomic % deviations from the chosen composition reported as mean values of five measurements each as a function of increasing ball-milling times (0h, 2h, 8h, 16 h). **b)** Fe contamination as a function of ball-milling time.

Due to the high level of Fe contamination detected in the powders milled for 8 and 16 hours, it was decided to prepare the pellets only with the calcined and 2 hours ball milled powders.

5.3.2 Processing and Characterization of the Ceramics

As shown in **Figure 5.3.4**, the XRD patterns acquired on the densified ceramic (1450°C for 2h) presented a tetragonal *P4mm* BCZT phase accompanied by secondary phases or unreacted precursors all belonging to the system (later found to be unreacted ZrO_2 and $CaTiO_3$).

It should be noted that the tetragonal distortion of the *P4mm* BCZT phase of the pellets prepared with calcined powder was estimated to be about c/a=1.003 with c= 4.0151 Å. By increasing the ball milling time up to 2h, the tetragonality of the BCZT lattice decreases becoming cubic c/a≃ 1.000 with c= 4.0150 Å. In fact, Fe does not form other secondary phases, but diffuses into the main lattice leading to disappearance of tetragonal distortion.

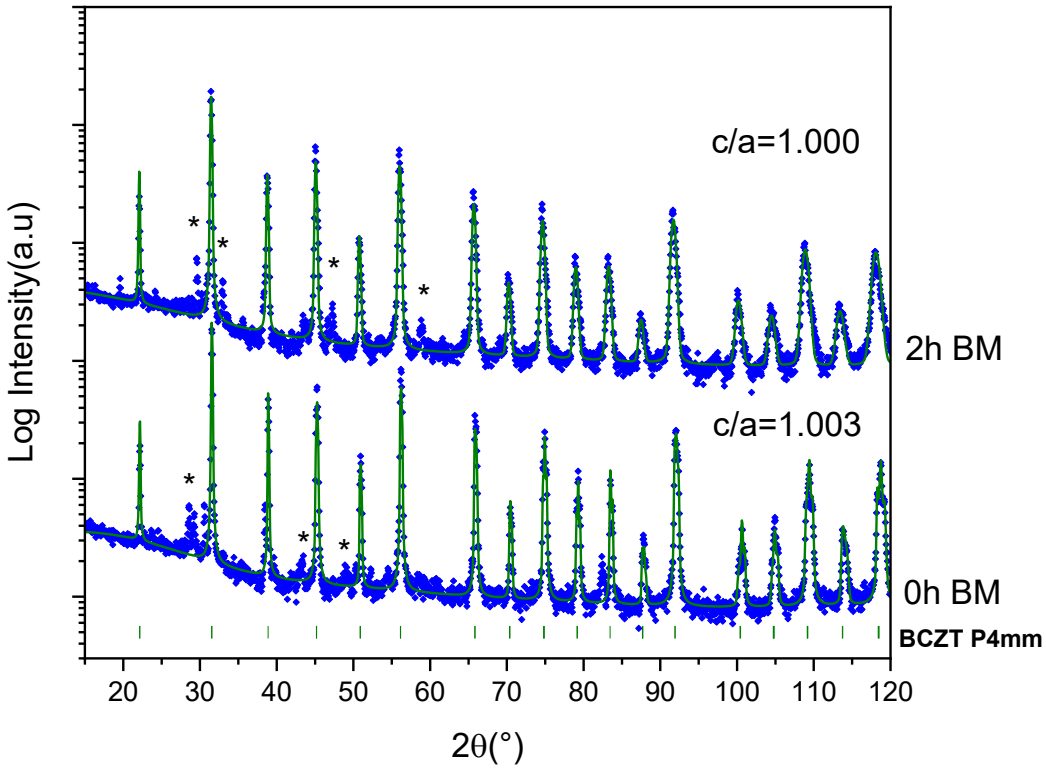

Figure 5.3.4 Rietveld Refinement of XRD diffraction pattern of ceramics produced with calcined powder subjected to a second ball-milling of 2h using a stainless-steel jar. Coloured bars and full coloured lines refer to *P4mm* BCZT reflections(olive). *Symbol corresponds to reflection of unreacted zirconia at lower angles and $CaTiO_3$ at higher angles respect to the main perovskite. Experimental points are indicated with blue dots.

As reported in **Figure 5.3.5**, both the pellets obtained showed a dense microstructure with a prevalent transgranular fracture, reaching high density values of 5.26g/cm^3 corresponding to 91% of theoretical density calculated for the specific composition. In Figure 3b, is possible to evince the presence of small grains in the ceramics bulk (about 3-4µm), whose dimensions are in perfect accordance with the literature regarding the Fe-doped system [4].

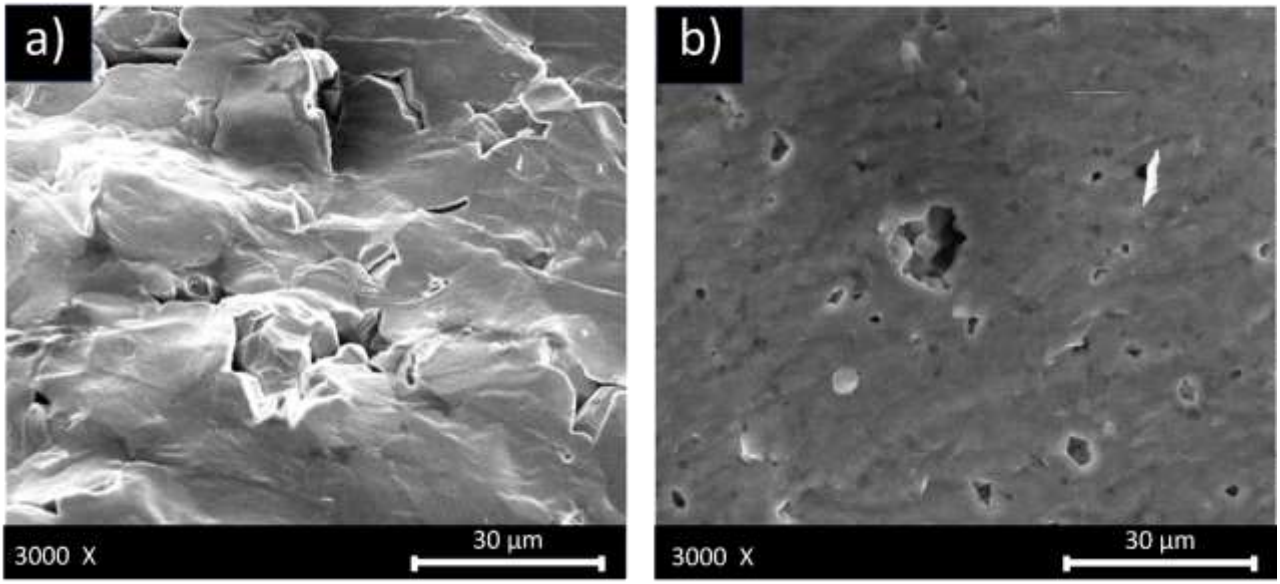

Figure 5.3.5 SEM micrographs of fractured surfaces of **a)** pellet prepared with as calcined powders and **b)** pellet prepared with calcined powders ball-milled for 2 h. In **Figure b** is possible to note small grains (inside the pore) of about 3-4 µm.

5.3.3 Electrical Characterization

Considering the XRD results, the poling process was only performed on the pellet prepared using the as calcined powders. The obtained electromechanical coupling factor and the frequency number of the planar resonance, together with the regression factor ($\mathbb{R}^2$) of the reconstructed to the experimental spectra ((R, G) plot in **Figure 5.3.6**). Piezoelectric, elastic and dielectric coefficients, including mechanical quality factors and dielectric loss factors, have been reported in **Table 5.3.1**.

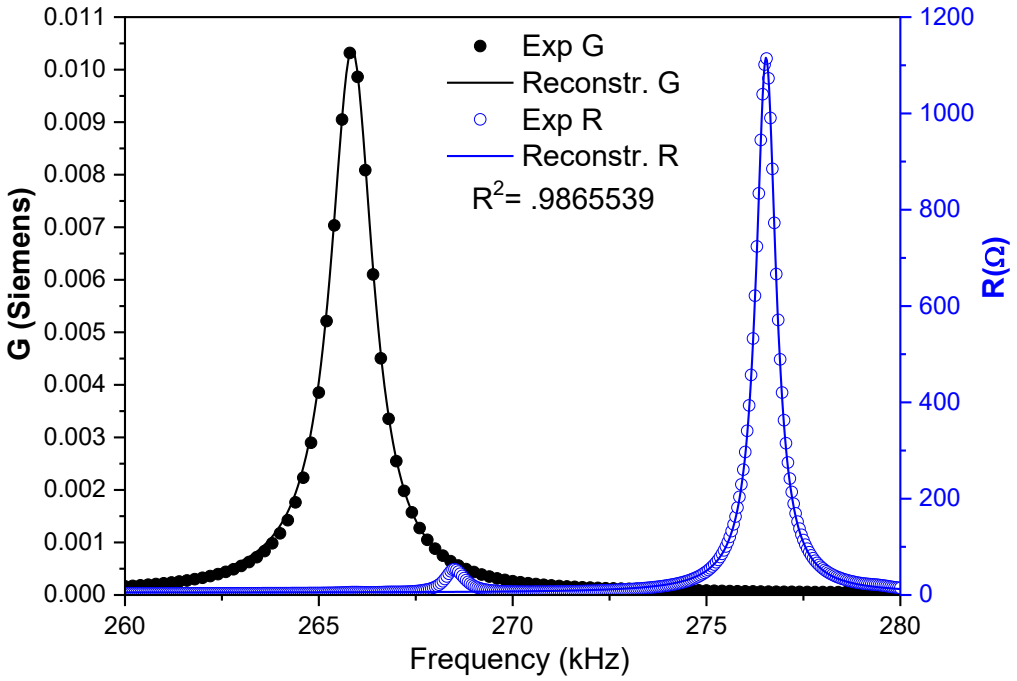

Figure 5.3.6 Equivalent representation of the impedance spectrum, (R, G) plot, used in the calculation of material coefficients by the iterative automatic method. Symbols are the experimental data and lines are the reconstructed peaks after coefficients calculation. Fundamental radial mode of resonance of a thin disk of BCZT ceramics prepared with as-calcined powders. It should be highlighted that precursors were previously treated with the same milling apparatus for 6 h (stainless-steel jar).

The electromechanical characterization evidences that the Fe contamination coming from the stainless-steel vial leads to low piezoelectric coefficient (d_{33}= 90 pc/N) compared to those reported for the same composition[2] together with a low electromechanical coupling factor(K_p= 14.59%).

Table 5.3.1 Some relevant material coefficients obtained from the radial mode characterisation of BCZT ceramics prepared with as calcined powders. [1] $c'^{p}_{11} = s^{E}_{11}/s^{E}_{12}$

Properties	
Density (g/cc)	5.20
Relative density (%)	90
d_{33} (pC/N)	90
R^2	0.9866
k_p (%)	14.59
N_p(kHz.mm)	2870
d'_{31} (pC/N)	-38.2814
$Q_p(d_{31})$	204
c'^{p}_{11} [1] (10^{10}N m^{-2})	9.5634
Q_m	202
ε'^{T}_{33} at 1 KHz	3300
tanδ at 1 KHz	0.1

5.4 Results and Discussion: Tungsten Carbide jar

5.4.1 Processing and Characterization of the Ceramics

Unlike what observed for Fe contamination, XRD analysis of the ceramics prepared using a tungsten carbide jar (**Figure 5.4.1**) revealed the formation of a secondary phase not belonging to the system, identifiable as Wolframate ($BaWO_4$). The amount of the $BaWO_4$ tetragonal phase increasing at increasing milling time. The pellets prepared from the as-calcined powders (without second ball milling) show a small tetragonal distortion with c = 4.0139 Å and c/a = 1.002. With 2h of ball-milling after calcination, the lattice of the BCZT *P*4*mm* becomes pseudo cubic with c = 4.0150 Å and c/a =1.001, but the amount of $BaWO_4$ increases to 2wt.%. After 8 h of ball-milling, a further decrease of tetragonal distortion was observed. The main BCZT lattice becomes perfectly cubic with c/a = 1.000 and c= 4.0138 Å. The XRD analysis reveals a higher amount of $BaWO_4$ tetragonal phase (about 7wt.%) and another unidentified secondary phase. Considering the absence of tetragonal distortion, the poling process was only possible for pellets produced from calcined, unmilled, powders. It must be underlined that due to the high conductivity the poling process resulted challenging.

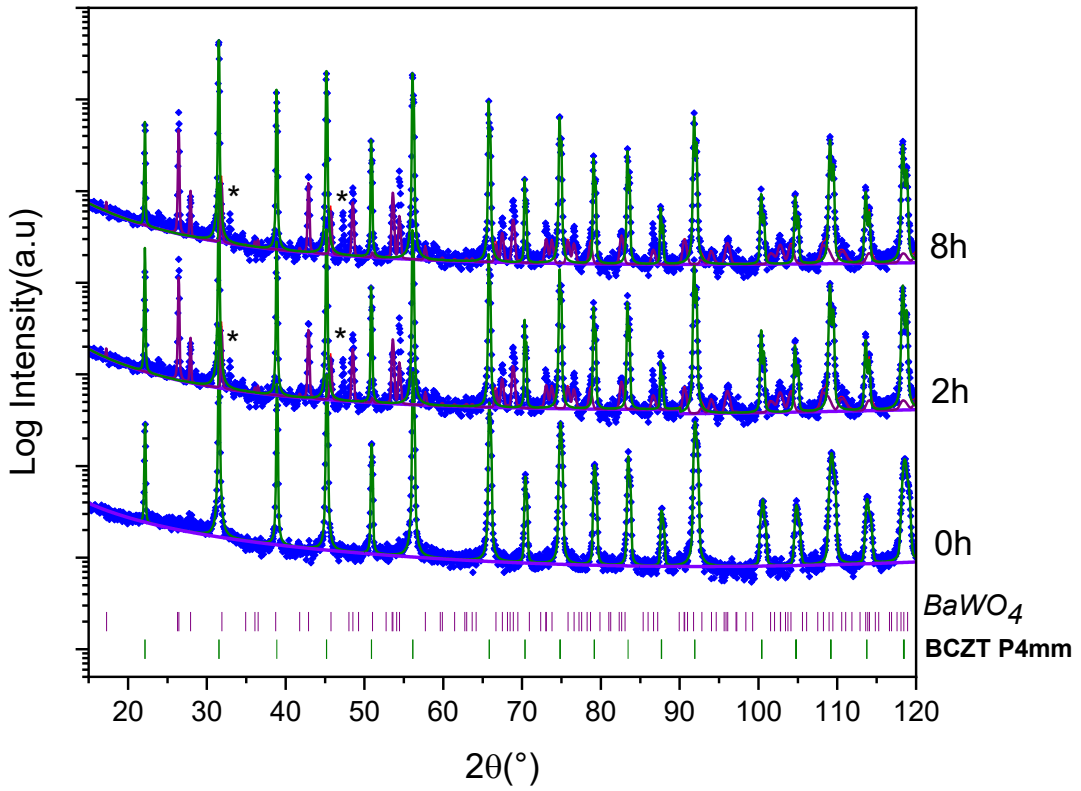

Figure 5.4.1 Rietveld Refinement of XRD diffraction pattern of ceramics produced with calcined (0h) powder subjected to a second ball-milling of 2h and 8h using a tungsten carbide jar. Coloured bars and full coloured lines refer to P4mm BCZT reflections(olive), and $BaWO_4$ (Wolframate-purple). *Symbol corresponds to reflection of $CaTiO_3$ at higher angles respect to the main perovskite.Experimental points are indicated with blue dots.

As reported in **Figure 5.4.2** all the ceramics obtained using 0h (**Figure 5.4.2 (a)**),2 h (**Figure 5.4.2 (b)**), and 8h **Figure 5.4.2 (c)** ball-milled powders, showed a transgranular fracture, reaching a relative density of 83, 88, 93%, respectively. As noticeable in **Figure 5.4.2(b)** (inside the pore) small grains were observed (about 5 µm).

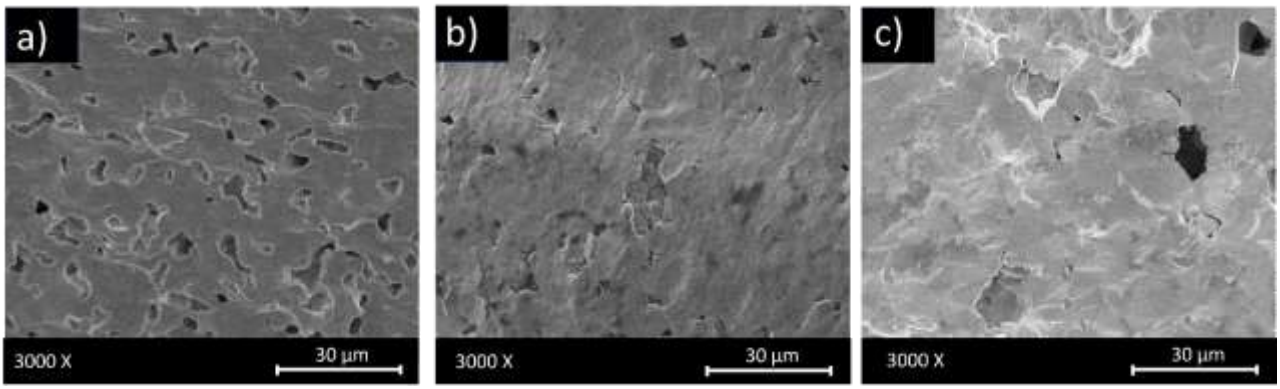

Figure 5.4.2 SEM micrographs of fractured surfaces of a) pellet prepared with as calcined powders (0h BM) and b) pellet prepared with powders ball-milled for 2 h and 8 h. In Figure b is possible to note a small grain inside a pore of about 5 µm.

5.4.2 Electrical Characterization

As in the previous case, only the ceramic prepared with as calcined powders was subjected to the poling process. Also for these ceramics, the obtained electromechanical coupling factor and the frequency number of the planar resonance, together with the regression factor ($\Re^2$) of the reconstructed to the experimental spectra ((R,G) plot in **Figure 5.4.3**). Piezoelectric, elastic and dielectric coefficients, including mechanical quality factors and dielectric loss factors have been reported in **Table 5.4.1.**.

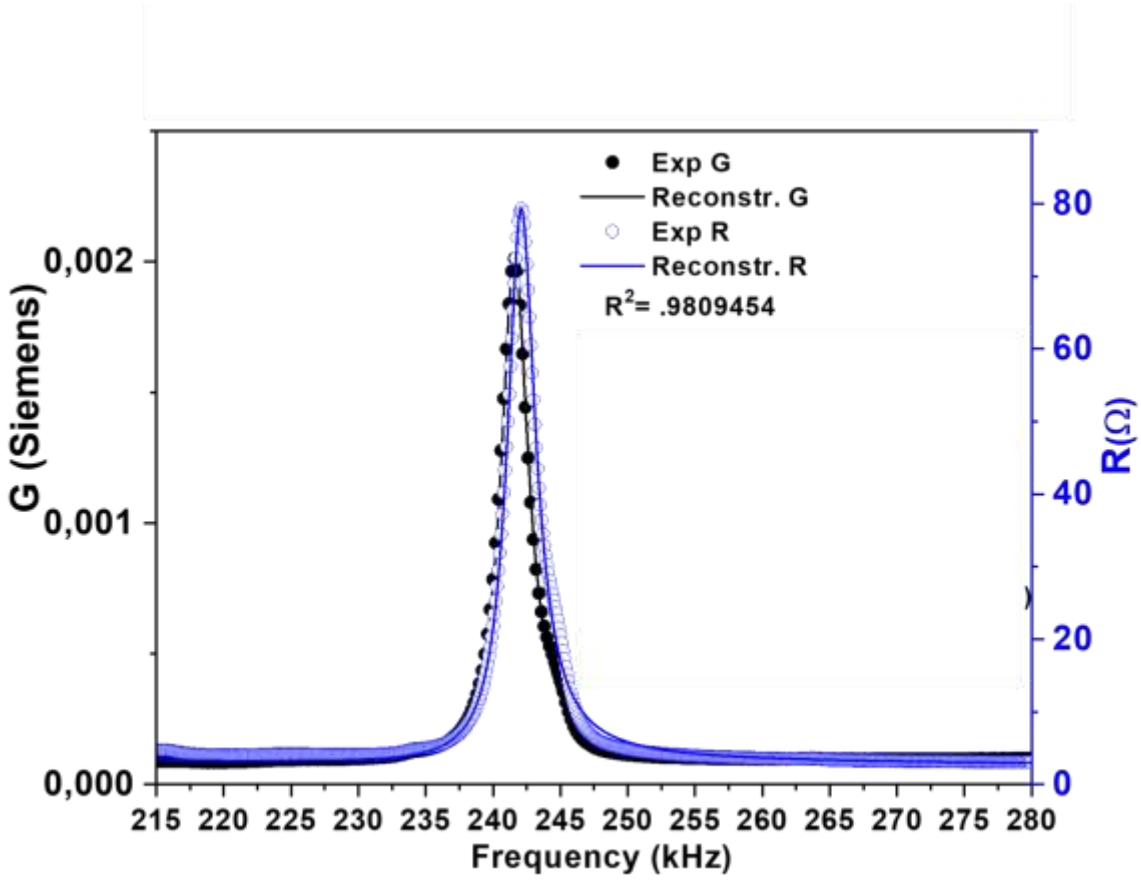

Figure 5.4.3 Equivalent representation of the impedance spectrum, (R, G) plot, used in the calculation of material coefficients by the iterative automatic method. Symbols are the experimental data and lines are the reconstructed peaks after coefficients calculation. Fundamental radial mode of resonance of a thin disk of BCZT ceramics prepared with as-calcined powders. N.B. Precursors were previously treated with the same milling apparatus for 5 h (tungsten carbide jar).

The electromechanical characterization evidences that the Fe contamination coming from the stainless-steel vial leads to low piezoelectric coefficient (d_{33}= 89 pc/N) compared to those reported for the same composition[2] together with a low electromechanical coupling factor(K_p= 7.21%).

Table 5.4.1 Some relevant material coefficients obtain from the radial mode characterisation of BCZT ceramics prepared with as calcined powders. [1] $c'^{p}_{11} = s^{E}_{11}/s^{E}_{12}$

Properties	
Density (g/cc)	5.07
Relative density (%)	88
d_{33} (pC/N)	89
R^2	0.98095
k_p (%)	7.21
N_p(kHz.mm)	2874.26
d'_{31} (pC/N)	-26.4448
$Q_p(d_{31})$	49
c'^{p}_{11} [1] (10^{10}N m^{-2})	8.9921
Q_m	97.74
ε'^{T}_{33} at 1 KHz	3996
tanδ at 1 KHz	0.015

5.5 Conclusions

Results confirmed that the ball-milling set-up has a great impact on the ceramics microstructure and electromechanical properties. The level of contamination coming from the vial material indicate that milling tool materials have to be carefully chosen to obtain a non-contaminated starting powder. Despite the high sintering temperatures (1450°C), these results indicate that a too energetic ball-milling leads to small grain size in the final ceramic. $BC_{15}TZ_{10}$ ceramics processed from ball-milled precursors, using two different material jars (stainless-steel and tungsten carbide), showed not optimal electromechanical properties with a poor d_{33}=90 pC/N and low K_p=7.21 and 14.59 %.

5.6 Bibliography

1. Thakur, O.P.; Feteira, A.; Kundys, B.; Sinclair, D.C. Influence of Attrition Milling on the Electrical Properties of Undoped-BaTiO3. *J. Eur. Ceram. Soc.* **2007**, *27*, 2577–2589, doi:10.1016/j.jeurceramsoc.2006.10.013.

2. Ciomaga, C.E.; Curecheriu, L.P.; Lukacs, V.A.; Horchidan, N.; Doroftei, F.; Valois, R.; Lheureux, M.; Chambrier, M.H.; Mitoseriu, L. Optimization of Processing Steps for Superior Functional Properties of (Ba, Ca)(Zr, Ti)O3 Ceramics. *Materials (Basel).* **2022**, *15*, doi:10.3390/ma15248809.

3. Di Loreto, A.; Frattini, A.; Stachiotti, M.G. Influence of Post-Calcination Grinding on the Properties of Ba0.85Ca0.15Zr0.1Ti0.9O3 Lead-Free Piezoceramics. *Mater. Lett.* **2017**, *191*, 69–72, doi:10.1016/j.matlet.2017.01.034.

4. Gao, M.; Ge, W.; Li, X.; Yuan, H.; Liu, C.; Zhao, H.; Ma, Y.; Chang, Y. Enhanced Dielectric and Energy Storage Properties in Fe-Doped BCZT Ferroelectric Ceramics. *Phys. Status Solidi Appl. Mater. Sci.* **2020**, *217*, 1–9, doi:10.1002/pssa.202000253.

5. Abid, A.; Islam, S.S.; Khanuja, M.; Jin, L.; Wei, X.; Shur, V.Y. Synthesis and Characterization of Fe Doped BCZT Piezoceramic. *AIP Conf. Proc.* **2020**, *2276*, doi:10.1063/5.0026153.

6. Ge, W.; Gao, M.; Wu, C.; Fang, Y.; Liu, C.; Zhao, H.; Yuan, H. Fe-Doping as a Universal Phase Boundary Shifter for BCZT Ceramics across the Morphotropic Phase Boundary. *J. Electroceramics* **2021**, *47*, 67–78, doi:10.1007/s10832-021-00265-4.

7. Gong, B.; Huang, F.; Shao, Y.; Lei, L.; Liu, L.; Wang, J.; Yan, S.; Lu, X.; Zhu, J. Multiferroic Properties and Magnetoelectric Coupling of Fe-Doped (Ba0.7Ca0.3)TiO3-Ba(Zr0.2Ti0.8)O3 Ceramics. *Phys. Status Solidi Appl. Mater. Sci.* **2020**, *217*, 1–9, doi:10.1002/pssa.201900826.

8. Zhang, Y.; Deng, H.; Si, S.; Wang, T.; Zheng, D.; Yang, P.; Chu, J. Band Gap Narrowing and Magnetic Properties of Transition-Metal-Doped Ba0.85Ca0.15Ti0.9Zr0.1O3 Lead-Free Ceramics. *J. Am. Ceram. Soc.* **2020**, *103*, 2491–2498, doi:10.1111/jace.16924.

9. Alemany, C.; González, A.M.; Pardo, L.; Jiménez, B.; Carmona, F.; Mendiofa, J. Automatic Determination of Complex Constants of Piezoelectric Lossy Materials in the Radial Mode. *J. Phys. D. Appl. Phys.* **1995**, *28*, 945–956, doi:10.1088/0022-3727/28/5/017.

10. Lutterotti, L.; Pillière, H.; Fontugne, C.; Boullay, P.; Chateigner, D. Full-Profile Search–Match by the Rietveld Method. *J. Appl. Crystallogr.* **2019**, *52*, 587–598, doi:10.1107/S160057671900342X.

6 A sustainable Pechini-modified sol-gel synthesis of Barium Calcium Zirconium Titanate ($BC_{10}TZ_{15}$)

6.1 Introduction

As deeply discussed in Chapter 3, the whole processing route for BCZT samples, and particularly the synthesis step, have a great influence on the ceramic final microstructure, which is closely related to the electromechanical properties. Moreover, since the processing temperatures required for the solid-state route are extremely high (up to 1300°C for the synthesis step and up to 1500°C for the sintering), different strategies are needed to overcome this critical barrier. Therefore, a low temperature synthesis that consents to allow a better stoichiometric control and to monitor/modulate the microstructure, particles and grains size distribution, is required. In this view, the sol-gel technique can be a promising alternative, as largely demonstrated in several works on BCZT material [1,2].

In the sol-gel technique, the ceramic precursors are mixed in solution, permitting an optimum mixing at a lower dimensional scale (colloidal), a more homogeneous composition and a consequent better control of particle size leading to a drastic drop of synthesis temperatures. Actually, as stated in Chapter 2, there is a deep correlation between the electromechanical properties and the complex microstructure of the material (ceramic structure (mm size) , ceramic microstructure (microns size) ceramic, domain configuration (submicron size) and crystal lattice (Å size), including composition (solid solution), type of crystal structure and crystal defects, its order or disorder in the solid solution) [3].

However, these syntheses usually require expensive reagents and careful control of the procedure [4,5]. In this sense, temperature and pH need a continuous check-up due to their strong influence on the reproducibility of the synthesis and the solubility of metal precursors. Additionally, if not properly controlled, their alterations can lead to the formation of solid precipitates with the consequent deviations from the desired stoichiometry. This drawback can be solved introducing appropriated chelating and esterifying agents.

The chelating agent commonly used in the Pechini method is the citric acid (CA). On the one hand it is cheap, available and permits a good control of particles morphology. On the other hand, it has a strong pH dependency that makes more complicated to control the synthesis[4].

In the modified Pechini method other chelating agents are used: lactic and glycolic acids, and EDTA (e(thylene)d(iamine)t(etraacetic)a(cid))([5]. The chelating agent prevents the metal segregation in the product, which is a consequence of the interaction between the metal ions in solution, since it allows the rate of hydrolysis of the alkoxide to be controlled by replacing a portion of the alkoxy group with the ligand. Chelation is fundamental to the gelling process and the final compound is influenced by the structure of the gel. [6]. EDTA, with respect to citric acid, is less sensitive to pH, has 4 carboxylic groups for polyesterification, and in the BCZT synthesis case, limits the formation of the undesired barium carbonate [7]. Concerning the esterifying agents, ethylene glycol is one of the most used in sol-gel synthesis, which, however, exhibits high renal, cardiac and pulmonary toxicity due to its metabolites, such as glycolaldehyde, glycolic acid and oxalic acid [8,9]. In contrast, the employment of glycerol as an esterifying agent, as substituted for ethylene glycol, has several advantages, such as low toxicity, low cost, high availability and high boiling point and low vapour pressure, like ionic liquid. It can therefore be considered a "green" reagent [10,11].

The first use of glycerol in the sol-gel synthesis was reported by Aziguli *et al*. [12], who highlighted the correlation between the improvement of the electrical properties of the material and the addition of glycerol in the synthesis. Its introduction significantly enhances the homogeneity of the microstructure and allows to increase the grains dimensions of densified materials.

Studies on the impact of esterifying agent and of chelating agent emerge in the literature. The role of glycerol [12] and Citric acid and EDTA are indagate [5–7,13], but there are no studies about the synthesis of BCZT using glycerol and EDTA simultaneously . In this work, a combination of glycerol and EDTA is used to assess whether these sol-gel agents could act in synergy to further improve final microstructure homogeneity and control of grains growth of the BCZT processed.

6.2 Materials and methods

6.2.1 Materials

Barium carbonate (CAS 513-77-9; 99%), calcium acetate (CAS 5743-26-0; 99%), zirconium (IV) butoxide (CAS 1071-76-7) and titanium tetraisopropoxide, or TTIP (CAS 546-68-9; 97%) were mixed in stoichiometric proportion according to the chosen composition $(Ba_{0.85}Ca_{0.15})$ $(Zr_{0.10}Ti_{0.90})$ O_3, $BC_{15}TZ_{10}$. In addition, for the sol-gel synthesis, EDTA (CAS 60-00-4; 99.4%), glycerol (CAS 56-81-5; 99.5%) and ammonia (CAS 7664-41-7) were employed. To compare the effect of combined glycerol/EDTA, another analogous synthesis was conducted, substituting the EDTA with citric acid (CA) (CAS 77-72-9; 99.5%).

6.2.2 Powders and Ceramics processing

Two different reactions were conducted at the same time in two different beakers: the first one starting from barium-calcium (BC) and the second one using zirconium-titanium organic precursors (ZT). The products obtained were subsequently merged to obtain the BCZT (**Figure 6.2.1**). As preliminary step, the solvent (H_2O) was heated at 60°C. Later, EDTA was added in both beaker systems and after its solubilization, barium carbonate and calcium acetate were added in the BC beaker and zirconium butoxide and TTIP in the ZT one.

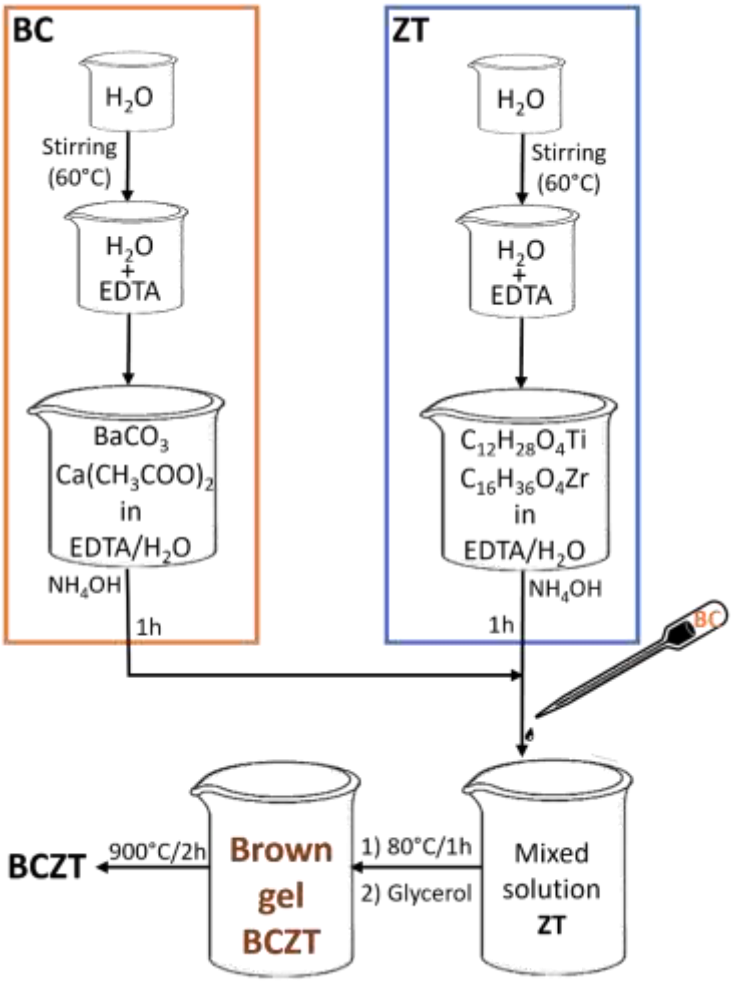

Figure 6.2.1 Flow-chart of the synthesis process.

After 30 minutes, an ammonium solution was added to the two systems. The BC solution was gradually poured in the ZT solution, in a controlled way, 1 hours later the ammonium addition. Subsequently, the system was annealed at 80°C for 1 hour. To promote the BCZT gel formation, glycerol was added to the solution, obtaining a brown gel, which was calcined in the muffle (model NEYO series 2), at 900 °C for 2 hours with a heating ramp of 5 °C/min. Two different syntheses were conducted in this work: glycerol-EDTA ($BCZT_{EDTA}$) and glycerol-CA ($BCZT_{CA}$).

The BCZT powder obtained was then mixed with few drops of PVA solution (3% wt.) and pressed into disk-shape pellets by using a uniaxial press (220 Kg/cm^2 for 30 min). The as-obtained green bodies were sintered by using a horizontal oven (Nabertherm) with an intermediate debinding step performed at 600°C for 2 hours,

followed by a final sintering plateau at 1400°C for 2 hours. Bulk densities were measured by employing a geometrical method.

The sintered ceramics were then reduced in thickness by polishing down to 1 mm of thickness. The silver paste was deposited on both main surfaces, and then sintered to obtain the Ag electrodes (400°C/1 h).

The samples were poled in thickness under an electric field of 15 kV/cm for 30 minutes at 50°C in a silicone oil bath, followed by a field cooling to room temperature.

6.2.3 Structural and microstructural characterization

The structural (XRD) analyses were conducted by a Bragg–Brentano rotating anode diffractometer (Smartlab Rigaku) equipped with a copper source ($Cu_{K\alpha}$ = 1.54178 Å). Data were acquired in the 2θ angular range from 10° to 120°, with a step size of 0.05 and with a fixed dwell time of 4 s. The XRD patterns were numerically refined by the Rietveld method using the MAUD software [14].

After the poling process, the quasi-static piezoelectric coefficient (d_{33}) was measured using a Berlincourt d_{33}-meter at 100 Hz (Sinocera YE2730).

6.2.4 Electromechanical characterization

Complex impedance, modulus and phase, as a function of the frequency, the so-called resonance curve, was measured with an impedance analyser (HP 4192A-LF) at the, electrically induced, radial extensional resonance of the thickness poled thin disks. An automatic iterative method was used in the analysis of the resonance curves to determine the complex electromechanical, elastic and dielectric properties of the ceramics, together with the electromechanical coupling factor[15].

The fresh fracture surface morphology of the samples was studied by Field Emission Scanning Electron Microscopy using a Phenom Pro G2 SEM microscope (Thermo Scientific, USA) operating at a beam voltage of 5 kV in a backscattering mode and an Electron Microscope (FEI Quanta 200).

6.3 Results and discussion

6.3.1 Processing and characterization of the Powders

Two different syntheses were carried out in this work: glycerol-EDTA (principal route: $BCZT_{EDTA}$) and glycerol-CA ($BCZT_{CA}$). The XRD patterns of the $BCZT_{EDTA}$ and $BCZT_{CA}$ powders are reported in **Figure 6.3.1.** The X-ray diffraction pattern of $BCZT_{EDTA}$ powders shows a pure BCZT tetragonal phase (*P4mm*), with c/a= 1.004 and c =4.025 Å. The XRD analysis of $BCZT_{CA}$ calcined powders, reveals the majoritarian presence of BCZT *P4mm* tetragonal phase with a low amount of impurities. In this case, the tetragonal distortion is slightly lower c/a= 1.003, with c = 4.026 Å.

From these analyses emerge that the effect of EDTA as a complexing agent seems to stabilise the ions in solution better than citric acid, regardless of the esterifying agent type. Moreover, it appears that the use of EDTA enabled a substantial improvement in the syntheses in terms of yield and of reduction of the synthesis temperature, allowing to obtain the BCZT P4mm pure tetragonal phase at only 900°C. This result is a real improvement in synthesis conditions, since in the literature similar systems are obtained using temperatures starting from 1000 °C [3,16,17].

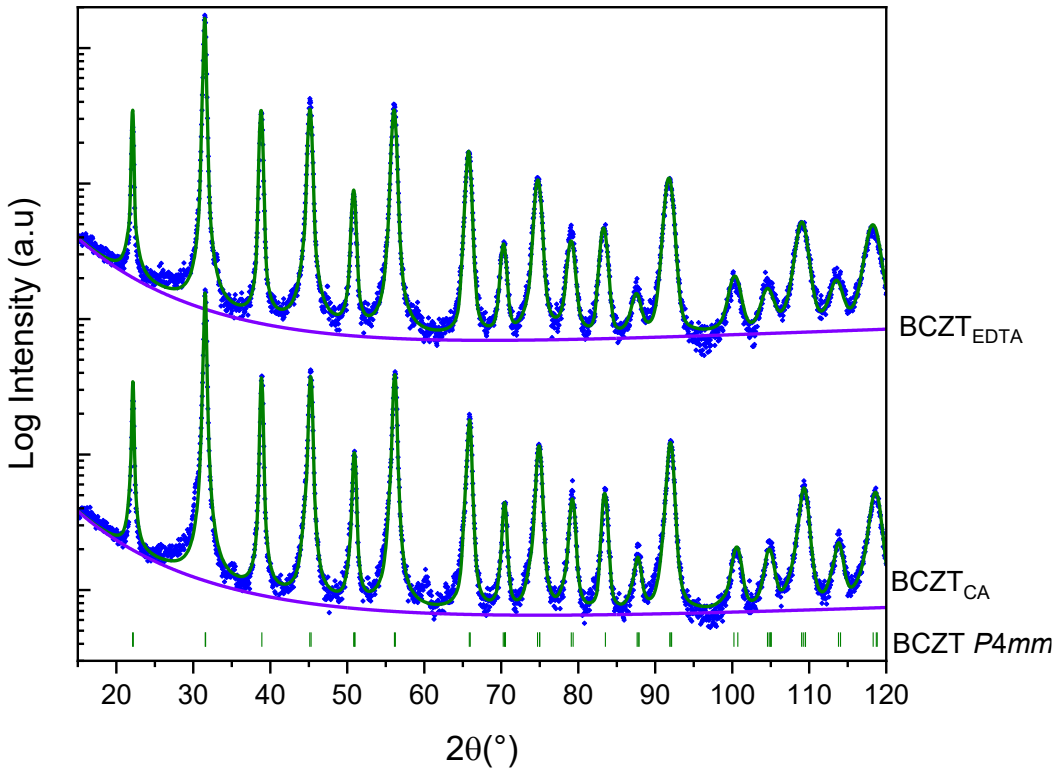

Figure 6.3.1 Rietveld Refinement of XRD diffraction pattern of $BCZT_{EDTA}$ and $BCZT_{CA}$ calcined powders.

Olive coloured bars at the bottom indicate the reflection of the *P4mm* BCZT phase. Experimental points are indicated with blue dots. Fitting curves are reported using the same colour (solid green line). Background is indicated in light purple.

6.3.2 Processing and characterization of the Ceramics

The Diffraction patterns of $BCZT_{EDTA}$ ($BCZT_{EDTAc}$) and $BCZT_{CA}$ ceramics ($BCZT_{CAc}$) reported in the **figure 6.3.2 (*Figure 6.3.2(a)*)** exhibit single tetragonal phase (*P4mm*). In the $BCZT_{EDTAc}$ pattern, the high-angle peaks result more sharply resolved (Fig. 3b), which indicate a higher degree of crystallinity of BCZTEDTA ceramics respect to $BCZT_{CA}$. Moreover, the shape of high-angle reflections is another proof of the tetragonality of the samples obtained. The tetragonal distortion of the $BCZT_{EDTA}$ ceramics corresponds to c/a= 1.003 with c =4.015 Å, still keeping enough lattice distortion for exhibiting a spontaneous polarisation. Instead, $BCZT_{AC}$ ceramics show a smaller tetragonal distortion with pseudocubic lattice symmetry, with c/a=1.001 and c =4.022 Å.

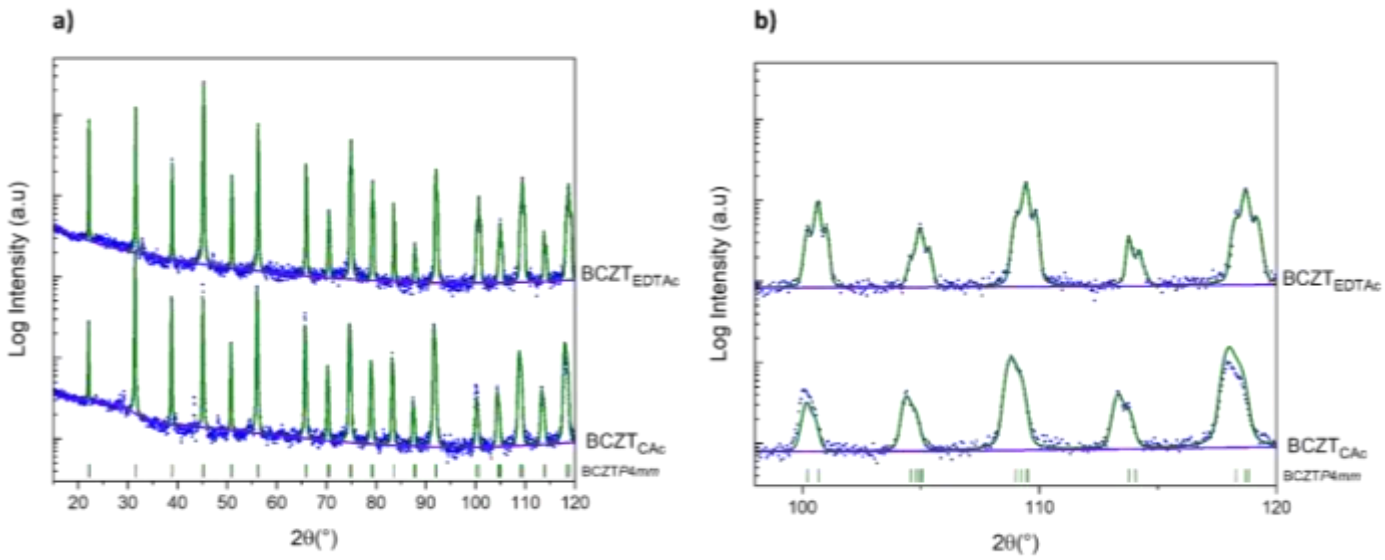

Figure 6.3.2 a) Rietveld Refinement of XRD diffraction pattern of ceramics produced with calcined BCZT$_{EDTA}$ powders and BCZT$_{CA}$ powders; **b)** Magnification of higher angles proving the higher tetragonality of BCZT$_{EDTA}$ ceramic. Olive coloured bars at the bottom indicate the reflection of the *P4mm* BCZT phase. Experimental points are indicated with blue dots. Fitting curves are reported using the same colour (solid green line). Background is indicated in light purple.

Representative SEM images of the fracture surfaces of sintered BCZT ceramics (**Figure 6.3.3**). All BCZT$_{EDTA}$ show densities about 91% of theoretical density (5,78 g/cm^3), whereas BCZT$_{CA}$ ceramics exhibit lower densities of 80%. BCZT$_{EDTA}$ ceramics (**Figure 6.3.3 (a)** and **(b))** show a transgranular fracture indicating the strengthen of grain boundaries and proper densification. However, as noticeable from SEM images reported in **Figure 6.3.3 (c)** and **(d)**, BCZT$_{CA}$ ceramics reveal inhomogeneous microstructure with densified areas with transgranular fracture and porous areas, revealing incomplete densification and inhomogeneous size distribution (from 2 µm to 10 µm). Moreover, these images show the general morphology of the main BCZT grains of the ceramic.

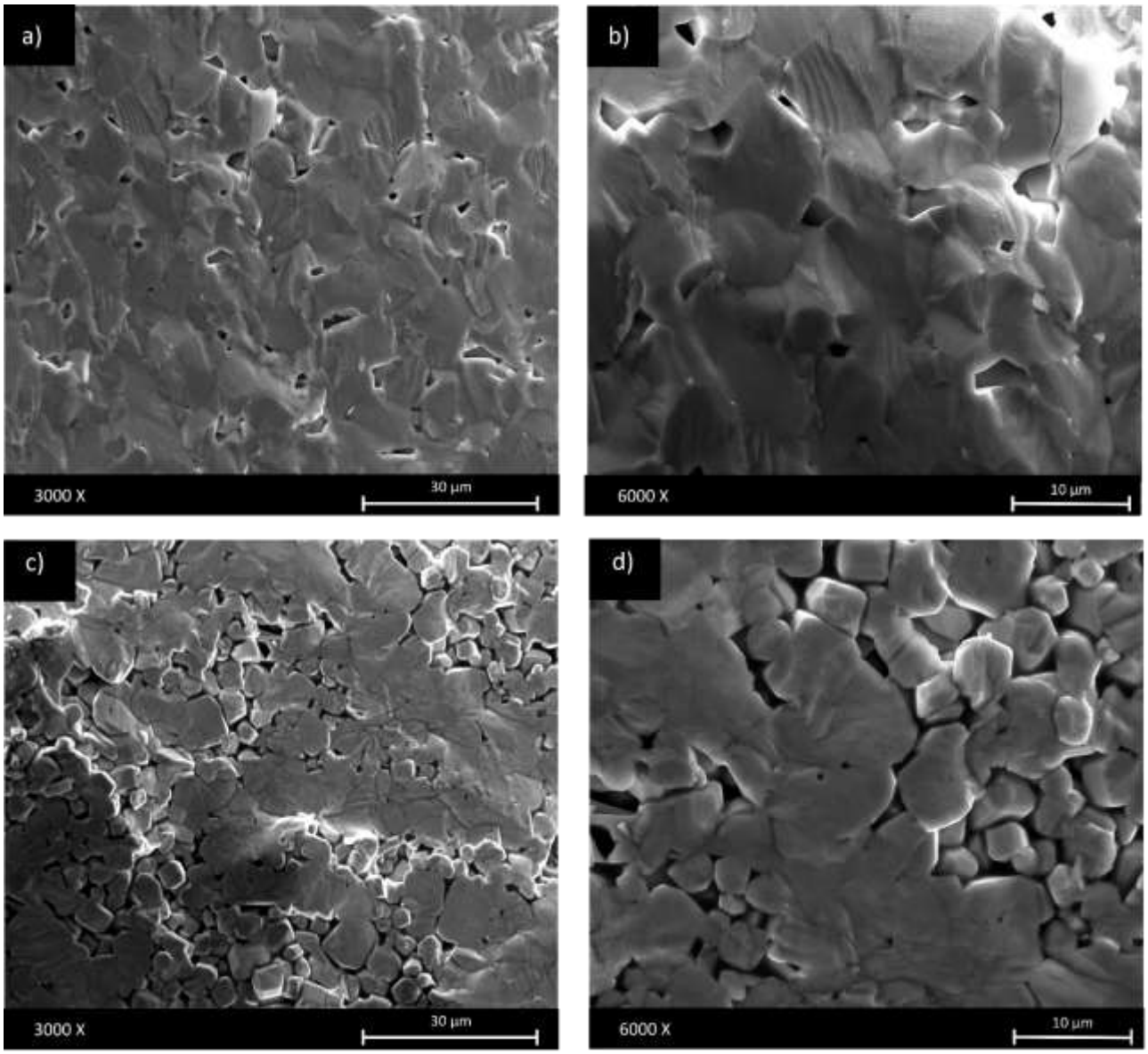

Figure 6.3.3 *Representative SEM images* (*secondary* electrons mode) of *the fracture surfaces of sintered BCZT ceramics (*FEI Quanta 200); **a)** and **b)** $BCZT_{EDTA}$ ceramics at two different magnifications; **c)** and **d)** $BCZT_{CA}$ ceramics at two different magnifications.

The SEM images of $BCZT_{EDTAc}$ (**Figure 6.3.4**), taken using a backscattering emission mode, the ceramics present a homogeneous grain size distribution (10 µm).

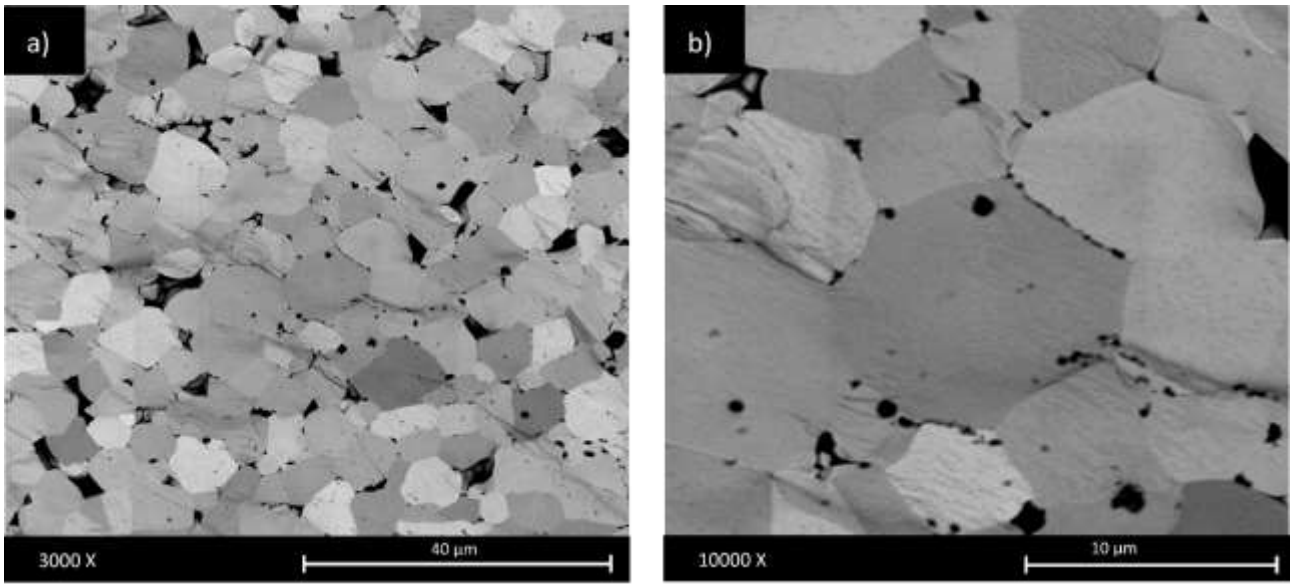

Figure 6.3.4 *Representative SEM images (backscattering mode) of the fracture surfaces of sintered BCZT ceramics.* **a)** and **b)** $BCZT_{EDTA}$ ceramics at two different magnifications. Phenom Pro G2 SEM microscope.

6.3.3 Electrical characterization

As emerges from the XRD analysis, the use of citric acid in the synthesis step leads to a decrease of tetragonal distortion, revealing a pseudo-cubic lattice structure in $BCZT_{CA}$ ceramics. According to these results, all the poled $BCZT_{CA}$ ceramics did not show any piezoelectricity after 2 h. However, the use of EDTA in combination with glycerol leads to high values of quasi-static piezoelectric coefficient, d_{33} =440 pC/N (d_{31}=- 160 pC/N) and high electromechanical coupling factor k_p=0.40. Due to the homogeneous microstructure the mechanical losses obtained are low as the mechanical quality factor is high (Q_m= 358). In **Table 6.3.1** are shown also elastic coefficients values. The electromechanical coupling factor and the frequency number of the planar resonance, together with the regression factor ($\Re 2$) of the reconstructed to the experimental spectra ((R, G) plot in **Figure 6.3.5**), as indication of the reliability of the obtained parameters, are also shown.

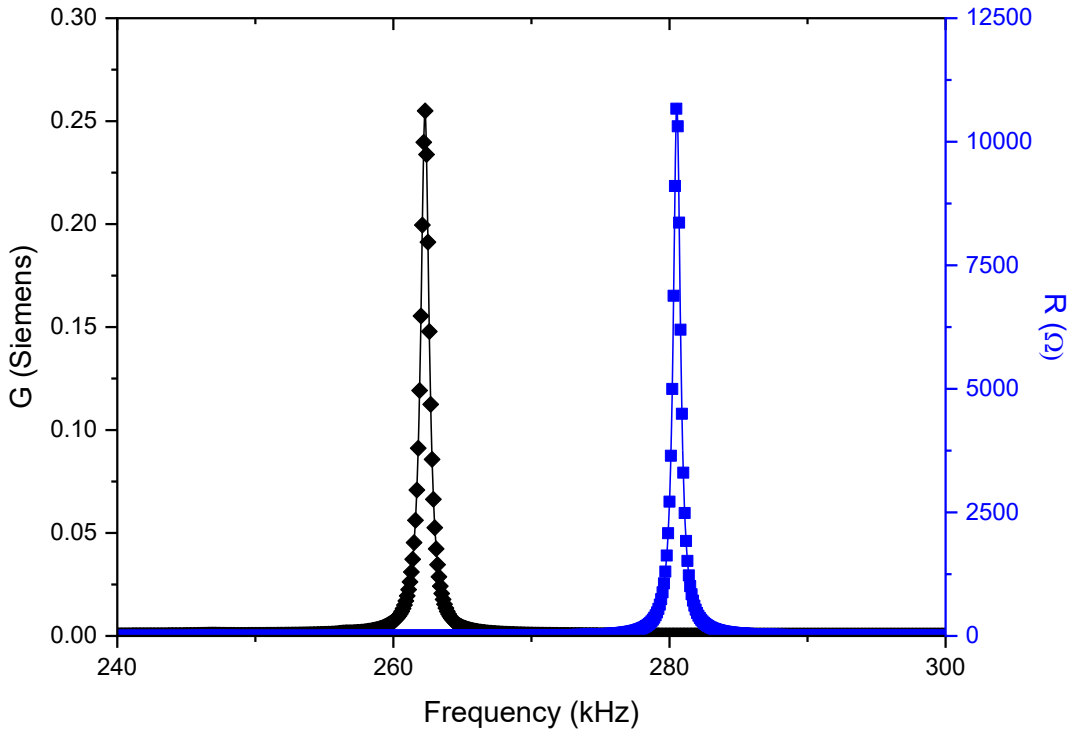

Figure 6.3.5 Equivalent representation of the impedance spectrum, (R, G) plot, used in the calculation of material coefficients by the iterative automatic method. Symbols are the experimental data and lines are the reconstructed peaks after coefficients calculation. Fundamental radial mode of resonance of a thin disk of $BCZT_{EDTA}$ ceramics.

Table 6.3.1 Some relevant material coefficients obtained from the Radial mode of resonance of the sintered BCZTEDTAs ceramics.

Properties	
Density (g/cc)	5.26
Relative density (%)	91
d_{33} (pC/N)	440
$\mathfrak{R}^2$	0.9986
k_p (%)	40.35
N_p(kHz.mm)	2898
d'_{31} (pC/N)	-160
$Q_p(d_{31})$	435
c'^{p}_{11} **(10^{10}N m^{-2})**	9.8038
Q_m	358
ε'^{T}_{33} **at 1 KHz**	4790

6.4 Conclusions

As alternative path, Pechini sol-gel route seems promising for identifying an alternative synthesis method for producing BCZT ceramics. This method also allows for stoichiometric and microstructure control leading to good electromechanical properties.

In particular, the effectiveness of glycerol as an esterifying agent was compared to ethylene glycol, and EDTA as a chelating agent. Their combination was also tested. To verify the impact of these reagents, two different synthetic processes for obtaining BCZT were developed: one using ethylenediaminetetraacetic acid and one using citric acid in combination with glycerol. Diffraction analysis of the synthesised powders showed that EDTA promoted the formation of a pure tetragonal phase of BCZT already at 900 °C. Moreover, it was found that the synthesis with EDTA was more efficient for obtaining ceramics with homogeneous grains size and respect to that with citric acid. Both the proposed sol-gel routes highly reduce synthesis temperature for BCZT currently used in conventional solid-state routes which typically needs more than 1000-1100°C for obtaining the same phase.

The results showed that the synthesis in which a combination of EDTA/glycerol was employed leads to promising electromechanical properties (d_{33}= 440 pC/N; d_{31}= - 160 pC/N; k_p= 0.40), together with low mechanical losses, due to homogeneous and relatively dense microstructure. In addition, this approach has demonstrated that the use of glycerol for the synthesis of BCZT is effective and able to substitute ethylene glycol. The use of citric acid seems to favour the persistence of unreacted precursors in the final material, affecting the product density at the end of the process.

In addition, the substitution of the ethylene glycol with glycerol makes this synthesis less toxic.

This promising property opens a new synthesis route that also provides a reduction of the synthesis temperatures. There is room for improvement by further reduction of the potential toxicity, for example by replacing organic precursors. Furthermore, is it important to highlight that this synthetic route suffer of poor scalability, principally due to the restricted amount of materials obtained per synthesis step.

6.5 Bibliography

1. Navas, D.; Fuentes, S.; Castro-Alvarez, A.; Chavez-Angel, E. Review on Sol-Gel Synthesis of Perovskite and Oxide Nanomaterials. *Gels* **2021**, *7*, 275, doi:10.3390/gels7040275.

2. Danks, A.E.; Hall, S.R.; Schnepp, Z. The Evolution of 'Sol–Gel' Chemistry as a Technique for Materials Synthesis. *Mater. Horizons* **2016**, *3*, 91–112, doi:10.1039/C5MH00260E.

3. Wang, Z.; Wang, J.; Chao, X.; Wei, L.; Yang, B.; Wang, D.; Yang, Z. Synthesis, Structure, Dielectric, Piezoelectric, and Energy Storage Performance of (Ba0.85Ca0.15)(Ti0.9Zr0.1)O3 Ceramics Prepared by Different Methods. *J. Mater. Sci. Mater. Electron.* **2016**, *27*, 5047–5058, doi:10.1007/s10854-016-4392-x.

4. Danks, A.E.; Hall, S.R.; Schnepp, Z. The Evolution of "sol-Gel" Chemistry as a Technique for Materials Synthesis. *Mater. Horizons* **2016**, *3*, 91–112, doi:10.1039/c5mh00260e.

5. Navas, D.; Fuentes, S.; Castro-Alvarez, A.; Chavez-Angel, E. Review on Sol-Gel Synthesis of Perovskite and Oxide Nanomaterials. *Gels* **2021**, *7*, doi:10.3390/gels7040275.

6. Kurajica, S. A Brief Review on the Use of Chelation Agents in Sol-Gel Synthesis with Emphasis on β-Diketones and β-Ketoesters. *Chem. Biochem. Eng. Q.* **2019**, *33*, 295–301, doi:10.15255/CABEQ.2018.1566.

7. Motta, M.; Deimling, C. V.; Saeki, M.J.; Lisboa-Filho, P.N. Chelating Agent Effects in the Synthesis of Mesoscopic-Size Superconducting Particles. *J. Sol-Gel Sci. Technol.* **2008**, *46*, 201–207, doi:10.1007/s10971-007-1673-0.

8. Ianculescu, A.; Berger, D.; Matei, C.; Budrugeac, P.; Mitoseriu, L.; Vasile, E. Synthesis of BaTiO3 by Soft Chemistry Routes. *J. Electroceramics* **2010**, *24*, 46–50, doi:10.1007/s10832-008-9521-3.

9. Leth, P.M.; Gregersen, M. Ethylene Glycol Poisoning. *Forensic Sci. Int.* **2005**, *155*, 179–184, doi:10.1016/j.forsciint.2004.11.012.

10. Gu, Y.; Jérôme, F. Glycerol as a Sustainable Solvent for Green Chemistry. *Green Chem.* **2010**, *12*, 1127–1138, doi:10.1039/c001628d.

11. Henderson, R.K.; Jiménez-González, C.; Constable, D.J.C.; Alston, S.R.; Inglis, G.G.A.; Fisher, G.; Sherwood, J.; Binks, S.P.; Curzons, A.D. Expanding GSK's Solvent Selection Guide – Embedding Sustainability into Solvent Selection Starting at Medicinal Chemistry. *Green Chem.* **2011**, *13*, 854–862, doi:10.1039/c0gc00918k.

12. Aziguli, H.; Zhang, T.; Yu, P. Effect of Additive Glycerol on Piezoelectric Properties of Modified Sol-Gel (Ba0.85ca0.15)(Ti0.9Zr0.1)O3 Ceramics. *Mater. Sci. Forum* **2020**, *993 MSF*, 791–798, doi:10.4028/www.scientific.net/MSF.993.791.

13. Danks, A.E.; Hall, S.R.; Schnepp, Z. The Evolution of "sol-Gel" Chemistry as a Technique for Materials Synthesis. *Mater. Horizons* **2016**, *3*, 91–112, doi:10.1039/c5mh00260e.

14. Lutterotti, L. Total Pattern Fitting for the Combined Size-Strain-Stress-Texture Determination in Thin Film Diffraction. *Nucl. Instruments Methods Phys. Res. Sect. B Beam Interact. with Mater. Atoms* **2010**, *268*, 334–340, doi:10.1016/j.nimb.2009.09.053.

15. Alemany, C.; Pardo, L.; Jimenez, B.; Carmona, F.; Mendiola, J.; Gonzalez, A.M. Automatic Iterative Evaluation of Complex Material Constants in Piezoelectric Ceramics. *J. Phys. D. Appl. Phys.* **1994**, *27*, 148–155, doi:10.1088/0022-3727/27/1/023.

16. Praveen, J.P.; Kumar, K.; James Raju, C.K.; Das, D. A Study of Piezoelectric Properties of (Ba0.85Ca

0.15)(Zr0.9Ti0.1)O3 Ceramics Synthesized by Sol-Gel Process. *AIP Conf. Proc.* **2013**, *1536*, 891–892, doi:10.1063/1.4810515.

17. Jaimeewong, P.; Promsawat, M.; Watcharapasorn, A.; Jiansirisomboon, S. Comparative Study of Properties of BCZT Ceramics Prepared from Conventional and Sol-Gel Auto Combustion Powders. *Integr. Ferroelectr.* **2016**, *175*, 25–32, doi:10.1080/10584587.2016.1199913.

Materials **2023**, *16*(3), 945;
https://doi.org/10.3390/ma16030945

7 Solid State Processing of BCZT Piezoceramics Using Ultra Low Synthesis and Sintering Temperatures

7.1 Introduction

Ferroelectric materials are a model of multifunctionality and new applications of complex compositions with perovskite-type and related crystal structures [1] are being investigated currently in the emerging energy fields of harvesting [2] and photovoltaic conversion [3] or those based on the magnetodielectric effect [4]. In the consolidated field of piezoelectric sensors, actuators, motors and other devices using electromechanical transduction, replacing the market-dominating PZT (Lead Zirconium Titanate)-based tridimensional perovskite has been one of the most investigated materials research topics over the last two decades [5,6]. In this respect, one of the most promising complex oxides with an alternative, lead-free composition, which respects the human health and protects the environment, is represented by the pseudo-ternary system $BaTiO_3$-$BaZrO_3$-$CaTiO_3$ [7], commonly known as BCZT (Barium Calcium Zirconate Titanate). BCZT has lower density than PZT (below 6 g/cm^3) and piezoelectric coefficient, d_{33},like the best hard PZT ceramics (up to 620 pC/N [8]). An advantage of BCZT in comparison with PZT is the lower volatility of raw materials, while the main drawback is represented by the higher synthesis (up to 1350 °C) and sintering temperatures (up to 1500 °C) required for its processing by the solid-state route [9-13]A recent review shows that, in these materials, dielectric and piezoelectric properties are closely related to an optimized ceramic microstructure (i.e., grain size, microporosity, etc.), that depends essentially on the fabrication process [14]. Furthermore, both raw powder particle size and sintered ceramic grain size play a crucial role in the optimization of the BCZT piezoceramics properties [15].

Although some efforts have been paid to the reduction of the processing temperatures by using chemical methods of synthesis [16-18], the use of a high thermal budget currently remains as a compulsory condition to obtain high piezoelectric coefficients in BCZT by the solid-state route [19]. BCZT is one of the most refractory lead-free piezoelectric materials, as it is also well-known for the unmodified barium titanate. This means that, when the solid-state route is used, the synthesis of the compound is usually carried at or above

1300 °C, for example in the seminal work [8]. More severe synthesis conditions are not unusual in the literature, for example, 1350 °C for 15 h in oxygen atmosphere [20]. There are a few works in which the synthesis is conducted at low conditions of 1250 °C for 2 h [21]. Only when more reactive powders are used, such as a previously mechanosynthesized powder by energetic milling in planetary mill for 12 h or sol-gel derived powders, very-low synthesis conditions of 900 °C for 1 h [22] or 1000 °C for 6 h [17], respectively, are reported.

As for the sintering conditions used by solid-state route, we can currently find reports of severe thermal treatments as, for example, 1450–1500 °C in the mentioned seminal work [8] or 1500 °C for 4 h in air, when using and additional mixing for 8 h after synthesis [23] or 1450 °C for 8 h in air [24]. Even when using synthesized sol-gel powder, the sintering was reported at 1420 °C for 6 h when the powder was ball-milled for 16 h after synthesis [17] or 1500 °C for 10 h [25].

However, ball-milling has proven to be effective in reducing the processing temperatures of electroceramics [26,27]. What is more, attrition ball-milling is very effective in homogenizing the particle size of raw materials, which leads to the decrease in the synthesis temperature, as previously reported for other lead-free materials [28,29]. Furthermore, another attrition ball-milling after synthesis seems to be necessary to decrease the sintering temperature, by reducing the initial particle size of calcined powders [30]. This is because the driving force for sintering is inversely proportional to the particle size, as previously reported [31]. However, in the case of BCZT piezoceramics, attrition milling for solid-state processing studies are lacking.

Within such context, the present investigation aims to analyse the effect of attrition ball-milling on the processing temperatures, the microstructural and piezoelectric properties of the here fabricated high sensitivity BCZT ceramics using the solid-state route.

7.2 Materials and Methods

7.2.1 Materials

Ceramic powders of nominal composition ($Ba_{0.92}$ $Ca_{0.08}$) ($Ti_{0.95}$ $Zr_{0.05}$) O_3 [32] (abbreviated as BCZT) were prepared by a solid-state route starting from a stoichiometric mixture of $BaCO_3$ (Merck, Darmstadt, Germany, >99%), $CaCO_3$ (Sigma Aldrich, St. Louis, MO, USA, >99%), TiO_2 (Merck, of nominal purity >99% composed of 85 wt.% of anatase and 15 wt.% of rutile) and ZrO_2 (Tosoh, Tokyo, Japan, monoclinic polymorph >99%).

7.2.2 Powder and Ceramics Processing

The raw materials were dried at 80 °C overnight, weighted according to the nominal composition indicated above and, finally, mixed. To activate these raw materials, they were mechanically treated by attrition ball milling (BM). For this process, to prevent contamination, a stainless-steel vial internally coated with Teflon® was chosen. Then, the mixed raw materials were milled for 6 h at 700 rpm in isopropanol as liquid medium with 3Y-TZP balls (d = 3 mm) with a Ball to Powder weight Ratio (BPR) of 30, according to previous adopted approaches [28,29,33].

The as-obtained slurry was then transferred into a beaker and heated in an oven at 80 °C to eliminate the solvent. Thermal characterization was conducted by a TG-DSC Q600 TA Instrument. Samples of mixed raw materials and ball-milled powders for 6 h were annealed from room temperature to 1100 °C with a heating ramp of 5 °C/min. The ball-milled powders were calcined in an electrical furnace, in air, inside a crucible covered with a lid. The calcined powders were ground to obtain a fine particulate material.

The influence of a second attrition ball milling on the ceramic microstructure was evaluated. For this purpose, (i) one fraction of the batch previously calcined and ground was directly sieved down to 50 µm (1 BM: one step milling process) and (ii) other fraction of the batch was attrition ball-milled again for 3 h within the same vial formerly used and was subsequently dried and sieved (2 BM: two-steps milling process).

Disc-shape pellets from each type of powder were obtained by uniaxial pressing (3 min 1.2 tons). Likewise, the discs of both 1 BM and 2 BM powders were sintered under the same conditions. Different sintering times

and temperatures were explored using a heating rate of 3 °C/min. The bulk densities were determined by the geometric method.

7.2.3 Structural and Microstructural Characterization

Structural investigations were conducted using a Bruker D8TT Advance diffractometer with a Cu anode (λ = 1.54178 Å) working at 40 kV and 30 mA with a graphite monochromator in a step-scanning mode from 20° to 60° (2Θ°), using 0.07° as step size and 2 s of integration time. For the sake of determination of secondary phases, more detailed patterns were acquired with 0.07° step and 4 s. Ceramic microstructure characterization of the fresh fracture surface of the pellets have been accomplished using a scanning electron microscopy (SEM G2 pro; Phenom, Thermo Fisher Scientific, Waltham, MA, USA, operated with a beam voltage of 5 kV).

7.2.4 Dielectric and Electromechanical Characterization

In order to measure electric properties, pellets of approximately 12 mm diameter were reduced in thickness by polishing to a typically 1mm thickness. Silver paste was attached on both surfaces of the thin disks and sintered at 400 °C for 1 h. After that, the conductivity of the electrodes, the DC resistance of the disk and the dielectric permittivity and losses at 1 kHz of the samples were measured at room temperature. Samples were poled in thickness under 10–15 kV.cm^{-1} at 40 °C for 1 h in a silicone oil bath, followed by field cooling (FC) to room temperature for the piezoelectric characterization.

The quasi-static d_{33} piezoelectric charge coefficient, which characterizes the sensor performance of the ceramic in the poling field direction, was measured with a Berlincourt d_{33}-meter at 100 Hz. Complex impedance as a function of the frequency was measured with an impedance analyzer (HP 4192A-LF) at the radial extensional resonance of the thickness poled thin disks. The impedance was plotted as Resistance(R) and Conductance (G) vs. frequency plots. The related piezoelectric, dielectric and elastic material coefficients, including all the losses, were determined using the software for automatic iterative analysis of R and G vs. frequency curves [34]. The residuals for these reconstructed R and G peaks to the experimental ones, quantified by the regression factor ($\mathfrak{R}^2$), accounts for the validity of the material model for the resonance

mode. The closer is the model to the experimental curves; the closer is $\mathfrak{R}^2$ to 1. For the planar mode, the complex material coefficients ($P^* = P' - iP''$) directly determined in this analysis are the piezoelectric charge coefficient, d_{31}, the dielectric permittivity, ε^T_{33}, and the elastic compliances, s^E_{11} and s^E_{12}. Additionally, a few other material coefficients are determined by the software from those, using well known relationships. These allow us to analyze the performances of the ceramic as generator (piezoelectric voltage coefficient g_{31}) and as energy transducer (electromechanical coupling factors (K_p, K_{31}) and frequency number ($N_p = f_s(kHz). D(mm)$, where D is the diameter of the disk)). Losses can be expressed for each material complex coefficient as loss tangent factor ($\tan\delta = P''/P'$), commonly used for the dielectric coefficients, or as a quality factor ($Q = P'/P''$), commonly used for the elastic coefficients.

7.3 Results and Discussion

7.3.1 Processing and Characterization of the Powders

The influence of the mechanical processing on the activation of the starting raw materials, has been evaluated by Thermogravimetry and Differential Scanning Calorimetry (TG-DSC) measurements reported in **Figure 7.3.1**. The weight loss process of BCZT mixed raw materials, as shown in **Figure 7.3.1(a)**, can be summarized in two main stages. At the first stage a weight loss of 2% is observed (green solid line) between 600 and 700 °C and it is associated with an endothermic peak in the corresponding DSC profile (blue solid line). This thermal event could be correlated with the decomposition of $CaCO_3$ to CaO and CO_2.

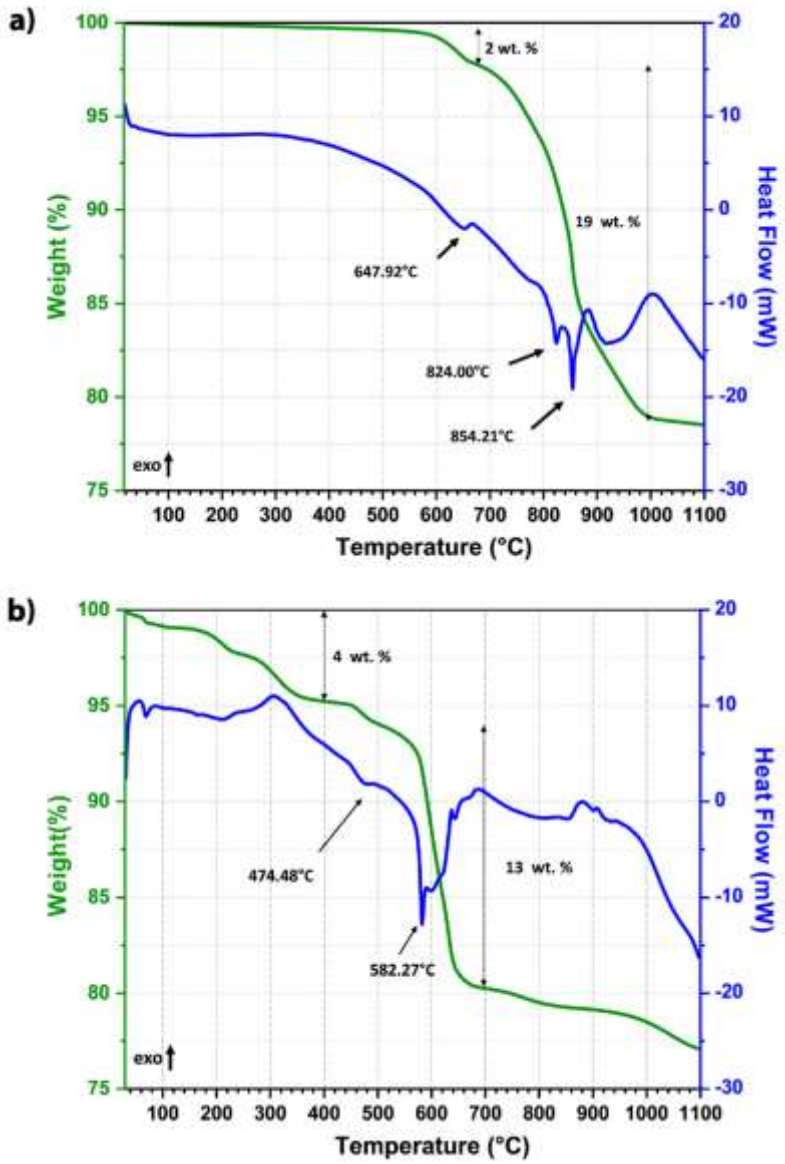

Figure 7.3.1 Thermal analysis (green solid line is weight of powder and blue solid line is heat flow) of mixed raw materials before **a)** and after **b)** attrition milling treatment for 6 h.

The second weight loss of around 19% occurred between 700 and 1000 °C and coincides with two endothermic peaks. According to the literature, the first sharp endothermic peak at ~824 °C, could be due to the reversible phase transformation α-$BaCO_3$→β-$BaCO_3$, while the second one, peaked 854 °C, is related to the decomposition of carbonates and formation of perovskite BCZT [35,36]. The broad exothermic peak around 1000 °C can then be ascribable to the crystallization of BCZT powders. The powder milled for 6 h, presents interesting differences in terms of TG-DSC profiles, as showed in **Figure 7.3.1(b)**. A first weight loss of 4% in the temperature range of 300–400 °C can be related with the evaporation of the organic compounds formed during the milling treatment performed using isopropanol. The endothermic peak associated with

the first decomposition of calcium carbonates appeared at lower temperature of 474 °C, if compared with those of the unmilled system. Interestingly, the main weight loss of 13% related to the endothermic events, which lead to the formation of BCZT phase, occurred between 500 °C and 700 °C, temperatures significantly lower than those achieved for the mixed raw materials.

To confirm the results of the DSC/TGA analysis, different synthesis treatments have been performed on the ball-milled powders at the different characteristic temperatures of the milled powder.

The evolution of the crystalline phases with the synthesis temperature has been investigated by using XRD analysis (**Figure 7.3.2(a)**) showing logarithmic scale intensities to highlight the occurrence of secondary weak phases that can escape the common analysis in the linear intensity domain, as the fraction of the BCZT perovskite is always estimated as being higher than 95% vol. The bottom pattern, corresponding to mixture of the raw materials after 6 h milling, shows a mixture of orthorhombic Witherite $BaCO_3$ (*Pncm*, a = 5.2926 Å, b = 8.947 Å 1, c = 6.4309 Å, Vc = 304.52 $Å^3$, not far from the value of 303.80 $Å^3$ reported in the literature), with an amount of ca 70.0 wt.% The residual 30.0 wt.% of the pattern was mainly TiO_2 in the anatase tetragonal form. There are also traces coincident with some peaks of monoclinic ZrO_2 and tetragonal rutile of TiO_2, but their appreciation is deteriorated by the noise of data. In such phase, the analysis $CaCO_3$ is missing, which was included originally under the form of Calcite. To explain this, notice that the orthorhombic aragonite polymorph of $CaCO_3$ is reported in the literature with the same space group of witherite and having lattice parameters a = 4.9652 Å; b = 7.9636 Å; and c = 5.7484 Å, respectively.

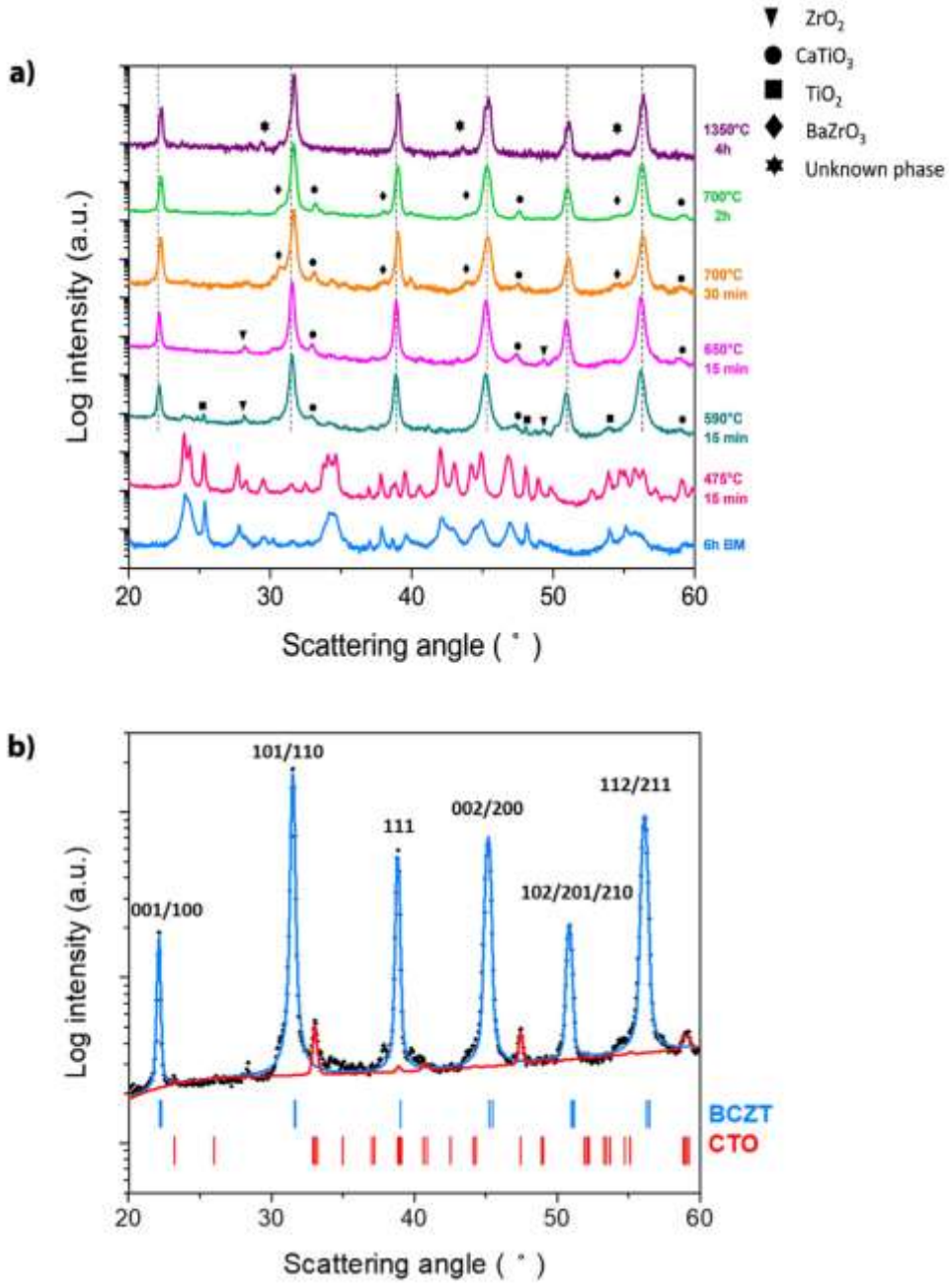

Figure 7.3.2 a) XRD diffraction patterns of the powder ball-milled for 6 h and calcined under variable time and temperature. Symbols indicate the secondary phases that accompany the main Barium Calcium Zirconium Titanate (BCZT) perovskite. Vertical dotted lines indicate the main BCZT perovskite reflections that are marked with the Miller indexes for the tetragonal prototype. **b)** Rietveld analysis of the calcined powder at 700 °C for 2 h, in which both BCZT and Calcium Titanate (CTO) stick patterns are shown.

The second pattern from the bottom of **Figure 7.3.2(a)**, corresponding to the milled powder treated at 475 °C, refers again to a mixture of Witherite and anatase in similar proportion 70.0 wt.% and 30.0 wt.%, where the lattice parameters for the orthorhombic phase evaluated this time are a = 5.3094 Å; b = 8.9053 Å and c = 6.4444 Å, Vc = 304.70 $Å^3$, respectively. The differences observed in the lattice parameters reported here

may be ascribed to the incorporation of ions into the orthorhombic dominant lattice of pure Witherite, which is partially destabilized with creation of various kinds of defects. Furthermore, the sharper peaks observed with respect to the as-milled powder are due to a growth process of the diffracting domain size, accompanied by a reduced degree of lattice disorder, affected by the thermal treatment conducted.

The main perovskite of BCZT is formed after treatment at 590 °C, as shown by the third pattern from the bottom of **Figure 7.3.2(a)** (green curve). This temperature corresponds well with the main endothermic peak of DSC analysis and the main weight loss of TGA, at 582 °C, in **Figure 7.3.1(b)**. At this temperature some residual raw materials (TiO_2 and ZrO_2), and a secondary phase ($CaTiO_3$) can also be observed.

By increasing the temperature to 650 °C, the small amount of TiO_2 cannot be observed anymore, but weak peaks attributable to monoclinic ZrO_2 and $CaTiO_3$ are still observed. The XRD analysis of the powder treated at 700 °C for 30 min (orange curve) shows weak shoulders marked with ◊ suggesting the formation of a secondary cubic compound, which might correspond to $BaZrO_3$ derived from ZrO_2 as previously reported [22,37]. However, the 2θ location of such shoulders occurs at values significantly different from those reported in the literature (JCPDS 6-0399), leading to a cubic lattice parameter a = 4.12 Å (to compare with the known value 4.18 Å). Moreover, another intermediate compound virtually disappears when increasing the dwell time to 2 h (light green curve).

Increasing the synthesis temperature to very high temperature (1350 °C) leads to the mentioned huge weight loss and the undesirable hard sintered powder agglomerates. After treatment at 1350 °C, the powder seems not to be either a single-phase BCZT, although it does not contain $CaTiO_3$ and has a higher distortion than that obtained at 590 °C (c = 4.0234 Å, a = 4.0020 Å, c/a = 1.005).

The reduction of the raw materials particle size leads to a decrease in synthesis temperature due to the creation of new surfaces and higher number of contact points between the particles. Moreover, the optimization and the particle refinement of the carbonates during their decomposition play a key role in the reduction of synthesis temperature to the formation of the BCZT ceramic by solid-state route [38].

As mentioned above, high-energy attrition ball milling is very effective in reducing the particle size of the raw materials. This is evident by comparing SEM images of unmilled powders (0 h) and attrition ball-milled powders for 6 h, as shown in **Figure 7.3.3 (a) and (b),** respectively.

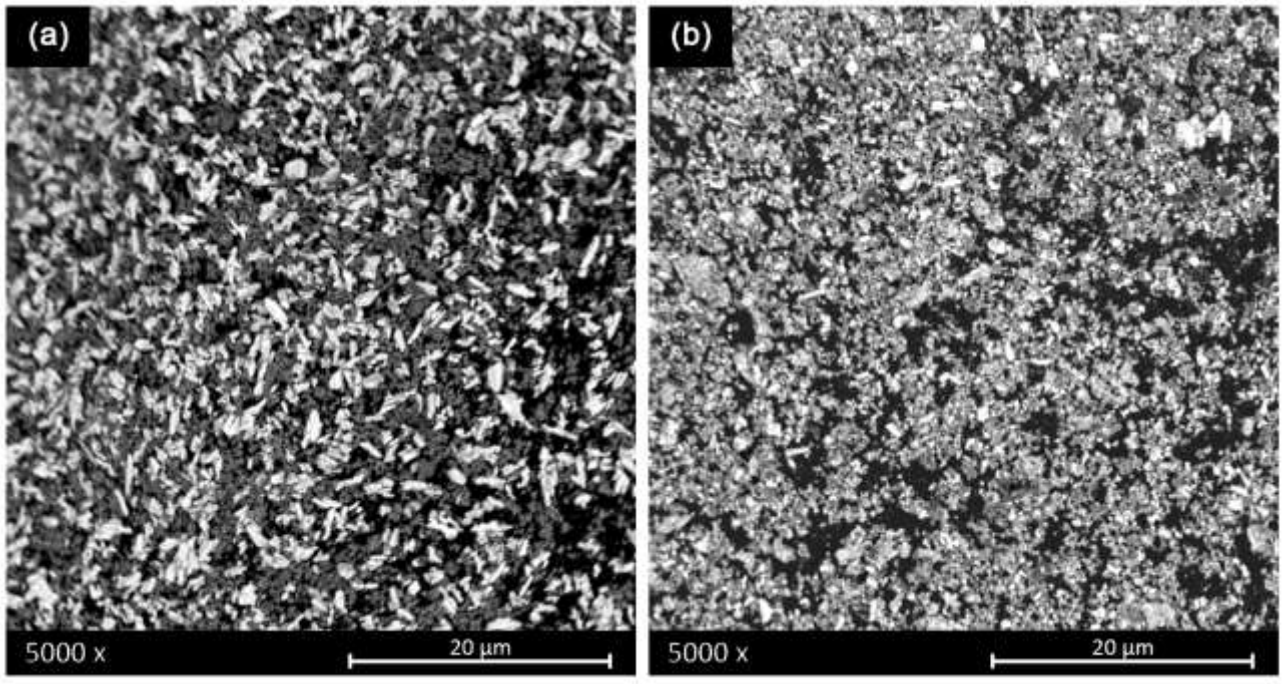

Figure 7.3.3 Shows the SEM micrographs of **a)** the mixed raw materials and **b)** the same mixture after activation by particles size reduction and homogenisation using attrition ball-milling and attrition ball-milled powders.

7.3.2 Processing and Characterization of the Ceramics

The comparison of the patterns for both ceramics sintered at 1260 °C for 30 min with (2 BM) and without (1 BM) a ball milling after synthesis reveals little differences from the structural point of view (**Figure 7.3.4**). However, in these two groups of samples, the density increased slightly from the sample 1 BM (4.5 g/cc) to the sample 2 BM (4.6 g/cc).

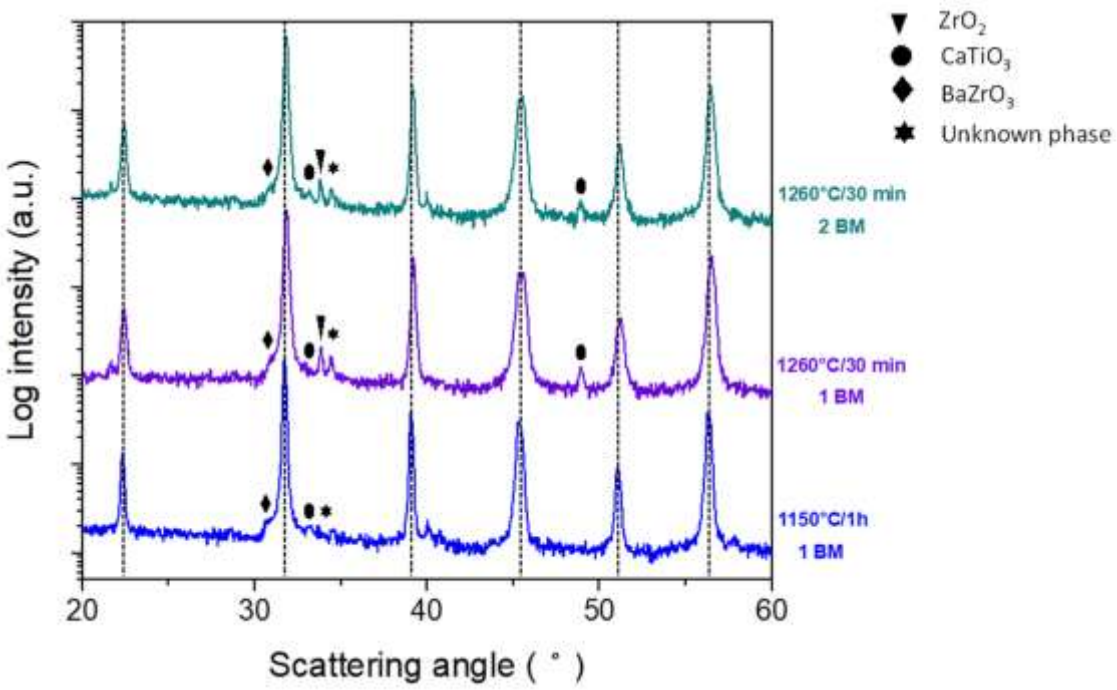

Figure 7.3.4 XRD diffraction patterns of the sintered ceramics, after synthesis at 700 °C for 30 min, at different sintering times and temperatures using a single sintering plateau, with and without a second ball milling treatment after synthesis (2 BM and 1 BM, respectively). Vertical dotted lines indicate the main BCZT perovskite reflections.

When using a one-step sintering method (**Figure 7.3.5**), the increase in the temperature or time of the sintering treatment fails to reduce the content of second phases (barium zirconate, titanium oxide, zirconium oxide and calcium titanate together with other, most probably transient, phases, such as $BaCaTiO_4$). This can be due to the incomplete incorporation of Zr^{4+} into the B crystallographic site in this secondary phase [19].

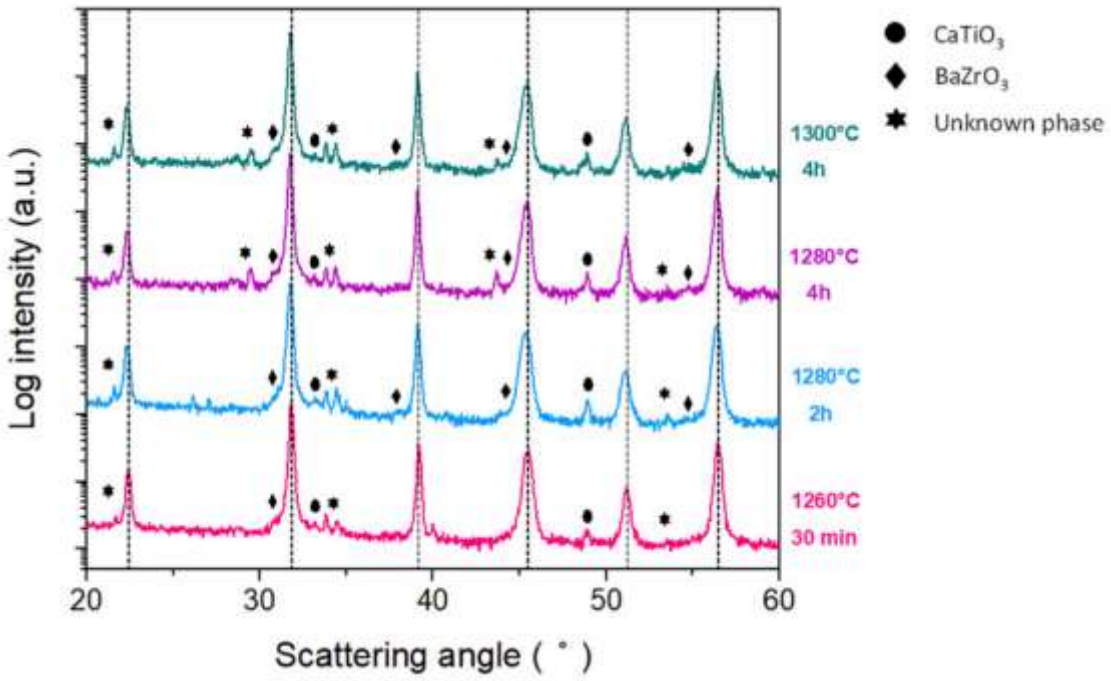

Figure 7.3.5 XRD diffraction patterns of the ceramics obtained by calcinating the powders at 700 °C for 30 min and subsequent sintering of the pellets at different sintering times and temperatures, using a single sintering plateau. Vertical dotted lines indicate the main BCZT perovskite reflections. The secondary phases that accompany the main BCZT perovskite are marked.

Previously [39], an enhanced sintering behaviour was observed in barium titanate by treatment of the aqueous processed powder at 950 °C for 15 h or performing such a treatment during heating of the samples up to the sintering temperature. Based on this, in light of the thermal analysis of the calcined and milled powders where the main exothermic peak can be observed at 900 °C (**Figure 7.3.1(b)**), a set of two-steps sintering experiments was conducted at 900 °C and different sintering times ranging between 1 and 4 h. The final sintering temperature was 1280 °C. The starting powder was synthesized at 700 °C for 2 h, aiming to enhance its homogeneity.

As shown in **Figure 7.3.6**, after an appropriate two-step sintering treatment (900 °C/3 h and 1280 °C/6 h) the secondary phases, such as raw materials and intermediate compounds, volatilize or incorporate into the main BCZT perovskite.

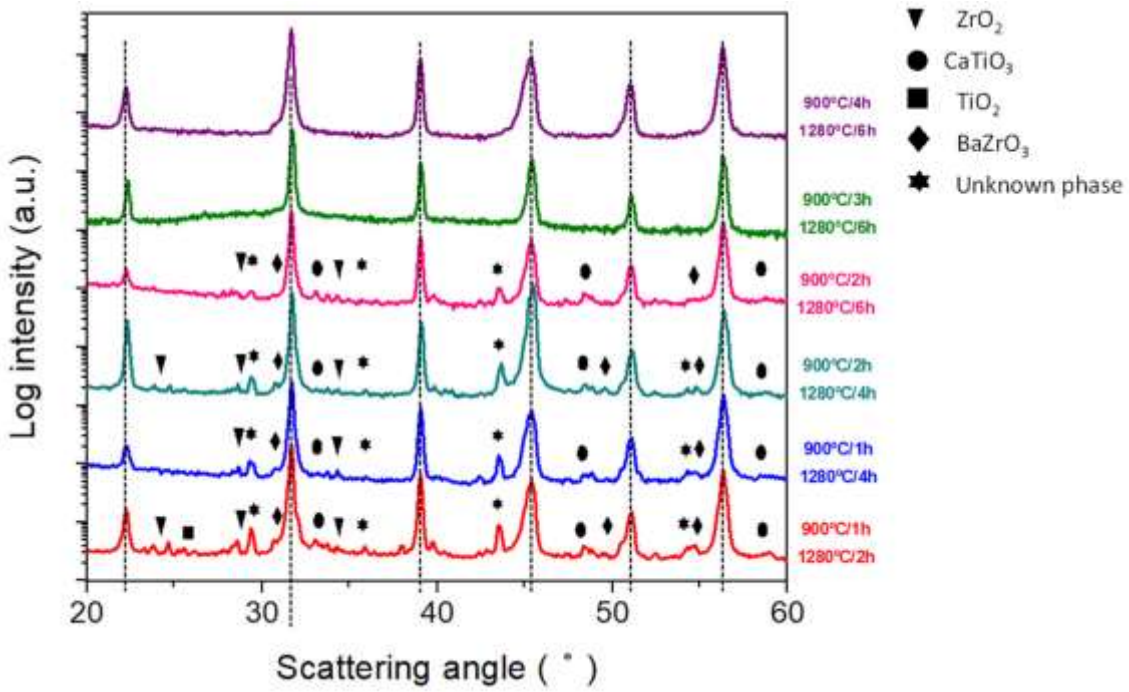

Figure 7.3.6 XRD diffraction patterns of the sintered ceramics after synthesis at 700 °C 2 h using a two-step sintering method at different sintering times and temperatures. Vertical dotted lines indicate the main BCZT perovskite reflections. Symbols indicate the secondary phases that accompany the main BCZT perovskite.

As mentioned at the beginning, the interesting piezoelectric properties are ascribable to the main tetragonal phase ascertained and characterized. Accordingly, **Table 7.3.1** shows the lattice parameters and the ratio c/a of the main perovskite phase.

Table 7.3.1 Rietveld analysis of the sintered ceramics after synthesis at 700 °C and 2 h under variable time and temperature using a two-step sintering.

Sintering Conditions	**Cell Parameters (Å) c**	**Cell Parameters (Å) a**	**Tetragonal Distortion c/a**	**Main Perovskite Phase G.P.**
900 °C/ 1 h + 1280 °C/2 h	4.0237	4.0030	1.005	P4*mm* BCZT
900 °C/ 1 h + 1280 °C/4 h	4.0306	4.0090	1.005	P4*mm* BCZT
900 °C/2 h + 1280 °C/4 h	4.0216	4.0011	1.005	P4*mm* BCZT
900 °C/2 h + 1280 °C/6 h	4.0143	3.9978	1.004	P4*mm* BCZT
900 °C/3 h + 1280 °C/6 h	4.0235	4.0099	1.003	Single Phase P4*mm* BCZT
900 °C/4 h + 1280 °C/6 h	4.0205	4.0030	1.004	Single Phase P4*mm* BCZT

Figure 7.3.7 shows the SEM micrographs of the fractured surfaces of the sintered ceramics obtained from powder calcined at 700 °C for 30 min and subsequent sintering of the pellets at different sintering times and temperatures using a one-step sintering method.

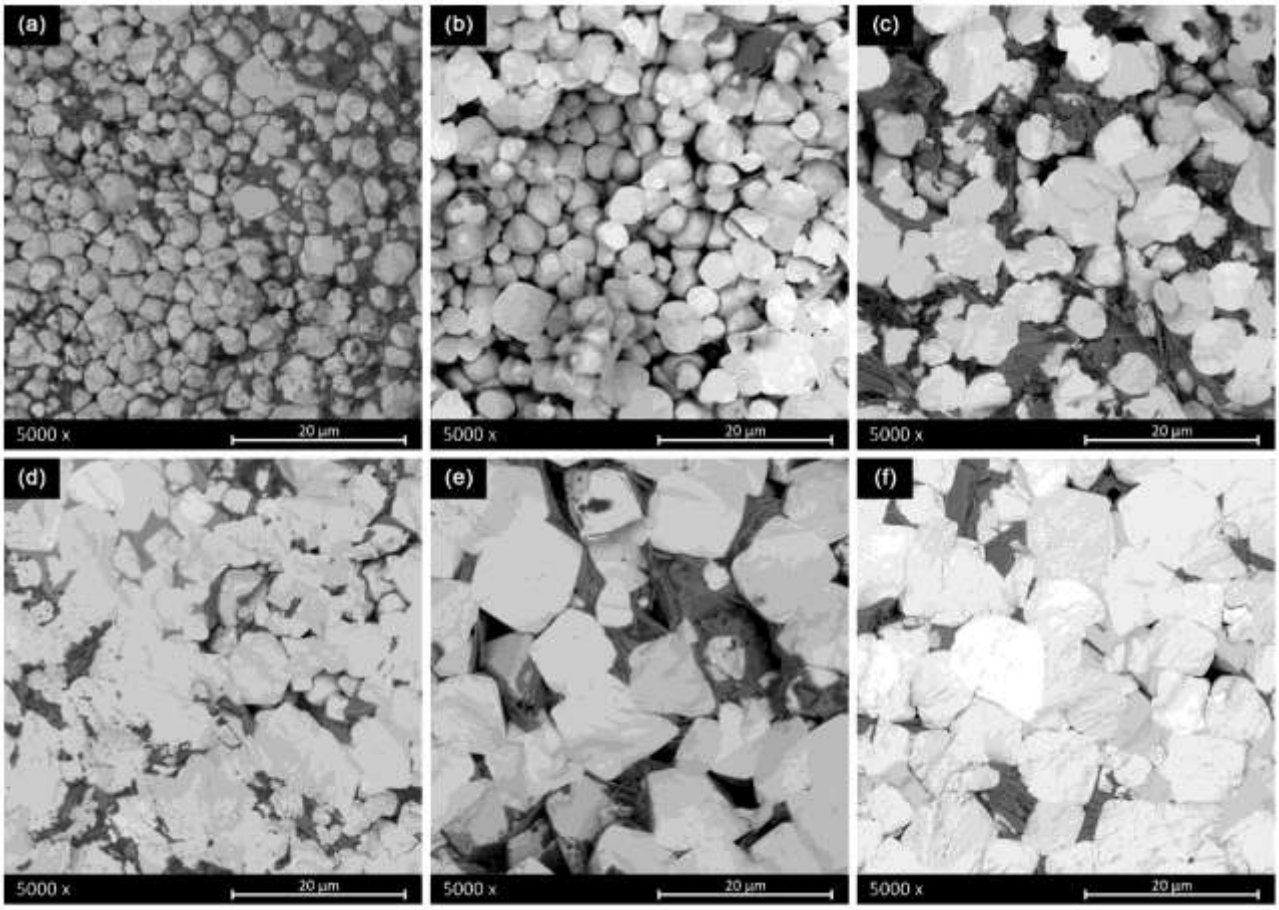

Figure 7.3.7 Scanning electron micrographs of the sintered ceramics obtained from powder calcined at 700 °C for 30 min, and subsequent sintering of the pellets at different sintering times and temperatures, using a single sintering plateau: **a)** 1150 °C for 1 h, 1 BM **b)** 1260 °C for 30 min, 1 BM, **c)** 1260 °C for 30 min, 2 BM **d)** 1280 °C for 2 h, 2 BM, **e)** 1280 °C for 4, 2 BM and **f)** 1300 °C for 4 h, 2 BM.

By comparing **Figure 7.3.7(a,b)**, it is evident that insufficient sintering temperature does not allow adequate grain growth. Furthermore, the samples (a) and (b) show an intergranular fracture, due to weak grain boundaries.

The comparison of images in **Figure 7.3.7(b,c)** of sintered ceramics under the same conditions proved that the second attrition ball milling promotes the grain growth using the same temperature. As the temperature increases, the grain size also increases and as the time (at the same temperature) increases, the homogeneity of grain size increases.

The underlaying mechanism of these development is the enhancement of the calcined powder reactivity through the dispersion of agglomerates of submicron size particles, which promotes higher contact points where the mass transport needed for the sintering is activated, confirmed by SEM analysis. By comparing

images in **Figure 7.3.7(c,f**), it is clear that the increase of the sintering time and temperature fails to eliminate the secondary phases, even though grain growth is promoted (from 2 μm to about 12 μm) and the samples reveal a majoritarian transgranular fracture, due to stronger grain boundaries. **Figure 7.3.7(f**) shows a degraded sintering stage with intragrain porosity. Therefore, single-step sintering is not effective in eliminating the secondary phases.

Figure 7.3.8 shows the SEM micrographs of the fractured surfaces of sintered ceramics obtained from powder calcined at 700 °C for 2 h and subsequent sintering of the pellets at different sintering times and temperatures using a two-step sintering method.

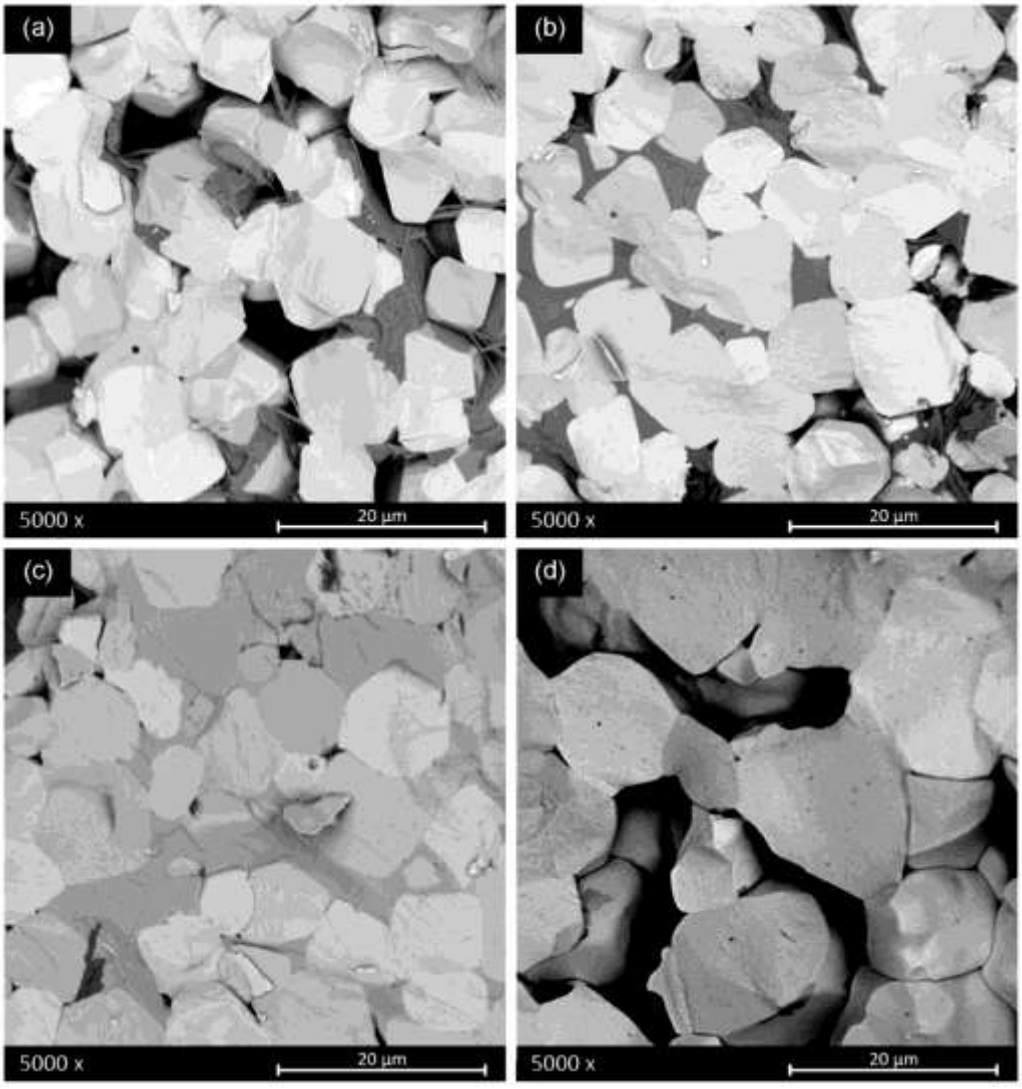

Figure 7.3.8 Scanning electron micrographs of the sintered ceramics obtained from powder calcined at 700 °C and subsequent sintering of the pellets at different sintering times and temperatures using a two-step sintering method: **a)** 900 °C for 1 h/1280 °C for 2 h **b)** 900 °C for 1 h/1280 °C for 4 h **c)** 900 °C for 2 h/1280 °C for 6 h and **d)** 900 °C for 4 h/1280 °C for 6 h.

As shown in **Figure 7.3.8**, an appropriate two-step sintering treatment promotes grain growth and allows the amount of crystallized secondary lamellar phase to decrease, resulting in a nearly pure BCZT perovskite

phase. The preliminary sintering step stabilizes the powder phase and promotes the decrease of secondary phases. During this step, the porosity created by the elimination of the secondary phase promotes adequate grain growth during the second sintering step (from about 6 µm to 20 µm).

7.3.3 Electrical Characterization

The electrical characterization was accomplished together with the structural one and with the determination of grain and porosity of the sintered ceramics. This allowed us to evaluate the structural and ceramic microstructural features that influenced the poling process of the sintered ceramics and determined the final material properties. All this provided integrated feedback for the decision taking stage for the next steps of the processing of the materials, aiming to get the optimal electromechanical activity of these high sensitivity piezoceramics.

Table 7.2 shows the preliminary electrical characterization of the ceramics sintered from powder calcined with the thermal budget of 700 °C for 30 min. The optimum sintering conditions for getting the highest density, resistivity and d_{33} piezo coefficient together with the lowest dielectric losses corresponds to a 2 BM ceramic sintered at 1280 °C for 4 h. These sintering conditions are well below those reported in the literature for solid-state route of processing, as explained in the introduction of this manuscript, to produce dense solid-state BCZT ceramics. This temperature reduction depends on the reactivity of the synthesized powder at these ultra-low conditions and reactivated by the second ball milling that aims to increase the grain size (**Figure 7.3.7**) and density of the sintered ceramic (**Table 7.3.2**). One could think that the simple action of increasing the sintering temperature could lead to a sample with better overall performance. Contrarily, the XRD pattern of **Figure7.3.5** and the SEM micrograph **Figure 7.3.7** of the sample sintered with this higher thermal budget show that the ceramic microstructure suffers a degradation. It shows lower density and intergranular porosity and, besides, that the secondary phases are not eliminated, which results in lowering the overall performance.

Table 7.3.2 Some properties of the sintered ceramic disks, after synthesis at 700 °C for 30 min., under variable time and temperature using a single sintering plateau.

Properties\Sintering Conditions	**1150 °C 1 h (1 BM)**	**1260 °C 30min (2 BM)**	**1280 °C 2 h (2 BM)**	**1280 °C 4 h (2 BM)**	**1300 °C 4 h (2 BM)**
Density (g/cc)	4.34	4.60	5.02	4.78	4.41
Relative density (%)	74	78	86	81	75
Resistance (MΩ)	0.6	0.4	2	30	15
Resistivity(MΩ·cm)	7.2	8.3	20.9	310.7	143.8
ε'^{T}/tanδ (at 1kHz) [1]	1671 0.264	3396 0.543	2306 0.286	1903 0.159	2463 0.175
d_{33} (pC/N) [2]	38	52	185	189	125

[1] before poling; [2] from Berlincourt meter at 100 Hz.

The relatively low performance of the mentioned best sample in this set of experiments, specifically the low d_{33} piezo coefficient (189 pC/N) reveals the key importance of the intergranular secondary phases (**Figure 7.3.5** and **Figure 7.3.7**) in the ceramic functionality. **Table 7.3.3** shows the preliminary electrical characterization of the ceramics sintered from powder calcined at 700 °C for 2 h and milling after synthesis using a two-step sintering method and the optimum final sintering temperature determined previously. The first thing that calls the attention to these results is that whereas the increase of the time at 1280 °C (from 2 to 6 h) results in an increase of density, the increase of the time at 900 °C (from 2 to 4 h) results in a decrease of the secondary phase. A simple discussion of the properties in terms of the variation of the density is not applicable here. The reason could be that there are two competitive driving forces in the thermal evolution of the microstructure. On the one hand, secondary phases can be observed in samples with only one sintering step (**Figure 7.3.5** and **Figure 7.3.7**) and the first stages of sintering with two-step (**Figure 7.3.6** and **Figure 7.3.8**) as pale liquid phase and crystallized lamella. These phases either volatilize or incorporate into the main BCZT grains from the intragrain volume, mainly at 900 °C, leaving a residual porosity. On the other hand, the reduction of the porosity and increase of grain size, mainly at 1280 °C, is more effective as the time at this temperature increases. However, the elimination of the secondary phases seems to be completed only after 3 h at 900 °C (**Figure 7.3.7**) and it seems to create an increasing porosity as the time at 900 °C increases. The densification procedure, at the last step of 1280 °C for 6 h, is limited when the sample is at 900 °C for 3 h and 4 h and their density decreases, though their porosity is constituted by micron-size porosity, which is

homogeneously distributed. Additionally, these ceramics have a single phase BCZT composition (**Figure 7.3.6** and **Table 7.3.1**) with homogeneous grain size above 10 µm (**Figure 7.3.8**). Despite the ultra-low conditions of synthesis and sintering used for their processing, their optimized structure and microstructure resulted in the achievement of high sensitivity BCZT ceramics (d_{33} piezo coefficient > 400 pC/N).

Table 7.3.3 Some properties of the sintered ceramics after synthesis at 700 °C for 2 h under variable time and temperature using a two-step sintering method.

Properties/ Sintering	**900 °C/1 h 1280 °C/2 h**	**900 °C/1 h 1280 °C/4 h**	**900 °C/2 h 1280 °C/6 h**	**900 °C/3 h 1280 °C/6 h**	**900 °C/4 h 1280 °C/6 h**
Density (g/cc)	4.30	4.45	4.47	4.32	4.28
Relative density (%)	73	76	76	74	73
Resistance (MΩ)	5	8	9	1	2
Resistivity (MΩ·cm)	58.9	80	106	13	30.7
ε'^{T}/tanδ (at 1 kHz) [1]	2100 0.326	2014 0.282	2158 0.262	3052 0.511	2833 0.251
d_{33} (pC/N) [2]	145	200	140	405	455

[1] before poling; [2] from Berlincourt meter at 100 Hz.

Resonance measurements at the planar mode of the electrically induced electromechanical resonance were made to complete the characterization of selected ceramic samples with important piezoelectric performance (d_{33} > 150 pC/N) with the calculation of piezo-elastic-dielectric coefficients including all losses by the iterative method (**Table 7.3.4**). In addition to this, and for the sake of comparison, a low density and fine grain size ceramic (<5 µm) prepared without a second ball milling from powder sintered at 700 °C for 30 min (**Figure 7.3.5**) and a dense ceramic (4.90 g/cc) prepared from powder synthesized at 1350 °C for 4 h and sintered at 1450 °C were also analysed.

Table 7.3.4 Some relevant material coefficients obtained from the Radial mode of resonance of the sintered ceramics after synthesis at 700 °C under variable sintering method. The complex material coefficients (P = P′ + iP′′) are given as real part (P′) and losses (piezoelectric and mechanical Q factor (P′/P′′) and dielectric tanδ (P′′/P′)). The data for the sample calcined at 1350 °C are also shown for comparison.

Properties\ Sintering Conditions	**1150°C 1 h (1 BM)**	**1280°C 2 h**	**1280°C 4 h**	**900 °C 1h 1280°C 4 h**	**900 °C 3 h 1280°C 6 h**	**900 °C 4 h 1280°C 6 h**	**1450°C 3 h [2]**
R^2	0.9996	0.9997	0.9995	0.9998	0.9999	0.9975	0.9964
k_p (%)	4.65	15.36	19.02	23.23	29.31	35.12	27.82
N_p(kHz.mm)	2652	2740	2874	2897	2339	2559	2742
d'_{31} (pC/N)	−9.89	−36.3	−45.0	−55.7	−99.6	−108.8	−68.17
$Q_p(d_{31})$	79	38	49	46	49	21	130
ε'^{T}_{33} / tanδ	947 0.026	1458 0.029	1542 0.022	1498 0.021	1897 0.020	1797 0.078	1540 0.013
g'_{31} (pC/N)	−1.18	−2.81	−3.30	−4.20	−5.93	−6.81	−5.0
c'^{p}_{11} [1] (10^{10}N m^{-2})	7.36	8.71	8.93	8.41	5.40	6.57	8.40
Q_m	208	162	197	188	120	155	157

[1] $c'^{p}_{11} = s^{E}_{11}/s^{E}_{12}$ [2] calcined at 1350 °C for 4 h.

The fine grain ceramic with low density and secondary phases sintered at 1150 °C for 1 h is characterized by a low k_p electromechanical coupling coefficient, low d_{31} and g_{31} coefficients, together with a low permittivity at resonance ε'^{T}_{33} and a high mechanical quality factor Q_m. Contrarily, the ceramic sintered at 1450 °C (d_{33} = 210 pC/N) has high coupling and piezoelectric coefficients, higher ε'^{T}_{33} and lower Q_m.

Among all ceramics prepared with ultra-low synthesis and sintering treatment and a second ball milling after synthesis, the performance of those obtained with one sintering step compares well from the mechanical and dielectric permittivity points of view, but they have lower coupling factor and piezoelectric coefficients.

Table 7.3.5 shows a comparison of the piezoelectric coefficient (d_{33}) of different compositions of BCZT ceramics prepared by different synthesis methods, such as solid-state and other synthesis routes and with Li-doping, a well-known agent to enhance sinterability. The composition more commonly reported in the BCZT ternary system is the $(Ba_{0.85}Ca_{0.15})$ $(Zr_{0.10}Ti_{0.90})$ O_3 (BCZT1510) while the nominal composition under study in the present work is the $(Ba_{0.92}Ca_{0.08})$ $(Zr_{0.05}Ti_{0.95})$ O_3 (BCZT0805) of which scarce information exists in the literature.

Table 7.3.5 Comparison of the piezoelectric coefficient (d_{33}) of different BCZT compositions prepared by different synthesis routes. SSR = solid-state route.

Synthesis Method	Synthesis T (°C)	Sintering T (°C)	d_{33} (pC/N)	Composition	Reference
SSR	1200	1450	365	BCZT0805	[32]
SSR	1100	1250	340	Li-modified BCZT0102	[40]
SSR	1350	1450 1500	620	BCZT1510	[8]
SSR	1250	1420	406	BCZT1510	[17]
SSR	1250	1400	410	BCZT1510	[21]
SSR	1250	1400	300	BCZT1010	[21]
SSR	1300	1500	330	BCZT1510	[10]
SSR	1200	1450	328	BCZT1610	[41]
Mechano-activation	900	1450	270	BCZT1510	[22]
Sol-gel	1000	1420	540	BCZT1510	[17]
Pechini	700	1275	390	BCZT1010	[16]
Hydrothermal	240	1300	164	BCZT1510	[18]

The performance of the optimized ceramics prepared with ultra-low synthesis and sintering temperatures with two-step sintering (900 °C for 3 h and 4 h and 1280 °C for 6 h) and a second ball milling after synthesis is characterized by higher piezoelectric sensitivity (coupling and piezoelectric coefficients) and higher dielectric permittivity, together with and moderate dielectric losses after poling and lower mechanical quality factor than the ceramics here prepared at 1450 °C for 3 h. **Table 7.3.5** also shows that the performance of these ceramics surpass the one of many other BCZT ceramics processed with higher temperatures. This takes place as a result of their chemical, crystallographic and microstructural homogeneity and absence of secondary phases.

7.4 Conclusions

A novel route of fabrication of BCZT piezoceramics, based on attrition milling in isopropanol, was developed. The efficiency of the attrition milling for 6 h in isopropanol is evidenced by the reduction of the temperature for the formation of the main perovskite structure, 854 °C in the unmilled powder to 582 °C for the 6 h milled powder.

The strong weight loss at the conventional synthesis conditions (1350 °C for 4 h) was drastically reduced by using an ultra-low thermal budget of 700 °C for 30 min. This leads to the formation of a majoritarian perovskite-type structure BCZT compound. However, in-depth analysis by XRD and SEM revealed that even for synthesis at 590 °C for 15 min, some secondary phases, mainly $CaTiO_3$, are formed simultaneously to the BCZT compound.

The sintering temperature of 1280 °C was found optimum, well below those conventionally reported (>1400 °C), due to the high reactivity of the powder calcined at ultra-low temperature. A second attrition ball milling after synthesis improved the grain size of the sintered ceramic body, while having little effect on the content of secondary phases in the final ceramic. Sintering at 1280 °C for 4 h gives place to a better densification and final properties than sintering at 1300 °C for 4 h. However, for this ultra-low sintering conditions, the best properties obtained (d_{33} = 189 pC/N, k_p = 19%, Q_m = 197) are below the expected values, because of the persistence of secondary phases.

To enhance sinterability, two-step sintering was conducted from powder synthesized at 700 °C 2 h. By this method, single-phase perovskite BCZT ceramic with high piezoelectric sensitivity were obtained for sintering at 900 °C for 3 h and 900 °C 4 h, with final plateau of 1280 °C for 6 h. The best electromechanical properties achieved were d_{33} = 455 pC/N, k_p = 35%, Q_m = 155. The results have been published in *Materials* **2023**, *16*(3), 945; https://doi.org/10.3390/ma16030945 .

Author Contributions: Marzia Mureddu, methodology, investigation, formal analysis, original draft preparation, review and editing; José F.Bartolomé, Sebastiano Garroni and Lorena Pardo, conceptualization, supervision, original draft preparation, review and editing; Sonia Lopez Esteban and Stefano Enzo, methodology and investigation; Maria Dore, investigation, data curation, writing—original draft preparation; Álvaro Garcia, methodology and software. All authors have read and agreed to the published version of the manuscript.

7.5 Bibliography

1. McCabe, E.E.; Bousquet, E.; Stockdale, C.P.J.; Deacon, C.A.; Tran, T.T.; Halasyamani, P.S.; Stennett, M.C.; Hyatt, N.C. Proper ferroelectricity in the Dion–Jacobson material $CsBi_2Ti_2NbO_{10}$: Experiment and Theory. Chem. Mat. **2015**, 27, 8298–8309. doi.org/10.1021/acs.chemmater.5b03564

2. Vázquez-Rodríguez, M.; Jiménez, F.J.; Pardo, L.; Ochoa, P.; González, A.M.; de Frutos, J. A New Prospect in Road Traffic Energy Harvesting Using Lead-Free Piezoceramics. Materials **2019**, 12, 3725. doi.org/10.3390/ma12223725

3. Wang, H.; Gou, G.; Li, J. Ruddlesden–Popper perovskite sulfides A3B2S7: A new family of ferroelectric photovoltaic materials for the visible spectrum. Nano Energy **2016**, 22, 507–513. doi.org/10.1016/j.nanoen.2016.02.036

4. Wendari, T.P.; Arief, S.; Mufti, N.; Blake, G.R.; Baas, J.; Suendo, V.; Prasetyo, A.; Insani, A.; Zulhadjri, Z. Lead-Free Aurivillius Phase $Bi_2LaNb_{1.5}Mn_{0.5}O_9$: Structure, Ferroelectric, Magnetic, and Magnetodielectric Effects. Inorg. Chem. **2022**, 61, 8644–8652. doi.org/10.1021/acs.inorgchem.1c03624

5. Garroni, S.; Senes, N.; Iacomini, A.; Enzo, S.; Mulas, G.; Pardo, L.; Cuesta-Lopez, S. Advanced Synthesis on Lead-Free $K_xNa_{(1-x)}$ NbO_3 Piezoceramics for Medical Imaging Applications. Phys. Status Solidi Appl. Mater. Sci. **2018**, 215, 1–15. doi.org/10.1002/pssa.201700896

6. Rödel, J.; Webber, K.G.; Dittmer, R.; Jo, W.; Kimura, M.; Damjanovic, D. Transferring Lead-Free Piezoelectric Ceramics into Application. J. Eur. Ceram. Soc. **2015**, 35, 1659–1681. doi.org/10.1016/j.jeurceramsoc.2014.12.013

7. McQuarrie, M.; Behnke, F.W. Structural and Dielectric Studies in the System (Ba, Ca) (Ti, Zr) O_3. J. Am. Ceram. Soc. **1954**, 37, 539–543. doi.org/10.1111/j.1151-2916. 1954.tb13986.x

8. Liu, W.; Ren, X. Large Piezoelectric Effect in Pb-Free Ceramics. Phys. Rev. Lett. **2009**, 103, 257602. doi.org/10.1103/PhysRevLett.103.257602.

9. Villafuerte-Castrejón, M.E.; Morán, E.; Reyes-Montero, A.; Vivar-Ocampo, R.; Peña-Jiménez, J.A.; Rea-López, S.O.; Pardo, L. Towards Lead-Free Piezoceramics: Facing a Synthesis Challenge. Materials **2016**, 9, 21. doi.org/10.3390/ma9010021

10. Hayati, R.; Fayazi, M.; Diargar, H.; Kaveh, M.; Tayebi, L. Electrical and Mechanical Properties of BZT−XBCT Lead-Free Piezoceramics. Int. J. Appl. Ceram. Technol. **2020**, 17, 1891–1898. doi.org/10.1111/ijac.13494

11. Li, W.; Xu, Z.; Chu, R.; Fu, P.; Zang, G. High Piezoelectric d_{33} Coefficient of Lead-Free $(Ba_{0.93}\ Ca_{0.07})(Ti_{0.95}\ Zr_{0.05})O_3$ Ceramics Sintered at Optimal Temperature. Mater. Sci. Eng. B Solid-State Mater. Adv. Technol. **2011**, 176, 65–67. doi.org/10.1016/j.mseb.2010.09.003

12. Xiao, A.; Xie, X.; He, L.; Yang, Y.; Ji, Y. Enhanced Piezoelectric Properties in a Single-Phase Region of Sm-Modified Lead-Free $(Ba,Ca)(Zr,Ti)O_3$ Ceramics. Materials **2022**, 15, 7839. doi.org/10.3390/ma15217839

13. Wu, J.; Xiao, D.; Wu, W.; Chen, Q.; Zhu, J.; Yang, Z.; Wang, J. Composition and Poling Condition-Induced Electrical Behavior of $(Ba_{0.85}\ Ca_{0.15})$ $(Ti_{1-X}\ Zr_x)O_3$ Lead-Free Piezoelectric Ceramics. J. Eur. Ceram. Soc. **2012**, 32, 891–898. doi.org/10.1016/j.jeurceramsoc.2011.11.003

14. Zhang, Y.; Sun, H.; Chen, W. A Brief Review of Ba $(Ti_{0.8}Zr_{0.2})O_3$-$(Ba_{0.7}Ca_{0.3})TiO_3$ Based Lead-Free Piezoelectric Ceramics: Past, Present and Future Perspectives. J. Phys. Chem. Solids **2018**, 114, 207–219. doi.org/10.1016/j.jpcs.2017.10.041

15. Bai, Y.; Matousek, A.; Tofel, P.; Bijalwan, V.; Nan, B.; Hughes, H.; Button, T.W. (Ba,Ca)(Zr,Ti)O_3 Lead-Free Piezoelectric Ceramics-The Critical Role of Processing on Properties. J. Eur. Ceram. Soc. **2015**, 35, 3445–3456. doi.org/10.1016/j.jeurceramsoc.2015.05.010

16. Reyes-Montero, A.; Pardo, L.; López-Juárez, R.; González, A.M.; Cruz, M.P.; Villafuerte-Castrejón, M.E. Lead-Free $Ba_{0.9}Ca_{0.1}Ti_{0.9}Zr_{0.1}O_3$ Piezoelectric Ceramics Processed below 1300 °C. J. Alloys Compd. **2014**, 584, 28–33. doi.org/10.1016/j.jallcom.2013.08.165

17. Wang, Z.; Wang, J.; Chao, X.; Wei, L.; Yang, B.; Wang, D.; Yang, Z. Synthesis, Structure, Dielectric, Piezoelectric, and Energy Storage Performance of ($Ba_{0.85}Ca_{0.15}$) ($Ti_{0.9}Zr_{0.1}$) O_3 Ceramics Prepared by Different Methods. J. Mater. Sci. Mater. Electron. **2016**, 27, 5047–5058. doi.org/10.1007/s10854-016-4392-x

18. Hunpratub, S.; Maensiri, S.; Chindaprasirt, P. Synthesis and Characterization of $Ba_{0.85}Ca_{0.15}Ti_{0.9}Zr_{0.1}O_3$ Ceramics by Hydrothermal Method. Ceram. Int. **2014**, 40, 13025–13031. doi.org/10.1016/j.ceramint.2014.04.166

19. Jiang, Y.P.; Tang, X.G.; Ju, S.G.; Liu, Q.X.; Zhang, T.F.; Xiong, H.F. Influence of Sintering Temperature on the Ferroelectric and Piezoelectric Properties of ($Ba_{0.85}Ca_{0.15}$) ($Zr_{0.1}Ti_{0.9}$)O_3 Ceramics. J. Mater. Sci. Mater. Electron. **2016**, 27, 3048–3052. doi.org/10.1007/s10854-015-4128-3

20. Keeble, D.S.; Benabdallah, F.; Thomas, P.A.; Maglione, M.; Kreisel, J. Revised Structural Phase Diagram of ($Ba_{0.7}Ca_{0.3}TiO_3$) -($BaZr_{0.2}Ti_{0.8}O_3$). Appl. Phys. Lett. **2013**, 102, 092903. doi.org/10.1063/1.4793400

21. Reyes-Montero, A.; Pardo, L.; López-Juárez, R.; González, A.M.; Rea-López, S.O.; Cruz, M.P.; Villafuerte-Castrejón, M.E. Sub-10 µm Grain Size, $Ba_{1-X}Ca_xTi_{0.9}Zr_{0.1O3}$ (x = 0.10 and x = 0.15) Piezoceramics Processed Using a Reduced Thermal Treatment. Smart Mater. Struct. **2015**, 24, 065033.doi.org/ 10.1088/0964-1726/24/6/065033

22. Amorín, H.; Venet, M.; Chinarro, E.; Ramos, P.; Algueró, M.; Castro, A. Lead-Free $Ba_{0.85}Ca_{0.15}Zr_{0.1}Ti_{0.9}O_3$ Ferroelectric Ceramics with Refined Microstructure and High Strain under Electric Field by Mechanosynthesis. J. Eur. Ceram. Soc. **2022**, 42, 4907–4916. doi.org/10.1016/j.jeurceramsoc.2022.04.061

23. Damjanovic, D.; Biancoli, A.; Batooli, L.; Vahabzadeh, A.; Trodahl, J. Elastic, dielectric, and piezoelectric anomalies and Raman spectroscopy of 0.5Ba ($Ti_{0.8}$ $Zr_{0.2}$)O_3-0.5($Ba_{0.7}$ $Ca_{0.3}$) TiO_3. Appl. Phys. Lett. **2012**, 100, 192907. doi.org/10.1063/1.4714703

24. Pisitpipathsin, N.; Kantha, P. Ferroelectric and Piezoelectric Properties of $Ba_{0.85}Ca_{0.15}Zr_{0.1}Ti_{0.9}O_3$ Ceramic with Various Sintering Times. Integr. Ferroelectr. **2018**, 187, 138–146. doi.org/10.1080/10584587.2018.1444886

25. Zhang, Q.; Cai, W.; Zhou, C.; Xu, R.; Zhang, S.; Li, Z.; Gao, R.; Fu, C. Electric Fatigue of BCZT Ceramics Sintered in Different Atmospheres. Appl. Phys. A Mater. Sci. Process. **2019**, 125, 759. doi.org/10.1007/s00339-019-3062-2.

26. Thanaboonsombut, A.; Vaneesorn, N. Effect of Attrition Milling on the Piezoelectric Properties of $Bi_{0.5}Na_{0.5}TiO_3$-Based Ceramics. J. Electroceramics **2008**, 21, 414–417. doi.org/10.1007/s10832-007-9216-1

27. Mittal, S.; Pahi, S.; Singh, K.C. Size Effect of Nano-Scale Powders on the Microstructure and Electrical Properties of $Ba_{0.85}Ca_{0.15}Zr_{0.1}Ti_{0.9}O_3$ Ceramics. J. Mater. Sci. Mater. Electron. **2019**, 30, 15493–15503. doi.org/10.1007/s10854-019-01926-5

28. Rubio-Marcos, F.; Romero, J.J.; Martín-Gonzalez, M.S.; Fernández, J.F. Effect of Stoichiometry and Milling Processes in the Synthesis and the Piezoelectric Properties of Modified KNN Nanoparticles by Solid-state Reaction. J. Eur. Ceram. Soc. **2010**, 30, 2763–2771. doi.org/10.1016/j.jeurceramsoc.2010.05.027

29. Rubio-Marcos, F.; Ochoa, P.; Fernandez, J.F. Sintering and Properties of Lead-Free (K,Na,Li)(Nb,Ta,Sb)O_3 Ceramics. J. Eur. Ceram. Soc. **2007**, 27, 4125–4129. doi.org/10.1016/j.jeurceramsoc.2007.02.110

30. Zuow, R.; Rödel, J.; Chen, R.; Li, L. Sintering and Electrical Properties of Lead-Free $Na_{0.5}K_{0.5}NbO_3$ Piezoelectric Ceramics. J. Am. Ceram. Soc. **2006**, 89, 2010–2015. doi.org/10.1111/j.1551-2916.2006.00991.x

31. Juhyun, Y.; Min, S.; Hong, J.; Suh, S.; Ur, S. Microstructural and Piezoelectric Characteristics of PSN-PMN-PZT Ceramics Produced by Attriction Milling. Trans. Electr. Electron. Mater. **2001**, 2, 18–23. koreascience.kr/article/JAKO200111920839105.pdf

32. Li, W.; Xu, Z.; Chu, R.; Fu, P.; Zang, G. Piezoelectric and Dielectric Properties of $(Ba_{1-X}Ca_x)(Ti_{0.95}Zr_{0.05})O_3$ Lead-Free Ceramics. J. Am. Ceram. Soc. **2010**, 93, 2942–2944. doi.org/10.1111/j.1551-2916.2010.03907.x

33. Thakur, O.P.; Feteira, A.; Kundys, B.; Sinclair, D.C. Influence of Attrition Milling on the Electrical Properties of Undoped-$BaTiO_3$. J. Eur. Ceram. Soc. **2007**, 27, 2577–2589. doi.org/10.1016/j.jeurceramsoc.2006.10.013

34. Alemany, C.; González, A.M.; Pardo, L.; Jiménez, B.; Carmona, F.; Mendiofa, J. Automatic Determination of Complex Constants of Piezoelectric Lossy Materials in the Radial Mode. J. Phys. D. Appl. Phys. **1995**, 28, 945–956. **doi.org/** 10.1088/0022-3727/28/5/017

35. Yang, R.B.; Fu, W.G.; Deng, X.Y.; Tan, Z.W.; Zhang, Y.J.; Han, L.R.; Lu, C.; Guan, X.F. Preparation and characterization of $(Ba_{0.88}Ca_{0.12})$ $(Zr_{0.12}Ti_{0.88})$ O_3 powders and ceramics produced by sol-gel process. Adv Mat Res. **2010**, 148–149, 1062–1066. doi.org/10.4028/www.scientific.net/AMR.148-149.1062

36. Ji, X.; Wang, C.; Li, S.; Zhang, S.; Tu, R.; Shen, Q.; Shi, J.; Zhang, L. Structural and electrical properties of BCZT ceramics synthesized by sol–gel process. J. Mater. Sci. Mater. Electron. **2018**, 29, 7592–7599. doi.org/10.1007/s10854-018-8751-7

37. Ciomaga, C.E.; Curecheriu, L.P.; Lukacs, V.A.; Horchidan, N.; Doroftei, F.; Valois, R.; Mitoseriu, L. Optimization of Processing Steps for Superior Functional Properties of (Ba, Ca)(Zr, Ti) O_3. Ceramics Mater. **2022**, 15, 8809. doi.org/10.3390/ma15248809

38. Baláž, P.; Achimovicová, M.; Baláž, M.; Billik, P.; Zara, C.Z.; Criado, J.M.; Delogu, F.; Dutková, E.; Gaffet, E.; Gotor, F.J.; et al. Hallmarks of Mechanochemistry: From Nanoparticles to Technology. Chem. Soc. Rev. **2013**, 42, 7571–7637. doi.org/10.1039/c3cs35468g

39. Nanni, P.; Leoni, M.; Buscaglia, V.; Aliprandi, G. Low-temperature aqueous preparation of barium metatitanate powders. J.Eur.Soc. **1994**, 14, 85–90. doi.org/10.1016/0955-2219(94)90048-5

40. Zhang, Y.; Sun, H.-J.; Chen, W. Li-modified $Ba_{0.99}Ca_{0.01}Zr_{0.02}Ti_{0.98}O_3$ lead-free ceramics with highly improved piezoelectricity. J. Alloy. Compd. **2017**, 694, 745–751. doi.org/10.1016/j.jallcom.2016.10.061

41. Li, W.; Xu, Z.; Chu, R.; Fu, P.; Zang, G. Polymorphic phase transition and piezoelectric properties of $(Ba_{1-x}Ca_x)$ $(Ti_{0.9}Zr_{0.1})$ O_3 lead-free ceramics. Phys. B **2010**, 405, 4513–4516. doi.org/10.1016/j.physb.2010.08.028

Journal of the European Ceramic Society, **2024**, Vol44(5),2944-2953

https://doi.org/10.1016/j.jeurceramsoc.2023.12.037

8 $BaZrO_3$-$BaTiO_3$-$CaTiO_3$ piezoceramics by a water-based mixed-oxide route: synergetic action of attrition milling and lyophilization

8.1 Introduction

Nowadays, the mainstream to avoid contamination to the soil, adjacent water bodies and the atmosphere when manufacturing, together with the trend to use environmentally benign raw materials and chemistry, have generated a high interest in water-based processing routes [1]. Piezoelectrics are an important class of electroceramics with wide range of applications, including clean and sustainable energy generation by piezoelectric harvesting. This field of research faces the challenge of substituting traditional compositions, which contains toxic lead-oxide, for the so-called "lead-free" compositions [2,3]. Compositions in the pseudo-ternary system of solid solutions $BaZrO_3$-$BaTiO_3$-$CaTiO_3$ (BCZT) are among those more promising for this replacement due to their high sensitivity [4-6]. In this context, exploring environmentally friendly routes for fabrication of lead-free ceramics becomes a considerably important issue.

The most widely used route for preparing piezoelectric ceramics is the solid-state route, also called *mixed-oxides route*, which is easy to carry out and scalable for industrial fabrication. Basically, it involves four steps. First, raw materials (oxides and carbonates) are mixed and wet milled, and the obtained slurry is dried in an oven, aiming to get a fine particle size and homogeneous powder. The second step is the solid-state synthesis at high temperature to form the solid solution, process also called *calcination*. Afterwards, the calcined powder is wet milled again to break hard agglomerates, which prevents non-uniformity and exaggerated grain growth. This process benefits the fourth and last step, which is the sintering at high temperature to obtain a dense ceramic body. One of the drawbacks of the BCZT compositions are the long times of milling (up to 24h) and the high synthesis temperature (above 1300°C) and further high sintering temperatures (up to 1500°C) needed for its fabrication by solid state route [5,7-9,10-12]Therefore, the development of alternative processing routes with reduced thermal budget has focused interest towards scalability to industrial fabrication [13-17].

Up to date, there are numerous articles in the literature dealing with different solid-state routes of preparing BCZT by milling in diverse liquid media, such as isopropanol [17], ethanol [11,12], unspecified alcohol [7]acetone [10],among others. However, scarce work [18,19] has been carried on in the processing of piezoelectric ceramics by mixed oxides route in water media. Particularly with regard to BCZT ceramics, previous reports using aqueous-based solid-state routes are lacking. One of the reasons why water is not used as liquid media for milling is because drying a water-based slurry is much slower than drying in any other organic solvents and, therefore, the risk of segregation of reactants as a function of the densities is higher. Besides, the common water sensitiveness of the ceramic powders and the consequent leaching of material components is considered a major drawback for water-based processing synthetic BCZT powders, leading to rather elaborated formation of surface treated BCZT particles for use in ceramic fabrication via colloidal methods (tape casting, slip casting, etc.) [20,21].The reason for the detrimental effects of water is believed to be the instability of alkaline-earth titanates in water causing their hydrolysis. Nevertheless, $BaTiO_3$ is produced commercially by the water-based hydrothermal synthesis [22] and there are, as well, examples in the literature of such a kind of synthesis [23]. It seems worthwhile to test if the restrictions to use water-based processing of BCZT could be related to the need of using prolonged milling times.

In this regard, attrition ball milling is believed to produce the finest product for a fixed energy input, and it is a technique widely used in industry. Recently, the authors of this work have shown the feasibility of fabrication of BCZT piezoceramics benefiting of ultra-low synthesis and sintering temperatures thanks to the efficient attrition ball milling in isopropanol [17].

Lyophilization or freeze drying consists on the sublimation of the ice at reduced pressure in a completely frozen sample. It is a fast-drying process, which is widely used in industry and research because of the easiness of use, cheapness, speed and reproducibility. That is the case of food industry [24,25], pharmaceutical industry [26], agricultural biotechnologies [27], vaccine delivery [28], microbiology [29], oral and dental tissue engineering[30], bone tissue engineering[31], etc. Furthermore, this is a water-based drying procedure and, therefore, an environmentally friendly process. There are examples in the literature of ceramics prepared by lyophilization [32-38].In general terms, an aqueous suspension of the ceramic particles

is prepared, homogenized and frozen, so as to preserve the uniformity of the suspension at all points. Such a suspension is lyophilized, giving rise to a uniform powder, without segregation of components, homogeneous in composition. However, to the best of our knowledge, up to date no works have been published regarding lyophilization in the production of bulk piezoelectric materials. Only a few recent works can be found in the literature regarding specific unidirectional porous freeze-casted piezoelectric materials, hierarchically structured [39,40].

In this context, the use of water for wet milling in an environmentally benign processing of BCZT relies on the one hand, on reducing the commonly used prolonged times of milling and, on the other, on using a drying procedure that keeps homogeneity by avoiding particle agglomeration and segregation. The aim of this work is to investigate a novel mixed oxides route of fabrication of BCZT piezoceramics, based on milling in water. This will be done by using attrition milling combined with non-oriented-freezing and subsequent lyophilization before calcination. The possibility of reducing the thermal budget of both the calcination and sintering steps will also be tested. Subsequently, the effect of this route on the structural, microstructural and electromechanical properties of the ceramics will be evaluated.

8.2 Materials and methods

8.2.1 Materials

Ceramic powders of nominal composition $(Ba_{0.92}\ Ca_{0.08})\ (Ti_{0.95}\ Zr_{0.05})\ O_3$ [7], abbreviated as BCZT0805, were prepared by a solid-state route starting from a stoichiometric mixture of $BaCO_3$ (Merck, Darmstadt, Germany, >99%), $CaCO_3$ (Sigma Aldrich, St. Louis, MO, USA, >99%), TiO_2 (Merck, of nominal purity >99% composed of 85 wt.% of anatase and 15 wt.% of rutile) and ZrO_2 (Tosoh, Tokyo, Japan, monoclinic polymorph >99%).

8.2.2 Powders and Ceramics Processing

The raw materials were dried at 80°C overnight, weighted according to the nominal composition indicated above and mixed. Once mixed, these raw materials were mechanically treated by Attrition Ball Milling (ABM) at 700 rpm for 5-6 hours in distilled water as liquid medium. The powder mixture to be ground is placed in a

tank of 500 ml with the grinding media. For minimum wear and contamination, media should be harder than the particles to be ground, thus, 3Y-TZP balls (d = 3 mm) with a Ball-to-Powder weight Ratio (BPR) of 30 were used, according to previous adopted approaches [13]and because higher slurry viscosity can reduce particle mobility. For this process, to prevent contamination, a stainless-steel tank, internally coated with Teflon® was chosen.

The as-obtained slurry was dried by lyophilization. First, after the ball milling, the suspension was promptly transferred into a beaker and frozen by immersion in a container with liquid nitrogen for about 30 minutes. The frozen suspension was subsequently lyophilized for 24 hours in a lyophiliser (Cryodos-50, IMA-TELSTAR, S.L., Barcelona, Spain) until completely dried. The temperature of the cold finger in this equipment is continuously set at -50°C±2°C. The freeze-dryer chamber pressure during the entire process was 0.06±0.01 mbar. Under these conditions, according to the phase diagram of water, the water exists as vapour. At the end of the process, a powder with a high degree of drying is obtained.

The resulting powder was calcined inside a crucible covered with a lid in an electrical furnace in air with a heating rate of 3°C/min until 700°C.

After calcination, the powder is subjected to a second ABM in distilled water for 3 hours under the same conditions described above for the mixture of raw materials. Size reduction by attrition is considered relatively faster for hard agglomerates, those expected to be present in the calcined powder, thus allowing reduction of the milling time of the calcined powder.

Disk-shape green bodies from each type of powder were obtained by uniaxial pressing (1.2 tons for 180 s) without binder. They were also sintered in a crucible covered with a lid. Different sintering times and temperatures were explored while keeping a constant heating rate of 5°C/min. The bulk densities were determined by the geometric method.

8.2.3 Characterization

The influence of ball milling and lyophilization on the powders has been evaluated by Differential Scanning Calorimetry (DSC) and Thermogravimetric Analysis (TGA). Thermal characterization was conducted in a TA

instruments (USA) SDT Q600 Thermogravimetric Analyzer & Differential Scanning Calorimeter in air and at a rate of 10°C/min.

Morphological characterization of the powder samples and fresh fracture surface of the sintered ceramic disks have been accomplished by Scanning Electron Microscopy (SEM) using a Phenom Pro G2 SEM microscope (Thermo Scientific, USA) operating at a beam voltage of 5 kV.

Powder particle size was analysed by Dynamic Light Scattering (DLS) using a Zetasizer Nano S (Malvern Instruments, United Kingdom).

Structural investigations of powder and sintered ceramic samples were conducted using a Rigaku Smartlab diffractometer, equipped with a rotating anode (CuK_α = 1.54178 Å) set at 40 kV and 100 mA. The diffractometer is equipped with a graphite monochromator and a scintillation tube in the diffracted beam. Measurements were performed in step-scanning mode, from 15° to 130° (2Θ), using 0.05° as step size and 4 s of integration time at each datum. Quantitative analysis of the crystalline phases and structure determinations were performed with the MAUD software, a Rietveld extended program [41]. The Crystallography Information Format (CIF) files of the phases assigned in the patterns were uploaded from the Crystallography Open Database [42]. Lattice parameters of the constituent phases were refined from the line peak positions after allowing a correction for the zero-offset, while crystallite size and lattice disorder contributions to the peak broadening were separated taking advantage of the wide angular diffraction range explored.

The fresh fracture surface morphology of the samples was studied by Field Emission Scanning Electron Microscopy at ultra-high resolution with Energy Dispersive X-ray spectroscopy (FESEM-EDX), with a FEI *NOVA NanoSEM 230* FE-SEM (Eindhoven, Netherlands). A semi-quantitative analysis of elements was accomplished with the Apollo 10 EDAX detector (Leicester, UK) operating at a maximum voltage of 20 kV to obtain well-resolved peaks. EDX spectra were conducted in specific regions in the interior of the grains and in triple junctions at 10 different locations on the sample.

To measure the electric properties, the sintered disks with a diameter of 11 mm were reduced in thickness by polishing down to ~ 1mm. Silver paste was attached on both surfaces of the thin disks and sintered at 400°C for 1 hour to obtain the electrodes. After that, samples were poled in thickness under a field of 15 kV/cm at 40°C for 1h in a silicone oil bath, followed by field cooling (FC) to room temperature. Measurements took place two hours after poling. Permittivity, real part and losses, was measured at 1 kHz using an impedance analyser (HP 4262A LCR meter). The quasi-static d_{33} piezoelectric charge coefficient was measured with a Berlincourt d_{33}-meter at 100Hz. Complex impedance, modulus and phase, as a function of the frequency, the so-called resonance curve, was measured with an impedance analyser (HP 4192A-LF) at the, electrically induced, radial extensional resonance of the thickness poled thin disks. An automatic iterative method was used in the analysis of the resonance curves to determine the complex electromechanical, elastic and dielectric properties of the ceramics, together with the electromechanical coupling factor [43].

8.3 Results and discussion

8.3.1 Processing and characterization of the Powders

The DSC-TGA profiles versus the scanning temperature illustrated in **Figure 8.3.1** are, mainly, characterized by four weight loss steps, corresponding to as many endothermic events. The first endothermic peak (93°C), with a weight loss of 0.7 wt.%, can be correlated with the evaporation of the residual water adsorbed on the processed powders. The second thermal event, peaked around 526°C, occurred with a weight loss of 2.4 wt.%. The third endotherm started at 600°C with a further mass loss of 12 wt.% until a plateau reached at 700°C. As previously observed by attrition ball milling in isopropanol at 474°C and 582°C [13], these two almost consecutive events, could be ascribable to the decomposition of calcium and barium carbonates, respectively, which lead to the formation of BCZT phase.

The efficiency of the attrition ball milling on the activation of the mixture of the reactants towards the calcinations step is evidenced by the reduction of the temperature of formation of the main perovskite structure (blue curves) when compared with the same temperature measured at the DSC-TGA curve of the

mere mixture of the reactants (grey lines) [17], also shown in **Figure 8.3.1** for clarity sakeness. The TGA curve of ABM powder in water (**Figure 8.3.1(b)**, blue curve) displays a temperature of 700°C in the final plateau, compared to the value of 1000°C observed in the curve of the mixture not subjected to ABM (Figure 1b, grey curve). In the final processing, this testifies a reduction of 300°C, indicating a noticeable activation carried out on the mixture of precursors.

Operated at a low rotor speed, the grinding action of the attrition milling can imitate that of a planetary or vibratory ball mill. However, at a higher rotor speed, the much higher power input per unit volume of media significantly increases the grinding kinetics [44]. Agitation of the grinding media is provided by a rotating central shaft with arms inside a stationary tank. The rotating arms exert enough stirring action to force the grinding media to move randomly through the entire tank. The rotating arms cause the irregular movements by exerting (a) impact action on neighbouring media that collide with other media, (b) rotational (shear) forces on the media, and (c) impact forces on the media fall into the void left by the arms. For efficient fine grinding, both impact forces and shear forces should be present. A key to its efficiency is that the power input is used directly for agitating media for grinding and is not used for rotating or vibrating a large, heavy vessel in addition to the media [45].

Notwithstanding the important reduction of the temperature of the BCZT formation in the milled with respect to the unmilled powder, it must be noted that temperatures of the pure BCZT synthesis by solid state route currently found in the literature are above 1200°C [5,7,9-12], a value much higher than that, noticeably, encountered after the water-based synthetic approach used here. Furthermore, this temperature can be compared with those used for other, more reactive, synthesis methods (mechanosynthesis, sol-gel) [9, 13] as it was already observed when attrition milling in isopropanol [17].

To extend the characterization of this activation process, the SEM images to determine the morphology of the unmilled mixture of reactants (**Figure 8.3.2(a)**) show that, as expected, this is far from being homogeneous at a few microns level, since it shows particle sizes of some 5 microns up to agglomerates of a few tens of microns (not shown here). Likewise, the ball-milled powder dried in oven overnight at 120°C (**Figure 8.3.2(b)**) is not homogeneous either, as it presents agglomerates that may affect the BCZT synthesis.

During a conventional liquid-phase drying process in oven or at room temperature (Figure 2b), the top layer of the liquid quickly evaporates, concentrating the particles near the surface. This develops an impenetrable skin that prevents the remaining suspension from drying. As a result, the suspension dries at dissimilar rates at different points. This process occurs for a long period in the case of water, which can favour the decantation of the heavier components and, therefore, a heterogeneous composition throughout the powder sample. Using alcohol, acetone, or similar organics, as liquid media helps reducing drying times, but at the expense of not being an environmental benign practice.

This lack of homogeneity of the dried powder evidenced the need to find a way to even sizes of the powder used for the BCZT synthesis.

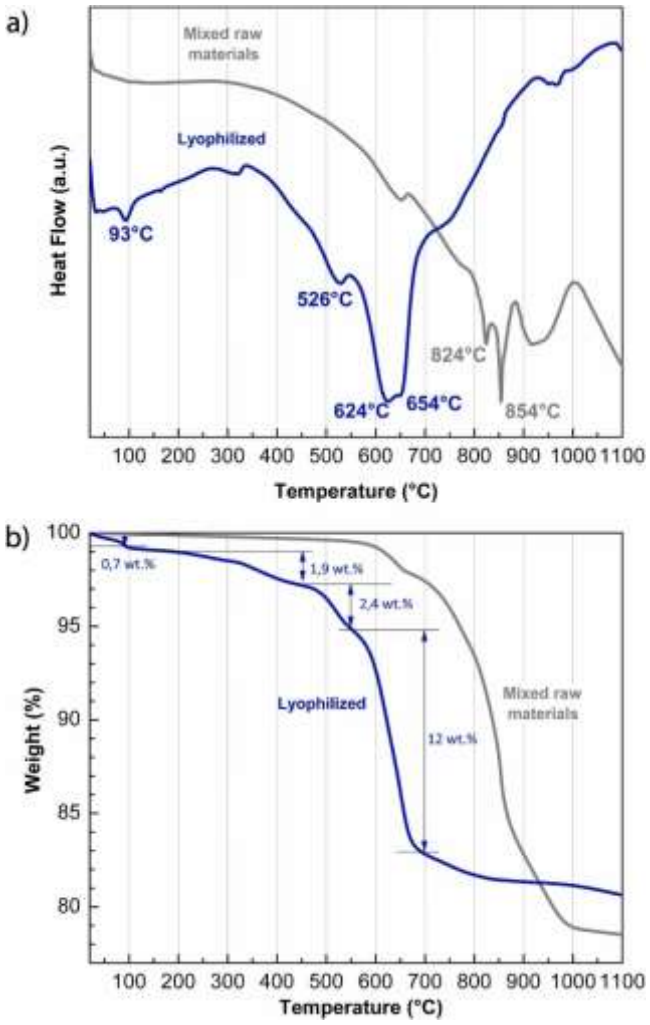

Figure 8.3.1 a) DSC analysis and **b)** TG analysis of the mixture of reactants (in grey colour) and the suspension ball-milled for 6h, subsequently frozen and lyophilized (in blue colour).

As shown in **Figure 8.3.2(c)**, the detrimental effects of drying in oven are avoided by lyophilization. First, the well-dispersed slurry must be frozen quickly, which allows preserving its volume uniformity. The subsequent lyophilization under vacuum and low temperature allows ice being sublimated. The primary benefit of lyophilization over liquid-phase drying is the ability to keep the suspension frozen throughout the drying process, which avoids components segregation, leading to better homogeneity all over the powder sample. Therefore, according to the corresponding SEM image (Figure 2c) freezing and lyophilization of the water-based slurry provides a very fine and uniform powder, with no presence of agglomerates, which guarantees greater homogeneity (both in particle size and in composition) than drying in oven.

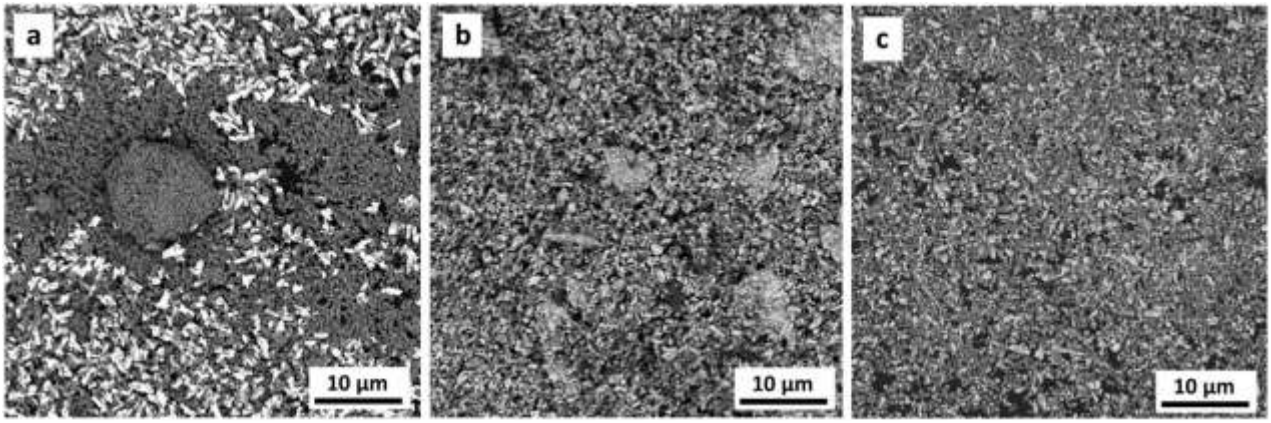

Figure 8.3.2 SEM micrographs of: **a)**mixed raw materials; **b)**mixed raw materials after 6h attrition ball-milling in water and dried in oven at 120°C; **c)**mixed raw materials, ball-milled in water for 6h, frozen and lyophilized

To further assess the benefits of freezing and lyophilizing the slurry just after attrition milling in water, **Figure 8.3.3** shows the SEM micrographs of powder samples at higher magnification and their particle size distribution after lyophilization at the different stages of the BCZT powder processing, prior to the sintering of the powders.

After the first attrition ball milling in water, the as-lyophilized powder presents a homogeneous appearance (**Figures 8.3.3a1 and 8.3.3a2**). The particle size distribution is monomodal and narrow, with submicronic particles, presenting a percentile D50 (average particle size) of 600 nm (**Figure 8.3.3a3**).

Once calcined at 700°C (**Figures 8.3.3b1 and 8.3.3b2**) the particles have deformed: necks between particles and new aggregates have formed. Therefore, a second ball milling seems mandatory. As shown in **Figure**

8.3.3b3, this powder presents the former main peak with a narrow distribution of submicronic size (around 700 nm) and a new peak at about 2 microns in size. The average particle size of this distribution has increased up to D50= 1.9 microns. The corresponding SEM images (**Figure 8.3.3b1** and **8.3.3b2**) corroborate this result, since it is easy to find a great number of hard agglomerates (**Figure 8.3.3b1**) and small particles as well (**Figure 8.3.3b2**) which are dispersed by the ultrasound treatment previous to the particle size measurement.

As a consequence of the second ABM in water for 3h (**Figures 8.3.3c1 and 8.3.3c2**), the BCZT calcined and milled powder presents only separated particles with a size distribution below 1 micron (**Figure 8.3.3c3**). The average particle size of this distribution has decreased to D_{50} = 0.5 microns, 4 times lower than the value obtained before the second ball-milling treatment. Therefore, only easily conformable small particles to be sintered can be observed, confirming that the aggregates produced after calcination have been broken.

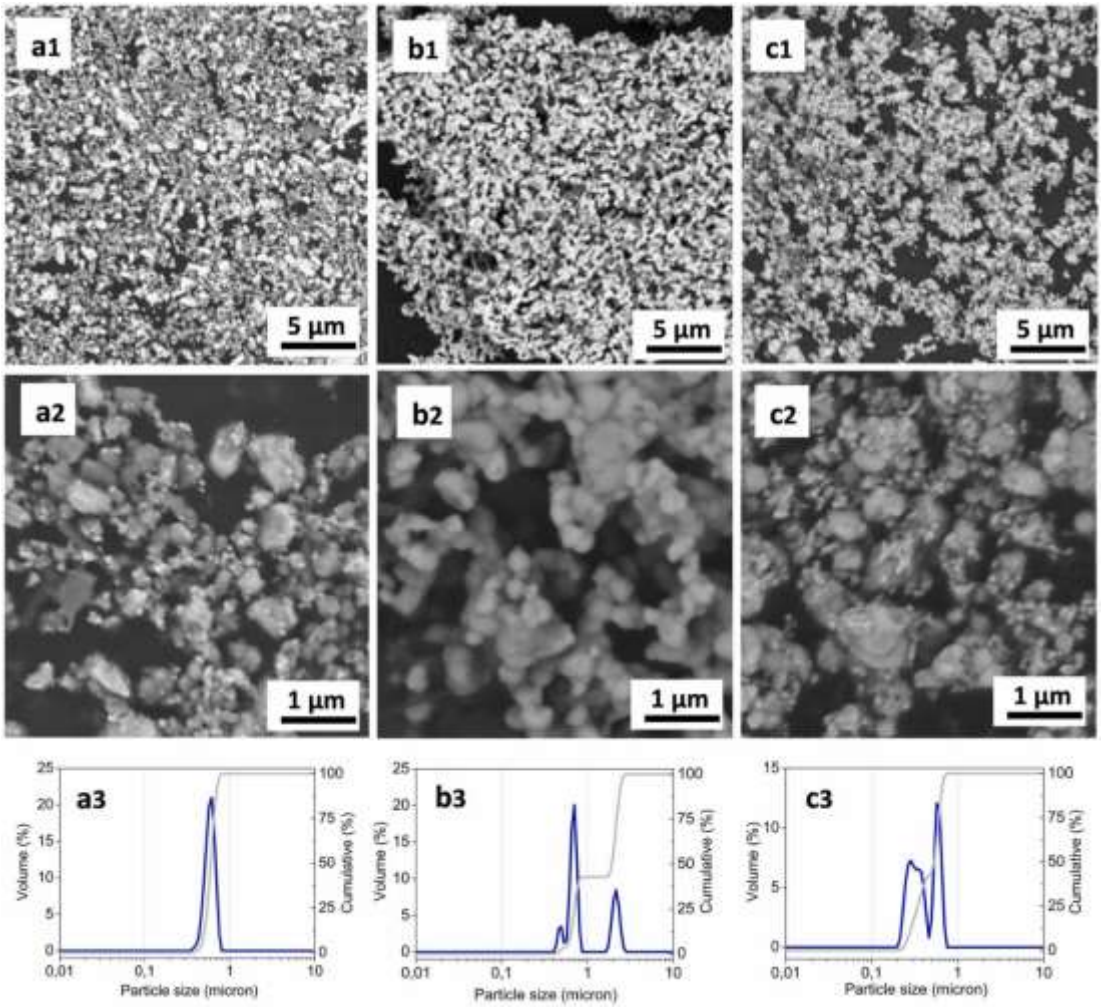

Figure 8.3.3 SEM micrographs, particle size distributions (blue curves) and cumulative particle size distributions (grey curves) of the following powders: **a)**First ABM for 6h in water and lyophilization, **b)**after subsequent calcination (700°C, 30 min), **c)**after the second ABM for 3h in water

To complete the description of the powder samples depicted, as an explanation of the DSC-TGA results (**Figure 8.3.1**) and morphological analysis (**Figures 8.3.2** and **8.3.3**), the as-lyophilized powder, previously subjected to 6h of ball-milling in water, was investigated by XRD. Subsequent thermal treatments and ex *situ* XRD experiments were also performed. To better describe the evolution of the crystalline phase, highlighting the presence of the minor ones, all the XRD analyses have been reported in logarithmic scale in **Figure 8.3.4**.

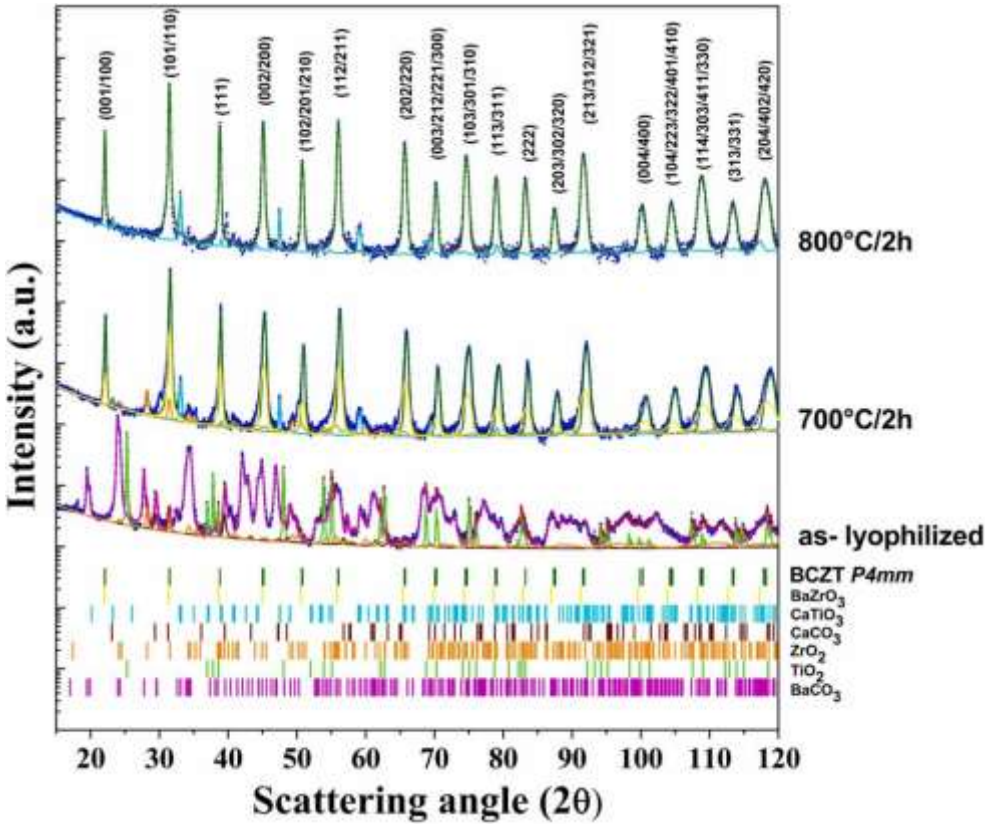

Figure 8.3.4 . From bottom to top: XRD patterns of the BCZT precursors obtained after 6h ABM in water and subjected to lyophilizing treatment, collected *ex situ* as a function of the reported calcination temperature. Fitting curves (coloured lines) of each phase component are obtained after Rietveld refinement. The contributing profiles of each phase are calculated on the basis of the structure (CIF files) as well as microstructure (peak broadening shape parameters) adjusted at the end of the fit. They are displayed as it follows: magenta line ($BaCO_3$) s.g. *Pmcn*, green line (TiO_2) s.g.*I41/amd*, orange line (ZrO_2) s.g. *P21/c*, burgundy coloured line ($CaCO_3$) s.g. *R-3c:H*, olive line (BCZT) s.g. *P4mm*, cyan line orthorhombic ($CaTiO_3$) s.g. *Pbnm*, yellow line, cubic ($BaZrO_3$) s.g. *Pm-3m*.

The bottom pattern refers to the as-lyophilized powders. This pattern is just composed by a mixture of the precursors used, such as titanium dioxide (TiO_2, 28 wt.%), barium carbonate ($BaCO_3$, 68 wt.%), calcium carbonate ($CaCO_3$, 2 wt.%) and zirconia (ZrO_2, 2 wt.%). This confirms the selected stoichiometry and lack of contamination of the mixture of reactants as wished for this processing step.

The formation of BCZT (tetragonal, *P4mm,* a= 4.0015 Å, c/a=1.005, 83 wt.%) is already observed for calcined powder at 700°C-30 min (not shown here). It should be noted the simultaneous formation of a small amount of perovskite $CaTiO_3$ (3 wt.%). Furthermore, the presence of zirconia can also be detected as unreacted precursor (2 wt.%). The presence of an intermediate compound can only be inferred from the careful analysis of the XRD pattern by a Rietveld refinement from the shoulders on each reflection of BCZT (12 wt.%). This

secondary phase has been found to be $BaZrO_3$. None of these secondary phases seem to be linked to the water-based procedure used here, as they were also found in previous organic-solvent based routes [46] [17].

The powder treated at 700°C -2h (**Figure 8.3.4**) shows a slightly higher amount of the same BCZT perovskite (87 wt.%.), while the amount of $BaZrO_3$ slightly decreases (down to 8 wt.%) and the percentage of $CaTiO_3$ and zirconia is unmodified.

Finally, by fixing the dwell time to 2 hours, but increasing the temperature to 800°C, the amount of the BCZT phase reaches 93 wt.%, but the cell parameters are: a= 4.0167 Å, c/a=1.003. Also, the percentage of $CaTiO_3$ remains almost unmodified (4 wt.%), and the formation of another, unassigned, secondary phase can be observed (estimated 3 wt.%). $BaZrO_3$ already disappears at 800°C, due to the diffusion of Zr^{4+} into the main lattice, as reported in literature [47].

Despite the higher conversion of the precursors into BCZT obtained at 800°C-2h, the synthesis conditions have been set to 700°C for 2 hours. The reason clearly emerges from the XRD analysis: by increasing the temperature, the c/a ratio shows a decrease in the tetragonal distortion (c/a), approaching to 1. This is directly related to the magnitude of the spontaneous polarization of the unit cell, which, in turn, is related to the potential piezoelectric activity of the final ceramic.

It is also important to highlight that the calcined powder obtained here is free of unreacted carbonates that could decompose at higher temperatures, which could cause porosity during sintering. Moreover, the weight loss of the calcined powder with respect to the milled precursors is higher when the synthesis is carried out at higher temperature. Instead of being lost by volatilization, it is currently observed that the secondary phase of the synthetic powder diffuses into the lattice and incorporates to the BCZT perovskite when confined in the pressed pellet during the sintering step at higher temperature [47,48]. Therefore, the presence of the unreacted zirconia and $BaZrO_3$ should not be considered an issue.

8.3.2 Processing and characterization of ceramics

Based on previous works showing enhancement of the densification and properties of pure $BaTiO_3$ and ceramics based on it [17,23], two types of sintering schedule with variable times and maximum sintering temperature of 1280°C were used: a single sintering plateau and a two-step sintering with an intermediate plateau at 900°C. **Figure 8.3.5** depicts a representative XRD pattern of ceramics after one and two-steps sintering. This comparison shows that the two selected sintering conditions chosen, have the same effect on the crystal structure of the ceramic material. All sintered ceramics present a majority of BCZT phase (Figure 8.3.5) with a= 4.0052 Å, c/a=1.004. Residual quantities of secondary phases (<2%), which can hardly be observed unless studied using Rietveld refinement, were mainly found in the one-step sintered samples (Figure 8.3.5). However, the $CaTiO_3$, detected in the synthesis step (see **Figure 8.3.4**), cannot be observed in any of the two types of ceramics. The XRD analysis does not appreciate sensible differences in the characteristics of the main BCZT phase for the two types of sintering conditions chosen.

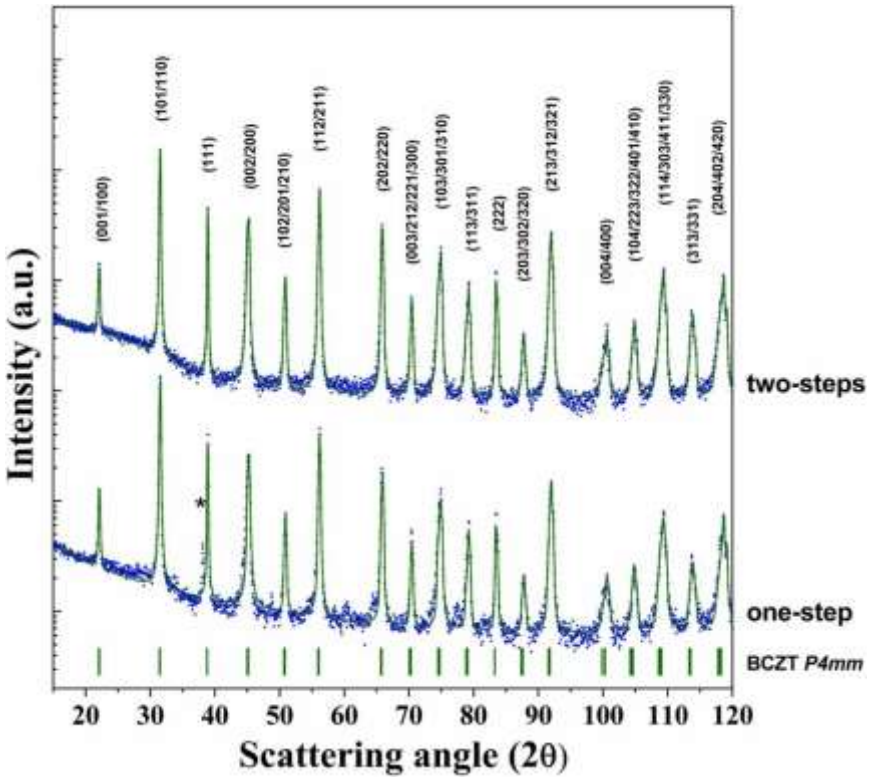

Figure 8.3.5 XRD diffraction pattern of a ceramics sintered with one and two sintering steps with final temperature at 1280°C. (*) Ag from electrode.

It has been reported that the electrical properties of the BCZT system strongly depend on processing conditions which, in turn, determine their crystallographic and ceramic microstructure [49]. The tetragonal distortion of the BCZT ceramics here obtained is of c/a=1.004, which indicates a spontaneous polarization smaller than in the as-synthesized powder. However, the BCZT still keeps a high enough lattice distortion that holds within the range needed for optimizing the piezoelectric response of the material.

Representative SEM images of the fracture surfaces of sintered BCZT ceramics with one and two-sintering steps are shown in **Figure 8.3.6**. All ceramics sintered with one step have densities lower than 90% (**Figures 8.3.6(a) and 8.3.6(b)**). An appropriate two-step sintering treatment promotes reduction of the number of pores and their size (**Figures 8.3.6(c) and 8.3.6(d)**).

It is also noticeable that, in all ceramics obtained in this work, the fracture is transgranular –as the second phase is mainly located at triple points-, which indicates strong grain boundaries and proper sinterability.

The SEM images in **Figure 8.3.6** have been taken using a backscattering emission mode. Typically, heavier elements can deflect incident electrons more strongly than lighter elements and, consequently, the regions rich in the heavier elements appear brighter. The areas marked with arrows in the SEM images of the one-step sintered ceramics (**Figure 8.3.6(b)**) appear darker than the main BCZT grains, which means that such areas are poorer in the heavy ion (barium) than the main BCZT grains. These darker areas of liquid-like metastable phase cannot be detected by XRD analysis because of its low amount and poor crystallinity. However, this could be confirmed by the complementary EDX compositional analysis in **Figure 8.3.7**. Two representative EDX spectra, taken (a) inside one of the BCZT grains and (b) in an area that contains the darker phase, are shown in Figure 7. The ratio between intensities of the main peaks, ascribed to O-Kα and Ti-Lα signal and to Ti-Kα and Ba-Lα signal, changes drastically from point (a) to point (b). There is an obvious relative decrease of the intensity of the peak that indicates the Ba content in the darker area (b), while the ratio of the intensity of the O-Kα and Ti-Lα signal with respect to the intensity of the other peaks (Zr- Lα signal and Ca-Kα signal), is almost unmodified. The presence of remaining Ba-Lα and Zr-Lα signal in the darker phase analysis comes, most probably, from the excited volume below the surface from which the signals are collected. By comparing Figure 6b (one-step sintered) to Figure 6d (after using an appropriated two-steps

sintering procedure), it can be observed that the amount of dark areas at the triple points has diminished in the second one. Therefore, two-steps sintering results in a major pure BCZT perovskite phase, as confirmed by the XRD study (**Figure 8.3.5**).

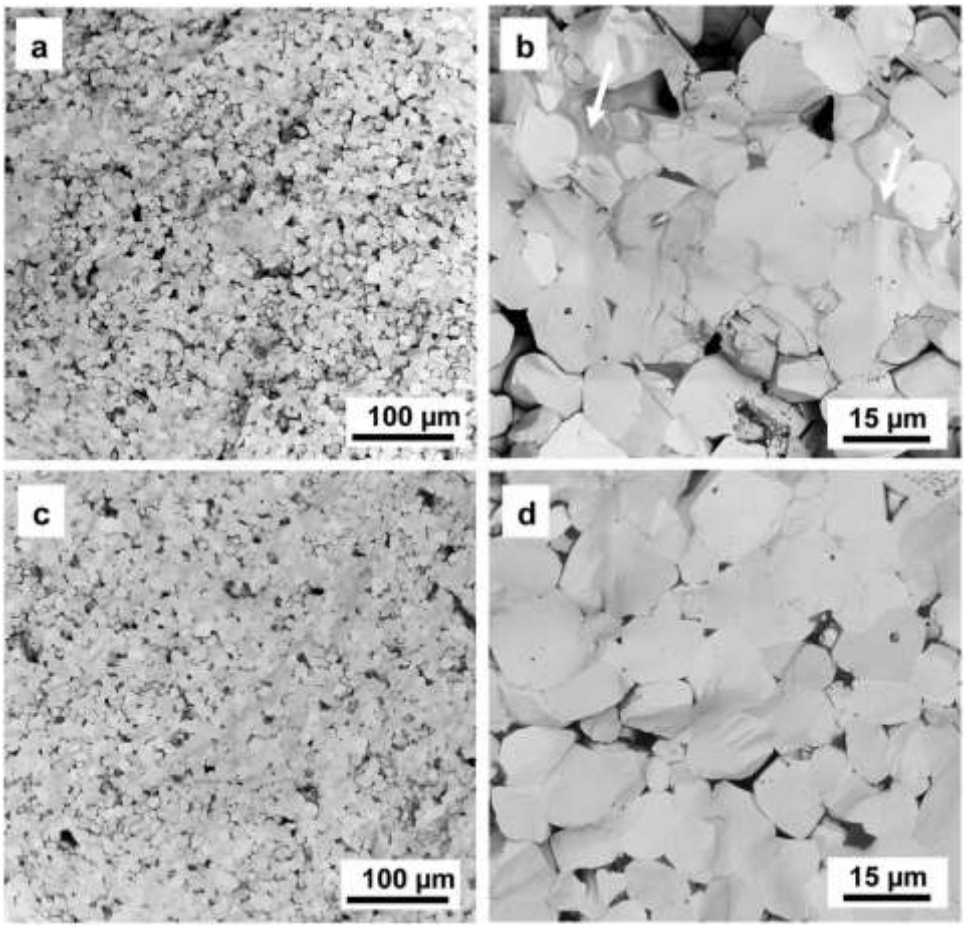

Figure 8.3.6 Representative SEM images (backscattering mode) of the fracture surfaces of sintered BCZT ceramics. **(a,b)** after one-step sintering and **(c,d)** after two-steps sintering with final temperature of 1280°C for 6 h.

The sintering schedule should be designed also to enable control of grain growth. This is of foremost importance to tailor the properties of the BCZT ceramics, as the latter are more dependent on the grain size rather than on the densification of the ceramic [50]. Average grain size over 25 microns contribute to decrease the piezoelectric activity. In this work, the grain size is controlled by the low sintering temperature of 1280°C to keep a proper value, roughly 10 microns, in the range needed to promote high piezoelectric sensitivity.

Up to this point, the analysis of powders and ceramics samples have shown that the proposed route using water as a solvent is as successful as any other route using organic solvents in preparing crystalline and nominally single-phase BCZT ceramics with an appropriated microstructure. It cannot be ignored that the electrical properties of $BaTiO_3$ are extremely sensitive to the presence of low levels of dopants (intentional or unintentional). Minor changes in composition can be detected by variations in polymorphic phase transition temperatures, subgrain microstructure, dielectric behaviour <200°C and/or electrical conductivity >300°C and piezoelectric properties. It has already been shown that attrition milling of $BaTiO_3$ powder using YSZ milling balls has a significant effect on the dielectric and conduction properties of $BaTiO_3$ ceramics and that this effect is related to unintentional contamination associated with the milling media and that it increases for prolonged milling times [50]. Homovalent substituents at the B-site (Zr^{4+}, Sn^{4+}, Hf^{4+}, Ce^{4+}) influence the transition temperature to the paraelectric phase more than those at the A-site (Ca^{2+}, Sr^{2+}), which are outside of the oxygen octahedra of the perovskite. The reason for this behaviour is considered that that B-site cations have a direct effect on the octahedral distortion, whereas A-site cations have an effect only on the strength of the Ti-O bond [51]. Among other potential problems to overcome in the processing of BCZT, the effect of the secondary $CaTiO_3$ paraelectric phase on the dielectric properties of $BaTiO_3$ has shown that the peak level of permittivity at the transition to the paraelectric phase decreases and the width of the peak increases [52].

Though such effects could also be present in the ceramics here prepared, all of them are common to the solid-state process using prolonged milling times or unappropriated sintering schedules, regardless of the substitution of organics by water as non-toxic solvent, which is the target of this work. Keeping these issues in mind, our processing approach was designed to avoid them. In the following we will focus on the piezoelectric characterization of the obtained ceramics to manifest their potential application as ultrasonic transducers.

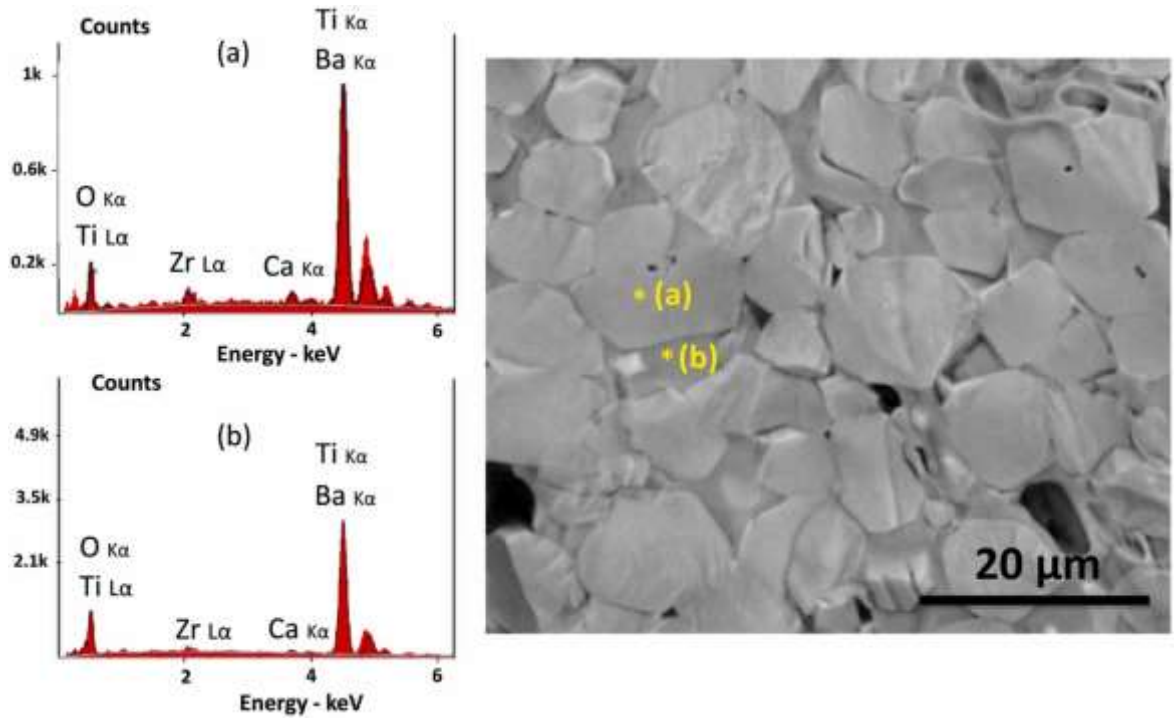

Figure 8.3.7 EDX spectra taken in two points of the surface, marked with asteriks in the corresponding FE-SEM micrograph, of the one-step sintered ceramic with final temperature of 1280 °C for 6 h.

Single step sintering leads to ceramic samples with high sensitivity and low dielectric losses, with maximum value of d_{33}=280 pC/N, ε'^{T}_{33} = 2862 and tanδ=0.047 at 1kHz when sintered at 1280°C/4h, which matches the previously reported value for this composition [7,17,49]. However, the presence of secondary phases affects their ultrasonic transduction, and the planar coupling factor is low (k_p=28.10%). This is not unexpected as uncorrelated high piezoelectric coefficient d_{33} and low coupling factor k_p have been observed in microstructurally damaged ceramics, due to the concomitant increase of the elastic compliance at resonance [53]. By further increasing the sintering temperature to 1300°C for 4h, there is a risk that the ceramic microstructure suffers degradation by increase of the grain size and formation of new intergranular porosity with subsequent reduction of the overall piezoelectric performance (d_{33}=224 pC/N, ε'^{T}_{33} = 2920 and tanδ=0.215 at 1kHz and k_p=25.00%).

In agreement with the XRD and SEM analysis of the sintered ceramics that shows the optimum crystal structure and ceramic microstructure for two-steps sintered ceramics, **Table 8.3.1** shows a better set of piezoelectric results. d_{33} coefficient and the piezoelectric, elastic and dielectric coefficients, including mechanical quality factors and dielectric loss factors are shown in **Table 8.3.1**. The electromechanical

coupling factor and the frequency number of the planar resonance, together with the regression factor of the reconstructed to the experimental spectra ((R, G) plot in **Figure 8.3.8**), as indication of the precision of the obtained parameters, are also shown. This were obtained from the measurement of the radial resonance of the poled ceramic disks from ABM powder for 6h in water, non-oriented freezed and lyophilized and calcined at 700°C for 2h, ABM for 3h in water after calcination and after two-step sintering at 900°C for 3 h followed by 1280°C for 6 h, aiming to enhance sinterability and to promote grain growth (**Figures 8.3.6(b) and 8.3.6(d)**).

Despite the ultra-low temperature conditions of synthesis and low sintering budget used for the processing of these ceramics, their optimized structure (**Figure 8.3.5**) and microstructure (**Figure 8.3.6**) resulted also in the achievement of high sensitivity BCZT ceramics, combining both higher d_{33} and k_p, together with reasonably low mechanical and dielectric losses at 1kHz and, also, for the planar resonance. All these characteristics are illustrated by the resonance curves (as (/Z/, θ) and (R, G) plots) depicted in **Figure 8.3.8**.

The electromechanical characterization evidence that the water-based approach for processing BCZT0805 ceramics here developed does not limit the obtention of high sensitivity BCZT piezoelectric ceramics. Contrarily, these results show that this is an appealing water-based and industrially scalable processing proposal for the development of lead-free piezoelectric materials with industrial uses.

Table 8.3.1 Some relevant material coefficients obtained from the Radial mode of resonance of the sintered ceramics. The complex material coefficients (P = P′ + iP′′) are given as real part (P′) and losses (piezoelectric and mechanical Q factor (P′/P′′) and dielectric tanδ (P′′/P′)). $c'^{p}_{11} = s^{E}_{11}/s^{E}_{12}$.

Properties/ Sintering Conditions	**900°C for 3 h followed by 1280°C 6 h**
Density (g/cc)	4.97
Relative density (%)	85
d_{33} (pC/N)	320
ε'^{T}_{33} at 1 kHz	3670
tanδ at 1 kHz	0.036
R^2	0.9998
k_p (%)	31.45
N_p(kHz·mm)	2759
d'_{31} (pC/N)	-110.25
$Q_p(d_{31})$	52
ε'^{T}_{33}	3283
tanδ	0.017
g'_{31} (10^{-3} mV/N)	-3.79
$Q_p(g_{31})$	452
c'^{p}_{11} [1] (10^{10}N·m^{-2})	8.23
Q_m	163

Similarly to what was commented for the synthesis temperatures, it must be pointed out that this final sintering temperature of 1280°C is remarkably lower than the range of temperatures currently used for solid state processing of undoped BCZT in general (1400-1500°C) [5,7,9-12] and, in particular, of BCZT0805 without the use of attrition milling (1450°C [7] and 1400°C [i]). Therefore, this water-based route is not detrimental to the processing and, besides, it provides the benefit of strong reduction of the overall thermal budget of the ceramic processing. This result takes place because of the crystallographic and microstructural homogeneity of the ceramic and minimization of the secondary phases provided by the processing approach explored in this work.

The sintering temperature reduction to 1280°C for obtaining the desired piezoelectric activity is a consequence of the reactivity of the majority BCZT phase with (a= 4.0109 Å, c/a=1.004) of the synthesized powder obtained using ultra-low thermal conditions (700°C-2h) and the fine and homogeneous powder obtained after the second ABM in water during 3h. This, in turn, is a consequence of the enhanced,

homogeneous and reactive, powder produced by the 6h ABM in water, subsequent freezing and final lyophilization processes. Besides, the second attrition ball milling in water media of the calcined powder provides a fine and deagglomerated powder suitable for molding.

Summarizing, this synergetic processing route allows to control the crystal structure, grain size and, ultimately, the properties of the sintered ceramic.

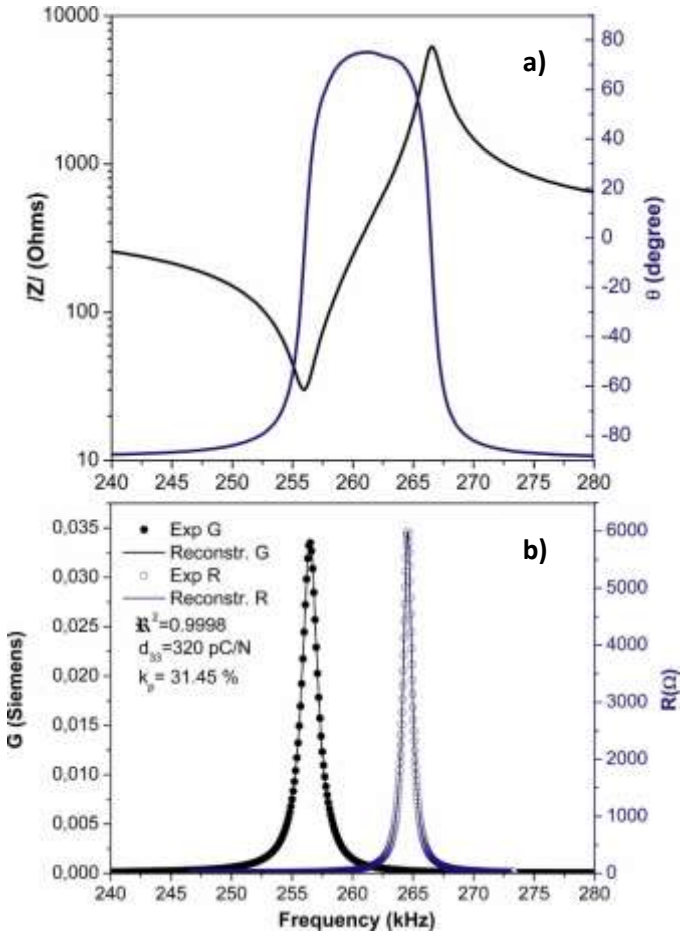

Figure 8.3.8 Fundamental radial extensional resonance mode of a thickness poled and excited thin disk of BCZT0805 ceramic sintered at 900°C-3h followed by 1280°C-6h. **a)**Impedance spectrum, as (/Z/, θ) plot, measured. **b)** Equivalent representation of the impedance spectrum, (R, G) plot, used in the calculation of material coefficients by the iterative automatic method. Symbols are the experimental data and lines are the reconstructed peaks after coefficients calculation.

8.4 Conclusions

A novel environmentally friendly mixed oxides route of fabrication of $(Ba_{0.92}Ca_{0.08})$ $(Ti_{0.95}Zr_{0.05})$ O_3 (BCZT0805) lead-free piezoceramics was developed in this work.

The synergetic effect of attrition milling in water and freezing-lyophilization processes allows to develop a precursor powder of monomodal and narrow size distribution with average particle size of 600 nm. The high homogeneity and reactivity of this powder, as demonstrated by the DSC-TG and FESEM analysis, allows the use of very low thermal budget (700°C-2h) for the solid-state synthesis of BCZT0805.

After a second ball milling in water for 3h, disaggregated particles with a size distribution below 1 micron were obtained. This fine ceramic powder allowed to achieve a reduction of the currently used sintering temperatures from 1400-1500°C down to 1280°C. The so obtained ceramics are well sintered, homogeneous, show transgranular fracture, grain size in the range of 10 microns and contains a major perovskite structure with tetragonal distortion c/a= 1.004. Besides, when two-steps sintering at 1280°C-6h including a plateau at 900°C-3h was used, the ceramic densification was improved, and secondary phases were minimized.

BCZT0805 ceramics processed by the two-steps sintering have electromechanical properties that reach those values obtained by any other processing route in organic media (d_{33}=320 pC/N, d_{31}= -110 pC/N, k_p=31.45 % and N_p=2750 kHz.mm, ε'^{T}_{33} =3670 and tanδ= 0.036 at 1kHz).

This result demonstrates that clean and sustainable water-based processing allows the production of high-sensitivity lead-free piezoelectric ceramics, which has a positive impact in a wide range of industrial applications. These results have been published in Journal of the European Ceramic Society, **2024**, Vol44(5),2944-2953 https://doi.org/10.1016/j.jeurceramsoc.2023.12.037.

Authors contribution: Marzia Mureddu and Sonia Lopez-Esteban: Methodology, Investigation, Validation, Visualization, Writing – original draft. José.F. Bartolomé, Sonia Lopez-Esteban, Sebastiano Garroni and Lorena Pardo: Conceptualization, Methodology, Supervision. Stefano Enzo, Maria Dore: Methodology, Investigation, Validation. Alvaro García: Methodology and Software. José F.Bartolomé, Sonia Lopez-Esteban, Stefano Enzo and Sebastiano Garroni: Resources. All authors: Writing – reviewing & editing.

8.5 Bibliography

1. Chemistry and Water: The Science Behind Sustaining the World's Most Crucial Resource, Ed. Ahuja Consulting, Calabash, NC, United States. Elsevier, Amsterdam, Netherlands (2017) ISBN 978-0-12-809330-6. In.

2. Villafuerte-Castrejón, M.E.; Morán, E.; Reyes-Montero, A.; Vivar-Ocampo, R.; Peña-Jiménez, J.A.; Rea-López, S.O.; Pardo, L. Towards Lead-Free Piezoceramics: Facing a Synthesis Challenge. *Materials (Basel).* 2016, *9*, 1–27, doi:10.3390/ma9010021.

3. Garroni, S.; Senes, N.; Iacomini, A.; Enzo, S.; Mulas, G.; Pardo, L.; Cuesta-Lopez, S. Advanced Synthesis on Lead-Free KxNa(1−x) NbO3 Piezoceramics for Medical Imaging Applications. *Phys. Status Solidi Appl. Mater. Sci.* 2018, *215*, 1–15, doi:10.1002/pssa.201700896.

4. McQuarrie, M.; Behnke, F.W. Structural and Dielectric Studies in the System (Ba, Ca) (Ti, Zr)O 3. *J. Am. Ceram. Soc.* 1954, *37*, 539–543, doi:10.1111/j.1151-2916.1954.tb13986.x.

5. Liu, W.; Ren, X. Large Piezoelectric Effect in Pb-Free Ceramics. *Phys. Rev. Lett.* 2009, *103*, 1–4, doi:10.1103/PhysRevLett.103.257602.

6. Panda, P.K.; Sahoo, B.; Thejas, T.S.; Krishna, M. High D33 Lead-Free Piezoceramics: A Review. *J. Electron. Mater.* 2022, *51*, 938–952, doi:10.1007/s11664-021-09346-0.

7. Li, W.; Xu, Z.; Chu, R.; Fu, P.; Zang, G. Piezoelectric and Dielectric Properties of (Ba1-XCa x)(Ti0.95Zr0.05)O3 Lead-Free Ceramics. *J. Am. Ceram. Soc.* 2010, *93*, 2942–2944, doi:10.1111/j.1551-2916.2010.03907.x.

8. Zhang, Y.; Sun, H.-J.; Chen, W. Li-Modified Ba0.99Ca0.01Zr0.02Ti0.98O3 Lead-Free Ceramics with Highly Improved Piezoelectricity. *J. Alloys Compd.* 2017, *694*, 745–751, doi:10.1016/j.jallcom.2016.10.061.

9. Wang, Z.; Wang, J.; Chao, X.; Wei, L.; Yang, B.; Wang, D.; Yang, Z. Synthesis, Structure, Dielectric, Piezoelectric, and Energy Storage Performance of (Ba0.85Ca0.15)(Ti0.9Zr0.1)O3 Ceramics Prepared by Different Methods. *J. Mater. Sci. Mater. Electron.* 2016, *27*, 5047–5058, doi:10.1007/s10854-016-4392-x.

10. Reyes-Montero, A.; Pardo, L.; López-Juárez, R.; González, A.M.; Rea-López, S.O.; Cruz, M.P.; Villafuerte-Castrejón, M.E. Sub-10 Mm Grain Size, Ba 1− x Ca x Ti 0.9 Zr 0.1 O 3 (x = 0.10 and x = 0.15) Piezoceramics Processed Using a Reduced Thermal Treatment. *Smart Mater. Struct.* 2015, *24*, 065033, doi:10.1088/0964-1726/24/6/065033.

11. Hayati, R.; Fayazi, M.; Diargar, H.; Kaveh, M.; Tayebi, L. Electrical and Mechanical Properties of BZT − x BCT Lead-free Piezoceramics. *Int. J. Appl. Ceram. Technol.* 2020, *17*, 1891–1898, doi:10.1111/ijac.13494.

12. Li, W.; Xu, Z.; Chu, R.; Fu, P.; Zang, G. Polymorphic Phase Transition and Piezoelectric Properties of (Ba1−xCax)(Ti0.9Zr0.1)O3 Lead-Free Ceramics. *Phys. B Condens. Matter* 2010, *405*, 4513–4516, doi:10.1016/j.physb.2010.08.028.

13. Reyes-Montero, A.; Pardo, L.; López-Juárez, R.; González, A.M.; Cruz, M.P.; Villafuerte-Castrejón, M.E. Lead-Free Ba0.9Ca0.1Ti0.9Zr0.1O3 Piezoelectric Ceramics Processed below 1300°C. *J. Alloys Compd.* 2014, *584*, 28–33, doi:10.1016/j.jallcom.2013.08.165.

14. Lu, X.; Fang, B.; Zhang, S.; Yuan, N.; Ding, J.; Zhao, X.; Wang, F.; Tang, Y.; Shi, W.; Xu, H.; et al. Decreasing Sintering Temperature for BCZT Lead-Free Ceramics Prepared via Hydrothermal Route. *Funct. Mater. Lett.* 2017, *10*, 1750046, doi:10.1142/S1793604717500461.

15. Ji, X.; Wang, C.; Luo, W.; Chen, G.; Zhang, S.; Tu, R.; Shen, Q.; Shi, J.; Zhang, L. Effect of Solution Concentration on Low-Temperature Synthesis of BCZT Powders by Sol–Gel-Hydrothermal Method. *J. Sol-Gel Sci. Technol.* 2020, *94*, 205–212, doi:10.1007/s10971-019-05177-y.

16. Hanani, Z.; Ablouh, E.-H.; Amjoud, M. 'bare.; Mezzane, D.; Fourcade, S.; Gouné, M. Very-Low Temperature Synthesis of Pure and Crystalline Lead-Free Ba .85 Ca .15 Zr .1 Ti .9 O 3 Ceramic. *Ceram. Int.* 2018, *44*, 10997–11000, doi:10.1016/j.ceramint.2018.03.022.

17. Mureddu, M.; Bartolomé, J.F.; Lopez-Esteban, S.; Dore, M.; Enzo, S.; García, Á.; Garroni, S.; Pardo, L. Solid State Processing of BCZT Piezoceramics Using Ultra Low Synthesis and Sintering Temperatures. *Materials (Basel).* 2023, *16*, 945, doi:10.3390/ma16030945.

18. Krauss, W.; Schütz, D.; Naderer, M.; Orosel, D.; Reichmann, K. BNT-Based Multilayer Device with Large and Temperature Independent Strain Made by a Water-Based Preparation Process. *J. Eur. Ceram. Soc.* 2011, *31*, 1857–1860, doi:10.1016/j.jeurceramsoc.2011.02.032.

19. Beltrami, R.; Mercadelli, E.; Baldisserri, C.; Galassi, C.; Braghin, F.; Lecis, N. Synthesis of KNN Powders: Scaling Effect of the Milling Step. *Powder Technol.* 2020, *375*, 101–108, doi:10.1016/j.powtec.2020.07.098.

20. Kaushal, A.; Olhero, S.M.; Ferreira, J.M.F. Lead-Free 0.5Ba(Zr0.2Ti0.8)O3–0.5(Ba0.7Ca0.3)TiO3 Powder Surface Treated against Hydrolysis – a Key for a Successful Aqueous Processing. *J. Mater. Chem. C* 2013, *1*, 4846, doi:10.1039/c3tc30741g.

21. Kaushal, A.; Olhero, S.M.; Singh, B.; Zamiri, R.; Saravanan, V.; Ferreira, J.M.F. Successful Aqueous Processing of a Lead Free 0.5Ba(Zr 0.2 Ti 0.8)O 3 –0.5(Ba 0.7 Ca 0.3)TiO 3 Piezoelectric Material Composition. *RSC Adv.* 2014, *4*, 26993–27002, doi:10.1039/C4RA03172E.

22. Karaki, T.; Yan, K.; Adachi, M. Barium Titanate Piezoelectric Ceramics Manufactured by Two-Step Sintering. *Jpn. J. Appl. Phys.* 2007, *46*, 7035, doi:10.1143/JJAP.46.7035.

23. Nanni, P.; Leoni, M.; Buscaglia, V.; Aliprandi, G. Low-Temperature Aqueous Preparation of Barium Metatitanate Powders. *J. Eur. Ceram. Soc.* 1994, *14*, 85–90, doi:10.1016/0955-2219(94)90048-5.

24. Garcia-Amezquita, L.E.; Welti-Chanes, J.; Vergara-Balderas, F.T.; Bermúdez-Aguirre, D. Freeze-Drying: The Basic Process. In *Encyclopedia of Food and Health*; Elsevier, 2016; pp. 104–109.

25. Marin, M. Freeze-Drying | Structural and Flavor (Flavour) Changes. In *Encyclopedia of Food Sciences and Nutrition*; Elsevier, 2003; pp. 2701–2705.

26. Kazarin, P.; Shivkumar, G.; Tharp, T.; Alexeenko, A.A.; Shang, S. Lyophilization Scale-up to Industrial Manufacturing: A Modeling Framework Including Probabilistic Success Prediction. *Chem. Eng. Res. Des.* 2023, *192*, 441–455, doi:10.1016/j.cherd.2023.02.044.

27. Durance, T.; Yaghmaee, P. Microwave Dehydration of Food and Food Ingredients. In *Comprehensive Biotechnology*; Elsevier, 2011; pp. 617–628.

28. Saleem, I.; Petkar, K.; Somavarapu, S. Rationale for Pulmonary Vaccine Delivery: Formulation and Device Considerations. In *Micro and Nanotechnology in Vaccine Development*; Elsevier, 2017; pp. 357–371.

29. Morgan, C.; Vesey, G. Freeze-Drying of Microorganisms. In *Encyclopedia of Microbiology*; Elsevier, 2009; pp. 162–173.

30. *L. Tayebi, K. Moharamzadeh, (Ed.), Biomaterials for Oral and Dental Tissue Engineering, Book, 2018. Hardback ISBN: 9780081009611, EBook ISBN: 9780081009673.*;

31. Bhattacharjee, P.; Gupta, P.; Joseph Christakiran, M.; Nandi, S.K.; Mandal, B.B. Silk-Based Matrices for Bone Tissue Engineering Applications. In *Nanostructures for the Engineering of Cells, Tissues and*

Organs; Elsevier, 2018; pp. 439–472.

32. Tallón, C.; Moreno, R.; Nieto, M.I. Synthesis of γ-Al2O3 Nanopowders by Freeze-Drying. *Mater. Res. Bull.* 2006, *41*, 1520–1529, doi:10.1016/j.materresbull.2006.01.021.

33. Deville, S.; Saiz, E.; Nalla, R.K.; Tomsia, A.P. Freezing as a Path to Build Complex Composites. *Science (80-.).* 2006, *311*, 515–518, doi:10.1126/science.1120937.

34. Gutierrez-Gonzalez, C.F.; Agouram, S.; Torrecillas, R.; Moya, J.S.; Lopez-Esteban, S. Ceramic/Metal Nanocomposites by Lyophilization: Processing and HRTEM Study. *Mater. Res. Bull.* 2012, *47*, 285–289, doi:10.1016/j.materresbull.2011.11.027.

35. Gutierrez-Gonzalez, C.F.; Agouram, S.; Torrecillas, R.; Moya, J.S.; Lopez-Esteban, S. Ceramic/Metal Nanocomposites by Lyophilization: Spark Plasma Sintering and Hardness. *Ceram. Int.* 2014, *40*, 4135–4140, doi:10.1016/j.ceramint.2013.08.068.

36. Cascales, A.; Tabares, N.; Bartolomé, J.F.; Cerpa, A.; Smirnov, A.; Moreno, R.; Nieto, M.I. Processing and Mechanical Properties of Mullite and Mullite–Alumina Composites Reinforced with Carbon Nanofibers. *J. Eur. Ceram. Soc.* 2015, *35*, 3613–3621, doi:10.1016/j.jeurceramsoc.2015.05.011.

37. Hu, H.-L.; Zeng, Y.-P.; Xia, Y.-F.; Yao, D.-X.; Zuo, K.-H. High-Strength Porous Si 3 N 4 Ceramics Prepared by Freeze Casting and Silicon Powder Nitridation Process. *Mater. Lett.* 2014, *133*, 285–288, doi:10.1016/j.matlet.2014.06.176.

38. Wang, Y.; Yan, Q. The Preparation of TiC Dispersion Strengthened Tungsten Alloy via Freeze-Drying Method. *Mater. Res. Express* 2019, *6*, 1165g7, doi:10.1088/2053-1591/ab51bc.

39. Yan, M.; Zhong, J.; Liu, S.; Xiao, Z.; Yuan, X.; Zhai, D.; Zhou, K.; Li, Z.; Zhang, D.; Bowen, C.; et al. Flexible Pillar-Base Structured Piezocomposite with Aligned Porosity for Piezoelectric Energy Harvesting. *Nano Energy* 2021, *88*, 106278, doi:10.1016/j.nanoen.2021.106278.

40. Ge, S.; Zhang, J.; Zhang, Y.; Shi, P.; Wang, H.; Liu, S.; Tian, Z.; Shi, Z. Anisotropic Piezoelectric Properties of Porous (Ba0.85Ca0.15)(Zr0.1Ti0.9)O3 Ceramics with Oriented Pores through TBA-Based Freeze-Casting Method. *Materials (Basel).* 2022, *15*, 3820, doi:10.3390/ma15113820.

41. Lutterotti, L.; Scardi, P. Simultaneous Structure and Size–Strain Refinement by the Rietveld Method. *J. Appl. Crystallogr.* 1990, *23*, 246–252, doi:10.1107/S0021889890002382.

42. Gražulis, S.; Chateigner, D.; Downs, R.T.; Yokochi, A.F.T.; Quirós, M.; Lutterotti, L.; Manakova, E.; Butkus, J.; Moeck, P.; Le Bail, A. Crystallography Open Database – an Open-Access Collection of Crystal Structures. *J. Appl. Crystallogr.* 2009, *42*, 726–729, doi:10.1107/S0021889809016690.

43. Alemany, C.; Gonzalez, A.M.; Pardo, L.; Jimenez, B.; Carmona, F.; Mendiola, J. Automatic Determination of Complex Constants of Piezoelectric Lossy Materials in the Radial Mode. *J. Phys. D. Appl. Phys.* 1995, *28*, 945–956, doi:10.1088/0022-3727/28/5/017.

44. M.C. Kerr, J.S.R. Comparative Grinding Kinetics and Grinding Energy during Ball Milling and Attrition MillingAm. Ceram. Soc. Bull., 71 (12) (1992), Pp. 1809-1816. In.

45. SA Padden, J.R. Grinding Kinetics and Media Wear during Attrition Milling Am. Ceram. Soc. Bull., 72 (3) (1993).

46. Amorín, H.; Venet, M.; Chinarro, E.; Ramos, P.; Algueró, M.; Castro, A. Lead-Free Ba0.85Ca0.15Zr0.1Ti0.9O3 Ferroelectric Ceramics with Refined Microstructure and High Strain under Electric Field by Mechanosynthesis. *J. Eur. Ceram. Soc.* 2022, *42*, 4907–4916, doi:10.1016/j.jeurceramsoc.2022.04.061.

47. Ciomaga, C.E.; Curecheriu, L.P.; Lukacs, V.A.; Horchidan, N.; Doroftei, F.; Valois, R.; Lheureux, M.; Chambrier, M.H.; Mitoseriu, L. Optimization of Processing Steps for Superior Functional Properties of

(Ba, Ca)(Zr, Ti)O3 Ceramics. *Materials (Basel).* 2022, *15*, 8809, doi:10.3390/ma15248809.

48. Hernández-Moreno, A.C.; Reyes-Montero, A.; Carreño-Jiménez, B.; Acuautla, M.; Pardo, L. Ferroelectric, Dielectric and Electromechanical Performance of Ba0.92Ca0.08Ti0.95Zr0.05O3 Ceramics with an Enhanced Curie Temperature. *Materials (Basel).* 2023, *16*, 2268, doi:10.3390/ma16062268.

49. Bai, Y.; Matousek, A.; Tofel, P.; Bijalwan, V.; Nan, B.; Hughes, H.; Button, T.W. (Ba,Ca)(Zr,Ti)O3 Lead-Free Piezoelectric Ceramics—The Critical Role of Processing on Properties. *J. Eur. Ceram. Soc.* 2015, *35*, 3445–3456, doi:10.1016/j.jeurceramsoc.2015.05.010.

50. Thakur, O.P.; Feteira, A.; Kundys, B.; Sinclair, D.C. Influence of Attrition Milling on the Electrical Properties of Undoped-BaTiO3. *J. Eur. Ceram. Soc.* 2007, *27*, 2577–2589, doi:10.1016/j.jeurceramsoc.2006.10.013.

51. Veerapandiyan, V.; Benes, F.; Gindel, T.; Deluca, M. Strategies to Improve the Energy Storage Properties of Perovskite Lead-Free Relaxor Ferroelectrics: A Review. *Materials (Basel).* 2020, *13*, 5742, doi:10.3390/ma13245742.

52. Hennings, D.; Schreinemacher, H. Temperature Dependence of the Segregation of Calcium Titanate from Solid Solutions of (Ba, Ca) (Ti, Zr)O3 and Its Effect on the Dielectric Properties. *Mater. Res. Bull.* 1977, *12*, 1221–1226, doi:10.1016/0025-5408(77)90177-5.

53. Mendiola, J.; Alemany, C.; Pardo, L.; Gonzalez, A. Poling Reversal Effects on Piezoelectricity of Calcium Modified Lead Titanate Ceramic. *Ferroelectrics* 1989, *94*, 209–214, doi:10.1080/00150198908014255.

9 Understanding the mechanism and kinetics of the formation of ($Ba_{0.92}Ca_{0.08}$) ($Ti_{0.9}Zr_{0.10}$) (BCZT) system synthesized by low temperature solid—state route.

9.1 Introduction

In the field of the eco-friendly lead-free piezoceramic-based devices, fervent efforts have been addressed to the development of materials capable to show high electromechanical properties comparable to the market-dominant lead-based PZT [1]. Currently, as clearly evidenced in the previous chapter of this thesis work, large interest is devoted towards a class of materials such as BCZT, due to their high promising piezoelectric properties [2]. Among the BCZT family systems, the ($Ba_{0.92}Ca_{0.08}$) ($Ti_{0.95}Zr_{0.05}$), abbreviated as BCZT0805 or $BC_{08}TZ_{05}$, presents the perfect features for a synthesis study, such as a pure tetragonal phase, and optimal electromechanical properties (d_{33}=365pC/N, K_p=48.5%, Q_m=120) [3]. However, due to its high temperature of formation under solid-state route (T > 1200 °C), does not meet the requirements set for the directive "Ceramic roadmap to 2050" [4]. Recently, in order to modulate the kinetic of the BCZT0805 formation process, the mechanical activation of reagents by ball-milling followed by thermal treatment, have been quite successful for reducing the calcination temperature of the BCZT [5-7]. In particular, as reported in chapter 7 of this thesis, lyophilization of ball milled reagents under distilled water, allow to obtain the formation of pure BCZT0805 at only 700 °C. This temperature of calcination is comparable with that used for sol-gel routes, with the further advantages to avoid toxic solvents [8]. Nevertheless, despite the very important result achieved, up to our knowledge, no experimental investigation is reported on the mechanism of the BCZT0805 formation when lyophilization step is introduced. For the sake of clarity, scarce studies and sometimes contradictory are reported in the literature for the other BCZT stoichiometries [9].

In this work, the impact of attrition ball-milling combined with freeze-drying techniques on the overall formation kinetics of ($Ba_{0.92}Ca_{0.08}$) ($Ti_{0.9}Zr_{0.10}$) (BCZT) system, was investigated by calorimetric techniques combined with *ex situ* XRD home laboratory experiments. Moreover, the solid-state reaction mechanism was

studied *in situ* with high-resolution synchrotron XRD experiments carried out in the temperature range from RT to 980 °C.

9.2 Materials and Methods

9.2.1 Materials and Powders processing

BCZT0805 powders were prepared by a solid-state route starting from a stoichiometric mixture of $BaCO_3$ (Merck, Darmstadt, Germany, >99%), $CaCO_3$ (Sigma Aldrich, St. Louis, MO, USA, >99%), TiO_2 (Merck, of nominal purity >99%) and ZrO_2 (Tosoh, Tokyo, Japan, monoclinic polymorph >99%).

Two different batches of powders with nominal composition $(Ba_{0.92}\ Ca_{0.08})\ (Ti_{0.95}\ Zr_{0.05})$ were prepared starting for the above reported precursors.

For the first batch, abbreviated as **MM_p**, the raw materials were dried at 80°C overnight, weighted according to the stoichiometry manually mixed into an agate mortar for five minutes. The second batch, from here indicated as ABLP, was prepared according to chapter 7 and the manuscript [8,10].

9.2.2 Materials Characterization

Thermal and calorimetric characterization was carried out by a TG-DSC Q600 TA Instrument. For this scope, 40 mg of **ABL_P** powders were annealed from room temperature to 1100°C with heating rate of 2°, 5, 8, 10 and 15 °C/min.

Ex situ XRD measurements were conducted using a SMARTLAB diffractometer with a rotating anode source of copper (λ = 1.54178 Å) working at 40 kV and 100 mA. The instrument is equipped with a graphite monochromator and a scintillation tube in the diffracted beam. The instrument function was determined separately on a LaB_6 standard, which enables peak broadening corrections and separation of the size dependent term from the lattice strain component in the reciprocal space.

In situ Synchrotron Radiation Powder X-ray Diffraction (SR-PXD) experiments were performed at Swiss-Norwegian beamline BM01, ESRF, Grenoble**.** A high temperature and pressure resistant sapphire capillary

was specifically employed for *in situ* monitoring of solid/ gas evolution. The manually mixed powder **MMp** was heated from room temperature (RT, 20 °C) to 977°C at a heating rate of 19 °C/min with 10 s per point exposure in a spinning mode. The beamline was set at a wavelength of λ = 0.72002 Å, corresponding to E = 17213 KeV. The mechanically activated and lyophilized powder **ABL$_P$** was heated from room temperature (RT) to 950 °C at a heating rate of 35 °C/min but using a 3s-per-temperature point exposure in spinning mode. In this experiment, the X-ray source had λ = 0.71648 Å, corresponding to E = 17298.5 KeV. To convert the two-dimension rings around the origin of the reciprocal space to a 1-D pattern of intensities vs 2, the Fit2D software was employed [11,12]. Quantitative analysis of the crystalline phases and structure refinements were performed with the MAUD software (Materials Analysis Using Diffraction), a Rietveld extended program [13] selected due to its friendly graphics and convenience in up-loading CIF files. Lattice parameters of the constituent phases were refined from the line peak positions after allowing a correction for the zero-offset. Also, microstructure parameters can be worked out from peak broadening analysis according to its isotropic or anisotropic dependency vs the $q = 4*\pi/\lambda \sin(\theta)$ reciprocal space variable.

9.3 Results and Discussion

TG/DSC profiles allowed to evidence the main weight losses attributable to the decomposition of carbonates used as precursors and associated with the main endothermic and exothermic events that lead to the formation and crystallisation of the main BCZT perovskite, as reported in our previous works [10,14]. The thermal evolution of unmilled MM Powders (**Figure 9.3.1**), from RT to 1100°C with a heating rate of 5°C/min, presents an evident split of the main endothermic peak associated to the main weight loss, ascribable to two distinct events, occurring at 824°C and 854°C, respectively. As reported in the literature, the first one can be attributed to the reversible transformation of α $BaCO_3$, orthorhombic polymorph, to β$BaCO_3$, trigonal one[15]. The second peak can be attributed to the formation of the main BCZT perovskite. The DSC profile of **ABL$_P$**, reported in Figure 2b appears different from the previous one, since it is not possible to clearly individuate the split of the main peak, but only the presence of an endothermic event that can correspond to the formation of the BCZT.

9.3.1 *Ex situ* experiments

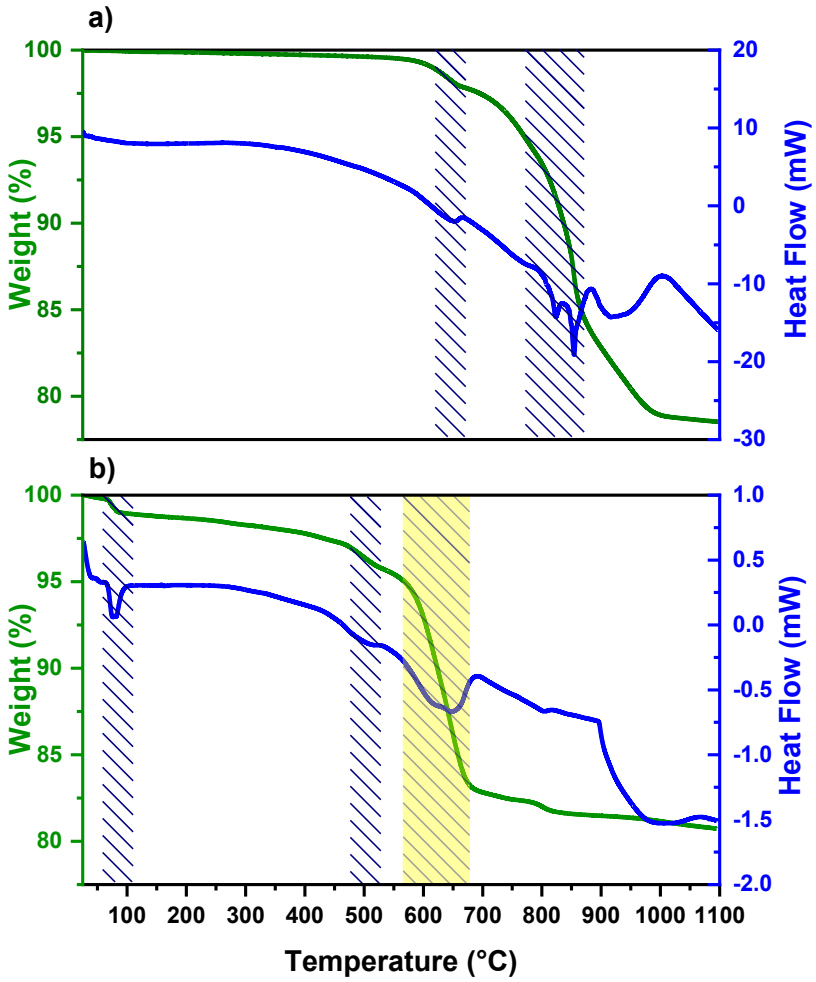

Figure 9.3.1 a) TGA/DSC profile of manually mixed powders and **b)** ball-milled and freeze-dried powders. Insets indicate the main endothermic events.

Based on the TGA/DSC analysis, several thermal treatments and *ex situ* XRD experiments were undertaken to further identify the formation temperature of the main BCZT perovskite phase (M-BCZT) and undesirable secondary phase presence. The exploration temperatures have been chosen analysing the onset and the offset of the endothermic peak. The powders have been then annealed at 400°C, 550°C and 690°C using a heating rate of 5°C/min and keeping the temperature fixed for 15 min. After these preliminary studies, to simulate the synthesis step, the temperature was then increased at 700°C varying the dwell time from 30

min to 2h. To evaluate the formation of other secondary phases higher temperatures 750°C and 800°C have been explored keeping the dwell time fixed at 2h.

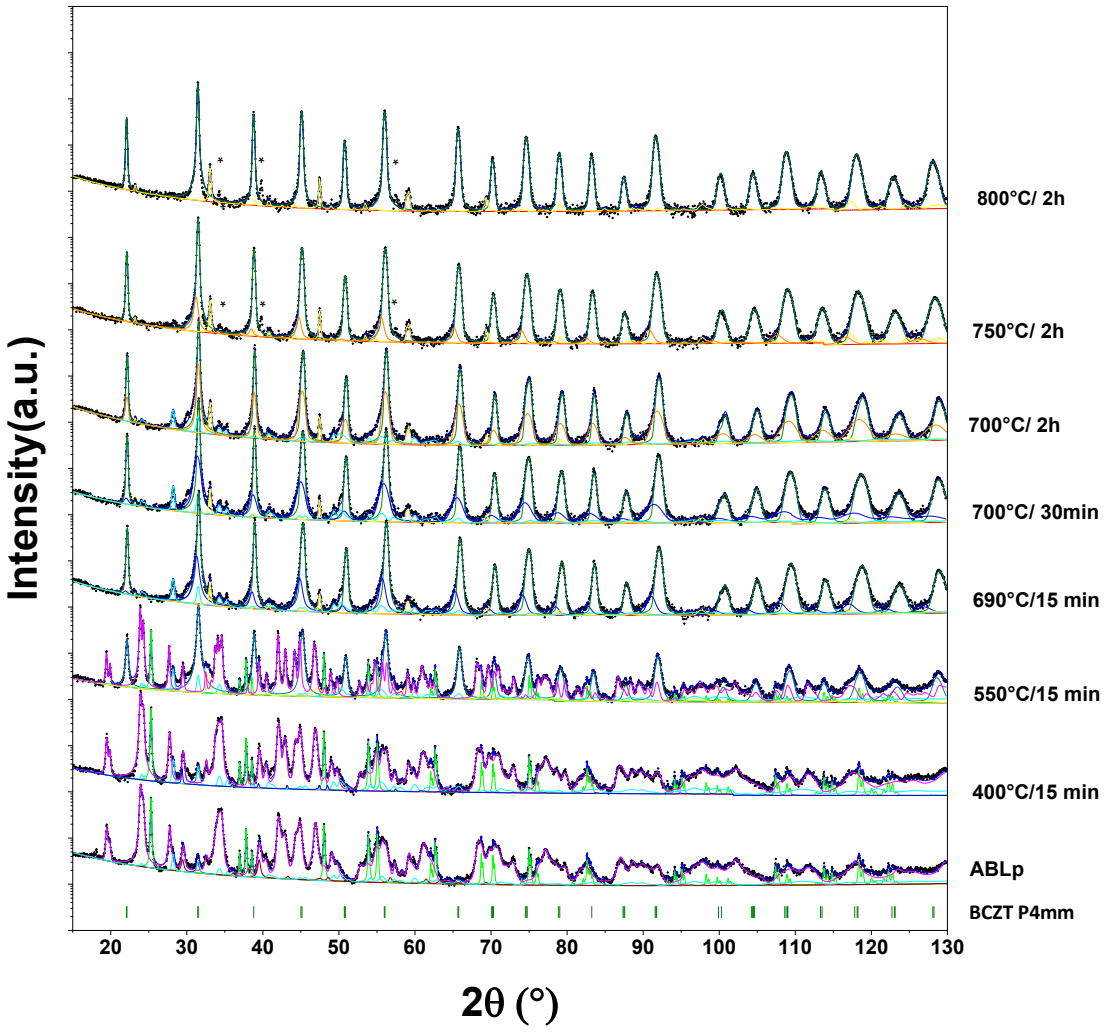

Figure 9.3.2. *From bottom to top: stick pattern (olive-coloured bars) of the i) BCZT perovskite phase (tetragonal, P4mm), ii) XRD patterns of ABL precursors obtained after lyophilizing treatment. Data points (blue dots) collected ex situ as a function of the temperature and different dwell times. Fitting lines of each phase component are obtained from Rietveld refinement (coloured full lines): magenta line ($BaCO_3$) s.g. Pmcn, green line (TiO_2) s.g. $I4_1/amd$, cyan line (ZrO_2) s.g. $P2_1/c$, burgundy coloured line ($CaCO_3$) s.g. R-3c:H, olive line (BCZT) s.g. P4mm, yellow line orthorhombic ($CaTiO_3$) s.g. Pbnm, orange line cubic ($BaZrO_3$) s.g. Pm-3m. * indicates the presence of unknown secondary phase.*

To describe better the evolution of the crystalline phase, highlighting the presence of the minor ones, all the XRD patterns were displayed in logarithmic scale.

With reference to **Figure 9.3.2**, the bottom pattern refers to the freeze-dried powders, previously subjected to 6h of ball-milling in water. In the pattern of powders treated at 400°C for 15 min, the same sequence of

peaks is noticeable, indicating that any phase reaction yet occurs. This is confirmed quantitatively by Rietveld refinement (see **Table 9.3.1**), from which it emerges that both the freeze-dried powders and those treated at 400°C for 15 min. are composed by the mixture of the precursors used, such as anatase (TiO_2) 28 wt.%, witherite ($BaCO_3$) 68 wt.%, calcite ($CaCO_3$) 2 wt.% and baddeleyite (ZrO_2) 2 wt.%. In conclusion, the first thermal treatment until 400 °C does not affect substantially the weight fraction distribution of precursor materials, except for the slight change in the average crystallite size observed for the main phase $BaCO_3$, extracted from line broadening.

The formation of the BCZT (tetragonal, *P*4*mm*) starts at 550°C with a weight amount, estimated according to the Rietveld method, to be 46 wt. % out of the total. We also observe the simultaneous appearance of a small amount of perovskite $CaTiO_3$ (3 wt.%) as secondary phase.

At higher temperatures, namely 690°C for 15 min and 700°C for 30 min, the amount of BCZT phase increased (88 wt.%), although the presence of $CaTiO_3$ is still evaluable (3 wt.%). Furthermore, the presence of zirconia can also be detected as unreacted precursor (3 wt.%). From a careful analysis of the XRD pattern, the presence of an intermediate compound can be inferred from pronounced shoulders on each reflection of M-BCZT (from 6 to 10 wt.%). This secondary phase is assigned to $BaZrO_3$, which disappears just at 800°C. Very likely, as reported in literature, [5] this is prompted by the diffusion of Zr^{4+} into the BCZT lattice. In addition, by comparing the patterns of the powders treated at the same temperature but with a longer dwell time, it can be noted that the amount of M- BCZT perovskite increases (91 wt.%.), while the amount of $BaZrO_3$ decreases (down to 2 wt.%). After keeping fixed the total dwell time to 2 h, but increasing the temperature, the amount of the M-BCZT phase reaches 94 wt.%. However, it can be observed that the percentage of $CaTiO_3$ remains unmodified with simultaneous formation of another unassigned secondary phase.

From the considerable line broadening observed for the *P4mm* progression peaks, we may surmise the presence of sensible effects due to lattice microstrain in addition to the reduced size extent of coherent domains of diffraction.

Despite the higher conversion of the precursors into M-BCZT obtained at 750°C and 800°C, the synthesis conditions have been set to 700°C for 2 h to avoid the formation of undesired compounds, which can be detrimental for the subsequent sintering treatment and eventually for the piezoelectric properties.

The presence of unreacted zirconia was not considered an important issue, since it should diffuse easily into the lattice of M-BCZT at the high temperatures reached during the subsequent final sintering step. Nonetheless, the formation of immiscible $CaTiO_3$ terminal solid solution could alter the stoichiometry of the M-BCZT for the desired nominal composition.

Lastly, by analysing the changes in the lattice parameters of M-BCZT, it clearly emerges that by increasing the temperature, firstly the c/a ratio shows an increase in tetragonality from 550°C where c/a =1.004 with(c=4.0228 Å), maintaining a constant value at 650°C c/a =1.004 (c=4.0186 Å), reaching c/a =1.005 (c=4.0196 Å) at 690°C, c/a =1.005 (c=4.0219 Å), at 700°C for 30 min, and at 700°C 2h c/a =1.005 (c=4.0206 Å). Further increasing the temperature at 750°C, c/a ratio slightly decreases to 1.004 (c=4.026 1Å), until reaching the minimum tetragonal distortion at 800°C with c/a =1.003 (c= 4.0283 Å). The reduction in the tetragonal distortion leads to a decrease in the spontaneous polarization.

Table 9.3.1 weight percentage of each crystalline phase as a function of the temperature

Phase (wt.%)	ABL_p	400°C/15 min	550°C/15min	690°C/15 min	700°C/ 30 min	700°C/2h	750°C/2h	800°C/2h
$BaCO_3$	68	70 (68)	35	-	-	-	-	-
$CaCO_3$	2	2	4	-	-	-	-	-
TiO_2	28	30 (28)	13	-	-	-	-	-
ZrO_2	2	2	2	3	2	2	-	-
BCZT	-	-	46	88	83	87	92	93
$BaZrO_3$	-	-	-	6-8	12	8	3	-
$CaTiO_3$	-	-	3	2-3	3	3	3	4
unknown							2	3

9.3.2 *In situ* experiments

To further confirm the effectiveness of ball-milling activation and freeze-drying on the decrease of the formation temperature of the BCZT perovskite, we conducted *in situ* XRD experiment. The 2D plate image plot of *in situ* SR-PXD, shown in **Figure 9.3.3**, reports the evolution of MM crystalline powder as a function of the temperature. For an immediate understanding in the upper and bottom section of the graph, we report coloured- bars corresponding to the reflections expected for each space group recognized. As easily visualised, at RT temperature is possible to distinguish the reflections belonging to the mixture of precursors used, such as $BaCO_3$, $CaCO_3$, ZrO_2 and TiO_2. As arguable from vertical bar behaviour, at 910°C some events have occurred, ascribable to the complete and reversible polymorphic transformation of orthorhombic $BaCO_3$ (*Pmcn*) into trigonal polymorphs (*R-3m* and *R-3c*) and the formation of the M-BCZT (*P4mm*). The bar sequence of such new phases formed are reported in the bottom part of the **Figure 9.3.3**.

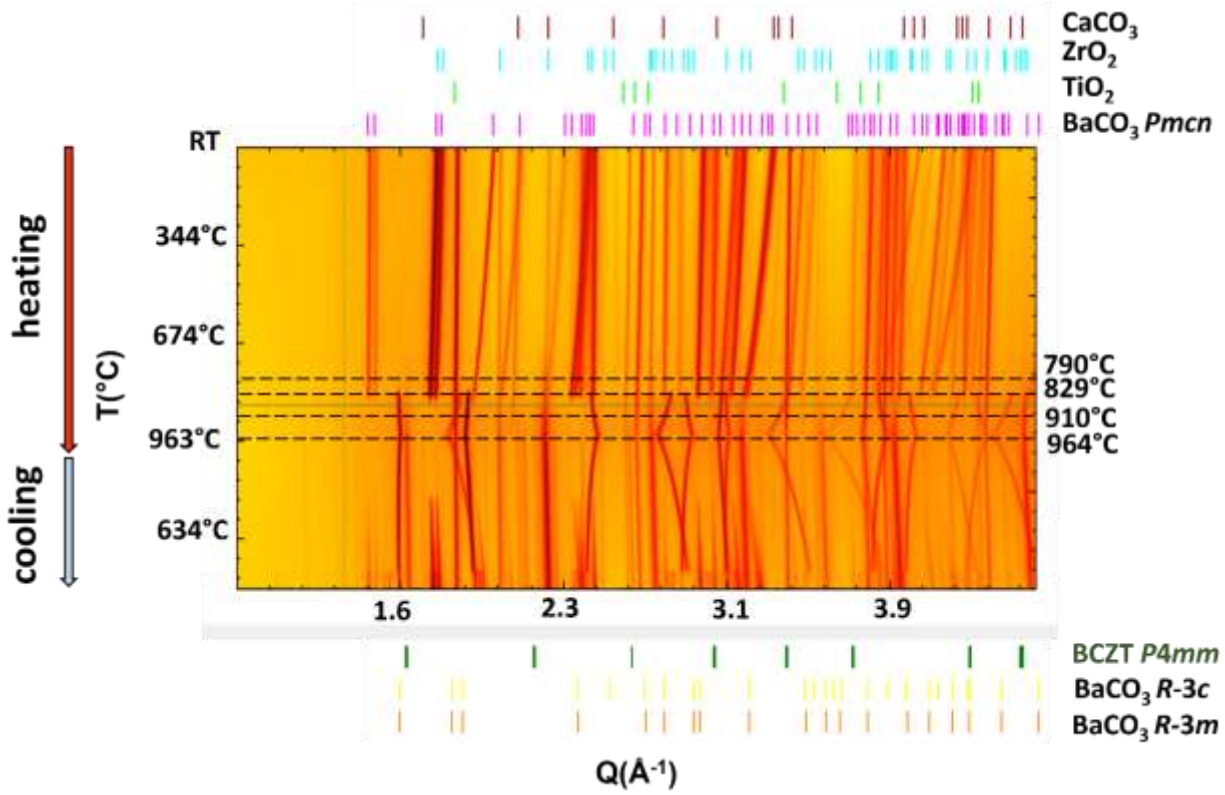

Figure 9.3.3 *In situ* SR-PXD measurements of the MMp mixture (2D plot). The powder was annealed from room temperature (RT- 20 °C) to 977°C at a heating rate of 25°C min^{-1} ramp rate with 10 s per point exposure in a spinning mode. We indicate reflections of crystalline phases of manually mixed powder (MMp) with coloured sticks as it follows: i) Top: $BaCO_3$ (orthorhombic) magenta, TiO_2 green line, ZrO_2 cyan and $CaCO_3$ burgundy colour, respectively. ii) Bottom: BCZT olive, $BaCO_3$ (trigonal) yellow R-3*m* and orange R-3*c* bars respectively.

To confirm the reversible transformation of $BaCO_3$ highlighted in **Figure 9.3.1a**, from α (orthorhombic structure) to β (trigonal polymorph), *in situ* XRD pattern collected at 910°C has been compared to that collected after annealing the MMp powder into an oven at 900°C for 15 min (followed by cooling), reported in the upper and the bottom graph of **Figure 9.3.4**, respectively. Starting from the upper graph, that corresponds to the pattern collected *in situ,* the Rietveld analysis assessed a small amount of BCZT *P4mm* phase about 6 wt.% while confirming the change in the crystalline structure of $BaCO_3$. In facts, at 910°C the *Pbnm* (orthorhombic) structure has been completely transformed into *R-3m* polymorph. Later the reasons why the *R-3m* (# 166 IT) space group of such high temperature polymorph may transform at least partially to a conventional calcite type *R-3c* (#167 IT) polymorph will be discussed.

The bottom pattern, referred to *ex situ* XRD after annealing, confirmed the reversible nature of this transformation. Indeed, the contribution of trigonal $BaCO_3$ is not detectable, whereas witherite *Pmcn* structure (magenta curve) is about 34 wt.%, coexisting with the main fraction that refers to a BCZT tetragonal *P4mm* phase (c/a=1.005 and c = 4.025 Å). Anatase wt.% is under 10, together with calcite and baddeleyite. The presence of a small amount of $BaTi_4O_9$ and TiO_2 rutile formed irreversibly at high temperature(2wt.%), in addition to calcite, can be assumed to be compatible with the experimental data. Some peaks still remain unidentified, but they are not of considerable importance. This is clearly shown in the 2D plot, many other secondary phases crystallize after cooling if exposed at intermediate temperatures, due to partial side reactions.

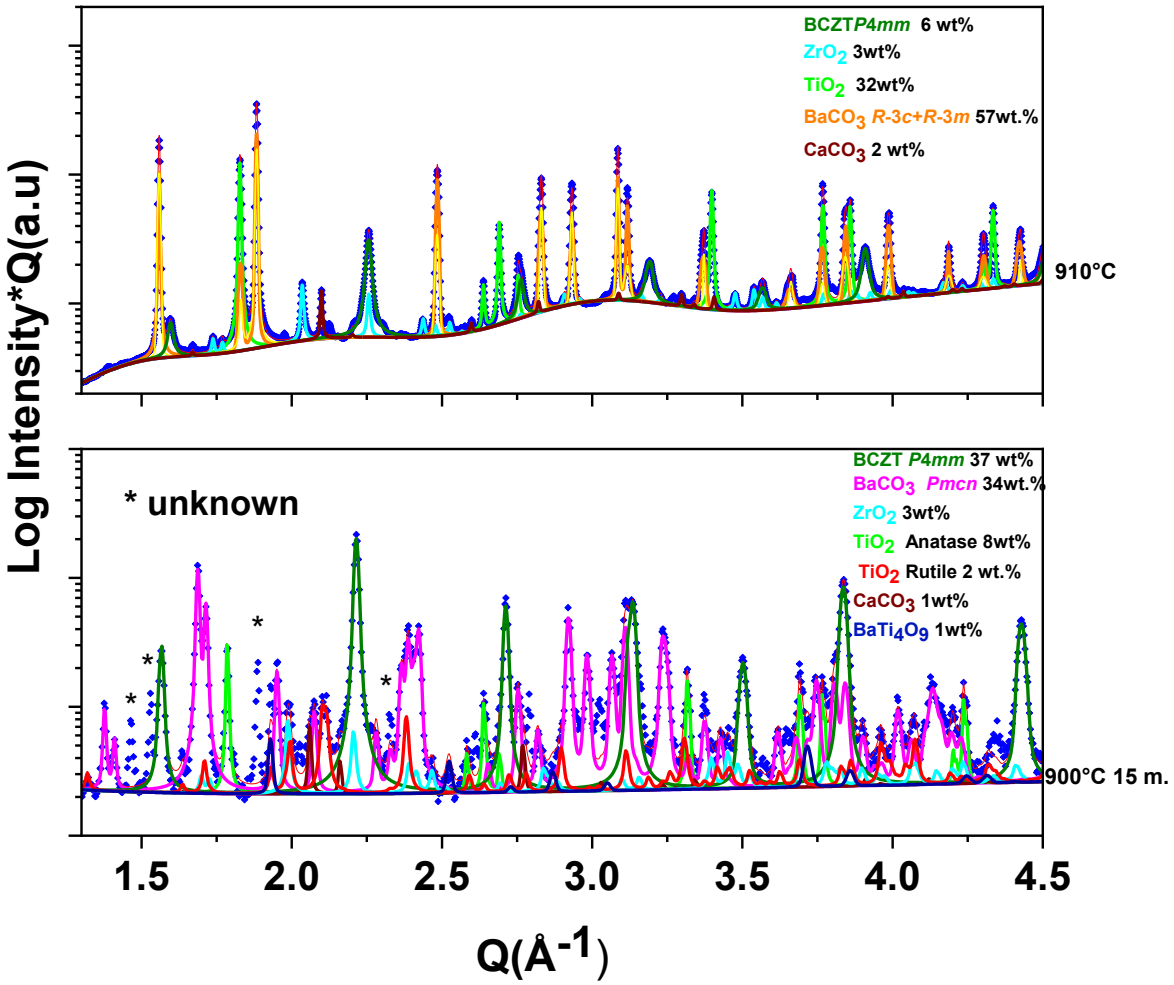

Figure 9.3.4 *in situ synchrotron high resolution measurement at 910°C for un-milled mixture showing a complete conversion to trigonal polymorphs (R-3m and/or R-3c) and a partial occurrence of Barium Titanate (BT)-type tetragonal structure with unreacted ZrO_2 and $CaCO_3$. The bottom pattern collected with a laboratory apparatus after heating at 900°C for 15 min and followed by cooling shows that the unreacted $BaCO_3$ returns*

*to the orthorhombic polymorph structure. Some peaks, indicated with * symbol, remain unattributed. Fitting lines of each phase component obtained from Rietveld refinement (colored full lines) magenta line ($BaCO_3$) s.g. Pmcn, green line (TiO_2) s.g.I41/amd, cyan line (ZrO_2) s.g. P21/c, burgundy colored line ($CaCO_3$) s.g. R-3c:H, olive line (BCZT) s.g. P4mm, orange R-3m and yellow R-3c. The legends of the Figure also associate corresponding colours.*

The 2Dplot of *in situ* SR-PXD measurements, shown in **Figure 9.3.5**, reports the evolution of ABLp powders as a function of the temperature. As in the previous Figure, in the upper and in the bottom section of the graph are reported the coloured- bars corresponding to the reflection of each phase**.** As for MMp, at RT temperature is possible to distinguish the reflections belonging to the freeze-dried precursors, such as $BaCO_3$, $CaCO_3$, ZrO_2 and TiO_2. At 650°C is possible to notice the disappearance of some reflection and the appearance of new ones, imputable to the formation of BCZT phase, in accordance with bottom olive bar.

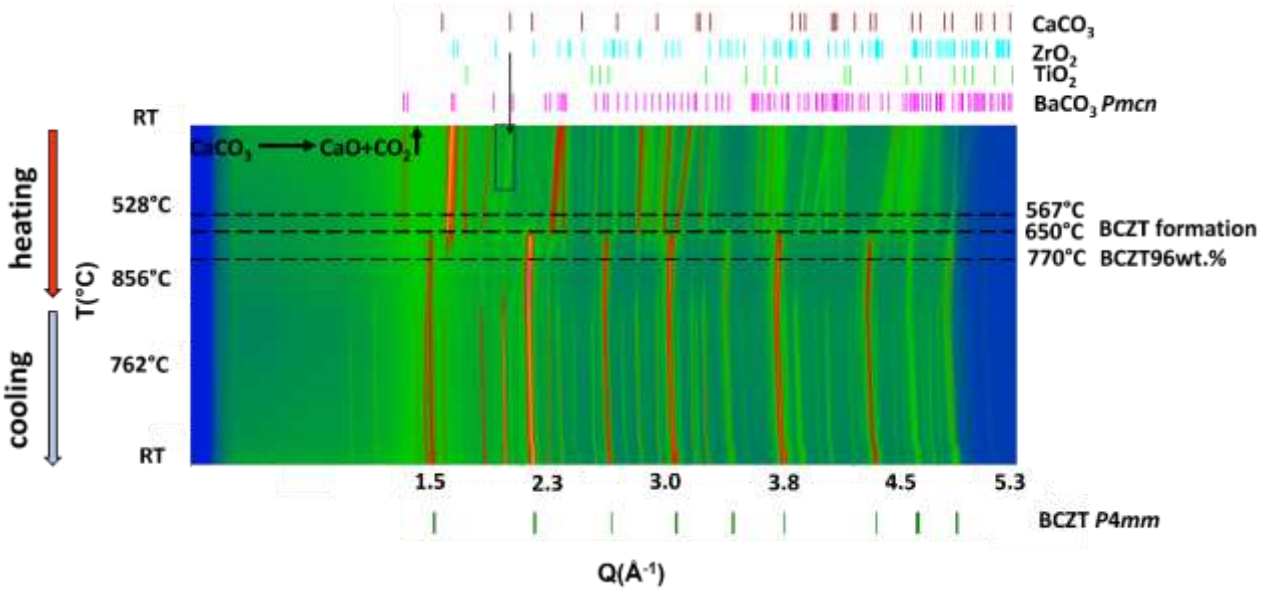

Figure 9.3.5 *In situ SR-PXD measurements of the freeze-dried ABLp powder (2D plot). The powder was annealed from room temperature (RT) to 950 °C at a heating rate of 25°C min-1 but using a 3s-per-temperature point exposure in spinning mode. Reflections of crystalline phases of freeze-dried ABLp are indicated with coloured sticks, as follows: i) Top: $BaCO_3$ (orthorhombic) magenta, TiO_2 green line, ZrO_2 cyan and $CaCO_3$ burgundy colour ii) Bottom: BCZT olive*.

The following figure displays the patterns, with Rietveld fitting profiles, of samples from MMp and ABLp batches treated at different temperatures. The temperatures have been chosen based on relevant events that occur within the powder associated to main changes in reflections as shown in **Figure 9.3.3** and **Figure 9.3.5**.

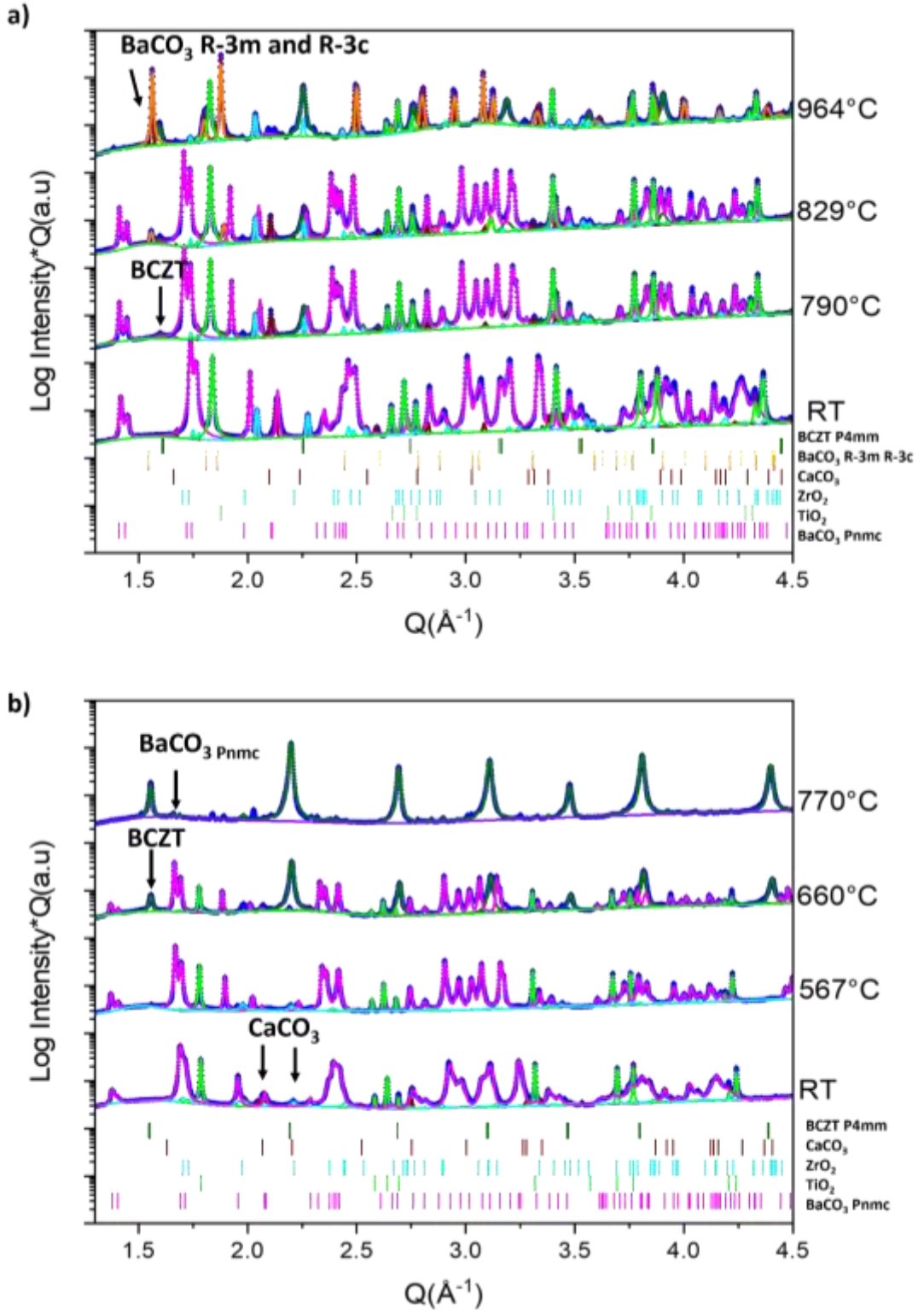

Figure 9.3.6 a) *In situ* SR-PXD measurements of MM_p and **b)** of the freeze-dried ABL_p powder (1D plot) at selected crucial temperatures. Reflections of crystalline phases of freeze-dried ABL_p are indicated with coloured sticks, as follows: $BaCO_3$ (orthorhombic) magenta, TiO_2 green, ZrO_2 cyan and $CaCO_3$ burgundy colour, BCZT olive, R-3m orange, R-3c yellow. Data points (blue dots) collected ex situ as a function of the temperature and different dwell times and iii) fitting lines of each phase component obtained from Rietveld refinement (coloured full lines) according to colours chosen for sticks.

The main events that can be individuate (**Figure 9.3.6(a)**) concerning the MMp powders are i) the formation of the M-BCZT and ii) the reversible transformation of orthorhombic $BaCO_3$ into trigonal structure. The formation of BCZT perovskite with a wt.% of 0.6 indicating the beginning of nucleation of perovskite, reaching the 3.3 wt.% at 855°C with a maximum value of 13wt.% at 988°C. It has to be underlined that the experiment ended at this temperature preventing a further analysis at higher temperatures. The great change occurs at 829°C where $BaCO_3$ begins to transform into the trigonal polymorph, that reaches the amount of 38wt.% at 855°C. At higher temperature of 869°C the presence of another trigonal polymorph of s.g. R-3c, can be observed leading to a better explanation of the experimental data. Summarising, the mixed powder turns out to be fairly inert up to 950°C except for the fact that the orthorhombic $BaCO_3$ undergoes a trigonal transformation around the temperature at 850°C , until completely converted .The results reported by Antao and Hassam[16] whose transformation began at 811°C (considering the fact that the heating rate is three times higher than that used by the authors 7°C/min) are in broadly accordance with these measurements. However, a slow onset of a tetragonal P4mm BCZT phase at the expense of TiO_2 and $BaCO_3$ can be seen. The trigonal structure of calcite ($CaCO_3$) remains almost invariant until 964°C except for the lattice expansion.

As shown in **Figure 9.3.6(b)** the behaviour of ABLp powders differs from that of the MMp. The principal events that can be found, can be summarized as follows: decomposition of $CaCO_3$, and formation of the M-BCZT perovskite. In the range of temperature between RT and 516°C the $CaCO_3$ decomposes to form CaO and CO_2. The CaO is not detectable due to the high heating rate used. The $BaCO_3$ phase that can be recorded is limited to the maximum temperature of 770°C (1wt%.), as the system undergoes a total reactive transformation in a temperature range between 620°C and 780°C until reaching 96wt.% of BCZT phase formed. There is still a partial presence of unreacted Zirconia (1wt.%). The trend in the lattice parameters shows an increase in the volume of the unreacted $BaCO_3$ elementary cell, similar to previous studies. However, simultaneously from 640°C there is a rapid growth of the tetragonal P4mm phase (BCZT with partial Zr^{4+} doping at B-site) whose lattice parameters are a=4.039 Å, c=4.048 Å at a temperature of 780°C. The different behaviour of MM_P and ALB_p is confirmed also by the analysis of the quantitative evolution of crystalline phases as function of the temperature, show in Figure 9.3.7(a) and (b), respectively.

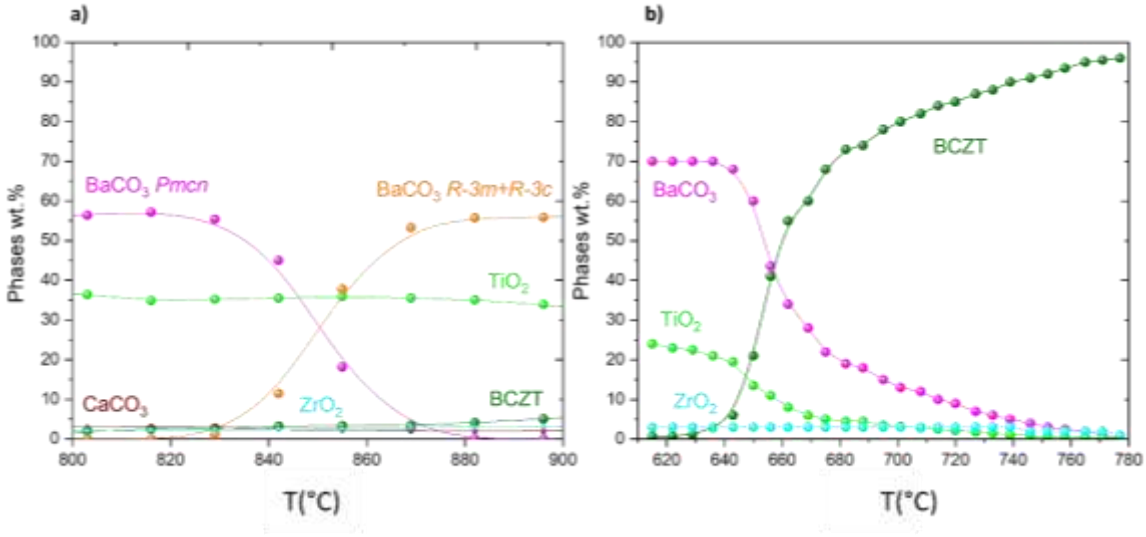

Figure 9.3.7 *Weight percentages of crystalline phases as a function of the temperature. a) MM_P powders. b)ALB_p powders*.

The data acquired at RT referring to the Pmcn orthorhombic $BaCO_3$ phase are slightly different from those reported in the literature by Antao and Hassam [16]. It should be underlined that the reciprocal space interval in these measurements is smaller than that scanned by the authors. Furthermore, it should be emphasised that sample capillary used has thinner walls, and the wavelength is shorter, which should ensure better handling of absorption phenomena. The elemental cell volume of $BaCO_3$ *Pmcn* at RT is relatively in agreement with values reported in the literature [17]. The lattice parameters remain almost unaltered at 60 °C. At 120 °C is possible to notice some appreciable change on the intermediate parameter. At 188 °C, the change in cell parameter continues, as shown also in the 1D patterns in **Figure 9.3.8**. It can be seen that the intermediate lattice parameter grows faster than the a and b lattice parameters as a function of temperature. As reported in **Figure 9.3.9** the lattice volume increases to 307.6 $Å^3$ at 220°C, of 312.71 $Å^3$ at 425°C, of 315 $Å^3$ at 600°C with a maximum value of 321$Å^3$ at 870°C.

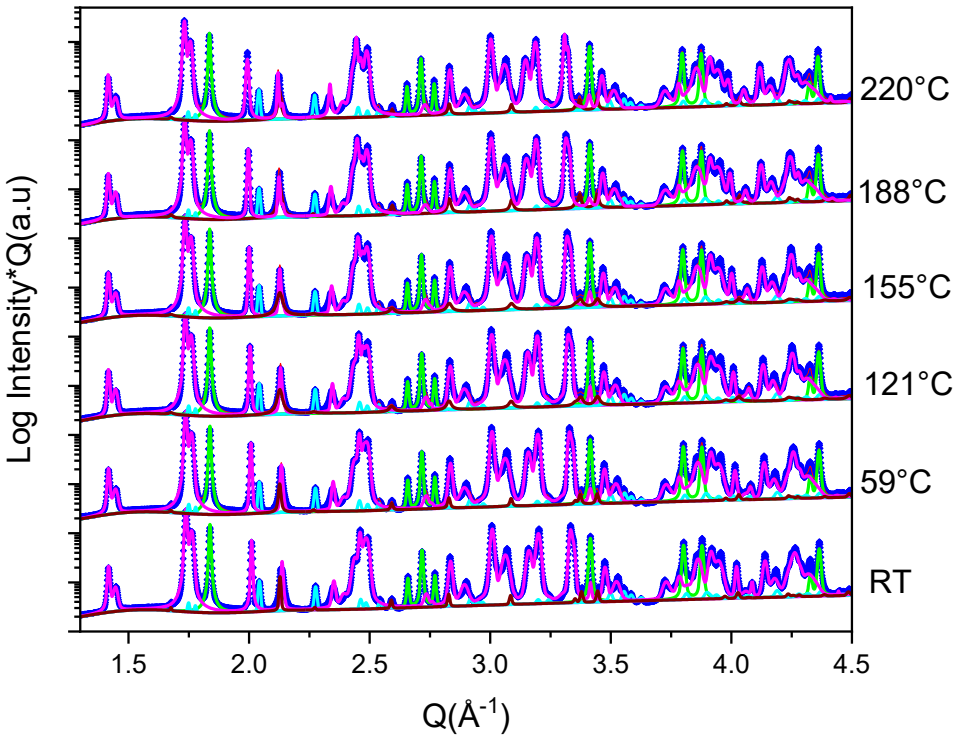

Figure 9.3.8 *in situ* synchrotron high resolution measurement from RT to 220°C for unmilled mixture showing a. iii) fitting lines of each phase component obtained from Rietveld refinement (colored full lines): magenta line ($BaCO_3$) s.g. Pmcn, green line (TiO_2) s.g.I41/amd, cyan line (ZrO_2) s.g. P21/c, burgundy colored line ($CaCO_3$) s.g. R-3c:H.

As reported in **Figure 9.3.9**, the variation of c-axis of witherite can be observed until 870°C where the amount of $BaCO_3$ Pmnc is about 1 wt.%.

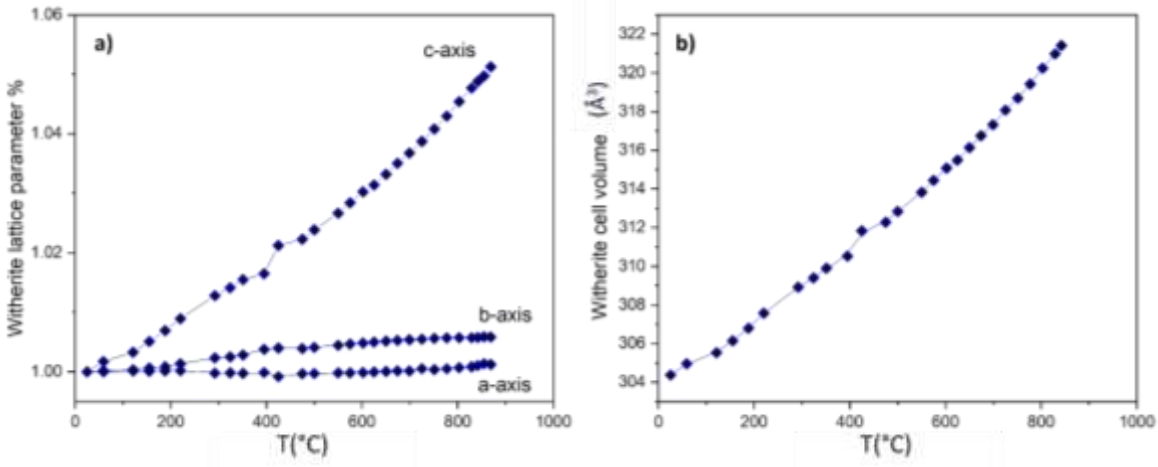

Figure 9.3.9 Variation of cell **a)** parameters a,b,c and **b)**volume of orthorhombic *Pnmc* $BaCO_3$ structure as a function of the temperature.

The transformation of orthorhombic BaCO3 into the trigonal polymorph can be noticed analysing the 1D patterns evolution shown in **Figure 9.3.10** in the range temperature from 829°C to 855°C.

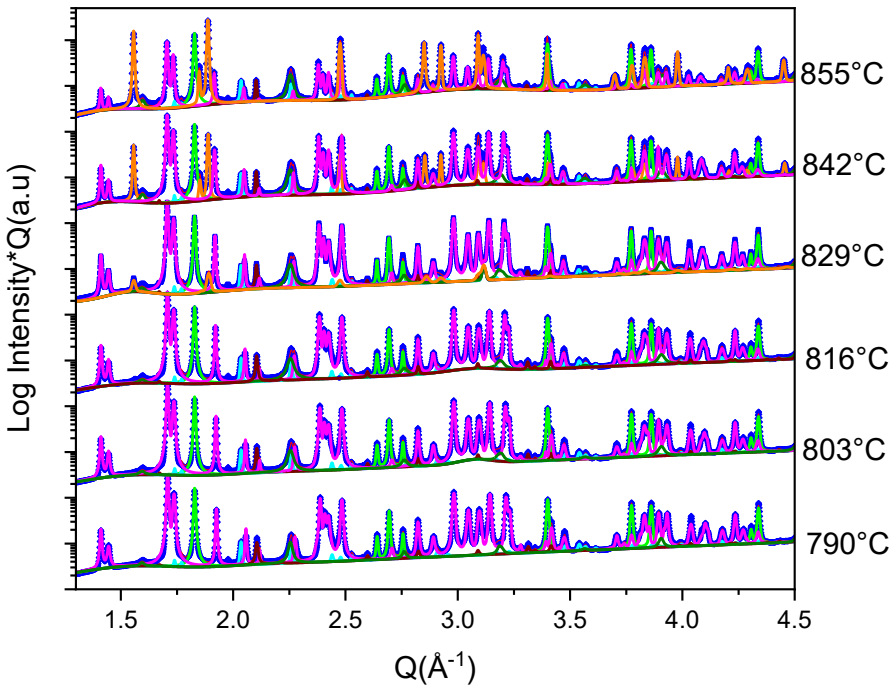

Figure 9.3.10 *in situ* synchrotron high resolution measurement from 790°C to 855°C for unmilled mixture showing a. iii) fitting lines of each phase component obtained from Rietveld refinement (coloured full lines). magenta line (BaCO3) s.g. Pmcn, green line (TiO_2) s.g.I41/amd, cyan line (ZrO_2) s.g. P21/c, burgundy coloured line (CaCO3) s.g. R-3c:H, olive line (BCZT) s.g. P4mm, orange line R-3m $BaCO_3$.

As reported in **Figure 9.3.11**, at 882°C the orthorhombic polymorph is totally converted into trigonal one and the amount of BCZT reaches the 13 wt.% at 988°C.

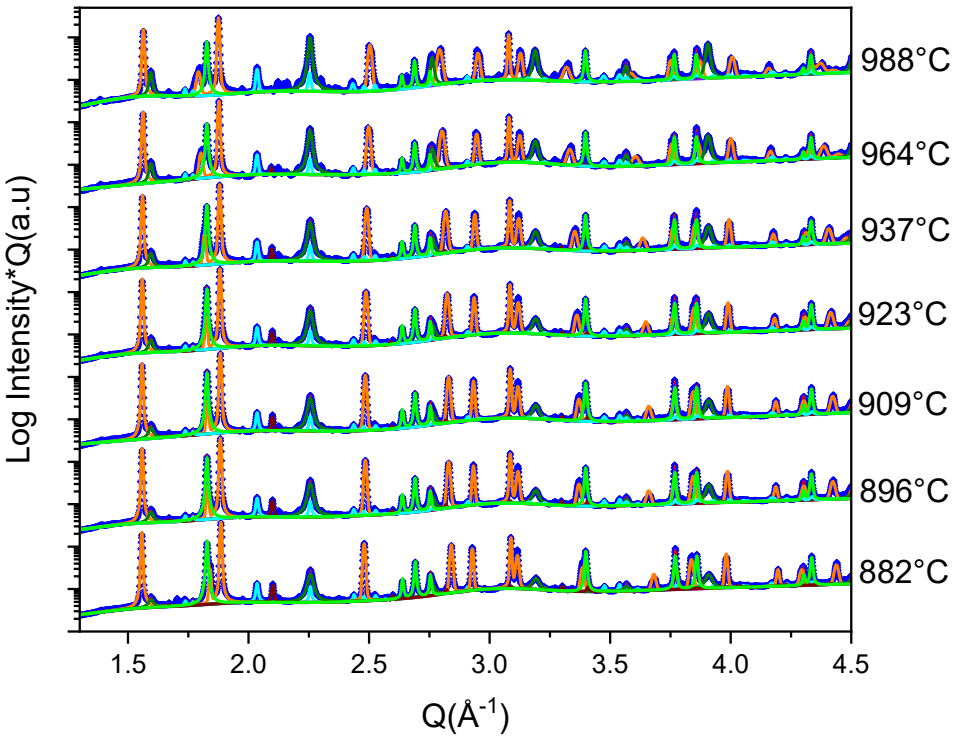

Figure 9.3.11 *in situ* synchrotron high resolution measurement from 882°C to 988°C for unmilled mixture showing a. iii) fitting lines of each phase component obtained from Rietveld refinement (coloured full lines). magenta line ($BaCO_3$) s.g. Pmcn, green line (TiO_2) s.g.I41/amd, cyan line (ZrO_2) s.g. P21/c, burgundy coloured line ($CaCO_3$) s.g. R-3c:H, olive line (BCZT) s.g. P4mm, orange line R-3m $BaCO_3$, yellow line R-3c $BaCO_3$.

As shown in **Figure 9.3.12(a)**, the most pronounced change in the lattice parameter of TiO_2 involves the c-direction, while the a-direction undergoes more modest positive changes. The volume of TiO_2 anatase reaches a value of 139 $Å^3$.

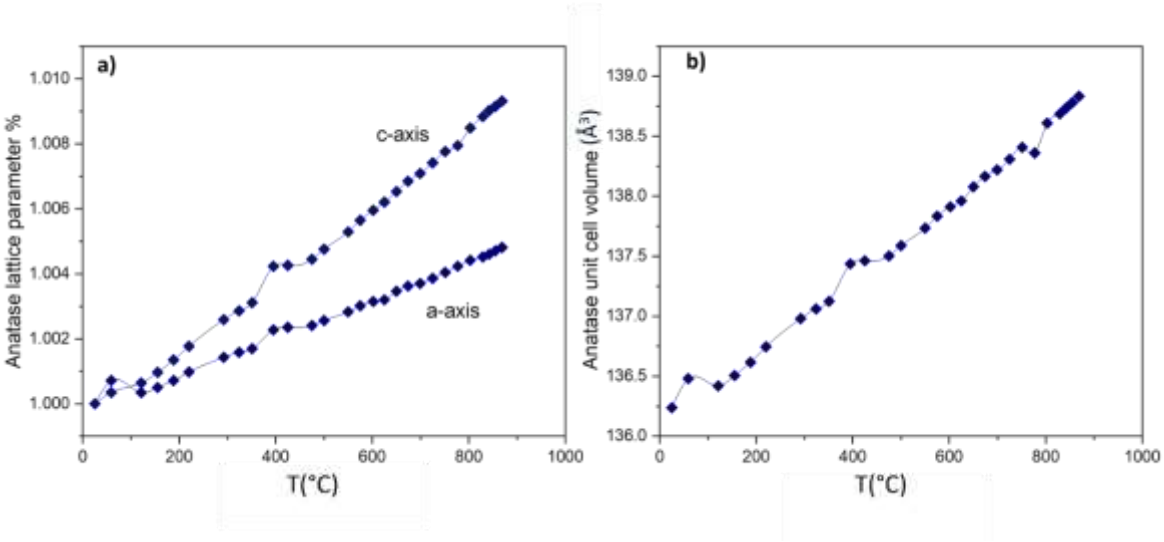

Figure 9.3.12 Variation of cell **a)** parameters a,b,c and **b)**volume of tetragonal TiO_2 Anatase structure as a function of the temperature.

As far as the evolution of calcite is concerned, it must be remembered that, as with ZrO_2, its presence in the pattern is extremely reduced, so that the structural parameters are difficult to determine, however it is confirmed that at high temperatures calcite retains its trigonal structure R-3c where the axes a and b remain largely unchanged(**Figure 9.3.13**) but the c-axis undergoes an elongation to 17.61 Å considering that it had started from 17.06 Å at RT.

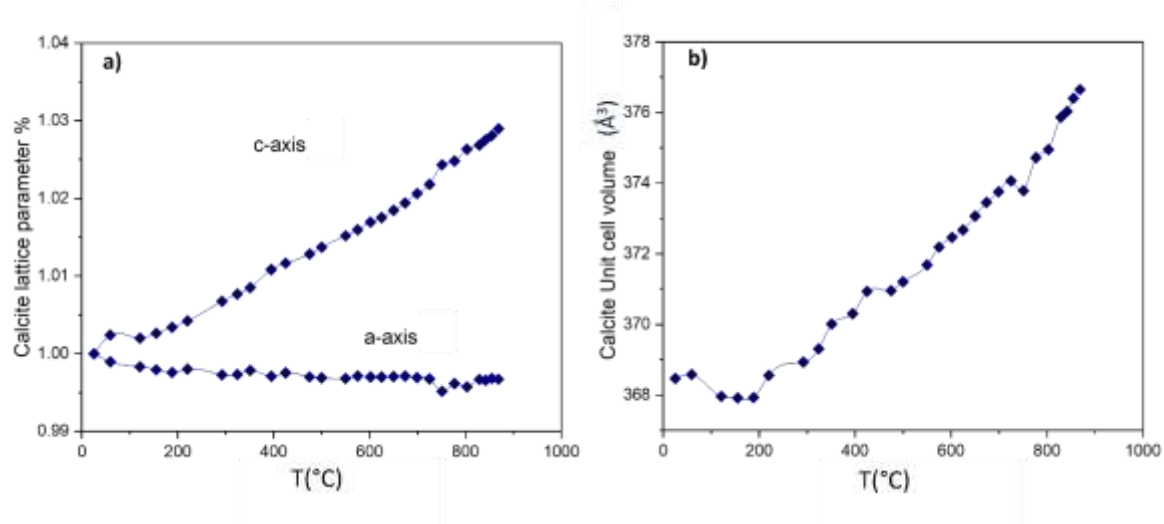

Figure 9.3.13 Variation of cell **a)** parameters a,b,c and **b)**volume of trigonal $CaCO_3$ calcite structure as a function of the temperature.

9.3.3 Detailed study: Attrition ball-milled and lyophilised precursors (ALB_p)

From RT to 386°C (**Figure 9.3.14**) the as-lyophilised precursors remain almost unchanged except for the expansion of $BaCO_3$ lattice that reaches a value of 311 $Å^3$ at 400°C, starting from 304 $Å^3$. The amount of $CaCO_3$ remains unchanged until this temperature.

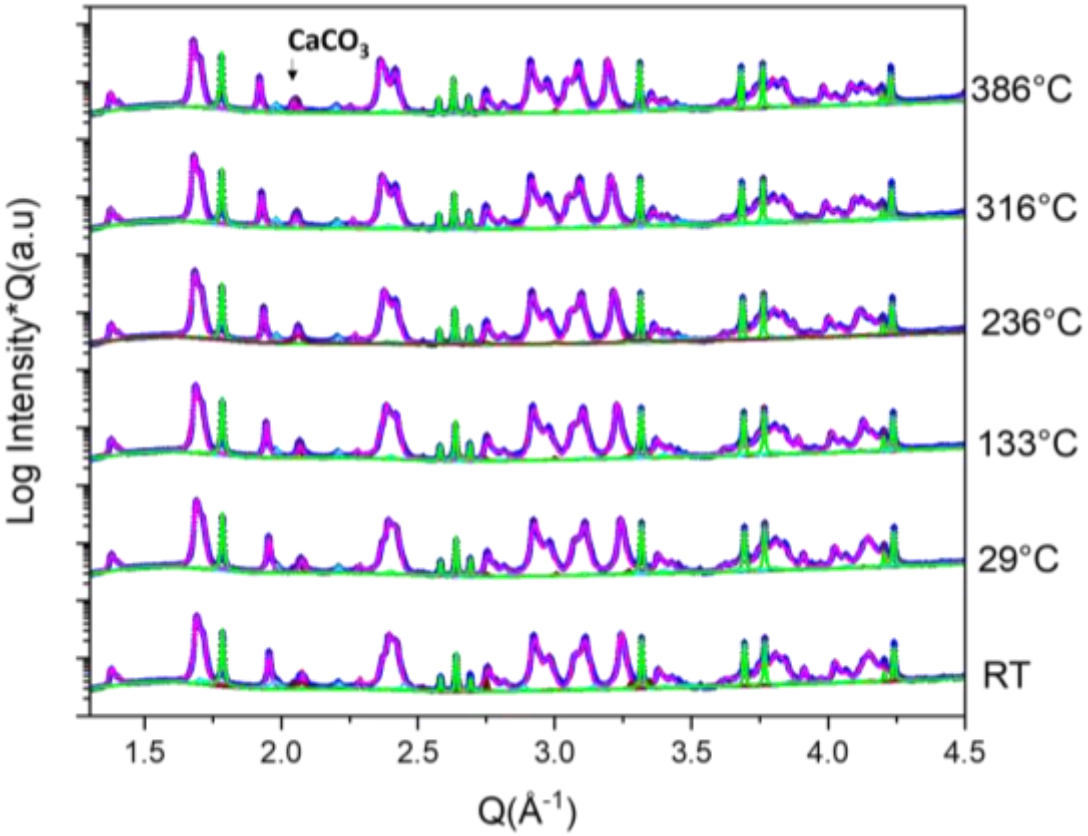

Figure 9.3.14 *in situ* synchrotron high resolution measurement from RT to 386°C for lyophilised powders showing a. iii) fitting lines of each phase component obtained from Rietveld refinement (colored full lines): magenta line ($BaCO_3$) s.g. Pmcn, green line (TiO_2) s.g.I41/amd, cyan line (ZrO_2) s.g. P21/c, burgundy colored line ($CaCO_3$) s.g. R-3c:H.

At higher temperatures, up to 567°C the $CaCO_3$ begins to decompose until being totally undetectable. From 550°C to 574°C a small amount of BCZT is barely perceptible (**Figure 9.3.15**). As shown in the graph below, indicated by arrows, at 597°C and 602°C the BCZT amount is about 0.6-1wt% (**Figure 9.3.16**).

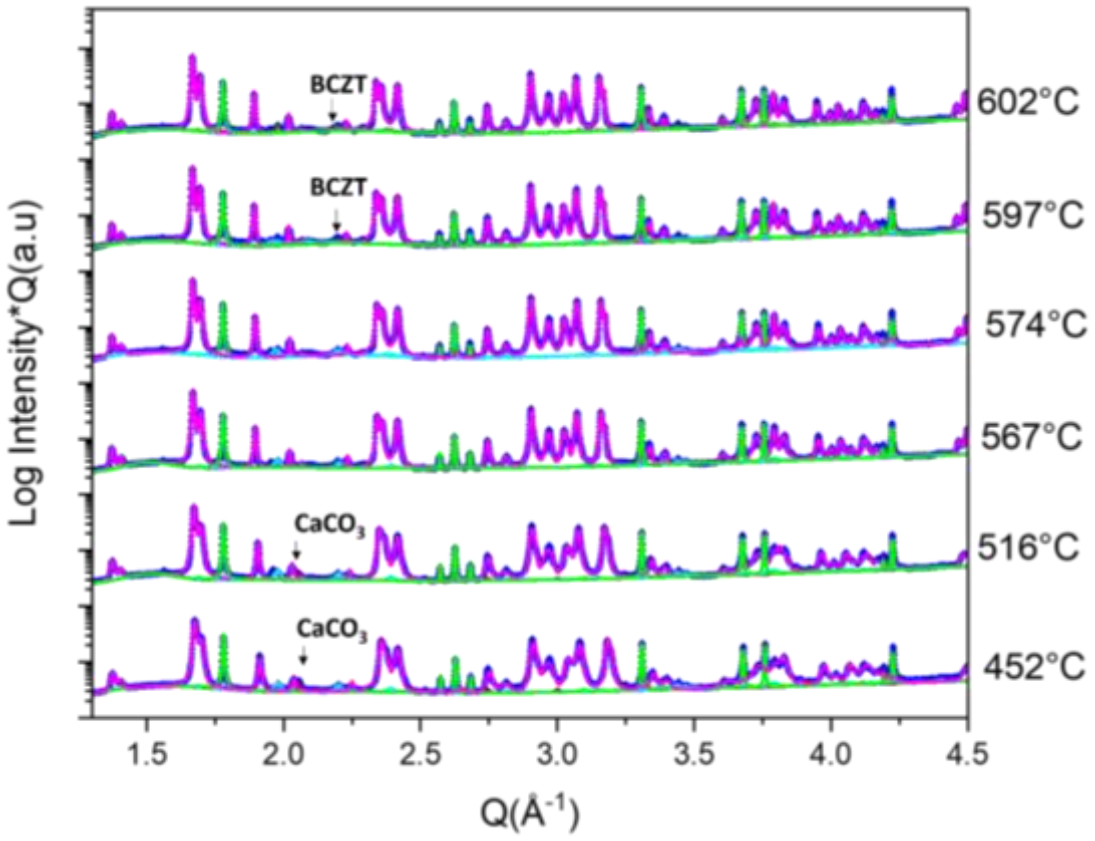

Figure 9.3.15 *in situ* synchrotron high resolution measurement from 452°C to 602°C for lyophilised powders showing a. iii) fitting lines of each phase component obtained from Rietveld refinement (colored full lines): magenta line ($BaCO_3$) s.g. Pmcn, green line (TiO_2) s.g.I41/amd, cyan line (ZrO_2) s.g. P21/c, burgundy colored line ($CaCO_3$) s.g. R-3c:H, olive line BCZT P4mm.

In the temperature range between 608°C and 758°C the BCZT completely forms until reaching an amount of 95-96 wt% at 770°C, accompanied by almost undetectable amount of unreacted ZrO_2 and $BaCO_3$(**Figure 9.3.16**).

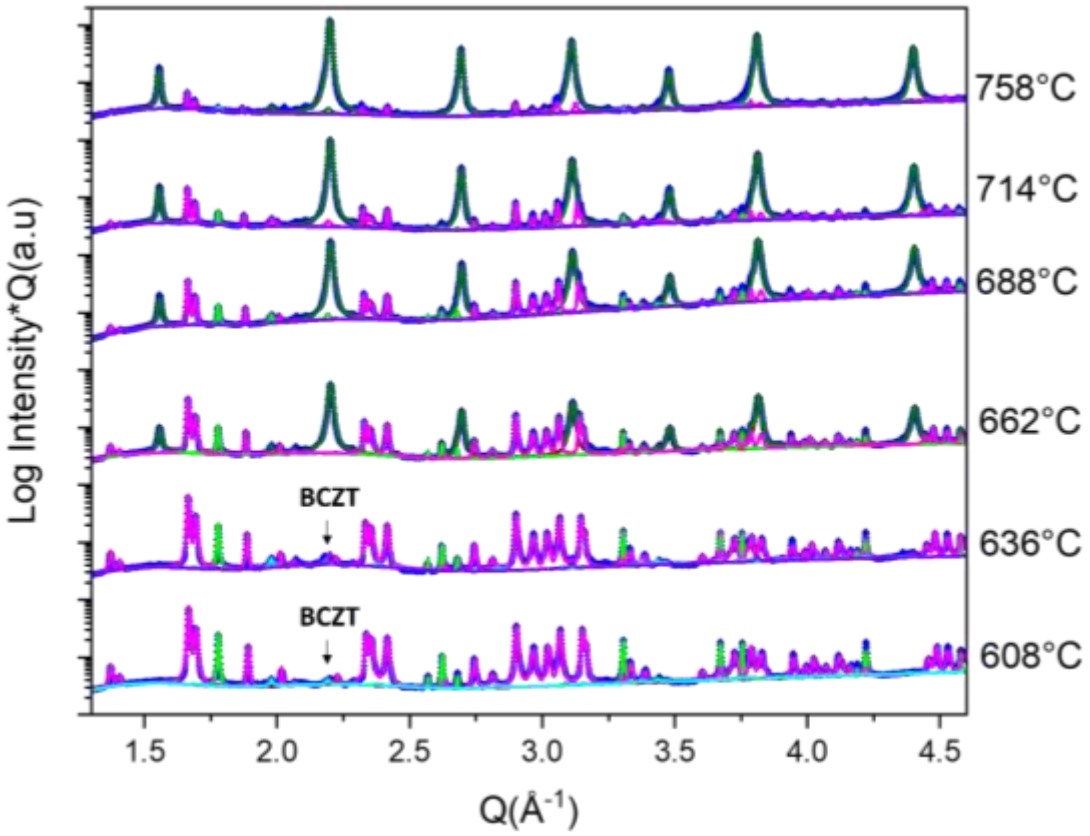

Figure 9.3.16 *in situ* synchrotron high resolution measurement from 608°C to 758°C for lyophilised powders showing a. iii) fitting lines of each phase component obtained from Rietveld refinement (coloured full lines): magenta line ($BaCO_3$) s.g. *Pmcn*, green line (TiO_2) s.g.*I*41*/amd*, cyan line (ZrO_2) s.g. *P*21*/c*, burgundy coloured line ($CaCO_3$) s.g. *R*-3*c:H*, olive line BCZT *P*4*mm*.

As shown in **Figure 9.3.17**, like in the unmilled powders the cell of orthorhombic $BaCO_3$ expands until reaching a value of 321 $Å^3$.

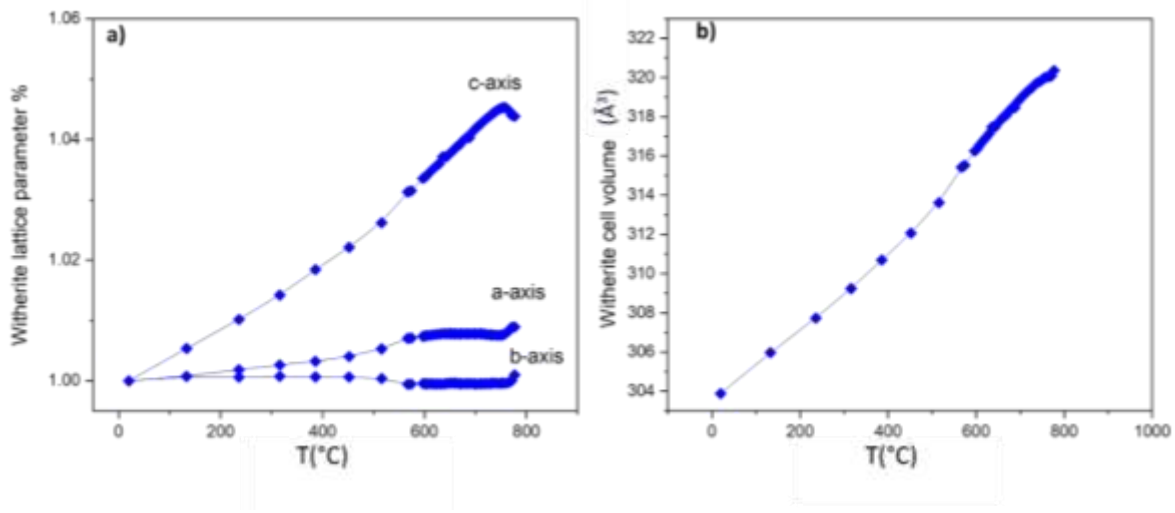

Figure 9.3.17 Variation of cell **a)** parameters a,b,c and **b)**volume of orthorhombic *Pnmc* $BaCO_3$ structure as a function of the temperature for ALBp.

The volume of the TiO_2 increases until reaching a maximum value of 138.6 $Å^3$ and then it drops to 136 $Å^3$ and the anatase is incorporated into the main lattice (**Figure 9.3.18**).

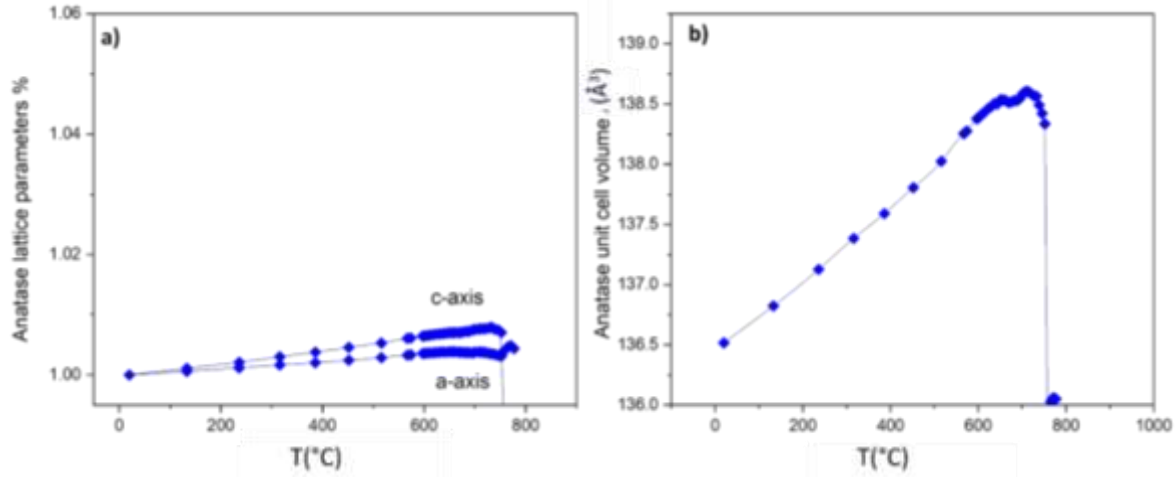

Figure 9.3.18 Variation of cell **a)** parameters a,b,c and **b)**volume of tetragonal TiO_2 structure as a function of the temperature for ALB_p.

After analysing the quantitative diffraction data of phase (**Figure 9.3.7**) in correspondence of the most significant temperature range suggested from the TG-DTA thermograms, it is clear that activated powders undergo significant low temperature reactivity in comparison to un-milled mixture. For the latter composition it appears that a fraction of thermal energy in the high temperature process is waste to assist an inefficient orthorhombic to-trigonal transformation of witherite, without any important reaction involving

anatase below 988 °C, the highest temperature accessed with the *in situ* experiment. Conversely, for the activated mixture, the transformation reaction of BCZT occurs at about 650 °C, simultaneous to the disappearance of the witherite *Pmcn* and anatase and tetragonal BCZT appearance (see relevant lattice parameters). As it concerns the role of Calcite and baddeleyite minor phases, it is not easy to devise a precise behaviour from the pattern evolution, given their relatively low wt.% in the mixture. However, for calcite we were able to follow as a function of temperature an increase of the lattice parameter c, while a = b parameter remaining approximately constant, in agreement with previous investigation (Antao and Hassam[16]) on the 100% phase. This supports indirectly the reliability and correctness of our numerical analysis. Unfortunately, in the case of baddeleyite, monoclinic ZrO_2, where we need to determine 4 lattice parameter a, b, c and β, respectively, their determination is not so accurate since the heavy peak overlapping with the main witherite and anatase phases. In any case, since they disappear at the later stages of the BCZT formation (whose curve is following in a first approximation at least a Gompertz function), we may surmise $CaCO_3$ is incorporated by witherite first to form a (Ba, Ca) CO_3 solid solution throughout ionic diffusion. Later, upon evolution of gaseous CO_2, the remaining (Ba,Ca)O quickly reacts with anatase to form tetragonal (Ba,Ca)TiO_3. From the SR-PXRD pattern evolution it seems that baddeleyite is incorporated in the BCT matrix as well.

It is important to remind that upon the integration of the logistic Gompertz function (**Figure 9.3.7(b)**), we implicitly assume the presence of two terms, the first independent from the temperature and the second dependent. We may ascribe the independent term to the higher activity of the powders due to the mechanical activation and lyophilization carried out. Unfortunately, there is no way to compare the reactivity for the un-activated mixture, since the experiment was stopped just below 1000 °C.

9.3.4 Non-Isothermal Kinetics Investigation on ABL_P

With the purpose to better clarify the influence of the reagents pretreatment, (attrition ball-milling and lyophilization) on the temperature formation of the BCZT during the calcination step, calorimetric measurements were performed at different heating rates. The measured DSC profiles of the as milled-lyophilized sample for selected heating rates, 2, 5, 8, 10, 15 °C/min, are depicted in **Figure 9.3.19(a)**.

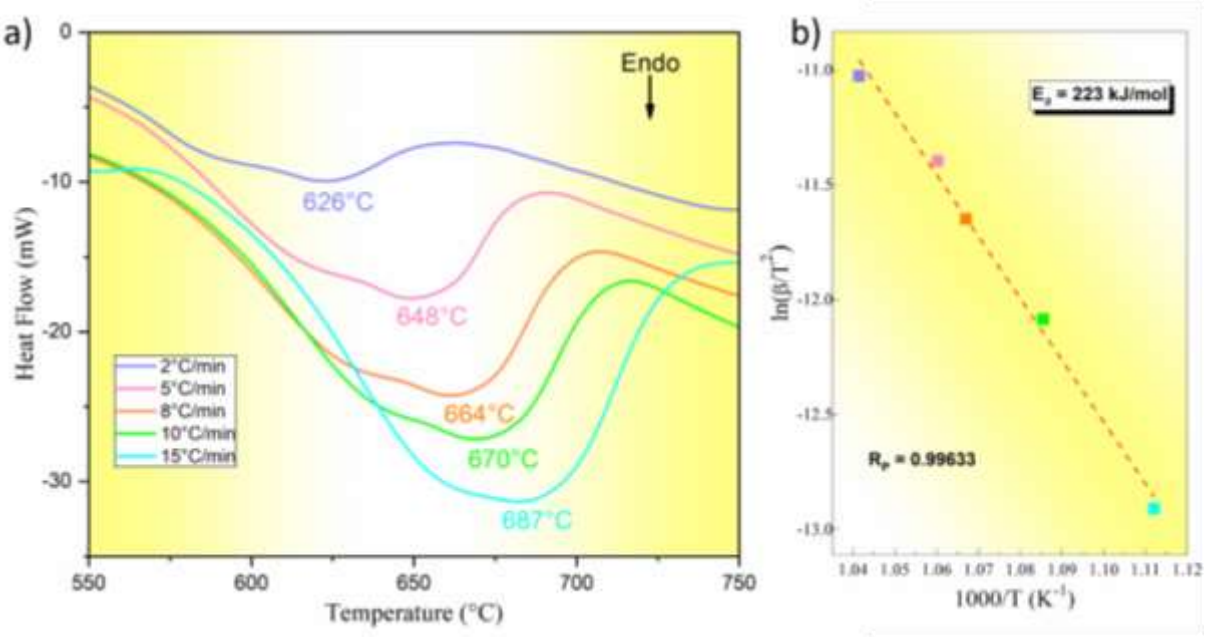

Figure 9.3.19 a) Endothermic DSC peaks versus temperature (550-750°C) of the post lyophilized powders acquired at different heating rates of 2, 5, 8, 10, and 15 °C/min. **b)**Kissinger plot.

From DSC profiles, at increasing heating rates, β[°C/min], the peak temperature, T_m [°C] shifts at high temperatures, whereas endothermic peak become sharper, characteristic of kinetically controlled process[18]. The subscript *m* indicates the temperature associated to the maximum rate.

The non-isothermal activation energy, E_a, for BCZT formation, was then estimated according to the Kissinger method, as expressed below:

$$ln\left(\frac{\beta}{T_m^2}\right) = ln\left(-\frac{AR}{E}f'(\alpha_m)\right) - \frac{E_a}{RT_m} \qquad (9.1)$$

where *R* is the gas constant (8.314 J / mol·K), *A* is the preexponential factor and $f'(\alpha_m)$ the first derivate of the kinetic model $f(\alpha_m)$. Plot of left-hand side of the **equation 9.1** versus 1000/T_p [K^{-1}] is shown in **Figure 9.3.19(b)**. Considering that $f(\alpha_m)$ does not vary with β, the value of the activation energy is calculated from the slope of the straight line (red dots) and it corresponds to 223 kJ/mol. Despite the excellent *Rp* achieved (0.99633), the activation energy estimated is limited by the fact that the Kissinger method produces a single value of the activation energy without considering the kinetic complexity of the process [19]. A satisfactory representation of a kinetic complex process (BCZT formation occurred almost simultaneously with the decomposition of $BaCO_3$) requires more than an activation energy value calculated at different extent of

reactions α. To this purpose, the extent of conversion of α have been calculated for the DSC profiles and shown as a function of the temperature and time in **Figure 9.3.20**.

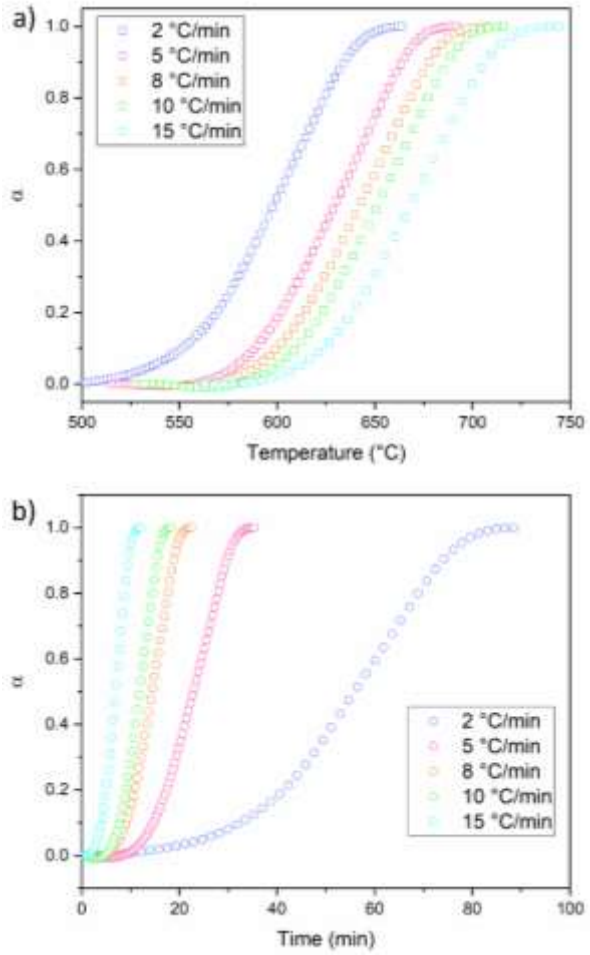

Figure 9.3.20 Normalized α-T **a)** and α-t **b)** plots corresponding to the DSC peaks. The relation between the formation temperature and time is provided by the following equation: $t = \frac{|T-T_i|}{\beta}$, where T is the formation temperatures, while T_i is the temperature at the beginning of the formation process.

The activation energy of the BCZT formation as a function of the extent of reaction was estimated by the Kissinger-Akahira-Sunose (KAS) isoconversional model-free method which is founded on this equation:

$$ln\left(\frac{\beta}{T_\alpha^2}\right) = C - \frac{E_a}{RT_\alpha} \qquad (9.2)$$

where C is constant and does not depend on T and β. According to the KAS equation all curves reported in **Figure 9.3.21** have been analysed. Considering a degree of conversion in the range of 0.1-0.9, $\ln\left(\frac{\beta}{T_\alpha^2}\right)$ are

plotted versus $\frac{1000}{T_\alpha}$ and shown in **Figure 9.3.21**, and the linear fitting (red solid line) resulted in the activation energy (**Table 9.3.2**).

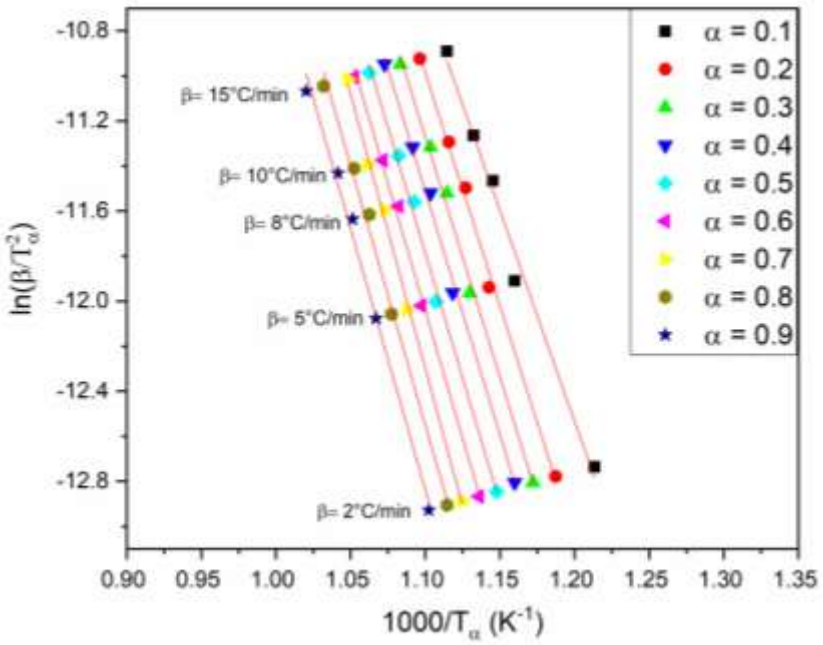

Figure 9.3.21 $\ln\left(\frac{\beta}{T_\alpha^2}\right)$ versus $\frac{1000}{T_\alpha}$ plot at different extent of reaction. Linear fits are indicated by solid red line.

Table 9.3.2 Parameters estimated by KAS method for different degrees of conversion α. R_p is the Pearson correlation coefficient. Ea is the activation energy calculated by multiplying the slope for the gas constant R (8.314 [J/ (mol K)]).

α	**Slope**	**R_p**	**Ea (kJ/mol)**
0.1	-18.734	0.9944	155.754
0.2	-20.680	0.9979	171.935
0.3	-21.313	0.9977	177.198
0.4	-21.651	0.9979	180.003
0.5	-22.225	0.9977	184.781
0.6	-22.653	0.9984	188.189
0.7	-24.350	0.9989	202.445
0.8	-22.990	0.9970	191.143
0.9	-23.163	0.9962	192.575

The activation energies values estimated by the KAS method, have been then plotted versus the selected α range 0.2-0.9 (**Figure 9.3.22**). An activation energy with an average value of 185 kJ/mol (± 4 kJ/mol) was calculated for the whole process, which resulted smaller with respect to those value previously obtained by the Kissinger equation (**Figure 9.3.19(b)**).

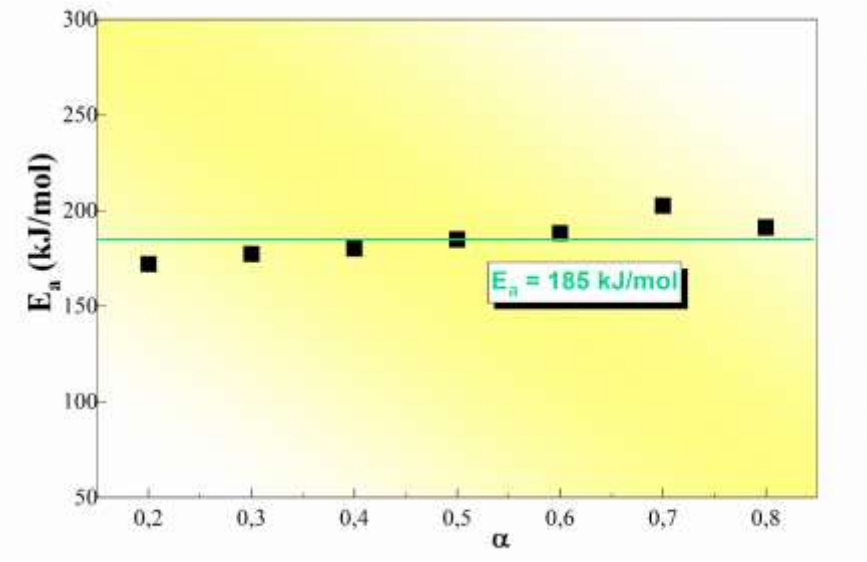

Figure 9.3.22 Activation energies obtained from the KAS approach, as a function of the extent of reaction α.

Despite the activation energies values indicated in **Figure 9.3.22** does not vary significantly with the degrees of conversion, it should be mentioned that for α lower than 0.3, the activation energies decrease of 30 kJ/mol. At low heating rate it emerges clearly that the BCZT formation pass through a complex mechanism which involves the decomposition of the solid solution composed by calcium and barium carbonates. Concerning the activation energy estimated in this work for the BCZT formation, it is important to highlight that this value is significantly lower than that reported in the current literature. Louaer and collaborators, upon a detailed kinetic studies, obtained an activation energy of 386 kJ/mol for the crystallization of the 0.5 $(Ba_{0.85}Ca_{0.15})$ TiO_3-$Ba(Zr_{0.1}Ti_{0.9})$ system prepared by mechanical processing (planetary mill) of the $BaCO_3$, $CaCO_3$, ZrO_2 and TiO_2 powders using ethanol as solvent[20]. Just for comparison, the activation energy for the formation of $BaTiO_3$ and $BaZrO_3$ were estimated to be 361 kJ/mol and 290 kJ/mol, respectively, when the solid-state reaction has been conducted under air [21,22].

Concerning the kinetic mechanism which governs the formation of the here investigated BCZT, a further kinetic analysis, free from a model assumption and kinetic parameters, was applied to the experimental DSC curved presented in Figure **Figure 9.3.23(a).**The approach used a truncated Sestak-Berggren equation here reported:

$$f(\alpha) = c\alpha^m(1-\alpha)^n \qquad (9.3)$$

Tuning *m* and *n* parameters it is possible to fit different kinetic model based on determined mechanism [19]. The kinetic analysis was then based on the equation 9.4:

$$ln\left(\frac{\frac{d\alpha}{dt}}{(1-\alpha)^n\alpha^m}\right) = ln\,(cA) - \frac{E_a}{RT} \qquad (9.4)$$

Where A is the pre-exponential factor or frequency factor. The left-hand side of the equation 9.4 was plotted against 1/T and the best linearity is determined varying *m* and *n* parameters to obtain the maximum linear correlation coefficient. For the experimental data introduced in the equation 9.4 (for α range of 0.1-0.9), the *m* and *n* values were 0.712 and 0.701, respectively, obtaining the function: $f(\alpha) = c\alpha^{0.712}(1-\alpha)^{0.701}$. This wan then normalized at α= 0.5 and compared with the theoretical kinetic model reported in **Table 9.3.3**.

Table 9.3.3 Differential form for the most frequently used mechanism of nucleation and growth models

Model	Differential Form	Description
Nucleation and growth models – Sigmoidal curves		
Avrami-Erofeyev A1 (n=1)	$n(1-\alpha)[\ln(1-\alpha)]^{1/n}$	One-dimensional growth with interface-controlled reaction rate
Avrami-Erofeyev A2 (n=2)		Two-dimensional growth of existent nuclei at constant interface rate
Avrami-Erofeyev A3 (n=3)		Three-dimensional growth of existent nuclei at constant interface rate

As shown in **Figure 9.3.23**, the parabolic Avrami-Erofeyev models, are the function that best described the experimental data for the BCZT formation process. The choice on the models presented in **Table 9.3.3**, was made according to the lower RSS (residual sum of squares) values for A2, A3, A3.5 and A4.

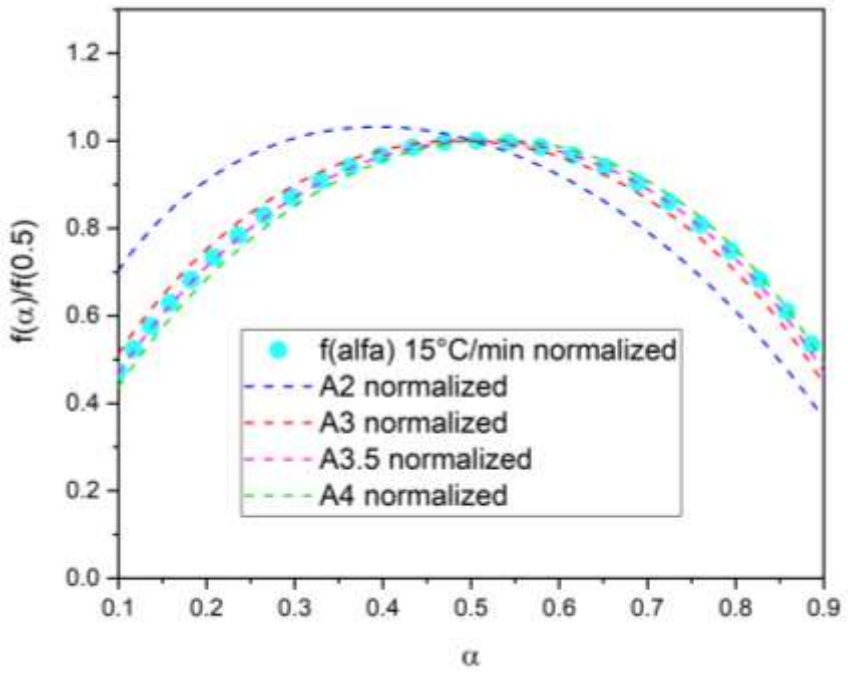

Figure 9.3.24 Comparison of ideal normalized kinetic models (dashed lines) with the $f(\alpha)$ function (pale blue solid circle) obtained from the kinetic analysis of the DSC curve acquired at heating rate of 15°C/min.

The 3.5 model presented the best results for the experimental data with β = 15°C/min, and according to the **Table 9.3.3**, it can be associated with a three-dimensional growth mechanism of the nuclei. This results, is only in part in agreement with the recent result reported by Louaer and collaborators, which evidenced a clear A3 model [20]. This further provides the fact that in the latter the formation of BCZT starting from the decomposition of β-$BaCO_3$ at high temperature, as also corroborated by the *in situ* experiment performed on the unmilled system. For the ABL_p system, the α-β transformation of the $BaCO_3$ phase did not occur because the reagents milled were able to react at lower temperature before that polymorphic transformation should take place. This provides an explanation why the micro mechanism of BCZT changed. Furthermore, in order to further assess the validity of combined kinetic model here presented, the reconstruction of the experimental curves (**Figure 9.3.20(b)**) has been obtained by using simulated kinetic curves with the form of:

$$\alpha = 1 - e^{-(k*t^n)} \qquad (9.5)$$

Where *n* is the Avrami parameter estimated from the model identified and *k* the apparent constant which can be calculated starting from the pre-exponential factor A, that was determined from the following equation:

$$A = \frac{-\beta E_a}{T_{max}^2 R\, f'(\alpha)} e^{\frac{E_a}{RT_{max}}} \qquad (9.6)$$

The subscript *max* is referred to the maximum rate of the differentiate kinetic curve at the heating rated used. **Figure 9.3.24** shows the numerically simulated curves (red solid line) which, for each heating rates, match very well the *α-t* curves, proving the validity of the kinetic parameters.

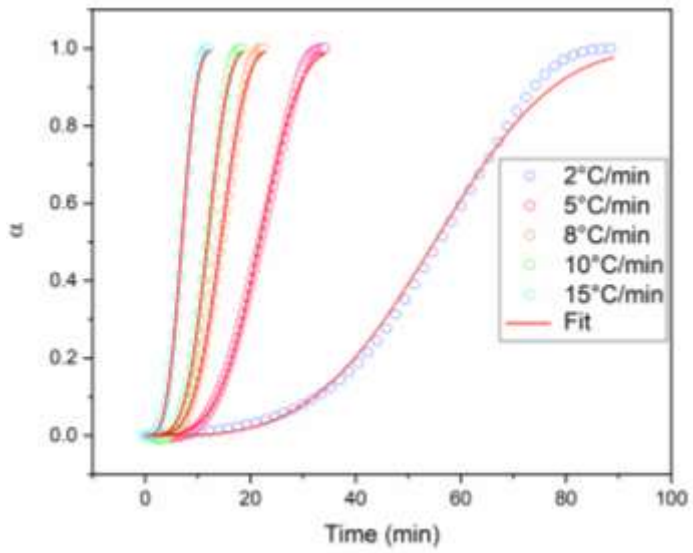

Figure 9.3.25 Curved simulated (red solid line) using the kinetic parameters estimated from the combined kinetic analysis applied to the experimental curves acquired at different heating rates.

Once the model is selected and verified, it has been used to fit the experimental XRD data reported in **Figure 9.3.7**, with the aim to better understand the mechanism which governs the whole process of the BCZT formation. The master plots have been applied to both the BCZT formation and $BaCO_3$ decomposition steps, which occurred simultaneously.

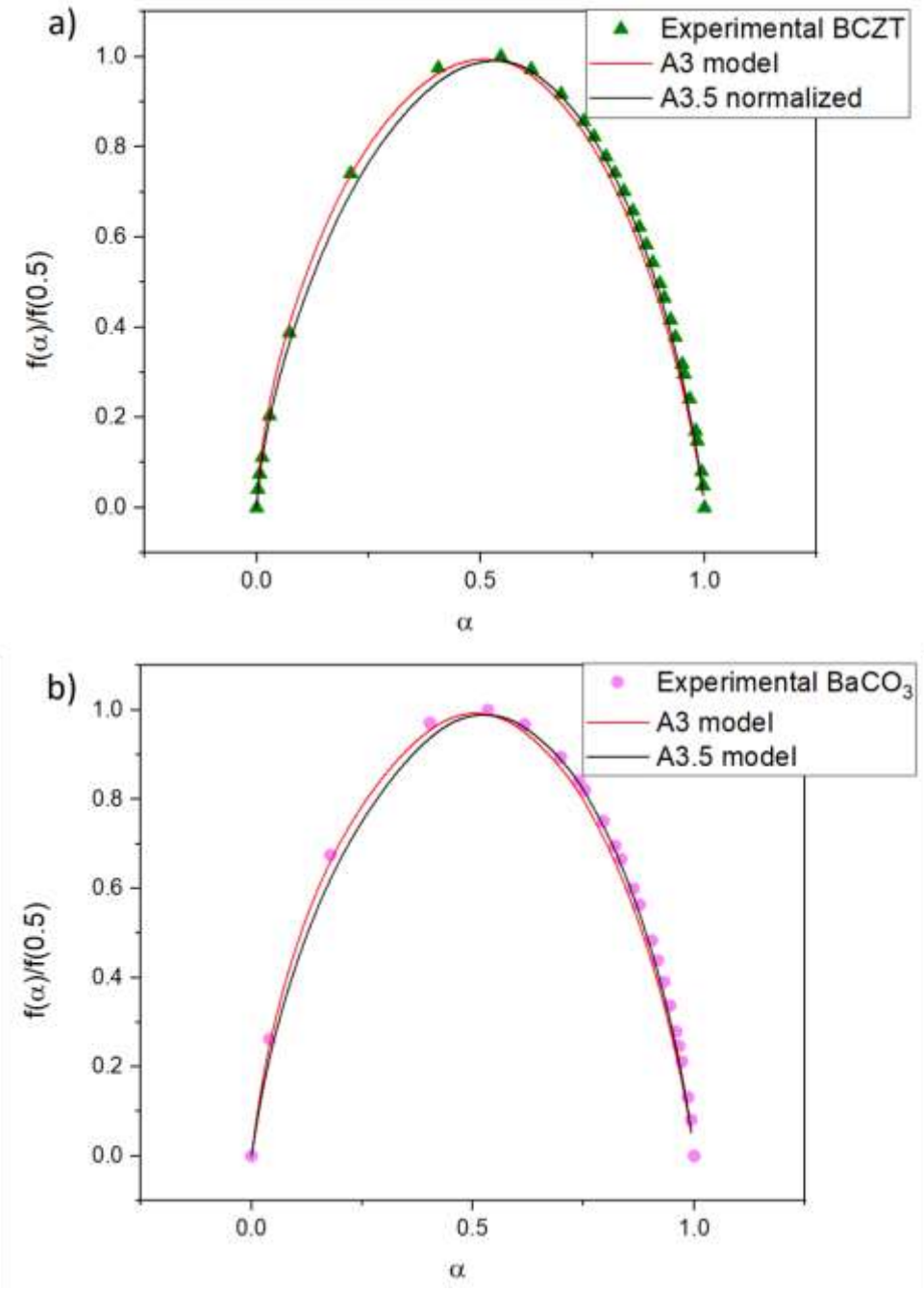

Figure 9.3.26 Comparison of ideal normalized kinetic models (solid lines) with the $f(\alpha)$ functions, obtained from the XRD data acquired at increasing temperatures.

As shown in **Figure 9.3.25**, the master plots A3 and A3.5 represent the best fits for both the curves (green triangles for the BCZT formation and magenta circles for the $BaCO_3$ decomposition). However, the mechanism supposed seems to vary at different extent of reaction ranging from A3 ($0<\alpha<0.5$) and A3.5 ($0.5<\alpha<1$). On the other hand, a tridimensional growth mechanism has been further support. Unfortunately, no data about the decomposition mechanism of α-$BaCO_3$ are reported in the current literature and, for this

reason, it is not possible at moment to have a comparison. In this sense, this work represents a first attempt this process and despite the promising result obtained, the kinetic study needs to be further corroborated by isothermal experiments.

9.4 Conclusions

In this work, we investigated the impact of processing route on thermal behaviour of BCZT precursors ($BaCO_3$, $CaCO_3$, ZrO_2, TiO_2). In order to characterize the decomposition products evolved and the formed compounds, we performed *in situ* SR-PXD experiments. It was assessed that a preliminary mechanical treatment is effective in reducing the BCZT temperature formation with respect to the un-milled mixture of reactants ($\Delta T=200°C$). Furthermore, the combination of attrition ball-milling and freeze drying allows to use distilled water as liquid medium. This can be promising for industrial scaling up allowing at the same time to decrease the synthesis temperature and to avoid the use of organic solvents. It must be highlighted that in the *in situ* experiments the formation of stable ternary oxides such as $CaTiO_3$ and $BaZrO_3$ was not noticed, maybe due to the high heating rate and/or because these phases need longer times to crystallise during the cooling step. As the decomposition of the barium carbonates occurred at low temperature, the polymorphic transformation has been hampered then modifying the kinetic mechanism. To support this experimental evidence, a combined kinetic analysis has been conducted on the DSC curves and *in situ* XRD data. Ther formation of BCZT follows an A3.5 Avrami-Erofeyev kinetic model with an activation energy of 185 kJ/mol, significantly lower with respect to the expected value. This support the thesis that the milling processing, conducted by attritor ball milling, is crucial to activate the reactants, allowing to decrease the BCZT formation temperature.

9.5 Appendix

Table A 9.5.1 Evolution of lattice parameters of $BaCO_3$ as a function of the temperature in the unmilled system MMp.

$BaCO_3$ Pnmc					
Temperature(°C)	a(Å)	b(Å)	c(Å)	Volume(Å^3)	Ref.
RT	5.3103	8.9122	6.4365	304.6	[16]
RT	5.2998	8.9343	6.4279	304.4	Our work
59	5.3006	8.9349	6.4383	304.9	Our work
121	5.3019	8.9364	6.4488	305.5	Our work
155	5.3033	8.9358	6.4604	306.2	Our work
188	5.3047	8.9368	6.4719	306.8	Our work
220	5.3072	8.9370	6.4851	307.6	Our work
257	5.3089	8.9348	6.4964	308.2	Our work
292	5.3123	8.9329	6.5099	308.9	Our work
298	5.3226	8.9213	6.5374	310.4	[16]
324	5.3134	8.9334	6.5183	309.4	Our work
350	5.3150	8.9328	6.5272	309.9	Our work
395	5.3204	8.9308	6.5641	311.9	Our work
425	5.3217	8.9326	6.5784	312.7	Our work
475	5.3208	8.9321	6.5708	312.3	Our work
486	5.3293	8.9275	6.6076	314.4	[16]
500	5.3218	8.9325	6.5809	312.8	Our work
550	5.3236	8.9333	6.5989	313.8	Our work
575	5.3248	8.9334	6.6103	314.4	Our work
602	5.3257	8.9339	6.6221	315.1	Our work
625	5.3264	8.9347	6.6294	315.5	Our work
650	5.3273	8.9357	6.641	316.1	Our work
674	5.328	8.9361	6.6528	316.8	Our work
691	5.3336	8.9354	6.6877	318.7	[16]
699	5.3286	8.9361	6.6639	317.3	Our work
725	5.3291	8.9397	6.6765	318.1	Our work
751	5.3297	8.9383	6.6898	318.7	Our work
777	5.3301	8.9395	6.7038	319.4	Our work
790	5.3303	8.9401	6.7116	319.8	Our work
794	5.3333	8.9417	6.7339	321.1	[16]
803	5.3302	8.9411	6.7187	320.2	Our work
816	5.3301	8.9419	6.7263	320.6	Our work
829	5.3303	8.9427	6.7341	321.0	Our work
842	5.3304	8.9446	6.7417	321.4	Our work
855	5.3312	8.9471	6.7472	321.8	Our work

Table A 9.5.2 Evolution of lattice parameters of $BaCO_3$ as a function of the temperature in the unmilled system MMp.

	$BaCO_3$ R-3m		$BaCO_3$ R-3c		
Temperature(°C)	a(Å)	c(Å)	a(Å)	c(Å)	Ref.
813	5.2223	10.49			[16]
825	5.2212	10.49			[16]
829	5.221	10.43			Our work
842	5.220	10.47			Our work
855	5.219	10.48			Our work
869	5.218	10.51	5.22	21.02	Our work
882	5.214	10.53	5.21	21.07	Our work
896	5.209	10.56	5.21	21.13	Our work
909	5.204	10.59	5.20	21.20	Our work
923	5.198	10.63	5.20	21.26	Our work
951	5.186	10.69	5.18	21.44	Our work
964	5.184	10.73	5.17	21.55	Our work

Table A 9.5.3 Evolution of lattice parameters of $BaCO_3$ as function of the temperature in the activated system ABLp.

$BaCO_3$ *Pnmc*					Wt. % of BCZT	BCZT crystallite size(Å)
Temperature(°C)	a(Å)	b(Å)	c(Å)	Volume($Å^3$)		
RT	5.2901	8.9423	6.4239	303.89	-	-
133	5.2942	8.9488	6.4584	305.98	-	-
236	5.2999	8.9477	6.4893	307.74	-	-
316	5.3040	8.9490	6.5151	309.24	-	-
386	5.3072	8.9483	6.5423	310.7	-	-
452	5.3114	8.9481	6.5661	312.07	-	-
516	5.3181	8.9457	6.5922	313.62	-	-
567	5.3273	8.9374	6.6249	315.43	-	-
574	5.3278	8.9375	6.6263	315.53	-	-
597	5.3291	8.9383	6.6395	316.26	-	-
602	5.3296	8.9379	6.6413	316.36	-	-
608	5.3300	8.9380	6.6448	316.56	-	-
615	5.3304	8.9379	6.6485	316.75	-	-
622	5.3308	8.9377	6.6519	316.93	1.48	-
629	5.3311	8.9379	6.6553	317.12	3.3	-
636	5.3315	8.9378	6.6624	317.48	9	-
643	5.3314	8.9383	6.6623	317.48	8	158
650	5.3316	8.9391	6.6660	317.7	22	331
656	5.3314	8.9390	6.6691	317.83	40	474
662	5.3314	8.9389	6.6725	317.99	55	493
669	5.3312	8.9382	6.6756	318.1	60	510
675	5.3315	8.9382	6.6792	318.29	65	525
682	5.3314	8.9383	6.6828	318.46	69	539
688	5.3314	8.9383	6.6828	318.46	69	538
695	5.3315	8.9383	6.6894	318.78	74	570
701	5.3314	8.9377	6.6931	318.93	80	575

708	5.3315	8.9381	6.6963	319.1	82	588
714	5.3313	8.9381	6.6993	319.23	83	600
720	5.3309	8.9383	6.7023	319.36	85	607
727	5.3306	8.9382	6.7052	319.48	87	610
733	5.3304	8.9389	6.7080	319.62	88	610
739	5.3302	8.9389	6.7106	319.73	90	610
746	5.3301	8.9383	6.7130	319.82	91	610
752	5.3302	8.9391	6.7145	319.93	92	610
758	5.3314	8.9389	6.7149	320.01	93	616
765	5.3338	8.9399	6.7120	320.05	94	622
771	5.3369	8.9425	6.7067	320.08	95-96	628

9.6 Bibliography

1. Rödel, J.; Webber, K.G.; Dittmer, R.; Jo, W.; Kimura, M.; Damjanovic, D. Transferring Lead-Free Piezoelectric Ceramics into Application. *J. Eur. Ceram. Soc.* **2015**, *35*, 1659–1681, doi: 10.1016/j.jeurceramsoc.2014.12.013.

2. Liu, W.; Ren, X. Large Piezoelectric Effect in Pb-Free Ceramics. *Phys. Rev. Lett.* **2009**, *103*, 1–4, doi:10.1103/PhysRevLett.103.257602.

3. Li, W.; Xu, Z.; Chu, R.; Fu, P.; Zang, G. Piezoelectric and Dielectric Properties of (Ba1-XCa x)(Ti0.95Zr0.05)O3 Lead-Free Ceramics. *J. Am. Ceram. Soc.* **2010**, *93*, 2942–2944, doi:10.1111/j.1551-2916.2010.03907. x.

4. Ros-Dosdá, T.; Fullana-i-Palmer, P.; Mezquita, A.; Masoni, P.; Monfort, E. How Can the European Ceramic Tile Industry Meet the EU's Low-Carbon Targets? A Life Cycle Perspective. *J. Clean. Prod.* **2018**, *199*, 554–564, doi: 10.1016/j.jclepro.2018.07.176.

5. Ciomaga, C.E.; Curecheriu, L.P.; Lukacs, V.A.; Horchidan, N.; Doroftei, F.; Valois, R.; Lheureux, M.; Chambrier, M.H.; Mitoseriu, L. Optimization of Processing Steps for Superior Functional Properties of (Ba, Ca) (Zr, Ti)O3 Ceramics. *Materials (Basel).* **2022**, *15*, doi:10.3390/ma15248809.

6. Frattini, A.; Di Loreto, A.; de Sanctis, O.; Benavidez, E. BCZT Ceramics Prepared from Activated Powders. *Procedia Mater. Sci.* **2012**, *1*, 359–365, doi: 10.1016/j.mspro.2012.06.048.

7. Ye, S.; Fuh, J.; Lu, L.; Chang, Y.L.; Yang, J.R. Structure and Properties of Hot-Pressed Lead-Free (Ba0.85Ca 0.15) (Zr0.1Ti0.9)O3 Piezoelectric Ceramics. *RSC Adv.* **2013**, *3*, 20693–20698, doi:10.1039/c3ra43429j.

8. Mureddu, M.; Bartolomé, J.F.; Lopez-Esteban, S.; Dore, M.; Enzo, S.; García, Á.; Garroni, S.; Pardo, L. BaZrO3-BaTiO3-CaTiO3 Piezoceramics by a Water-Based Mixed-Oxide Route: Synergetic Action of Attrition Milling and Lyophilization. *J. Eur. Ceram. Soc.* **2024**, *44*, 2944–2953, doi: 10.1016/j.jeurceramsoc.2023.12.037.

9. Louaer, A.; Chaguetmi, S.; Taibi, A.; Layachi, A.; Satha, H. Crystallization Kinetics and Growth Mechanism of 0.5 (Ba 0.85 Ca 0.15) TiO 3 −0.5 Ba (Zr 0.1 Ti 0.9) O 3 Powders Prepared via Solid-State Reaction. *Phase Transitions* **2020**, *93*, 116–133, doi:10.1080/01411594.2019.1692014.

10. Mureddu, M.; Bartolomé, J.F.; Lopez-Esteban, S.; Dore, M.; Enzo, S.; García, Á.; Garroni, S.; Pardo, L. Solid State Processing of BCZT Piezoceramics Using Ultra Low Synthesis and Sintering Temperatures. *Materials (Basel).* **2023**, *16*, 945, doi:10.3390/ma16030945.

11. FiT2D Available online: https://www.esrf.fr/computing/scientific/FIT2D/.

12. Hammersley, A.P. FIT2D: A Multi-Purpose Data Reduction, Analysis and Visualization Program. *J. Appl. Crystallogr.* **2016**, *49*, 646–652, doi:10.1107/S1600576716000455.

13. Lutterotti, L.; Scardi, P. Simultaneous Structure and Size-Strain Refinement by the Rietveld Method. *J. Appl. Crystallogr.* **1990**, *23*, 246–252, doi:10.1107/S0021889890002382.

14. Mureddu, M.; Bartolomé, J.F.; Lopez-Esteban, S.; Dore, M.; Enzo, S.; García, Á.; Garroni, S.; Pardo, L. BaZrO3-BaTiO3-CaTiO3 Piezoceramics by a Water-Based Mixed-Oxide Route: Synergetic Action of Attrition Milling and Lyophilization. *J. Eur. Ceram. Soc.* **2023**, doi: 10.1016/j.jeurceramsoc.2023.12.037.

15. Yang, R.B.; Fu, W.G.; Deng, X.Y.; Tan, Z.W.; Zhang, Y.J.; Han, L.R.; Lu, C.; Guan, X.F. Preparation and Characterization of (Ba0.88Ca0.12)(Zr0.12Ti0.88)O3 Powders and Ceramics Produced by Sol-Gel Process. *Adv. Mater. Res.* **2010**, *148–149*, 1062–1066, doi:10.4028/www.scientific.net/AMR.148-

149.1062.

16. Antao, S.M.; Hassan, I. BaCO3: High-Temperature Crystal Structures and the Pmcn → R3m Phase Transition at 811°C. *Phys. Chem. Miner.* **2007**, *34*, 573–580, doi:10.1007/s00269-007-0172-8.

17. COD Database Available online: https://www.crystallography.net/cod/result.php.

18. Gil-González, E.; Perejón, A.; Sánchez-Jiménez, P.E.; Medina-Carrasco, S.; Kupčík, J.; Šubrt, J.; Criado, J.M.; Pérez-Maqueda, L.A. Crystallization Kinetics of Nanocrystalline Materials by Combined X-Ray Diffraction and Differential Scanning Calorimetry Experiments. *Cryst. Growth Des.* **2018**, *18*, 3107–3116, doi: 10.1021/acs.cgd.8b00241.

19. Vyazovkin, S.; Burnham, A.K.; Criado, J.M.; Pérez-Maqueda, L.A.; Popescu, C.; Sbirrazzuoli, N. ICTAC Kinetics Committee Recommendations for Performing Kinetic Computations on Thermal Analysis Data. *Thermochim. Acta* **2011**, *520*, 1–19, doi: 10.1016/j.tca.2011.03.034.

20. Louaer, A.; Chaguetmi, S.; Taibi, A.; Layachi, A.; Satha, H. Crystallization Kinetics and Growth Mechanism of 0.5 (Ba 0.85 Ca 0.15) TiO 3 −0.5 Ba (Zr 0.1 Ti 0.9) O 3 Powders Prepared via Solid-State Reaction. *Phase Transitions* **2020**, *93*, 116–133, doi:10.1080/01411594.2019.1692014.

21. Ubaldini, A.; Buscaglia, V.; Uliana, C.; Costa, G.; Ferretti, M. Kinetics and Mechanism of Formation of Barium Zirconate from Barium Carbonate and Zirconia Powders. *J. Am. Ceram. Soc.* **2003**, *86*, 19–25, doi:10.1111/j.1151-2916. 2003.tb03271.x.

22. Kozawa, T.; Onda, A.; Yanagisawa, K. Accelerated Formation of Barium Titanate by Solid-State Reaction in Water Vapour Atmosphere. *J. Eur. Ceram. Soc.* **2009**, *29*, 3259–3264, doi: 10.1016/j.jeurceramsoc.2009.05.031.

10 Toxicology Assessment of BCZT ceramics with different composition and prepared using different milling jars.

10.1 Introduction

As stated in Chapter 3, alternative uses of piezoceramics in biomedical field, included new frontier applications, such as piezocatalytic medicine [1], are sparking the interest of researchers in the toxicological characterization of these materials. The main characteristics that a piezoelectric material must have to be used for this purpose can be summarized as follows: excellent piezoelectric properties, good biocompatibility, degradability, and targeted stimulation of the extracellular matrix. Among others, one of the most interesting applications is tissue regeneration [2] and, in particular, bone regeneration [3]. In this scenario, Poon et al. studied the piezoelectric properties of bulk ceramic BCZT1510 and its compatibility with primary human osteoblast cells (HOBs) and primary human umbilical vein endothelial cells (HUVECs), demonstrating the high potential of BCZT as a bone replacement material due to good biocompatibility and cell proliferation and promising viability results. The authors conclude that BCZT can be successfully employed as an electrical stimulation source for bone tissues regeneration [4]. They can also be used as electroactive materials (ES) that simulate the electrophysiological microenvironment to promote bone regeneration [5]. Increased Ca^{2+} within the cell, due to the opening of voltage-gated Ca^{2+} channels, leads to increased expression of various growth factors that promote regeneration of damaged bone tissue. [6].Moreover, the inverse piezoelectric effect can have an effect on bone healing by inducing microscopic mechanical deformation of bone tissue when subjected to electrical stimulation, promoting cell differentiation and inducing biochemical changes in microcirculation around osteoblasts. Other effects detected concerns the increase of calcium deposition that leads to bone calcification and to the activation of the cyclic adenosine phosphate system in bone cells by triggering enzyme activation. In general, electrical stimulation promotes microcirculation in tissues by causing a series of cascading effects [7]. In addition, the combination of nanocrystalline BCZT with hydroxyapatite in biocompatible piezo composites has been shown to be useful for bone regeneration[8]. Among other applications, nontoxic BCZT-TiO_2 polarized coatings in

combination with low-intensity pulsed ultrasound promote calcium deposition, making them suitable for dental implants[9]. In addition, there are reports in the literature on the effectiveness of BCZT piezoelectric films as a suitable support for osteogenic differentiation of mesenchymal stem cells in bone marrow[10], in nanogenerators for biomechanical energy harvesting with BCZT nanowires and nanofibers [11], in BCZT-Ag antibacterial coatings for orthopaedic implants[12]. The interaction between these functional materials and the human organism is rather complex and the mechanism is not yet well defined. For this reason, further in-depth *in vitro* and *in vivo* studies are needed. In this scenario, due to the variability in processing routes followed and the possibility of introducing foreign ions in the material, the aim of this study was to extend the toxicological evaluation to different compositions and to evaluate the influence of different jar materials used for the ball-milling step of the solid-state processing route. The effect of these parameters on the viability of the A549 cells and the yeast *Saccharomyces cerevisiae* was evaluated. As reference, a sample produced starting from commercial $BaTiO_3$ was used (here indicated as BCZT_3).

10.2 Materials and methods

10.2.1 Materials

Ceramic powders of BCZT_1 and BCZT_2 were prepared by a solid-state route starting from a stoichiometric mixture of $BaCO_3$ (Merck, Darmstadt, Germany, >99%), $CaCO_3$ (Sigma Aldrich, St. Louis, MO, USA, >99%), TiO_2 (Merck, of nominal purity >99% composed of 85 wt.% of anatase and 15 wt.% of rutile) and ZrO_2 (Tosoh, Tokyo, Japan, monoclinic polymorph >99%). BT ceramics (BCZT_3) were prepared starting from commercial barium titanate powders (Sigma Aldrich, 99.9% trace metals basis). For BCZT_4 and BCZT_5 the following reagents have been used: $BaCO_3$ Sigma Aldrich, St. Louis, MO, USA, >99%orthorhombic (Witherite), TiO_2 Sigma Aldrich, St. Louis, MO, USA,>99.9% (99 wt.% anatase,1 wt.% rutile), ZrO_2 Alfa Aesar >99% monoclinic, $CaCO_3$ Fluka >99% trigonal polymorph.

10.2.2 Powders and ceramics processing

BCZT_1 Ceramic powders of nominal composition ($Ba_{0.92}$ $Ca_{0.08}$) ($Ti_{0.95}$ $Zr_{0.05}$) were prepared according to the powder processing described in Chapter 6. To obtain BCZT_2 ($Ba_{0.85}$ $Ca_{0.15}$) ($Ti_{0.90}$ $Zr_{0.10}$) the same procedure was followed for the BCZT_1 except for the composition chosen.

BCZT_4 ($Ba_{0.85}$ $Ca_{0.15}$) ($Ti_{0.90}$ $Zr_{0.10}$) was obtained by ball-milling the precursors using a Spex 8000 apparatus and stainless-steel jar for 6h. For BCZT_5 ($Ba_{0.85}$ $Ca_{0.15}$) ($Ti_{0.90}$ $Zr_{0.10}$) was followed the same procedure of BCZT-4 except for the material of the vial (tungsten carbide). These procedures have been reported in Chapter 5. The as-obtained powders were calcined at 1200°C for 4 h of dwell time, then shaped into disks and sintered at 1450°C for 2 h in air with a heating rate of 3°C/min.

Table 10.2.1 Procedure followed to prepare powders for toxicological evaluation.

Sample name	Composition	BM-a BM-h	Vial material	Solvent
BCZT_1	BCZT0805	ABM 6h	Teflon	Isopropanol
BCZT_2	BCZT1510	ABM 6h	Teflon	Isopropanol
BCZT_4	BCZT1510	Shaker-Spex 6h	Stainless steel	ethanol
BCZT_5	BCZT1510	Shaker Spex 5h	Tungsten Carbide	Ethanol

Legend. BM-a: Ball-milling apparatus. BM-h: Ball-milling time(h) ABM:attrition ball-milling .

The materials under study and the reference sample (BCZT_1, BCZT_2, BCZT_3, BCZT_4 and BCZT_5) were smashed in a mortar and sieved (0.125 mm mesh size) to obtain a uniform powder. Stocks of the powder materials resuspended in milli-q water and 0.05% BSA (bovine serum albumin) at 2.56 g/L were prepared to carry out the experiments. Before performing the tests, samples were vortexed at full speed and then subjected to ultrasonication for 5 min at an amplitude of 40%. Finally, before preparing the different concentrations used in the experiments, samples were vortexed again.

10.2.3 Toxicological assays: Experiments using the A549 cell line

The A549 human cell line (ATCC, CCL-185) was cultured in DMEM (Dulbecco's Modified Eagle's Medium) supplemented with 10% FCS (fetal bovine serum) and 1% penicillin/streptomycin (Sigma-Aldrich) and

maintained in an incubator under optimal growth conditions (95% humidity, 5% CO_2 and 37 °C). To evaluate the toxicity of the materials, the neutral red uptake assay was carried out. Briefly, cells were seeded in 96 well plates at a density of 3 x 10^4 cells/well and, after being incubated for 24 hours, exposed to different concentrations of the materials (6.4, 32 y 160 mg/L) diluted in DMEM supplemented with 1% FCS during 24 h. After this incubation, cells were washed with DPBS (Dulbecco´s phosphate buffered saline), and 100 µL of a neutral red solution (40 µg/mL) were added to each well and incubated for 2.5 h protected from light. Cells were then washed with DPBS, fixed with 4% formaldehyde for 2 min and washed again with DPBS. Subsequently, 150 µL of an extraction solution containing 50% ethanol 96°, 49% distilled H_2O and 1% acetic acid was added to each well, and the plate was subjected to a 10 min-moderate shaking step. Finally, 100 µL of this solution was transferred to an opaque 96 well plate, and the fluorescence was measured with a microplate reader (BioTek Synergy HT, excitation: 530/25; emission: 645/40).

10.2.4 Toxicological assays: Experiments using *Saccharomyces cerevisiae*

S. cerevisiae strain BY4741 was grown in liquid YPD medium (1% yeast extract, 1% peptone and 2% dextrose) at 30 °C on an orbital shaker at 180 rpm and, after reaching exponential growth phase (OD600=1), exposed to 160 mg/L of the materials diluted in YPD medium for a period of 2 and 24 h. To determine their effect in the viability of this microorganism, serial dilutions of each sample were prepared and seeded on YPD agar plates, which were incubated at 30 °C to determine the number of CFUs (colony forming units).

10.2.5 Statistical analysis

Data used for statistical analysis are presented as mean ± standard deviation (SD). Performing the one-way analysis of variance (ANOVA), followed by Dunnet *post hoc* test to make comparisons between every mean to the control. Statistical analyses were performed with Prism 8.0.2 (GraphPad Prism, GraphPad Software, Inc.). Differences were considered significant at $P \leq 0.05$.

10.3 Results:

10.3.1 Viability of A549 cells exposed to the materials

The viability of the A549 cell line after being exposed during 24 h to different concentrations of the materials (6.4, 32, 160 mg/L), was determined by neutral red uptake assay. The results obtained are shown in **Figure 10.3.1**. None of the compositions (including the reference sample) and jar materials caused a negative effect on the cell viability, showing all of them a similar percentage of viable cells than that of the control (cells in the absence of materials).

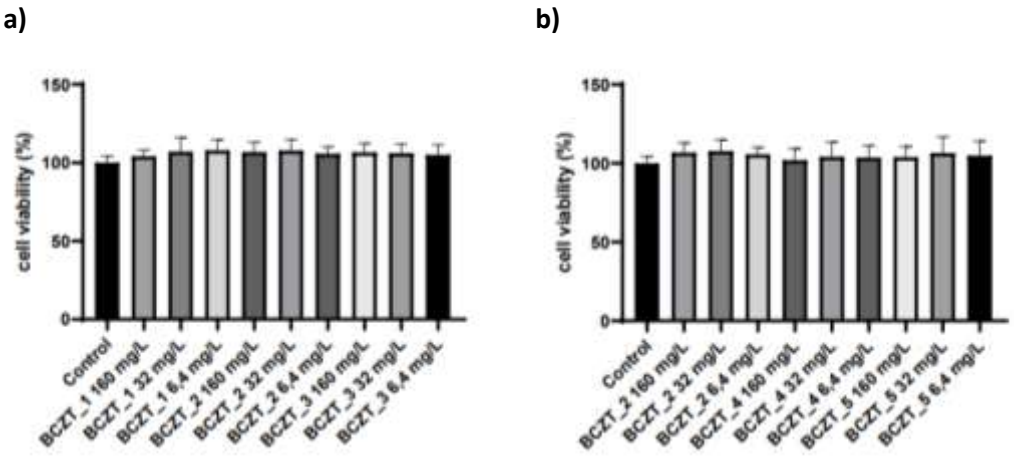

Figure 10.3.1 Viability of A549 cells (neutral red assay) after exposure to different concentrations of piezoelectric materials with different compositions **a)**and after exposure to the same material milled in different jars **b)**Results are expressed as % of control (cells in the absence of materials). Data represent the mean of 6 biological replicates obtained in 2 independent experiments ± standard deviation, SD. Differences were established using a one-way ANOVA followed by a Dunnet *post hoc* test to compare each mean to the control and were considered significant at $P \leq 0.05$.

10.4 Viability of the yeast *Saccharomyces cerevisiae* exposed to the materials

To determine the toxicological potential of these materials, the yeast *S. cerevisiae*, a widely used model organism, was used in the assays. The concentration of 160 mg/L was assessed at 2 and 24 h of exposure time. **Figure 10.4.1** shows that none of these materials, including the reference sample, caused a negative

effect on the yeast viability at both exposure times. By the same token, the different jar materials used during the ball milling step did not show to decrease this parameter.

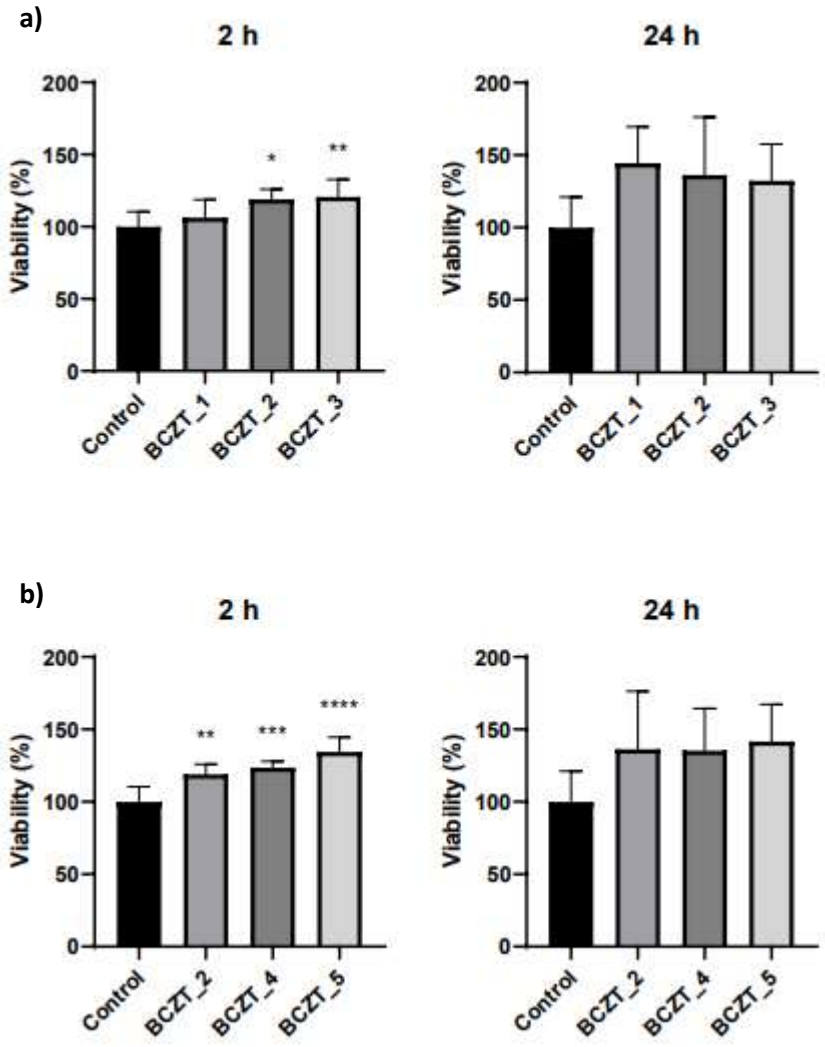

Figure 10.4.1 Colony forming units (CFUs) of *S. cerevisiae* cells after exposure to different concentrations of piezoelectric materials with different compositions **a)**and after exposure to the same material milled in different jars **b)**at two different exposure times (2 and 24 h). Results are expressed as the percentage (%) of CFUs determined for each exposure condition using as reference value non-exposed cells condition, which was assigned a value of 100%. Data represent the mean of at least 5 biological replicates obtained in 2 independent experiments ± standard deviation, SD. Differences were established using a one-way ANOVA followed by a Dunnet post hoc test to compare each mean to the control and were considered significant at $P \leq 0.05$. $**P \leq 0.01$, $***P \leq 0.001$, $****P \leq 0.0001$

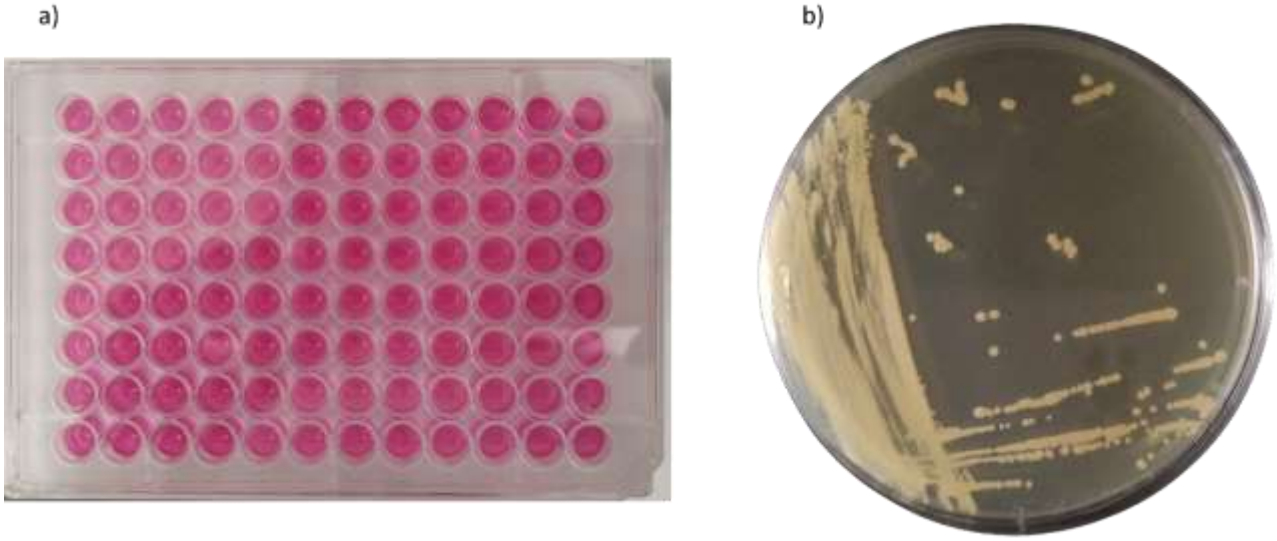

Figure 10.4.2 a)A549 cell plate, **b)***Saccharomyces cerevisiae* agar petri plate.

10.5 Conclusions

The toxicological tests carried out using both model organisms showed that neither the composition of the piezoelectric materials analysed, nor the jar materials used during the ball milling negatively affected their viability. In conclusion, these toxicological assays reveal that the BCZT materials analysed in this study are safe in terms of viability of A549 cells, a model of human cells, and *S. cerevisiae*, and a model of an environmental organism (yeast). This could be considered a first step for further studies to confirm its use in biomedical applications. In particular, biocompatibility with osteoblasts or chondrocytes also needs to be thoroughly studied by evaluating cell attachment or proliferation on surfaces made with the BCZT material. Unfortunately, regarding the concrete application of the analysed materials, as reported in Chapter 5, BCZT_4 and BCZT_5 pellets showed deteriorated piezoelectric properties due to contamination from the material jar. However, pellets prepared from powders treated with attrition ball milling equipment and a Teflon jar (BCZT_1), using appropriate calcination and sintering conditions, as reported in Chapter 7, achieved optimal piezoelectric properties (d_{33}= 455pC/N) and may be really promising for these new uses.

Based on these preliminary results, our goal in the near future is to evaluate the toxicity of pellets prepared according to the more environmentally friendly method described in Chapter 8 (d_{33}=320pC/N) and to assess the potential of these optimized materials to promote bone regeneration.

10.6Bibliography

1. Chen, S.; Zhu, P.; Mao, L.; Wu, W.; Lin, H.; Xu, D.; Lu, X.; Shi, J. Piezocatalytic Medicine: An Emerging Frontier Using Piezoelectric Materials for Biomedical Applications. *Adv. Mater.* **2023**, *35*, doi:10.1002/adma.202208256.

2. Rajabi, A.H.; Jaffe, M.; Arinzeh, T.L. Piezoelectric Materials for Tissue Regeneration: A Review. *Acta Biomater.* **2015**, *24*, 12–23, doi:10.1016/j.actbio.2015.07.010.

3. Yang, C.; Ji, J.; Lv, Y.; Li, Z.; Luo, D. Application of Piezoelectric Material and Devices in Bone Regeneration. *Nanomaterials* **2022**, *12*, 4386, doi:10.3390/nano12244386.

4. Poon, K.K.; Wurm, M.C.; Evans, D.M.; Einarsrud, M.A.; Lutz, R.; Glaum, J. Biocompatibility of (Ba,Ca)(Zr,Ti)O3 Piezoelectric Ceramics for Bone Replacement Materials. *J. Biomed. Mater. Res. - Part B Appl. Biomater.* **2020**, *108*, 1295–1303, doi:10.1002/jbm.b.34477.

5. Tigunta, S.; Pisitpipathsin, N.; Kantha, P.; Eitssayeam, S.; Rujijanagul, G.; Tunkasiri, T.; Pengpat, K. Electrical Properties of Calcium Phosphate/BZT Bioglass-Ceramics Prepared by Incorporation Method. *Ferroelectrics* **2014**, *459*, 188–194, doi:10.1080/00150193.2013.849527.

6. Zheng, T.; Huang, Y.; Zhang, X.; Cai, Q.; Deng, X.; Yang, X. Mimicking the Electrophysiological Microenvironment of Bone Tissue Using Electroactive Materials to Promote Its Regeneration. *J. Mater. Chem. B* **2020**, *8*, 10221–10256, doi:10.1039/d0tb01601b.

7. Jin, Z.; Lu, B.; Xu, Y.; Zhang, X. Lead-Free Piezoelectric Ceramics – An Electroactive Material That Provides Electrical Stimulation Cues for Bone Regeneration. *Process. Appl. Ceram.* **2023**, *17*, 214–235, doi:10.2298/PAC2303214J.

8. Manohar, C.S.; Kumar, B.S.; Sadhu, S.P.P.; Srimadh, S.K.; Muthukumar, V.S.; Venketesh, S.; Varma, K.B.R. Novel Lead-Free Biocompatible Piezoelectric Hydroxyapatite (HA)-BCZT (Ba0.85Ca0.15Zr0.1Ti0.9O3) Nanocrystal Composites for Bone Regeneration. *Nanotechnol. Rev.* **2019**, *8*, 61–78, doi:10.1515/ntrev-2019-0006.

9. Wu, C.; Zhang, C.; Yan, X.; Cheng, J.; Chen, L.; Tang, Y.; Zhao, K. Preparation and Biological Properties of BCZT/TiO2 Electrokinetic Conversion Coating on Titanium Surface in Vitro for Dental Implants. *Surf. Coatings Technol.* **2023**, *468*, 129746, doi:10.1016/j.surfcoat.2023.129746.

10. Scarisoreanu, N.D.; Craciun, F.; Ion, V.; Birjega, R.; Bercea, A.; Dinca, V.; Dinescu, M.; Sima, L.E.; Icriverzi, M.; Roseanu, A.; et al. Lead-Free Piezoelectric (Ba,Ca)(Zr,Ti)O3 Thin Films for Biocompatible and Flexible Devices. *ACS Appl. Mater. Interfaces* **2017**, *9*, 266–278, doi:10.1021/acsami.6b14774.

11. Hanani, Z.; Izanzar, I.; Amjoud, M.; Mezzane, D.; Lahcini, M.; Uršič, H.; Prah, U.; Saadoune, I.; Marssi, M. El; Luk'yanchuk, I.A.; et al. Lead-Free Nanocomposite Piezoelectric Nanogenerator Film for Biomechanical Energy Harvesting. *Nano Energy* **2021**, *81*, doi:10.1016/j.nanoen.2020.105661.

12. Wu, C.; Zhang, C.; Yan, X.; Liang, Q.; Zhao, K.; Tang, Y. Preparation and Antibacterial Properties of BCZT-Ag Piezoelectric Coating on Titanium Surface for Orthopedic Implants. *Ceram. Int.* **2024**, *50*, 4296–4306, doi:10.1016/j.ceramint.2023.10.261.

11 *In situ* poling/temperature experiments using an innovative multifunctional device: preliminary results on BCZT ceramics.

11.1 Introduction

As remarked in the previous Chapter, *in situ* XRD experiments can provide a lot of important crystallographic information, useful to investigate the synthesis step [1]. Other uses include phase diagram investigations, such as those conducted by Keeble and colleagues which exploited *in situ* measurements to reformulate the structural phase diagram of the BCTZ, introducing the orthorhombic phase in addition to the rhombohedral and tetragonal ones [2]. Since post-processing steps are of equal importance in obtaining optimal piezoelectric properties, *in situ* studies can also be used to optimise the poling process. In this view, Li and coauthors carried out electric field dependent XRD experiments using photon source and temperature in the range of −53 °C to 120 °C on BZT-BCT piezoceramics. They conclude that the Field cooling technique was found to be very effective in increasing ceramics performances [3]. Another use of *in situ* diffraction is the evaluation of the percentage of 90° domains reorienting with the application of the Electric Field and the observation of relaxation phenomena after its subtraction [4,5]. Using Synchrotron X-ray absorption near edge structure (XANES) technique Munthala and his group investigated the local structure, the domain orientation, and Ti off-center displacement in unpoled and poled BCZT ceramics retrieving the quantitative and qualitative analysis of domain orientation and Ti off-center displacement [6]. As demonstrated by Reyes-Montero et al, synchrotron XRD measurements together with Confocal Raman and Photoacustic study can help in understanding the relevance of field- induced and compositionally driven phase transitions in BCZT1510 [7]. On the one hand, all the data collected allow us to implement knowledge on these functional materials, on the other hand, the above-mentioned measurements are difficult to perform for this type of investigation, because they are usually carried out at synchrotron beamlines and cannot be performed routinely with laboratory equipment. Combining multiple and alternative *in situ* laboratory techniques, such as laser vibrometer, *in situ* quasi static method and variable temperature X-ray diffraction and dielectric

temperature spectrum test, Zhao et al. revealed the origin of thermal depolarization of piezoceramics, included BCZT [8]. Guo et al performed *in situ* XRD experiments on BCZT1015 investigating on the poling and repoling microstructural origins. The authors conclude that the ceramic is extremely responsive to the poling fields and that the extraordinary piezoelectricity is due to the structural instability and the elastic softening. They observed the presence of a unique single-domain state with poling fields in the range of 3–6 kV/cm in addition to polarization domains phenomenon [9]. Laying on this basis, our group developed a patented multifunctional device, called X-poll cell, for *in situ* poling/temperature measurement customized to the common laboratory diffractometers [10]. The principal innovation of this poling apparatus is the possibility of heating the sample and applying the electric field and at the same time monitoring the evolution of crystalline phases. These features can be very useful for studying lead-free piezoceramics like BCZT. As reported in Chapter 4, the X-poll cell allows to perform the ceramic poling the material by applying an adequate electric field (up to 30 KV/cm) in the range of temperature of 25 °C - 140°C. In order to monitor crystalline changes as a function of the applied electric field, it is necessary to apply an electrode that does not interfere with the signals of the perovskite lattice and that guarantees good electrical conductivity to allow the poling process. In this aim, a thin layer of nanometric Au was applied on ceramics. To find the optimal Au electrode thickness, avoiding the variability due to not optimal microstructure, several preliminary tests were conducted, first on barium titanate (BT) ceramics, then the acquired know-how was applied to BCZT ceramics. The composition selected, BCZT0805, is the same investigated for the isopropanol (and water routes, described in Chapter 7 and 8, respectively. In addition, since it was found out that it presented a single tetragonal P4mm crystal structure, accurately determined at synchrotron Alba facility, it can allow an easier control of *in situ* poling process. This feature is a key point for the industrial production of piezoelectric ceramics. Starting from the work of Guo et al. on BCZT1015 composition [9], we performed *in situ* XRD experiments using the X-poll device and the common laboratory diffractometer in the aim of monitoring the lattice evolution as a function of Electric Field and temperature to individuate poling microstructural origins.

11.2 Materials and methods

11.2.1 Powders and ceramics processing

BT ceramics were prepared starting from commercial barium titanate powders (Sigma Aldrich, 99.9% trace metals basis). The powders were ground into an agate mortar for 3 minutes, then few drops of PVA binder solution (3 wt.%) were added. The forming step was performed using a hydraulic press with 220 kg/cm^2 of pressure for 30 minutes. The as-obtained green body was then sintered at 1300°C for 2h in air.

BCZT0805 ceramics were prepared according to the experimental section of Chapter 7 and Chapter 8, summarised as follows: after being lyophilised the powder has been calcined at 700°C for 2 h, milled with attrition ball-mill and then pressed into pellet with a uniaxial press (1.2 tons for 3 min) and the densified by using a two-step sintering method at 900°C for 3 h and 1280°C for 6 h as final plateau.

BT and BCZT sintered pellets have been polished down to 1 mm and then annealed again (1150°C 15 min) to remove stress and preferential crystallographic orientation. The density was then measured by using geometrical method. *In situ* XRD synchrotron experiments were performed at BL16 Notos Beamline (Alba). One selected pellet was polished and measured at the lowest energy value at which there was sensible transmission, *e.g.*, 21 KeV, equivalent to λ = 0.59037 Å (E = hc/l). The measurement was performed in transmission without spinning, taking different 5 measurements in different points of the sample moving the beam (800 microns x 400 microns, horizontal x vertical) to get a better average measurement and to avoid the influence of the texture. The average measurement has been considered in the final resulting curve.

Based on previous experiments on Barium Titanate ceramics, *in situ* poling/temperature experiments measurements were performed on BCZT ceramics using the X-poll cell, already described in Chapter 4 and here reported in Figure 1. For *in situ* temperature measurements the pellet was used as annealed. Whereas, for *in situ* poling experiments Au electrodes have been applied using an auto sputter coater (Agar Scientific) equipped with graphite and Au deposition system.

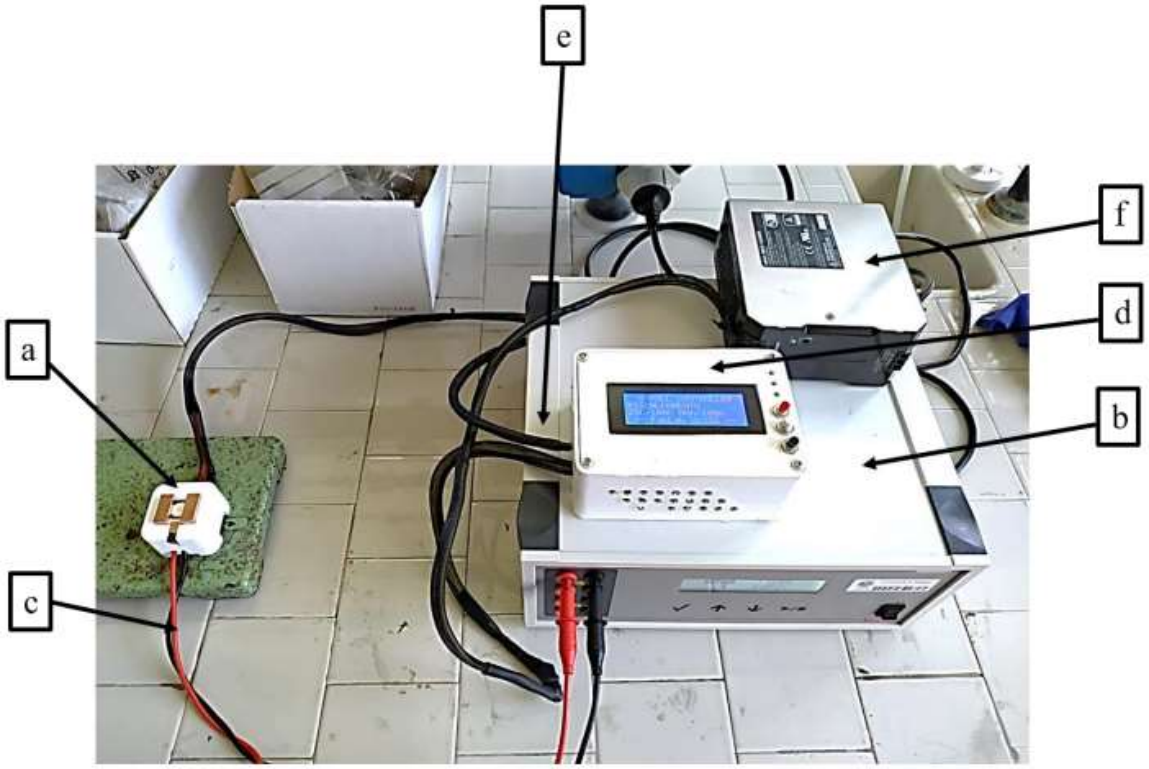

Figure 11.2.1 Complete setup assembled of X-Poll cell. Poling cell **a)** Current generator or power supply **b)** Positive and negative connection cables **c)** between X-poll cell and current generator ARDUINO temperature control circuit **d)** Connection cables **e)** for temperature control and poling cell Heating system power supply **f)** [10].

Structural *in situ* and *ex situ* investigations were conducted using a Rigaku SMARTLAB diffractometer with a rotating anode source of copper (λ = 1.54178 Å) working at 40 kV and 100 mA. The diffractometer is equipped with a graphite monochromator and a scintillation tube in the diffracted beam and with an automatically alignment system (Z-scan alignment). The specific set-up used for *in situ* temperature and poling experiments is shown in **Figure 11.2.2 a** e **b** respectively.

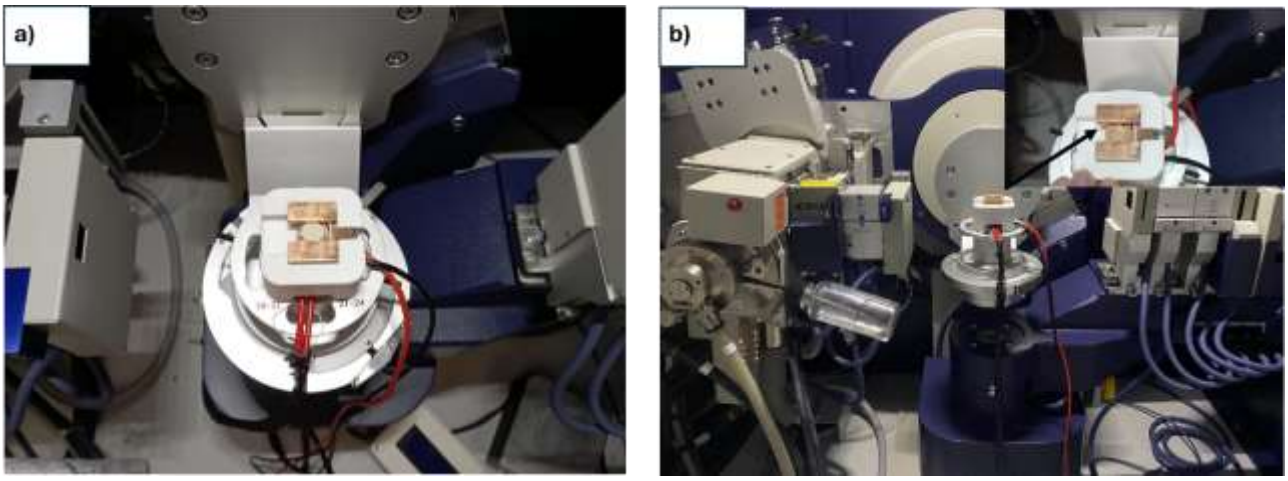

Figure 11.2.2 Set-up for *in situ* **a)** temperature and **b)** poling experiments. The inset image in b showing the top view of pellet covered with Au layer. The X-poll cell is placed inside the diffractometer chamber.

For the *in situ* temperature and poling experiments, XRD patterns were recorded in the angular range of 15-130° using a step size of 0.05° and 4s of dwell time. The measurement was then repeated at the same temperature in the diagnostic range (44-46°) with 10s of dwell time. For *in situ* electric field experiments, XRD patterns were collected (44-46.5°) using 10s of dwell time. Both the measurement started after about 3 minutes from reaching the set temperature and the isovoltage step, respectively.

11.3 Results

BT ceramics showed a density of 5.58 g/cm^3, corresponding to 93% of the theoretical density. As shown in **Figure 11.3.1**, all the ceramics show a pure *P4mm* tetragonal structure.

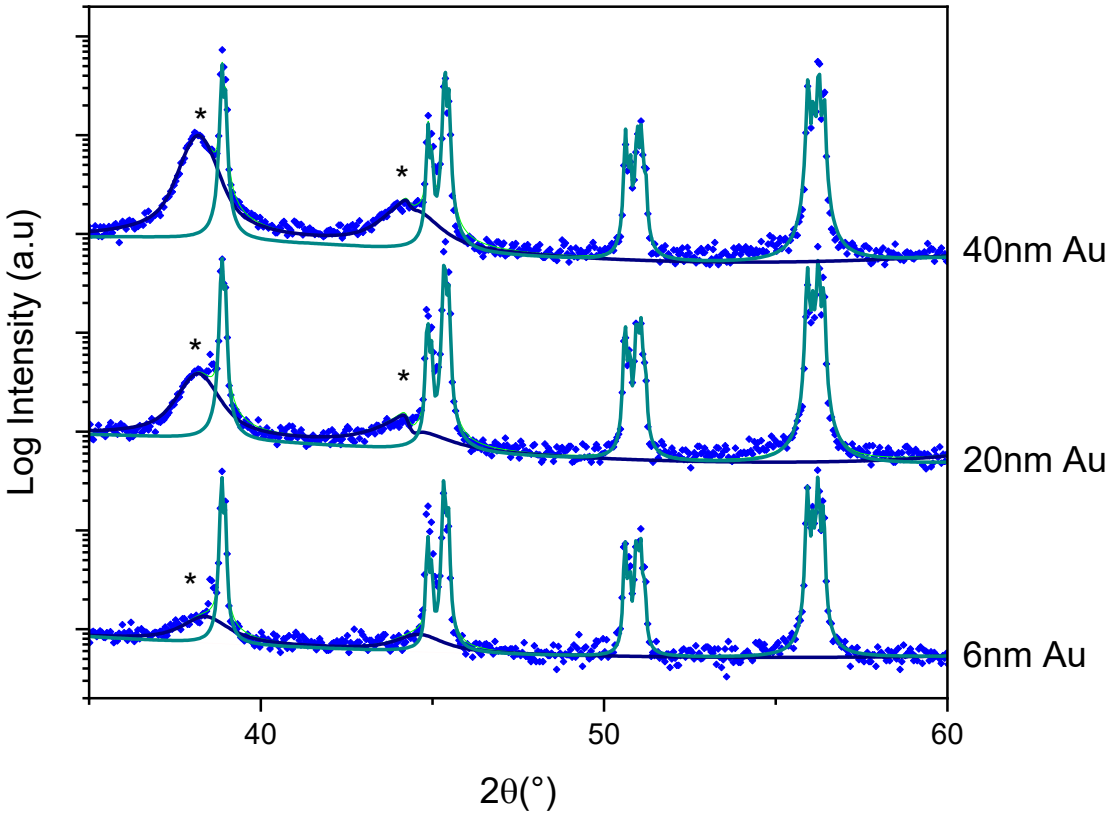

Figure 11.3.1 XRD pattern of sintered BT pellets covered with a thin layer of Au (main Bragg reflections indicated with *). From bottom to top increasing Au layer thickness (6 nm,20 nm, 40 nm). *Data points are indicated with blue dots. Fitting lines of P4mm BT phase are obtained from Rietveld refinement (olive-coloured full lines).*

As reported in **Figure 11.3.2** and **Table 11.3.1**, all the ceramics exhibit an evident tetragonal distortion. As clearly shown, the Au shows the typical cubic *Fm*-3*m* structure, and it does not interfere with the XRD analysis of the main perovskite.

Table 11.3.1 Crystallographic information obtained from Rietveld refinement of sintered BT ceramics at room temperature after the application of Au layer of increasing thickness (6nm, 20nm, 40nm). The cell parameter obtained for Au lattice have been also reported.

Au thickness(nm)	BT *P4mm* a (Å)	BT *P4mm* c(Å)	c/a	Au *Fm-3m* a(Å)
6	3.9972	4.0372	1.0100	4.074
20	3.9964	4.0379	1.0104	4.085
40	3.9959	4.0365	1.0102	4.036

To assess the validity of Au layers as electrodes, the BT ceramic have been successfully poled (15KV/cm and 20Kv/cm for 30 min) reaching values of d_{33} = 100-140 pC/N after 2h comparable with those reported the literature for undoped BT-based piezoceramics [11].

The as-obtained BCZT0805 pellets showed the best bulk density achieved of 5.10 g/cm^3 after polishing, corresponding to 89% of the theoretical density calculated for the specific composition. All the ceramics obtained showed a pure *P4mm* tetragonal phase without the presence of coexisting polymorphs or secondary phases. The Rietveld refinement of XRD patterns revealed a small tetragonal distortion for all reproduced ceramics (c/a= 1.004 ± 0.001) with c = 4.0202 Å.

To further assess the tetragonality of BCZT phase, a synchrotron XRD measurement was performed, and the subsequent Rietveld refinement confirmed the presence of pure tetragonal polymorph with a=4.0056 Å and c= 4.0172 Å and c/a= 1.003 ± 0.001, being in good agreement with laboratory diffractometer results (**Figure 11.3.2 and 11.3.3**).

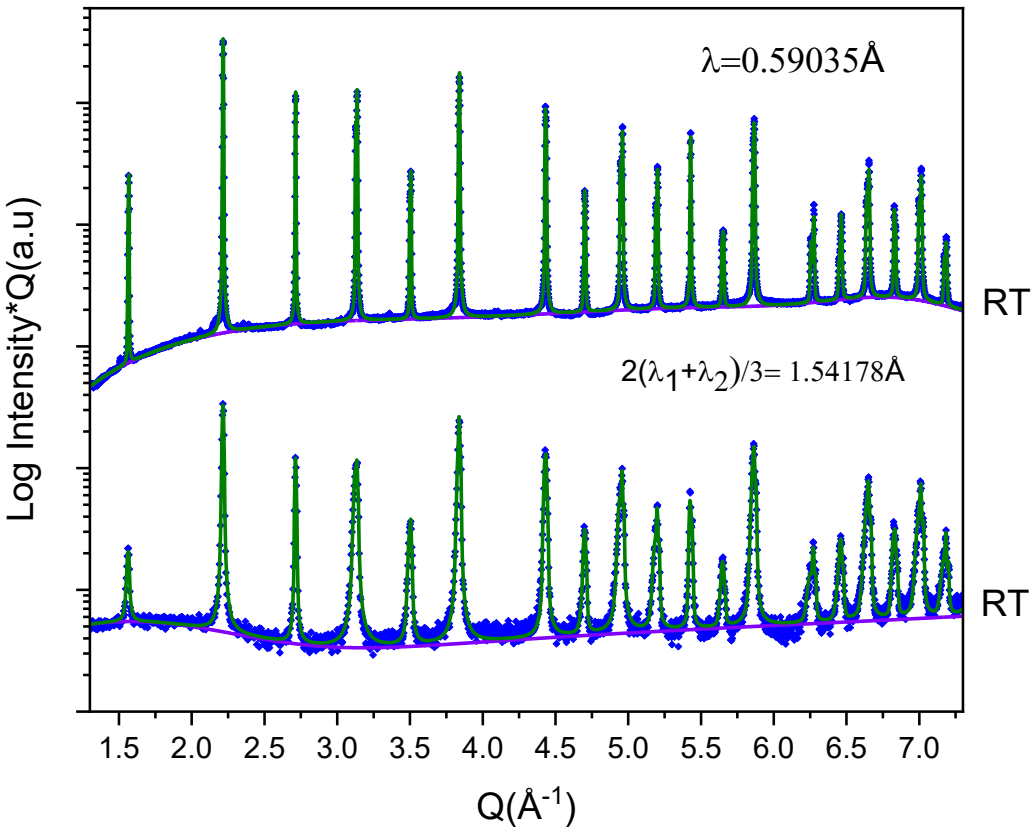

Figure 11.3.2 . Rietveld fit of XRD pattern of sintered BCZT pellets at RT at different wavelengths reported in the graph. Bottom: pattern acquired with Rigaku smart lab diffractometer. Upper: pattern acquired at synchrotron NOTOS beamline. To facilitate the comparison the measurements have been reported in Q (A^{-1}), reciprocal space. RT is for room temperature. *Data points are indicated with blue dots. Fitting lines of P4mm BCZT phase are obtained from Rietveld refinement (olive-coloured full lines).*

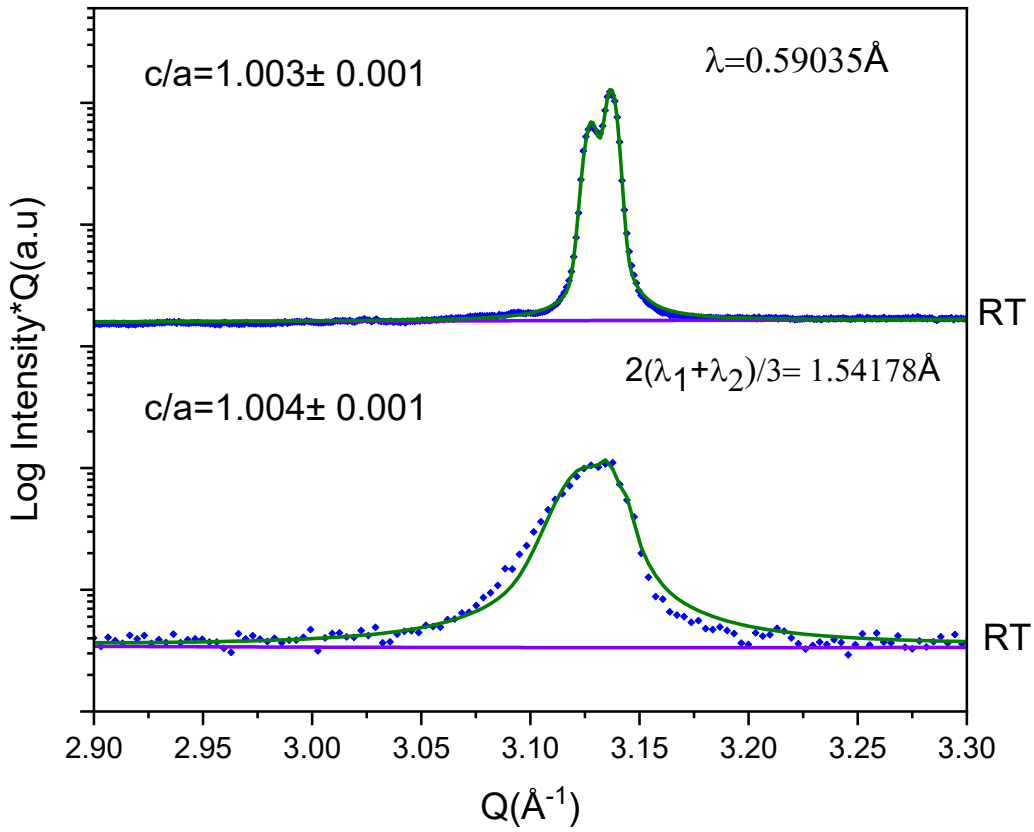

Figure 11.3.3 Magnification of diagnostic peak corresponding to 45° 2 theta. Rietveld fit of XRD pattern of sintered BCZT pellets at RT at different wavelengths. Bottom: pattern acquired with Rigaku smart lab diffractometer. Upper: pattern acquired at synchrotron NOTOS beamline. To facilitate the comparison the measurements have been reported in Q (A^{-1}), reciprocal space. *Data points are indicated with blue dots. Fitting lines of P4mm BCZT phase are obtained from Rietveld refinement (olive-coloured full lines).*

The re-annealed pellet after polishing was subjected to increasing temperatures (40°C, 60°C, 80°C and 100°C) but it was not possible to determine the exact Curie Point, corresponding to the transition from Tetragonal structure to cubic one due to the too small tetragonal distortion. For this reasons, in **Figure 11.3.4** is just reported the magnification of the diagnostic peak of XRD pattern collected *in situ* at RT and then heated at 100°C, in which the crystalline cell transformation into cubic polymorph is evident, in perfect accordance with the peak profiles evolution of BCZT ceramics as a function of the temperature, reported by Zhao et al [8].

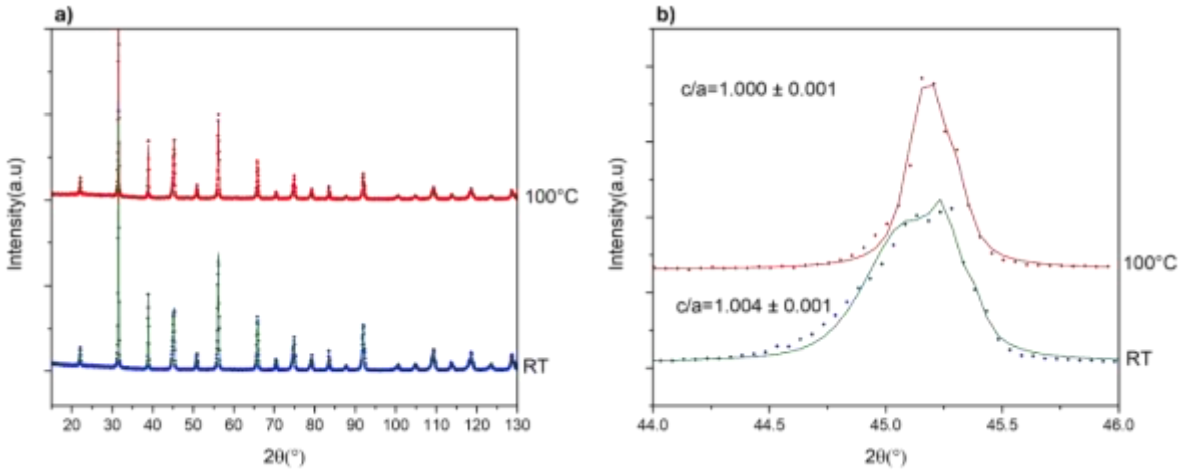

Figure 11.3.4 a) Phase evolution as a function of temperature of sintered BCZT ceramic at two different significative temperatures (RT and 100°C); **b)** Magnification of the diagnostic peak at around 45°. *Data points are indicated with blue dots. Fitting lines of P4mm BCZT phase are obtained from Rietveld refinement (olive-coloured full lines). Fitting lines of Pm-3m BCZT are obtained from Rietveld refinement (red-coloured full lines).*

As reported above for the *in situ* poling experiments, the electrodes have been successfully applied on both surfaces by using sputtering technique. The preliminary test conducted on BT ceramics allowed to apply an adequate Au layer of 40 nm. As evident in **Figure 11.3.5**, Au peaks do not overlap the BCZT peaks, especially at 45°, enabling the monitoring of crystalline phase evolution as a function of the Electric Field applied.

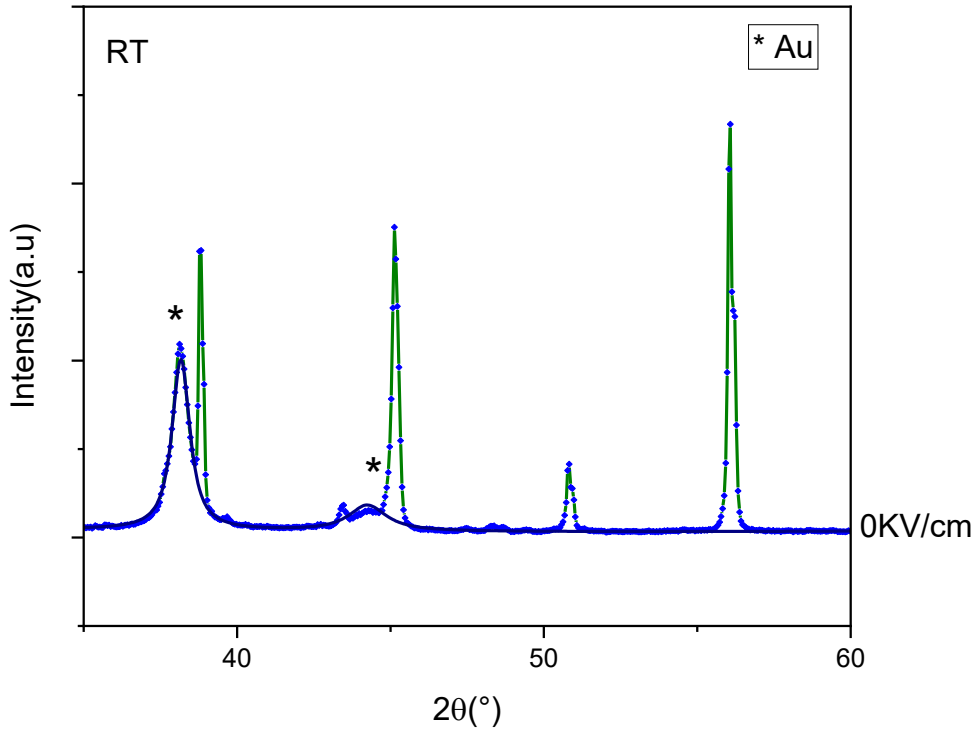

Figure 11.3.5 XRD pattern of sintered and re-annealed BCZT disk covered with a thin layer of Au.. *Fitting lines of P4mm BCZT are obtained from Rietveld refinement (olive-coloured full lines).*

Figure 11.3.6 shows the evolution, at room temperature, of the diagnostic peak at 45° as a function of the poling electric field (0-12 kV/cm). As clearly emerges, the application of the Electric Field does not have any influence on lattice tetragonal distortion. The only variation is imputable to the decrease in intensity of 002 crystalline family plane.

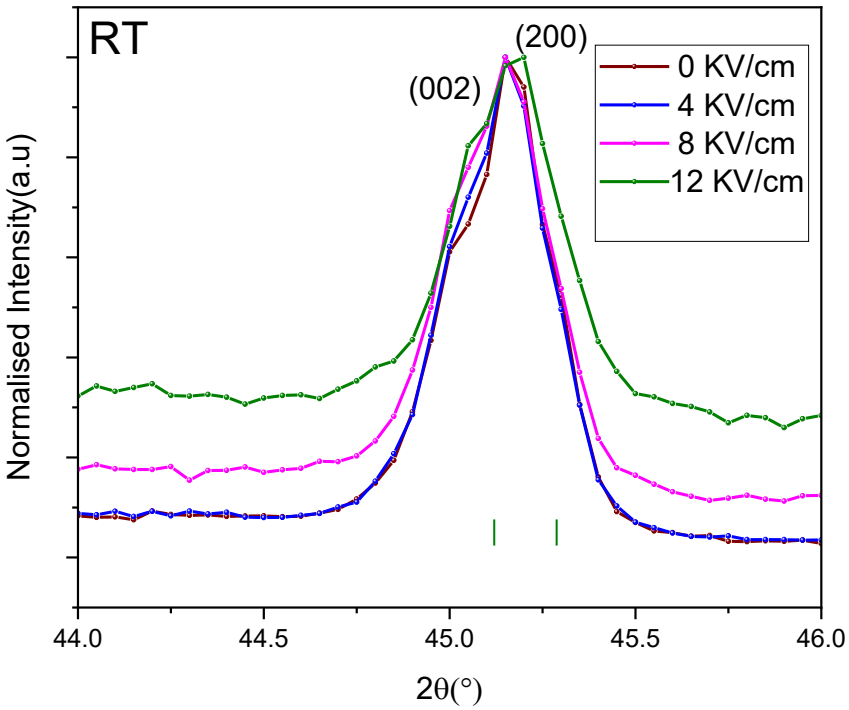

Figure 11.3.6 Room temperature *in situ* electric field experiments of sintered BCZT. Magnification of the diagnostic peak at 44-46° 2 theta. In the legend are indicated the colours corresponding to increasing Electric Field applied. Olive bars correspond to the reflections of BCZT P4mm phase in the selected angular range of 2 theta.

During poling process, as well known, two main phenomena occur perovskite ferroelectrics with tetragonal structure: the 180° domain reversal and 90° domain reorientation [12]. The intensity change of diffraction peaks is attributable to 90° domains rearrangement. As inferred in **Figure 11.3.6**, the 90° domain reorientation leads to an exchange of a- (200) and c-axis (002) of the tetragonal structure are exchanged increasing the Electric Field applied. Analysing Figure in detail, it emerges that the application of the electric field determines the preferential growth of the (002) domain, which is in agreement whit the conclusions of other authors [13].

11.4Conclusions

This work provides a demonstration of potentialities of the X-poll cell apparatus used for measuring, for the first time by our knowledge, BCZT lead-free ceramics in lab-scale facilities. Both *in situ* poling and heating tests were successfully performed. The poling experiment allowed to monitor the 90° domains reorientation,

whereas the heating one permitted to broadly determine the range of FE-PE transition. Due to the small degree of tetragonality and high porosity of the sample, it was difficult to perform all the studies planned. In the future further implementation are needed and further investigations will be provided in this direction.

11.5 Bibliography

1. Shu, C.; Reed, D.; Button, T. Mechanism of Ca-Ba Diffusion in Lead-Free (Ba,Ca)TiO 3 Piezoelectrics . *MRS Proc.* **2015**, *1782*, 23–28, doi:10.1557/opl.2015.668.

2. Keeble, D.S.; Benabdallah, F.; Thomas, P.A.; Maglione, M.; Kreisel, J. Revised Structural Phase Diagram of (Ba0.7Ca 0.3TiO3)-(BaZr0.2Ti0.8O3). *Appl. Phys. Lett.* **2013**, *102*, 0–12, doi:10.1063/1.4793400.

3. Li, B.; Ehmke, M.C.; Blendell, J.E.; Bowman, K.J. Optimizing Electrical Poling for Tetragonal, Lead-Free BZT-BCT Piezoceramic Alloys. *J. Eur. Ceram. Soc.* **2013**, *33*, 3037–3044, doi: 10.1016/j.jeurceramsoc.2013.05.032.

4. Mendiola, J.; Pardo, L. A XRD Study of 90° Domains in Tetragonal PLZT Uncer Poling. *Ferroelectrics* **1984**, *54*, 199–202, doi:10.1080/00150198408215850.

5. Pardo, L.; Carmona, F.; Gonzalez, A.M.; Alemany, C.; Mendiola, J. 90° Domain Reorientation as a Function of the Field on Ca-Modified Lead Titanate Ceramics by XRD. *Ferroelectrics* **1992**, *126*, 329–333, doi:10.1080/00150199208227081.

6. Munthala, D.; Sonklin, T.; Buatip, N.; Pomyai, P.; Amonpattaratkit, P.; Klysubun, W.; Pojprapai, S. Angle Dependent Synchrotron X-Ray Absorption Spectroscopic Structural Studies on Ba0.85Ca0.15Zr0.1Ti0.9O3 Ferroelectric Ceramics. *Scr. Mater.* **2020**, *188*, 249–253, doi: 10.1016/j.scriptamat.2020.07.021.

7. Reyes-Montero, A.; Rubio-Marcos, F.; Fuentes-Cobas, L.E.; Campo, A. Del; Castañ Eda-Guzmán, R.; Villafuerte-Castrejón, E.; Pardo, L. Confocal Raman Microscopy, Synchrotron X-Ray Diffraction, and Photoacoustic Study of Ba 0.85 Ca 0.15 Ti 0.90 Zr 0.10 O 3 : Understanding Structural and Microstructural Response to the Electric Field. **2021**, doi:10.1021/acsaelm.1c00103.

8. Zhao, H.; Hou, Y.; Zheng, M.; Yu, X.; Yan, X.; Li, L.; Zhu, M. Revealing the Origin of Thermal Depolarization in Piezoceramics by Combined Multiple In-Situ Techniques. *Mater. Lett.* **2019**, *236*, 633–636, doi: 10.1016/j.matlet.2018.11.032.

9. Guo, H.; Voas, B.K.; Zhang, S.; Zhou, C.; Ren, X.; Beckman, S.P.; Tan, X. Polarization Alignment, Phase Transition, and Piezoelectricity Development in Polycrystalline 0.5Ba(Zr0.2 Ti0.8)O3-0.5(Ba0.7 Ca0.3)TiO3. *Phys. Rev. B - Condens. Matter Mater. Phys.* **2014**, *90*, 1–10, doi:10.1103/PhysRevB.90.014103.

10. Antonio Iacomini, Davide Sanna, Sebastiano Garroni, Andrea Melis, Pier Nicola Labate, Alberto Mariani, Stefano Enzo, G.M. Polarisation and Measurement Cell for Piezoelectric Ceramic Materials 2023.

11. Villafuerte-Castrejón, M.E.; Morán, E.; Reyes-Montero, A.; Vivar-Ocampo, R.; Peña-Jiménez, J.A.; Rea-López, S.O.; Pardo, L. Towards Lead-Free Piezoceramics: Facing a Synthesis Challenge. *Materials (Basel).* **2016**, *9*, 1–27, doi:10.3390/ma9010021.

12. Zhang, X.; Lei, C.; Chen, K. Ferroelectric 90° Domain Evaluation in Tetragonal Pb(Mg 1/3 Nb 2/3)O 3 – PbTiO 3 Ceramics. *J. Am. Ceram. Soc.* **2005**, *88*, 335–338, doi:10.1111/j.1551-2916.2005.00101.x.

13. Valot, C.M.; Floquet, N.; Perriat, P.; Mesnier, M.; Niepce, J.C. Ferroelectric Domains in BaTiO 3 Powders and Ceramics Evidenced by X-Ray Diffraction. *Ferroelectrics* **1995**, *172*, 235–241, doi:10.1080/00150199508018481.

12 Conclusions e future perspective

In recent years we have witnessed a revolution in the piezoceramics market. Several companies have begun producing lead-free materials and are working to replace the toxic lead zirconate titanate, known as PZT, which dominates the market. The drive for change emerges from the new EU directives, such as “Restriction of Hazardous Substances (RoHS) Directive” of 2002, its revision (RoHS 2) in 2011 and the “Roadmap for moving to a competitive low-carbon economy in 2050” .According to these guidelines, among others, the major goals for the near future include research and development of more sustainable materials, reduction in the use of so-called critical raw materials, and new eco-sustainable processing routes with lower energy budgets, suitable for industrial scalability.

Although, as pointed out in the introduction of this thesis, some market-leading companies are already producing lead-free products, further steps are still needed for industrial production and commercialization of the barium-calcium zirconate-titanate system, well known as BCZT. Indeed, from a careful analysis of the state of the Art (Chapter 3), it emerged that there are still open issues to produce the system at industrial level. Among others, we can individuate i. The difficult reproducibility due to the complexity of the pseudo-ternary systems and the piezoceramic microstructure. ii. The scalability of processing routes proposed at laboratory level. iii. The absence of a systematic study that relates mechanical activation of powders and the decrease in processing temperatures. iv. Environmentally friendly processes. v. The partial knowledge of the toxicity of the system and few non-toxic alternative chemical methods. vi. The incomplete understanding of the formation mechanism and its kinetics, the limited availability of affordable and readily available *in situ* study methods as an alternative to expensive synchrotron facilities. In this scenario, this thesis work aims to clarify some blind spots and improve knowledge of the system under study.

The first part of this work was devoted to the analysis of the first step of the solid-state route, namely the reagents milling process, and its effects on the ceramic properties. As described in Chapter 5, for the firsts test, a shaker-type ball milling (Spex 8000 Mix/mill) was used, while different milling component (vial and ball materials of stainless-steel and tungsten carbide) have been employed for comparing the effect of metal contamination. Results of these experiments showed that the contamination coming from the milling media

and a too energetic ball-milling can lead to a decrease in the piezo and mechanical properties of the well-known composition $BC_{15}TZ_{10}$ composition. Realising the great impact of the milling materials on the ceramic electromechanical properties was a crucial starting point for the evolution of the work.

On a parallel path, aiming to get better stoichiometric control, we propose in this Thesis work an alternative and non-toxic method to produce BCZT ($BC_{15}TZ_{10}$) ceramics compared to the solid-state route. In this view, a Sol-gel Pechini modified synthesis was developed (**Chapter 6**). The first innovation concerns the substitution of toxic ethylene glycol by innocuous glycerol. The preliminary results showed that the combination of EDTA and glycerol allows obtaining final ceramics with good piezoelectric properties. In the future, we will conduct further experiments to decrease processing times-temperatures making further use of this reactive process and its flexibility to develop different compositions. Further tests are also needed to improve the quality and microstructure of the resulting ceramic.

Concerning the mixed oxides route, in the aim of overcoming the contamination issue of the milling step, a novel and straightforward protocol for the fabrication of BCZT piezoceramics, based on attrition-type ball milling in isopropanol, was developed (**Chapter 7**). The results evidenced the effectiveness of mechanical treatment, after only 6 h, in reducing the formation temperature of the main BCZT perovskite structure (from 854 °C in the unmilled powder to 582 °C for the 6 h milled powders). Single-phase perovskite BCZT ceramic with high piezoelectric sensitivity were obtained using ultra-low temperatures (700°C/2h for the synthesis and 1280 °C/6 h for the sintering as final plateau). The effectiveness of the two-step sintering method (with an intermediate step at 900°C/3h) in achieving an optimal microstructure has been demonstrated for a composition scarcely explored to date ($Ba_{0.92}Ca_{0.08}Ti_{0.95}Zr_{0.05}O_3$ or BC_8TZ_5). The as-obtained ceramics showed optimal electromechanical properties comparable to those obtained using higher energetic budgets (up to 1200°C for synthesis and up to 1450°C for sintering).

The third important innovation and achievement of this thesis work, which is based on the success of the use of attrition-type ball milling for BC_8TZ_5, was the development of a new environmentally friendly route for the fabrication of the same piezoceramics in water, using the same ultra-low temperatures reported above (**Chapter 8**). The use of distilled water as a liquid medium for attrition ball milling treatment of precursors

was made possible by the combined use of the freeze-drying technique, also a widely used technique in the industry. The second attrition ball milling of the calcined powder gave place to as-processed ceramics exhibiting a single tetragonal structure and homogeneous ceramic microstructure. After poling, the electromechanical properties comparable with other processing routes in organic media confirming the feasibility of this new route. These results represent a turning point for industrial scalability.

Based on the state of the art, the scientific community called for more in-depth studies on the synthesis step. Clarifying the mechanisms and kinetics that lead to the formation of the system is a starting point for being able to obtain the perovskite phase synthesis at lower temperatures. In this work we analysed this almost unexplored and critical aspect **(Chapter 9).** *In situ* synchrotron XRD measurements, as a function of the temperature, allowed to shed light on the impact of precursors pretreatment (attrition ball-milling and lyophilisation), on the formation of the BCZT perovskite. This study is a step toward a better understanding of the system.

With a view to alternative uses in the biomedical field, another relevant contribution of this Thesis work was the toxicological evaluation of the resulting materials (**Chapter 10**). In vitro toxicological assays performed on the final ceramics using two representative cellular models, such as A549 cells (human adenocarcinoma basal alveolar epithelium cells) and the yeast *Saccharomyces cerevisiae*, revealed the non-toxicity of the material. These results represent the first step in demonstrating the total biocompatibility of the system. In this regard, we will conduct new experiments on osteoblast cells to confirm the potential of this material for biomedical applications, particularly for bone tissue regeneration.

The last section of this Thesis work (**Chapter 11**) is dedicated to the validation for BCZT ceramics of the monitoring at industrial or laboratory scale, with the use of commonly available Cu-cathode conventional diffractometers of the *in situ* poling or *in situ* heating XRD measurement with the common laboratory diffractometer as a valid alternative to the more expensive and of more difficult accessibility, synchrotron X-ray facilities. This was done for the tetragonal structure and high piezoelectric sensitivity BC_8TZ_5 ceramics. For this scope, an innovative patented cell, totally developed at University of Sassari, was employed. The preliminary results obtained showed also that this device can be a useful tool to perform *in situ* diffraction

experiments of other lead-free piezoceramics. The possibilities for improving the cell and the quality of experiments have been evaluated and are extensive and currently ongoing.

In this Thesis work viable and scalable processing routes for producing BC_8TZ_5 and $BC_{15}TZ_{10}$ ceramics were developed. The energy budget has been strongly reduced considering both ball-milling times (6 h of attrition ball-milling before calcination and 3 h before sintering) and ultra-low processing temperatures (700°C/2 h for the synthesis and 1280°C/6h as final temperature for the sintering). Alternative, we propose a non-toxic Pechini modified sol-gel method for obtaining BCZT powders. The eco-sustainable water-based route lays the foundations for industrial scalability. The preliminary toxicological evaluation confirms the non-toxicity of BCZT. With our study on the formation process of BCZT we aimed to give further insights for a better understanding of the system that shall results in further improvements. We also think that our cell for *in situ* application of electric field and temperature can be used in the future to perform *in situ* XRD experiments with the common laboratory on other lead-free ceramics. To conclude, based on optimal piezoelectric properties achieved (graphically summarised in **Figure 12.1.1.**) at room temperature, we can affirm that the as-obtained materials are suitable for emerging biomedical applications. Further studies on piezoelectric and dielectric properties as a function of frequency and temperature will be conducted in the future to assess the material potential for other applications.

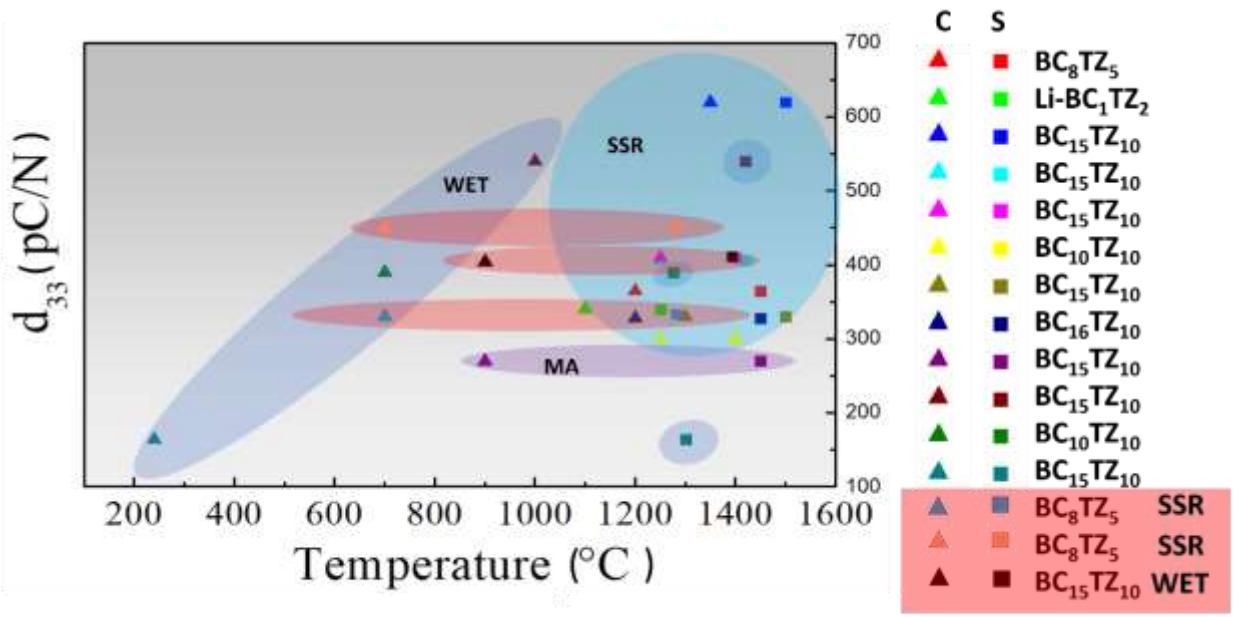

Figure 12.1.1. Comparison of the relevant piezoelectric coefficient obtained in this Thesis work with those reported in the literature (already shown in Table 7.3.5) for the same compositions and routes. C indicates the calcination step; S indicates the sintering process. WET: wet chemistry, MA: Mechano-chemical activation, SSR: Solid state route. The red insets highlight the results obtained during this thesis for the water-based route (described in Chapter 8 and shown here in blue), the route developed using isopropanol (described in Chapter 7 and shown here in orange) and the sol-gel route (Chapter 6 and shown here in black).

13 Appendix: Publication list and conferences

13.1 Publications

1. Mureddu, M.; Bartolomé, J.F.; Lopez-Esteban, S.; Dore, M.; Enzo, S.; García, Á.; Garroni, S.; Pardo, L. Solid State Processing of BCZT Piezoceramics Using Ultra Low Synthesis and Sintering Temperatures. *Materials (Basel).* 2023, 16, 945, doi.org/10.3390/ma16030945

2. Mureddu, M.; Bartolomé, J.F.; Lopez-Esteban, S.; Dore, M.; Enzo, S.; García, Á.; Garroni, S.; Pardo, L. BaZrO3-BaTiO3-CaTiO3 Piezoceramics by a Water-Based Mixed-Oxide Route: Synergetic Action of Attrition Milling and Lyophilization. *J. Eur. Ceram. Soc.* 2024, *44*, 2944–2953, doi: 10.1016/j.jeurceramsoc.2023.12.037.

3. Iacomini, A.; Garroni, S.; Mulas, G.; Enzo, S.; Cappai, L.; Mureddu, M.; Cau, C.; García, Á.; Pardo, L. Processing, Phase Evolution and Electrical Properties of “Lead Free” KNN–BF–CuO Eco-Piezoceramic from Mechanochemically Activated Precursors. *Open Ceram.* 2022, *9*, doi: 10.1016/j.oceram.2022.100247.

4. Iacomini, A.; Tamayo-Ramos, J.A.; Rumbo, C.; Urgen, I.; Mureddu, M.; Mulas, G.; Enzo, S.; Garroni, S. Processing Optimization and Toxicological Evaluation of “Lead-Free” Piezoceramics: A Knn-Based Case Study. *Materials (Basel).* 2021, *14*, 1–13, doi:10.3390/ma14154337.

5. Iacomini, A.; Garroni, S.; Mureddu, M.; Malfatti, L.; Thakkar, S.; Orrù, R.; Barbarossa, S.; Pakhomova, E.; Cao, G.; Tamayo-Ramos, J.A.; et al. Processing, Microstructure, Electrical Properties and Cytotoxic Behaviour of Lead-Free 0.99K0.5Na0.5NbO3-0.01BiFeO3 Piezoceramics Prepared Using Spark Plasma Sintering (SPS). *J. Solid State Chem.* 2022, *316*, doi: 10.1016/j.jssc.2022.123589.

6. Ren, J.; Stagi, L.; Malfatti, L.; Paolucci, V.; Cantalini, C.; Garroni, S.; Mureddu, M.; Innocenzi, P. Improving the Photocatalytic Activity of Mesoporous Titania Films through the Formation of WS2/TiO2 Nano-Heterostructures. *Nanomaterials* 2022, *12*, doi:10.3390/nano12071074.

13.2 Conferences and Proceedings

Marzia Mureddu, Antonio Iacomini, Luca Cappai, Costantino Cau, Gabriele Mulas, Stefano Enzo, Sebastiano Garroni, Sonia Lopez-Esteban, Jose' F. Bartolome' and Lorena Pardo. Impact of High-Energy Ball Milling on piezoelectric properties of lead-free BCZT (Barium Calcium Zirconate Titanate) piezoceramics. Poster Ceramics in Europe 2022, 10-14/07 /2022 Krakow, Poland.

Marzia Mureddu, Antonio Iacomini, Luca Cappai , Costantino Cau , Gabriele Mulas , Stefano Enzo, Jose' F. Bartolome' ,Sonia Lopez-Esteban , Lorena Pardo , Sebastiano Garroni. Effect of ball milling on the microstructure and piezoelectric properties of BCZT ceramics prepared by low-temperature solid state route Oral communication, Next generation chemist "La parola ai giovani".05/11/2022 Cagliari, Italy, 2022.

Marzia Mureddu, José F. Bartolomé, Sonia Lopez-Esteban, Maria Dore, Stefano Enzo, Antonio Iacomini , Álvaro García , Sebastiano Garroni and Lorena Pardo . Influence of the processing route on the performance of BCZT ceramics prepared by Solid-state route. Oral communication. XVI Spanish National Meeting on Electroceramics 28th to 30th June 2023 in Jaca, Huesca (Spain)

Marzia Mureddu, José F. Bartolomé, Sonia Lopez-Esteban, Maria Dore, Stefano Enzo, Antonio Iacomini , Álvaro García , Sebastiano Garroni and Lorena Pardo . Mechanical activation in the reduction of processing temperatures of BCZT ceramics prepared by Solid-state route. Oral communication. XVIIIth Conference of the European Ceramic Society Lyon, on 2-6 July 2023.

Marzia Mureddu, José F. Bartolomé, Sonia Lopez-Esteban, Maria Dore , Stefano Enzo , Antonio Iacomini, Álvaro García , Sebastiano Garroni and Lorena Pardo High-performance BCZT Piezoelectric ceramics achieved by ultra-low temperature processing using an environmentally friendly processing route. Oral communication. 12th Joint International Conference – Piezo2023 with Ferroelectrics: Electroceramics for End Users XII 6/11/2023 to 8/11/2023

Acknowledgments

I end this trip with immense joy and satisfaction. I am infinitely grateful for this second life as a student, for all the things I learned, for all the places I visited, for all the new experiences and for all the people I met. Each one gave me all the strength I needed to move forward.

I would like to thank my mentors,

Professor Lorena Pardo Mata, who as scientific godmother, welcomed me into the world of piezoelectric materials, teaching me everything, encouraging me, supporting me. Words cannot express the admiration I feel for you. An example for women in science, strong, determined and brilliant. Thank you for having faith in me.

Professor Stefano Enzo, who gave me the keys to the gateway to the world of crystallography, teaching me the secrets of reciprocal space. I will treasure all this. Thank you for the encouragement, with "Forza Wallace", for making learning fun, for the jokes that make a simple group a team. With your energy you have made every day less tiring.

I would like to thank my supervisor, Professor Sebastiano Garroni, who, like a coach with his athlete, took me all the way to the finish line, teaching me that marathons require perseverance and effort, but can also bring joy and satisfaction. Thank you for believing that I could do it, in all circumstances and occasions.

I would like to thank Prof. Gabriele Mulas for his support, the welcome and trust shown over the years and Dr Fabrizio Murgia for his scientific support.

I am grateful to people who become examples of life. Thank you, Sonia Lopez-Esteban, in my eyes you are a super woman, brilliant researcher, loving and extraordinary mom, generous and reliable person. You have all the superpowers. Thank you for all the things you taught me, for the days you spent together in the lab.

Many thanks to Josè Bartolomè, who welcomed me and taught me the secrets of ceramic materials always with a smile and a joke ready. Thanks to Pedro Rodriguez-Pascual Garcia for the perfect pellets and the time spent together. Thanks to the research group at ICMM, we are a great team!

Thanks to the group in Burgos, Carlos Rumbo, Sandra de la Parra and Sara. Looking forward to seeing you again and work with you!

To all my colleagues and friends in the group InmateLab, thank you for the moments we spent together, for the help and encouragement, again Fabrizio Murgia (Professeur Le Plateau), Luca Cappai(Luke Fumecase) , Costantino Cau(The Constant), Antonio Iacomini(Jack Iacomini), Laura Caggiu (Miss Cheese), Maria Domenica Simula (Mary Sunday) Matteo Poddighe (Mattew Finger). To the students, young researchers,

Simona Castia, Aurora Foddai, Roberto Dore, Ivan Da Crema, Gabriele Masia, to whom I wish a bright future. Please remember that a sandwich at Renato's or a kebab cannot be denied to anyone! Behind the researchers, professors and students there is a hidden world, the family. Like the roots of a tree, family always nourishes, supports, accompanies and welcomes. Thanks to my mother, my root and safe haven. She is home. The dictionary would not be enough to describe what you are, but there is one word that encapsulates everything: mother. Thanks also to my brother Mauro, together we have been through difficult times, but we will make it because we have those who protect us.

Last but not least, Andrea, who with love and patience not only did not clip my wings but helped me strengthen them. And nothing seems so difficult when you have someone to support you.